Title
Trash to Treasure: Extracting Cosmological Utility from Sparsely Observed Type Ia Supernovae

Author
Stahl, Benjamin Ernest

Publication Date
2021

Peer reviewed|Thesis/dissertation

Trash to Treasure:
Extracting Cosmological Utility from Sparsely Observed Type Ia Supernovae

by

Benjamin Ernest Stahl

A dissertation submitted in partial satisfaction of the

requirements for the degree of

Doctor of Philosophy

in

Physics

in the

Graduate Division

of the

University of California, Berkeley

Committee in charge:

Professor Alexei V. Filippenko, Co-chair
Associate Professor Daniel Kasen, Co-chair
Professor Saul Perlmutter
Professor Uroš Seljak

Spring 2021

Trash to Treasure:
Extracting Cosmological Utility from Sparsely Observed Type Ia Supernovae

Abstract

Trash to Treasure:
Extracting Cosmological Utility from Sparsely Observed Type Ia Supernovae

by

Benjamin Ernest Stahl

Doctor of Philosophy in Physics

University of California, Berkeley

Professor Alexei V. Filippenko, Co-chair

Associate Professor Daniel Kasen, Co-chair

Type Ia supernovae (SNe Ia) are magnificent explosions in the Cosmos that are thought to result from the thermonuclear runaway of white dwarf stars in multistar systems (see, e.g., Jha et al. 2019, for a recent review). Though the exact details of the progenitor system(s) and explosion mechanism(s) remain elusive, SNe Ia have proven themselves to be immensely valuable in shaping our understanding of the physical laws that govern the evolution of the Universe (i.e., physical cosmology). This value is manifested chiefly in two empirical facts: (i) SNe Ia are incredibly luminous (reaching the equivalent of several billion Suns), and (ii) the relatively similar peak luminosities that all "normal" SNe Ia reach can be further homogenized by exploiting a correlation with the rate of photometric evolution (e.g., Phillips 1993). Together, these facts make SNe Ia excellent extragalactic distance indicators, and their use as such led to the discovery of the accelerating expansion of the Universe (Riess et al. 1998; Perlmutter et al. 1999). Through this, the current cosmological paradigm came into favor — the so-called ΛCDM model, where the Universe consists primarily of repulsive dark energy (of which a leading candidate is Einstein's cosmological constant, Λ) and cold dark matter (CDM).

In this thesis, I present a comprehensive study that follows the entire SN Ia cosmology life-cyle, from data acquisition to cosmological analysis (albeit of a different flavor than those mentioned above). While these "bookends" provide natural segmentation points in this thesis, there is a third, intermediate segment which serves to present a complementary method for SN Ia distance measurement that is far less data intensive than conventional approaches. In this way, the segments are hierarchical, each depending on its predecessor and enabling its successor.

After appropriately setting the stage in Chapter 1, I delve into the first segment (data

acquisition) with Chapter 2, a data release and analysis of 93 multipassband SN Ia light curves collected between 2005 and 2018, and Chapter 3, a complementary release of 637 low-redshift SN Ia optical spectra from a similar time interval. In both, I describe open-source software I developed for data processing and analysis purposes, and make — in addition to the data themselves — useful, value-added data products (e.g., fitted parameters from light curves) available to the community. When combined with prior releases, the Berkeley SN Ia sample now reaches nearly 2000 optical spectra and more than 250 multiband light curves, all observed and processed with the utmost care for quality and internal consistency.

This large, homogeneous sample proves critical for the second segment of this thesis, in which I ultimately develop and validate the aforementioned technique — the snapshot distance method (SDM) — for estimating the distance to an SN Ia from sparse observations. As a prerequisite to the SDM, I develop, in Chapter 4, an open-source software package called `deepSIP` that is capable of determining the phase and light-curve shape of an SN Ia — both of which conventionally require a well-sampled light curve — from a single optical spectrum. At its heart, `deepSIP` consists of a set of three convolutional neural networks trained on a significant fraction of all publicly available SN Ia optical data (including those presented in the first segment of this thesis), with judicious augmentation steps included to promote telescope agnosticism and model robustness. The impressive performance of `deepSIP` enables the SDM, which, as I demonstrate in Chapter 5, is capable of deriving an SN Ia distance estimate from as little as one optical spectrum and one epoch of 2+ passband photometry with notable precision over a wide range of SN Ia parameters.

This leads, finally, into the last segment of this thesis (cosmological analysis), where I use the SDM to turn *trash* (i.e., SN Ia observations that were previously unusable owing to data sparsity) into *treasure* (i.e., reliable distance estimates to be used in a cosmological study). In particular, in Chapter 6, I combine a novel sample of 137 SDM-resurrected SNe Ia with a large literature sample of SNe Ia and SNe II to measure peculiar velocities and set leading (from an SN-only perspective) constraints on the cosmological parameter combination $f\sigma_8$ and the nature of bulk flows in the local Universe. Moreover, the methods by which I perform this analysis establish a reproducible and extensible blueprint for future such analyses as large-scale surveys come online and unleash an unprecedented data volume.

Dedicated to those across the globe whose lifestyles, livelihoods, and very lives have been disrupted by the COVID-19 pandemic. That this dissertation was completed in the midst of a global crisis is a testament not to myself, but to my privilege.

Contents

List of Figures

List of Tables

Acknowledgments

The profound awe of the Cosmos that was the fundamental driver in my undertaking this dissertation was born late at night sitting with my dad as a young child, just looking at the stars. To my parents, Jan and Bob: on top of the love, support, and encouragement you have always given me, I thank you most here for embracing my curious nature so early on. You didn't have the answer to every question I asked, but you encouraged me to find the answers for myself. This dissertation represents the answer to some of those questions.

As with most things worth doing, the earning of a PhD is *challenging*. It would be very easy to give all of oneself to conquering the challenge — indeed many do — but balance is the key to fulfillment. Thank you, Bodhi, Eli, and friends whose names are too numerous to list, for patiently but persistently reminding me of this on long bike rides, over shared meals, in contentious Scrabble games, during Battlestar Galactica binges, and between sips of craft beer. I also thank fellow graduate students, Caleb and Sam, for the (let's be honest, wimpy) gym sessions, help through a year of Quantum Mechanics, and hearing damage incurred at death metal shows in Oakland.

Beyond what was taught in lecture halls, I am eternally grateful to the many academic mentors who have honored me with their time, advice, and experience in my journey through higher education. To Jo-Ann Panzardi at Cabrillo College: thank you for making room for me at the last second, for the many opportunities to assist you in teaching your courses, and for so deeply and genuinely caring about me and all of your students. I'm (not) sorry I decided to pursue Physics instead of Engineering, but you should really blame Carlos! Carlos Figueroa, thank you for bringing me to the "dark side" and for sharing your infectious admiration for the beauty of Physics with me. You are a world class educator.

My heartfelt gratitude goes to Professor J. Xavier Prochaska at UC Santa Cruz, whose *Advanced Astronomy Lab* was, without reservation, the most practically useful, rewarding, and enjoyable course I have taken anywhere, ever. Moreover, X, I thank you for your generous and expediently rendered advice on graduate school. Also at UC Santa Cruz, I thank Professor Tesla Jeltema, my undergraduate thesis advisor, for meaningfully integrating me into her vibrant research group. I am so fortunate to have been able to travel with you to Keck Observatory (a feat that I did not repeat while a student at Berkeley), and to have had your support in my transition to graduate school.

At Berkeley, the list is long. First, I thank Professor Josh Bloom for sharing his intellect and "his" postdoc, Jorge Martínez-Palomera, on what proved to be an integral part of this dissertation. What would have been satisfactory became truly outstanding as a result of your and Jorge's contributions. Next, I thank my committee members, Professors Dan Kasen, Saul Perlmutter, and Uroš Seljak — I'm sure one's qualifying exam is always memorable, but perhaps mine will especially be so; your faces on Zoom are permanently burned into my memory. Thank you for assembling on my behalf during a time of worldwide crisis, for meeting with me, and for providing such valuable advice.

To Alex Filippenko, my doctoral advisor: thank you for your unwavering support these last five years, for your trust in allowing me to develop as an independent researcher, for

your monumental contributions to humanity's scientific understanding, for your tireless enthusiasm for communicating said understanding, and for providing $\gtrsim 150$ pounds of pizza[1] that I personally consumed. Amongst the many ways in which your support enabled this dissertation, I want to call particular attention to the high-caliber team you've maintained for many years. First, to your former graduate students, Mohan Ganeshalingam and Jeffrey Silverman: thank you for laying the foundations atop which Chapters 2 & 3 sit. To former graduate student Isaac Shivvers: thank you for showing me the ropes while our tenures briefly overlapped, and for being a sounding board in the years since. To my frequent collaborators, group members Thomas de Jaeger and WeiKang Zheng: you two (and possibly my wife) are the only ones who really know what all of this took. Thank you for being with me at every step of the journey, for teaching me so much, and for allowing our relationship to evolve from mentor/mentee to peer/peer. The honor is, and has always been, mine. I also want to thank all of the brilliant undergraduate students in our group, past and present, whom I've had the honor of working with. In particular, to Goni Halevi for your outstanding edits to the journal versions of Chapters 2 & 3, to Keto Zhang for help with all things statistical, and most of all, to Yukei Murakami: I have cherished our work and its unexpected offshoots. Finally, Tom Brink, I thank you for "saving" me from many a sleepless night (and for the company on sleepless nights) at the controls of the telescopes our group is fortunate to use.

To have significant portions of this dissertation published in the peer-reviewed scientific literature is a legacy I will deeply cherish. I thank all of those individuals not already mentioned above who helped make this a reality. To the referees of my papers: thank you for holding me accountable and for pushing me to do the best science possible. To all of my coauthors: thank you for your contributions, feedback, and patience. Chapters 2 & 3 would not have been possible without the herculean efforts of dozens of (mostly undergraduate) observers over the past decade, and for this, I offer my deepest gratitude. I am grateful for the excellent staff at both Lick and Keck Observatories — in particular, Elinor Gates and Paul Lynam — for their support and service to the astronomical community. I also wish to recognize and acknowledge the very significant cultural role and reverence that the summit of Maunakea has always had within the indigenous Hawaiian community. I am most fortunate to have the opportunity to conduct observations from this mountain.

During my time at Berkeley, I was supported in part by the Marc J. Staley Graduate Fellowship in Astronomy. Marc, although we will never meet, know that your generosity has made an impact not just for myself and some of my predecessors, but for the scientific community and humanity as whole through the research you've enabled. Rest in peace.

Finally, to my wife, Darla, and son, Silas: there are not words strong enough to express the extent of my gratitude, but I will try. Dar, to paraphrase a line from our wedding vows, *I spend a great deal of my time literally looking at the heavens [as evidenced by this thesis], but I need look no further than your embrace to find sublime happiness, comfort, and love.* You've been with me every step of the way, from my graduation from UC Santa Cruz, to uprooting your life and moving to Berkeley, to helping me see past my own doubts; enabling me, with

[1]The derivation of this amount is left as an exercise for the reader.

your encouragement, to fully realize my potential. I could not have done this without you. Si, you've helped me find a part of my heart that I didn't know existed. You've also taught me a lot about productivity — what a privilege it has been to think about Astrophysics while taking you for walks, changing your diaper, and reading to you (yes, parents quickly become multitasking masters). May you have, and capitalize on, all the opportunities that I have been so fortunate to have; but never forget to step back, share, and have an open, inquisitive mind. As with science, life is best practiced inclusively and with balance.

Chapter 1

Introduction

Supernovae (SNe), titanic explosions that demarcate the one-way boundary between life and death for some stars, have long been the subject of human fascination. Though formally recognized as a class of astrophysical objects in the early 1900s (the so-called "super-novae" Baade and Zwicky 1934), SNe can be found in the historical record at least as early as the year 185 AD, when a bright "guest star" was noted by Chinese astronomers. SNe occur at a rate of roughly twice per century in a galaxy the size of the Milky Way; thus, the discovery of $> 20,000$ such objects over the last 130 years (Stritzinger and Moriya 2018) is a truly incredible accomplishment. Only through dedicated telescope surveys (e.g., the Lick Observatory Supernova Search with the robotic Katzman Automatic Imaging Telescope Li et al. 2000; Filippenko et al. 2001; Ganeshalingam et al. 2010) have we been able to probe a sufficiently vast portion of space to discover so many in such a relatively short amount of time. As part of this thesis (Chapters 2 & 3), I present contributions that further extend this collective sample.

Before delving into these contributions and the studies that they afford, it is prudent to describe SNe more substantially. The remainder of this chapter therefore serves to introduce our understanding of the physical underpinnings of SNe, the tools with which an observational astronomer studies them, and their broader utility in refining our knowledge of the basic laws that govern the Universe (i.e., physical cosmology). My coverage of these topics is, necessarily, incomplete. Indeed, even after decades of intensive study, such a basic detail as the progenitor system(s) for some SNe (see Section 1.1.2) is not fully understood. Moreover, I aim for brevity, deferring the reader to seminal articles and reviews where possible.

1.1 Supernovae

As astrophysical objects, SNe can be broadly classified into two groups based upon their underlying explosion mechanisms: core-collapse SNe (hereafter CCSNe; see Section 1.1.1) and thermonuclear SNe (hereafter SNe Ia; see Section 1.1.2). However, as *observable* objects, SNe have traditionally been classified into four distinct categories (see, e.g., Filippenko 1997,

for a review of spectroscopic classifications of SNe): those with features of hydrogen (SNe II) and those without (SNe I) — and of the latter, there are those with silicon features (SNe Ia; the class of objects studied herein) and those without silicon that do have features of helium (SNe Ib) or do not have helium (SNe Ic). If this weren't convoluted enough, it is now known that SNe II, SNe Ib, and SNe Ic are all, in fact, CCSNe. As I move into a discussion of the aforementioned explosion mechanisms (and their constituent SNe), I emphasize that the broad classes mentioned here can all be divided into observationally distinct subgroups. Indeed, and as we shall see, there exists a specific set of SNe Ia that behave as "standardizeable candles" (i.e., those SNe Ia that follow the Phillips relation; Phillips 1993), a property that makes them immensely useful as cosmological distance indicators. Such SNe Ia are integral to the work I present in Chapters 4, 5, and 6.

1.1.1 Core-Collapse Supernovae

Most high-mass stars (i.e., those with $M \gtrsim 8M_{\odot}$)[1] end their lives as CCSNe. As such stars evolve, their luminosity is powered by the fusion of progressively heavier elements in their cores. This proceeds until iron builds up in the core, which, owing to its nuclear stability, marks the end of (exothermic) fusion. Eventually the inert iron core approaches the Chandrasekhar limit (see Section 1.1.2 for further discussion), and the electron degeneracy pressure that supports the core can no longer balance the inward pressure due to gravity. Collapse promptly ensues, accelerating as neutrinos carry away energy, and proceeds until the core's rising density reaches roughly that of an atomic nucleus. At this density, neutron degeneracy pressure and the strong nuclear force take over and halt the collapse. Infalling matter from the outer layers then rebounds, producing a shock wave that propagates through the star, though the energy responsible for actually unbinding the star is carried by neutrinos. This basic physical picture has been in place for roughly 50 years (e.g., Colgate and White 1966), but unresolved details remain (for a slightly dated review, see Woosley and Janka 2005)

As noted above, this basic mechanism is responsible for SNe II, Ib, and Ic, which are (observationally) segmented by the presence or absence of hydrogen and helium in their spectra. Physically, these realizations correspond to the state of the progenitor star prior to explosion. If the outermost hydrogen and helium layers have been lost[2] prior to explosion, the result is an SN Ic; if just the hydrogen layer has been lost, the result is an SN Ib; and if no layers have been lost, the result is an SN II. Left undiscussed here, and throughout this thesis, are the multitude of subtypes into which CCSNe can be categorized (see Shivvers et al. 2017, and references therein).

[1] $1\,M_{\odot} \approx 2 \times 10^{33}$ g is the mass of the Sun.

[2] The stripping of outer layers is thought to be driven by stellar winds and/or mass transfer to a binary companion.

1.1.2 Thermonuclear Supernovae

As opposed to high-mass stars, those with relatively low masses (i.e., $M \lesssim 8M_{\odot}$) are not guaranteed to end their lives in violent explosions. Instead, they "retire" as white dwarfs (WDs) — incredibly dense stellar remnants, usually made up mostly of carbon and oxygen (hereafter, C/O), that are supported against gravitational collapse by electron degeneracy pressure. There is a preponderance of convincing, albeit circumstantial, evidence that SNe Ia result from the complete thermonuclear runaway of C/O WDs (e.g., lack of hydrogen and helium in observations, significant production of ^{56}Ni, predisposition of WDs to runaway burning, energetics), and direct evidence, though not conclusive, is mounting (e.g., Bloom et al. 2012a). Taking this to be the truth, the question is, then, how to initiate the thermonuclear runaway?

The conventional picture is that the WD is not solitary, but rather in a binary system in which it can accumulate matter from its companion. The physics of electron degeneracy dictates an upper bound on the mass of a WD, above which it is unable to support itself against its own gravity (this is known as the Chandrasekhar limit, with a value of $\sim 1.4M_{\odot}$ for a nonrotating WD). If the companion is nondegenerate (i.e., it is not supported by degeneracy pressure), then as the WD accretes from it and approaches the Chandrasekhar limit, it *shrinks* in size and increases its core temperature to the extent that carbon fusion can be ignited. Then, in this "single-degenerate channel" (e.g., Whelan and Iben 1973), the WD is completely unbound by runaway nuclear fusion, manifesting in a brilliant SN Ia. A "double-degenerate scenario" also exists (e.g., Webbink 1984; Iben and Tutukov 1984), in which the WD merges with a degenerate companion. This second scenario is often invoked to explain "super-Chandrasekhar" SNe Ia (e.g., Silverman et al. 2011, though "normal" SNe Ia can result from this channel as well), and is, in fact, suspected as the dominant mechanism by which SNe Ia are produced (see Jha et al. 2019, for a recent review), though the matter is far from settled. A third scenario, in which two WDs in a triple-star system collide head on, has also received some attention (Katz and Dong 2012; Kushnir et al. 2013; Dong et al. 2015). I emphasize that much is still unknown about the explosion mechanism(s), the exact properties of the binary companion, and how these factors manifest the observably distinct subtypes that have been identified.

Despite these gaps in our understanding, the fact remains that SNe Ia are incredibly luminous ($L_{\rm peak} \approx 10^{43}\,{\rm erg\,s^{-1}}$) and *relatively* homogeneous (known empirically, and often "justified" with the ultimate $\sim 1.4M_{\odot}$ mass of the WD in the canonical single-degenerate channel). Moreover, it has been demonstrated that there exists a specific subclass of SNe Ia (hereafter, "normal" SNe Ia) whose peak luminosities can be standardized by accounting for the shape of their light curves (i.e., the timescale over which they brighten and fade). Though this so-called "width-luminosity relation" (WLR) has some theoretical support (e.g., Kasen and Woosley 2007), it has remained largely empirically rooted in its further development (e.g., Guy et al. 2007; Jha et al. 2007; Burns et al. 2011). Regardless, the WLR imbues SNe Ia with the property of being excellent cosmological distance indicators. Despite being

observationally expensive to compile[3], efforts to produce a significant dataset of SN Ia-inferred distances were rewarded with the paradigm-shifting discovery of the accelerating expansion of the Universe (Riess et al. 1998; Perlmutter et al. 1999). A major focus of this thesis is estimating the distances to "normal" SNe Ia from far fewer observations than have traditionally been required (see Chapter 5). Accordingly, my coverage of the plethora of "peculiar" SN Ia subtypes is intentionally sparse (see Jha et al. 2019, for a comprehensive discussion of the "Thermonuclear Supernova Zoo").

1.2 Observables

Distinct from virtually all other physical sciences, observational astronomy has no laboratory with which to conduct experiments. Instead, the observational astronomer discovers, infers, and conducts their scientific inquiries by, well, *observing*. Such observing is done predominantly with telescopes (both on Earth and in space) that gather light (i.e., electromagnetic radiation) after it has traversed vast distances through the Cosmos. Owing to the finite speed of light and the truly immense distances in question, this mode of inquiry allows us to study the Universe at great distances both in space and (backwards) in time. In this thesis, I present extensive observations of SNe Ia conducted primarily within the optical[4] range of the electromagnetic spectrum. Two distinct techniques — photometry (Chapter 2) and spectroscopy (Chapter 3) — are employed. I provide an introduction and background to both in the following paragraphs, with emphasis placed on their relevance to the subsequent chapters of this thesis.

1.2.1 Photometry

Photometry is a technique which allows astronomers to quantitatively measure the light intensity of an object. The basic apparatus consists of a telescope, camera (e.g., a charge-coupled device — CCD), and optionally, a filter to selectively block certain wavelength ranges. In observation-based SN Ia science, photometry plays two pivotal roles: (i) discovery and (ii) the monitoring of flux evolution.

In modern surveys, (i) is accomplished by periodically monitoring a large number of galaxies (or in the case of wide-field surveys, large patches of sky). The constituent images are then "differenced" against template images using sophisticated subtraction algorithms, resulting most of the time in nothing, but occasionally in a point source — a candidate SN. Figure 2.2 shows an example of the procedure, which my illustrious advisor likes to summarize, in jest, as discovering SNe by "looking for the arrows." I discuss the primary means by which candidate SNe are formally classified in Section 1.2.2. The majority of the aforementioned sample of $> 20,000$ SNe have been discovered in the last ~ 30 years using

[3]Standardizing an SN Ia requires extensive observations to properly measure the light-curve shape.

[4]The optical range ($\sim$ 3500–7500 Å) is well suited to SN Ia observations, as a majority of their luminosity emerges at such wavelengths.

this methodology, and in the upcoming ten-year Legacy Survey of Space and Time (LSST) to be conducted by the Vera C. Rubin Observatory, a further $\gtrsim 10^6$ SNe are projected to be discovered using this technique (LSST Science Collaboration et al. 2009).

Photometry enables (ii), or the construction of "light curves" in the usual parlance, in a very natural way. By performing photometry on images (typically in several filters) collected over the rise and subsequent decline from peak brightness, one can sample the photometric evolution[5] of an SN Ia (or other transient) at whatever cadence is dictated by their scientific objectives. I present multifilter photometry for 93 SNe Ia at a median cadence of 5.4 days in Chapter 2. For SN Ia observations intended to result in a distance estimate, it is best to have light curves sampled at a relatively high cadence, so as to allow the peak *observed* brightness and light-curve shape to be precisely determined. As previously mentioned, a significant component of this thesis is a technique — the snapshot distance method (SDM; Chapter 5) — that renders these (observationally) expensive requirements largely obsolete.

1.2.2 Spectroscopy

In essence, spectroscopy can be thought of as photometry in the limit where a large number of *very* narrow filters are used contemporaneously (in this way, spectra *inherently* contain more information than light curves). In practice, spectroscopy is performed by using an optical element (e.g., a prism or diffraction grating) to disperse the light from an astrophysical object collected by a telescope into its constituent wavelengths. The brightness at each of these wavelengths is then recorded using a CCD (as with photometry), yielding a spectrum. At early times, SN spectra consist of a blackbody continuum with superposed P Cygni profiles corresponding to species found in the ejecta. Thus, it is through spectra that we know SNe Ia lack hydrogen but have silicon[6] (or rather, the reverse: SN Ia are classified as such owing to these spectral markers, amongst others). Indeed, most SNe are classified based on the presence (or absence), shape, and location of features in their spectra. I present a sample of 637 optical spectra of 247 SNe Ia in Chapter 3.

Though SN Ia spectra allow for a vast array of diagnostics (e.g., probing chemical composition and the motions of ejecta), we focus on how they can contribute to SN Ia distance estimation. This can be decomposed into at least two distinct facets: the way(s) in which spectra might improve the *quality* of photometric distance estimates, and the way(s) in which they might improve the *efficiency* of such distance estimates. Efforts to address the former have been substantial and fruitful (e.g., Fakhouri et al. 2015, and references therein), but work on the latter has been notably absent from the recent literature despite indications that SN Ia follow a *spectral* analog to the photometric WLR (Nugent et al. 1995). I present significant progress in addressing this latter area in Chapter 4, demonstrating that modern machine-learning techniques can recover the light-curve shape of an SN Ia (amongst other quantities) from a single optical spectrum (I also provide this functionality to the community

[5]SN Ia light curves are powered predominantly by the radioactive decay chain $^{56}\mathrm{Ni} \rightarrow {}^{56}\mathrm{Co} \rightarrow {}^{56}\mathrm{Fe}$.

[6]A broad absorption complex produced by Si II $\lambda\lambda 6347, 6371$ (collectively called Si II $\lambda 6355$ hereafter) is omnipresent in near-maximum-light SN Ia spectra.

as an open-source software package called `deepSIP`[7]). In turn, this enables one to estimate the distance to an SN Ia from a single epoch of spectroscopy and an epoch of multifilter photometry (see Chapter 5).

1.3 Supernova Cosmology

Setting aside a number of tantalizing open questions surrounding SNe Ia (e.g., details of the explosion mechanisms, progenitor systems, and many more), I focus now on their utility in cosmological studies. Such studies typically probe the expansion history of the Universe, with the emergent picture being that we live in a Universe that is currently dominated ($\Omega_\Lambda \approx 0.7$) by a repulsive and mysterious "dark energy" (see, e.g., Scolnic et al. 2018, for recent SN Ia based constraints) and that is currently expanding at a rate of $H_0 \approx 74\,\mathrm{km\,s^{-1}\,Mpc^{-1}}$ (Riess et al. 2019). Though the latter does call some things into question (see Riess 2019, for a succinct review), the ΛCDM model still offers a compelling and exquisitely well-substantiated description for the evolution and content of the Universe, having notched many successes including explaining the existence and structure of the cosmic microwave background (CMB), the observed abundances of hydrogen, helium, and lithium, and of course, the accelerating expansion of the Universe that brought it into favor when discovered through SN Ia observations (Riess et al. 1998; Perlmutter et al. 1999). In this thesis, I focus on a distinct way in which SNe Ia can test ΛCDM; I defer the reader to the references above (and those therein) for more detail on the aforementioned probes and cosmological parameters.

Henceforth, my focus is not on constraining the cosmological model directly, but rather on the scatter about the best-fitting model. As we shall see, this allows one to measure the growth of structure of the Universe, which, at the low redshifts I consider, yields constraints on the nature of gravity. Chapter 6 covers the quantitative foundations of this test, but here I introduce it at a more fundamental level. I start with the unrealistic — but conceptually simplifying — assumptions that SNe Ia can be perfectly observed (i.e., that their *observed* redshifts and magnitudes can be known with infinite precision and accuracy) and standardized (i.e., that the SN Ia WLR leaves nothing unmodeled and thus perfectly reconstructs *intrinsic*, absolute magnitudes), and moreover that the effects of dust can be perfectly taken into account and that redshifts are sufficiently low that K-corrections are negligible. In such a scenario one might assume that there would be no remaining dispersion in the SN Ia Hubble diagram (see Figure 6.2 for an example), but this is not true — I have carefully stripped away all sources of scatter with my simplifying assumptions except for one: peculiar velocities (i.e., motions that deviate from the smooth Hubble flow) induced by the gravitational pull from large-scale structure. Parametrically, this scatter is due to the difference between the observed redshift, z_{obs}, and the cosmological redshift, $\tilde{z}$, which relate

[7] `https://github.com/benstahl92/deepSIP`

to the line-of-sight peculiar velocity, v, by

$$v = \mathbf{v} \cdot \hat{\mathbf{r}} = \left(\frac{z_{\rm obs} - \tilde{z}}{1 + \tilde{z}} \right) c, \tag{1.1}$$

where c is the speed of light and $\hat{\mathbf{r}}$ is a unit vector pointing from the observer to a given SN Ia (though the notion can be applied to any object for which the redshift can be directly observed and then inferred through distinct observations and a given cosmological model). In the case of SNe Ia, the path to $\tilde{z}$ from observations begins with a distance modulus; I defer the reader to Chapter 6 for more details. I do emphasize, however, that SNe Ia are an attractive class of objects with which to measure peculiar velocities because of the precision afforded by modern implementations of the WLR. Moreover, being induced by large-scale structure, SN Ia-inferred peculiar velocities offer a direct probe of the *total* matter distribution (thus bypassing the tedious "bias corrections" that must be made when measuring galaxy distributions).

In Chapter 6, I compile a vast collection of SN Ia-based peculiar-velocity measurements using a literature sample and a number of new estimates derived using my SDM (see Chapter 5), to which I add a modest sample of SNe II. I then aggregate over the constituent peculiar velocities to measure the bulk flow of our Local Group relative to the CMB, finding a result that agrees with the expectation inferred from ΛCDM. Also, by comparing against a *reconstructed* peculiar-velocity field, I derive the tightest ever SN-based constraints on the growth rate of structure normalized by the standard deviation of overdensities in $8\,h^{-1}\,$Mpc spheres (i.e., $f\sigma_8$, where f is the growth rate of structure and σ_8 is the normalization factor). As explained in Chapter 6, this provides an exquisite test of general relativity (spoiler alert: test passed).

1.4 This Thesis

I organize the remainder of this thesis to largely follow the development given thus far. The two following chapters are used to present significant, new sets of photometric (Chapter 2) and spectroscopic (Chapter 3) observations and analyses of relatively nearby SNe Ia. I then combine portions of these datasets with a substantial and carefully reprocessed literature sample to form the compilation of SN Ia spectra with corresponding light-curve-derived parameters used to develop and evaluate `deepSIP` (Chapter 4), an open-source software package that measures the phase and — for the first time ever using deep learning — light-curve shape of an SN Ia from a single optical spectrum. Using this tool, I demonstrate how the SDM of Chapter 5 can be used to estimate the distance to an SN Ia from just one optical spectrum and one epoch of multifilter photometry. Finally, I use the SDM in Chapter 6 to estimate the distances to a significant number of sparsely observed SNe Ia, which I then combine with a literature sample of SN Ia and SN II distances to study the bulk flow of the local Universe and set stringent constraints on the degenerate cosmological parameter combination, $f\sigma_8$. Brief concluding remarks are given in Chapter 7.

Chapter 2

Lick Observatory Supernova Search Follow-Up Program: Photometry Data Release of 93 Type Ia Supernovae

A version of this chapter was originally published in *The Monthly Notices of the Royal Astronomical Society* (Stahl et al. 2019).

Chapter Abstract

We present *BVRI* and unfiltered light curves of 93 Type Ia supernovae (SNe Ia) from the Lick Observatory Supernova Search (LOSS) follow-up program conducted between 2005 and 2018. Our sample consists of 78 spectroscopically normal SNe Ia, with the remainder divided between distinct subclasses (three SN 1991bg-like, three SN 1991T-like, four SNe Iax, two peculiar, and three super-Chandrasekhar events), and has a median redshift of 0.0192. The SNe in our sample have a median coverage of 16 photometric epochs at a cadence of 5.4 days, and the median first observed epoch is $\sim$ 4.6 days before maximum B-band light. We describe how the SNe in our sample are discovered, observed, and processed, and we compare the results from our newly developed automated photometry pipeline to those from the previous processing pipeline used by LOSS. After investigating potential biases, we derive a final systematic uncertainty of 0.03 mag in *BVRI* for our dataset. We perform an analysis of our light curves with particular focus on using template fitting to measure the parameters that are useful in standardising SNe Ia as distance indicators. All of the data are available to the community, and we encourage future studies to incorporate our light curves in their analyses.

2.1 Introduction

Type Ia supernovae (SNe Ia) are objects of tremendous intrigue and consequence in astronomy. As individual events, SNe Ia — especially those at the extremes of what has been previously observed (e.g., Filippenko et al. 1992b,a; Foley et al. 2013a) — present interesting case studies of high-energy, transient phenomena. Collectively, SNe Ia are prized as "cosmic lighthouses" with luminosities of several billion Suns, only a factor of 2–3 lower than an L^* host galaxy of $\sim 10^{10}\,L_\odot$. The temporal evolution of the luminosity of a SN Ia, which is powered largely by the radioactive decay chain $^{56}\mathrm{Ni} \rightarrow {}^{56}\mathrm{Co} \rightarrow {}^{56}\mathrm{Fe}$, is codified by light curves (typically in several broadband filters). With some variation between filters, a SN Ia light curve peaks at a value determined primarily by the mass of ^{56}Ni produced and then declines at a rate influenced by its spectroscopic/colour evolution (Kasen and Woosley 2007). With the advent of empirical relationships between observables (specifically, the rate of decline) and peak luminosity (e.g., Phillips 1993; Riess et al. 1996; Jha et al. 2007; Zheng et al. 2018a), SNe Ia have become immensely valuable as cosmological distance indicators. Indeed, observations of nearby and distant SNe Ia led to the discovery of the accelerating expansion of the Universe and dark energy (Riess et al. 1998; Perlmutter et al. 1999), and they continue to provide precise measurements of the Hubble constant (Riess et al. 2016, 2019).

The aforementioned light-curve "width-luminosity" relations form the basis for the use of SNe Ia as cosmological distance indicators. To further refine these relationships as well as understand their limitations, extensive datasets of high-precision light curves are required. At low redshift, multiple groups have answered the call, including the Calán/Tololo Supernova Survey with $BVRI$ light curves of 29 SNe Ia (Hamuy et al. 1996), the Harvard-Smithsonian Center for Astrophysics (CfA) Supernova Group with > 300 multiband light curves spread over four data releases (Riess et al. 1999; Jha et al. 2006; Hicken et al. 2009a, 2012, henceforth CfA1-4, respectively), the Carnegie Supernova Project (CSP) with > 100 multiband light curves (Contreras et al. 2010; Folatelli et al. 2010; Stritzinger et al. 2011; Krisciunas et al. 2017, henceforth CSP1, CSP1a, CSP2, and CSP3, respectively), and our own Lick Observatory Supernova Search (LOSS) follow-up program with $BVRI$ light curves of 165 SNe Ia (Ganeshalingam et al. 2010, henceforth G10). More recently, the Foundation Supernova Survey has published its first data release of 225 low redshift SN Ia light curves derived from Pan-STARRS photometry (Foley et al. 2018). Despite these extensive campaigns, there exist many more well-observed light curves for high redshift ($z \gtrsim 0.1$) SNe Ia than for those at low redshift (Betoule et al. 2014). As low-redshift SNe Ia are used to calibrate their high-redshift counterparts, a larger low-redshift sample will be useful for further improving width-luminosity relations, gauging systematic errors arising from the conversion of instrumental magnitudes to a uniform photometric system, and for investigating evolutionary effects over large timescales.

The LOSS follow-up program has been in continuous operation for over 20 years. The result is an extensive database of SN Ia photometry from images obtained with the 0.76 m Katzman Automatic Imaging Telescope (KAIT) and the 1 m Nickel telescope, both located

at Lick Observatory. G10 released SN Ia light curves from the first 10 years of the LOSS follow-up campaign, and in this paper we publish the corresponding dataset for the following 10 years (2009–2018). We also include several earlier SNe Ia that were omitted from the first publication. In aggregate, our dataset includes *BVRI* light curves of 93 SNe Ia with a typical cadence of ~ 5.4 days drawn from a total of 21,441 images.

Our dataset overlaps with those of CfA3, CfA4, and CSP3. In particular, we share 7 SNe with CfA3 and 16 with CfA4; however, we expect the upcoming CfA5 release to have considerable overlap with ours, as it will be derived from observations over a similar temporal range. With regard to CSP3, we have 16 SNe in common. Accounting for overlaps, 28 SNe in our sample have been covered by at least one of these surveys, thus leaving 65 unique SNe in our sample.

The remainder of this paper is organised in the following manner. Section 3.2.2 details our data acquisition, including how our SNe are discovered and which facilities are employed to observe them. In Section 2.3 we discuss our data-reduction procedure, with particular emphasis placed on our automated photometry pipeline. Section 6.4 presents our results, including comparisons with those in the literature that were derived from the same KAIT and Nickel images, when such an overlap exists. We derive and discuss the properties of our light curves in Section 5.4, and our conclusions are given in Section 6.5.

2.2 Observations

2.2.1 Discovery

Many of the SNe Ia presented here were discovered and monitored by LOSS using the robotic KAIT (Li et al. 2000; Filippenko et al. 2001, see G10 for remarks on SN Ia discovery with LOSS). We note that the LOSS search strategy was modified in early 2011 to monitor fewer galaxies at a more rapid cadence, thus shifting focus to identifying very young SNe in nearby galaxies (e.g., Silverman et al. 2012b). Consequently, the proportion of our sample discovered by LOSS is less than in that presented by G10. Those SNe in our sample that were not discovered with KAIT were sourced from announcements by other groups in the SN community, primarily in the form of notices from the Central Bureau of Electronic Telegrams (CBETs) and the International Astronomical Union Circulars (IAUCs). Whenever possible and needed, we spectroscopically classify and monitor newly discovered SNe Ia with the Kast double spectrograph (Miller and Stone 1993) on the 3 m Shane telescope at Lick Observatory. Discovery and classification references are provided for each SN in our sample in Table 2.3.

While the focus in this paper is on SNe Ia, we have also built up a collection of images containing SNe II and SNe Ib/c (see Filippenko 1997, for a discussion of SN spectroscopic classification). These additional datasets have been processed by our automated photometry pipeline and will be made publicly available pending analyses (T. de Jaeger et al. 2019, in prep., & W. Zheng et al. 2019, in prep.; for the SN II and SN Ib/c datasets, respectively).

2.2.2 Telescopes

The images from which our dataset is derived were collected using the 0.76 m KAIT ($\sim 86\%$ of the total) and the 1 m Nickel telescope ($\sim 14\%$ of the total), both of which are located at Lick Observatory on Mount Hamilton near San Jose, CA. The seeing at this location averages $\sim 2''$, with some variation based on the season.

KAIT is a Ritchey-Chrétien telescope with a primary mirror focal ratio of $f/8.2$. Between 2001 September 11 and 2007 May 12 the CCD used by KAIT was an Apogee chip with 512×512 pixels, and henceforth it has been a Finger Lakes Instrument (FLI) camera with the same number of pixels. We refer to these as KAIT3 and KAIT4, respectively[1]. Both CCDs have a scale of $0\farcs8$ pixel^{-1}, yielding a field of view of $6\farcm7 \times 6\farcm7$. As a fully robotic telescope, KAIT follows an automated nightly procedure to acquire data. Observations of a target are initiated by submitting a request file containing its coordinates as well as those of a guide star. A master scheduling program then determines when to perform the observations with minimal disruption to KAIT's SN search observations. Under standard conditions we use an exposure time of 1–6 min in B and 1–5 min in each of VRI.

The 1 m Nickel is also a Ritchey-Chrétien telescope, but with a primary mirror focal ratio of $f/5.3$. Since 2001 April 3 its CCD has been a thinned, Loral, 2048×2048 pixel chip located at the $f/17$ Cassegrain focus of the telescope. With a scale of $0\farcs184$ pixel^{-1}, the field of view is $6\farcm3 \times 6\farcm3$. In March of 2009 the filter set was replaced — we refer to the period before as Nickel1[2] and after as Nickel2. Pixels are binned by a factor of two to reduce readout time. Since 2006, most of our Nickel observations have been performed remotely from the University of California, Berkeley campus. Our observing campaign with Nickel is focused on monitoring more distant SNe and supplementing (particularly at late times) data taken with KAIT. Under standard conditions, we use exposure times similar to those for KAIT.

In Figure 2.1 we compare the standard throughput curves of Bessell (1990) to those of the two Nickel 1 m configurations covered by our dataset (G10 show the analogous curves for KAIT3 and KAIT4). We find good agreement between both Nickel1 and Nickel2 filter responses in the VR bands with the corresponding Bessell curves. In B, the agreement is good for Nickel2 but there is a noticeable discrepancy between the Nickel1 filter response compared to that of Bessell. The filter response in I for both Nickel configurations shows the most substantial departures from the Bessell standard, with Nickel2 exhibiting the most egregious disagreement. Nevertheless, the transmission curve has been verified through repeated measurements.

[1] G10 use KAIT1 and KAIT2 for earlier CCD/filter combinations. Our use of KAIT3 and KAIT4 is consistent with theirs.

[2] Our Nickel1 is referred to as Nickel by G10.

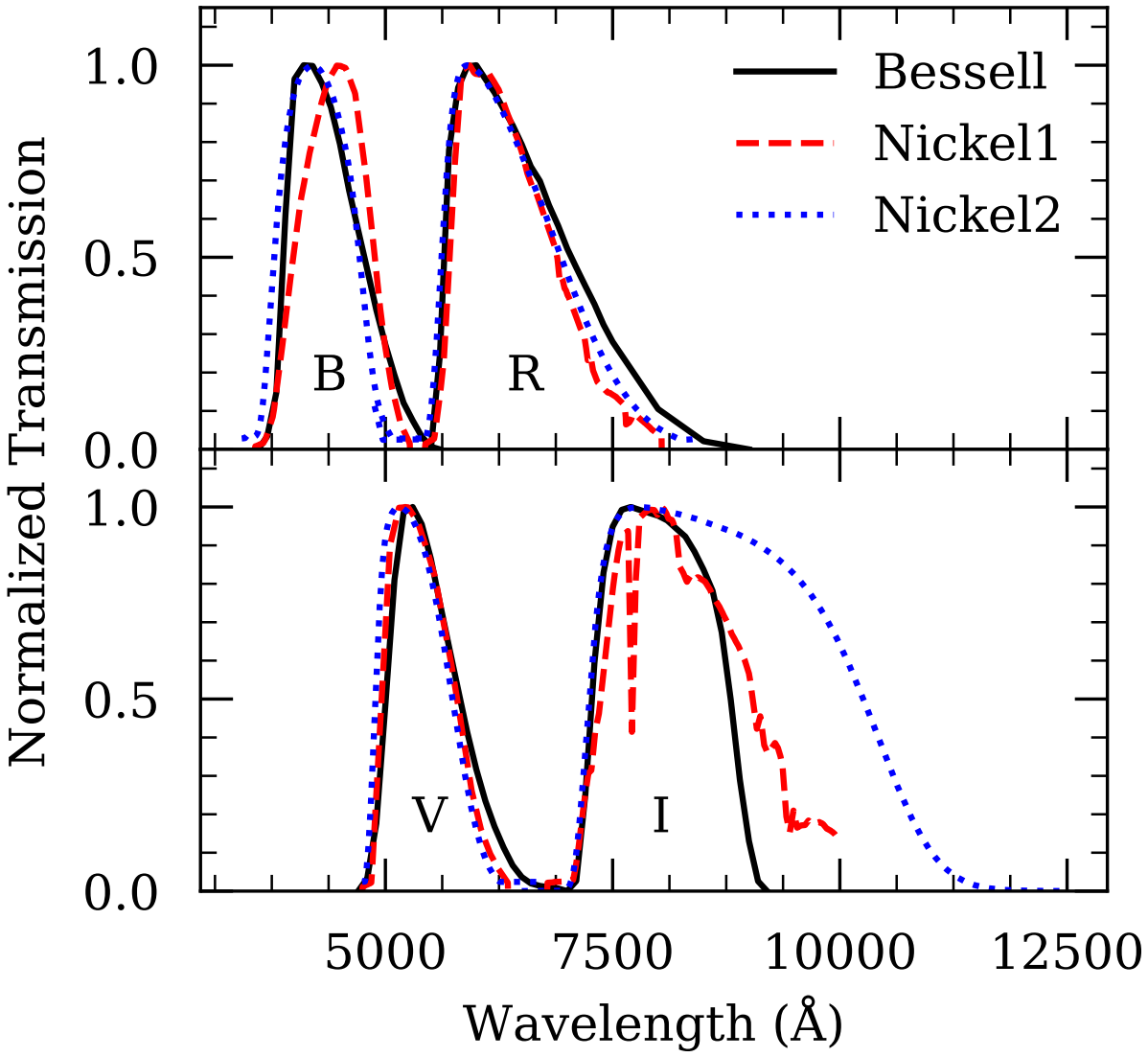

Figure 2.1: Transmission curves for the two Nickel 1 m configurations covered by our dataset compared with standard Bessell (1990) *BVRI* curves.

2.3 Data Reduction

With over 21,000 images spanning 93 SNe Ia with a median of 16 observed epochs, our dataset is too large to manually process. We have therefore developed an automated photometry pipeline[3] to calculate light curves from minimally preprocessed[4] KAIT and Nickel images (those from other telescopes could be incorporated with minimal modifications). Although it makes use of distinct software packages and utilises components written in several different programming languages, the pipeline is wrapped in a clean Python interface. It automatically performs detailed logging, saves checkpoints of its progress, and can be run interactively if desired — thus, in cases where the data require special care, the user is able to perform each processing step manually with increased control. We detail the primary steps performed by the pipeline in the following sections.

2.3.1 Start Up and Image Checking

At a minimum, the pipeline requires four pieces of information to run: the coordinates of the target (right ascension and declination), the name of an image to use for selecting candidate calibration stars (henceforth, the "reference image"), and a text file containing the name of each image to process. In the absence of additional information, the pipeline will make sensible assumptions in setting various parameters during the start up process.

Processing commences by performing several checks on the specified images to see if any should be excluded. The first removes any images collected through an undesired filter, and the second excludes those collected outside a certain range of dates. In processing our dataset, we allow only unfiltered (referred to as "*Clear*") images and those collected through standard *BVRI* filters between 60 days prior to, and 2 yr after, discovery as specified on the Transient Name Server (TNS)[5], to continue to subsequent processing steps.

2.3.2 Selection of Calibration Star Candidates

In the next processing step, candidate calibration stars are identified in the reference image using a three-stage process. First, all sources above a certain threshold in the image are identified and those that are farther than 8″ from that target are retained.

Next, a catalog of potential calibration stars in the vicinity of the SN is downloaded (in order of preference) from the archives of Pan-STARRS (PS1; Chambers and Pan-STARRS Team 2018), the Sloan Digital Sky Survey (SDSS; Alam et al. 2015), or the AAVSO Photometric All-Sky Survey (APASS; Henden et al. 2018). The 40 brightest stars common to the reference image and the catalog are then retained. If the pipeline is being run interactively, the user can visually inspect the positions of these stars against the reference image and

[3] `https://github.com/benstahl92/LOSSPhotPypeline`

[4] Preprocessing consists of removing bias and dark current, flatfielding, and determining an astrometric solution.

[5] `https://wis-tns.weizmann.ac.il/`

Table 2.1: Summary of Colour Terms

System	C_B	C_V	C_R	C_I
KAIT3	−0.057	0.032	0.064	−0.001
KAIT4	−0.134	0.051	0.107	0.014
Nickel1	−0.092	0.053	0.089	−0.044
Nickel2	0.042	0.082	0.092	−0.044

remove any that should not be used (such as those that are not well-separated from the target's host galaxy).

Finally, the magnitudes (and associated uncertainties) of the selected catalog stars are converted to the Landolt system (Landolt 1983, 1992) using the appropriate prescription[6], and subsequently to the natural systems of the various telescope/CCD/filter sets that are spanned by our dataset as discussed in Section 2.2.2. Conversion from the Landolt system to the aforementioned natural systems is accomplished using equations of the form

$$b = B + C_B(B - V) + \text{constant}, \tag{2.1a}$$
$$v = V + C_V(B - V) + \text{constant}, \tag{2.1b}$$
$$r = R + C_R(V - R) + \text{constant, and} \tag{2.1c}$$
$$i = I + C_I(V - I) + \text{constant}, \tag{2.1d}$$

where lower-case letters represent magnitudes in the appropriate natural system, upper-case letters represent magnitudes in the Landolt system, and C_X is the linear colour term for filter X as given in Table 2.1. The KAIT3, KAIT4, and Nickel1 colour terms were originally given by G10, while those for Nickel2 are presented here for the first time. We derive the Nickel2 colour terms (and atmospheric correction terms, k_i; see Section 2.3.8.2) as the mean values of the appropriate terms measured over many nights using steps from the calibration pipeline described by G10.

2.3.3 Galaxy Subtraction

A large proportion of SNe occur near or within bright regions of their host galaxies. It is therefore necessary to isolate the light of such a SN from that of its host prior to performing photometry. This is accomplished by subtracting the flux from the host at the position of the SN from the measured flux of the SN. To measure such host fluxes for the SNe in our sample needing galaxy subtraction (as determined by visual inspection and consideration of the

[6]The transformation given by Tonry et al. (2012) is used for PS1 catalogs, whereas SDSS and APASS catalogs are treated with the prescription of Robert Lupton in 2005 (`https://www.sdss.org/dr12/algorithms/sdssUBVRITransform/`)

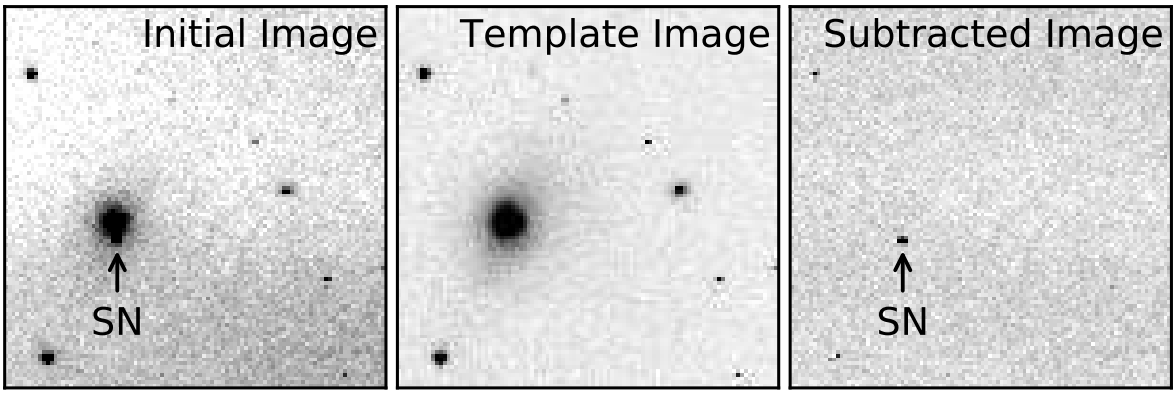

Figure 2.2: Example of our galaxy-subtraction procedure. The left image shows SN 2013gq on 2013 March 25 UT, with the SN flux clearly contaminated by the host galaxy. The centre image is the host-galaxy template used for subtraction, and the right image is the result of our galaxy-subtraction procedure.

offsets given in Table 2.3), we obtained template images using the 1 m Nickel telescope (for *BVRI* images) and KAIT (for unfiltered images) after the SNe had faded beyond detection, or from prior to the explosions if available in our database. Template images selected for use in galaxy subtraction are preprocessed identically to science images as described above.

The first step in our subtraction procedure is to align each science image to its corresponding template image. We do this by warping each template such that the physical coordinates of its pixels match those of the science image. Next, we perform the subtraction using the ISIS package (Alard and Lupton 1998; Alard 1999), which automatically chooses stars in both images and uses them to compute the convolution kernel as a function of position. We use ten stamps in the x and y directions to determine the spatial variation in the kernel. ISIS matches the seeing between the warped template image and the science image by convolving the one with better seeing and then subtracts the images. An example image with subtraction applied is shown in Figure 2.2.

Some SNe in our dataset occurred sufficiently far from the nuclei of their host galaxies to not suffer significant contamination from galaxy light. In these cases, we did not perform galaxy subtraction. Table 2.3 includes a column that indicates whether host-galaxy subtraction was performed for each SN in our sample.

2.3.4 Photometry

After galaxy subtraction has been performed (or skipped if not needed), the pipeline performs photometry on the target SN and each selected calibration star. For images that have been galaxy subtracted, photometry is only performed on the SN (as the calibration stars

will have been subtracted out), and photometry of the calibration stars is measured from the unsubtracted images. This requires the user to take care when doing calibration (see Section 2.3.5) to ensure that the calibration stars used are not themselves contaminated by light from the SN's host galaxy.

By default, both point-spread function (PSF) and aperture photometry (through multiple apertures), along with standard photometry uncertainty calculations for each, are performed using procedures from the IDL Astronomy User's Library[7]. Henceforth, we consider only PSF photometry.

The pipeline automatically keeps track of failures and removes the associated images from further processing. The user can easily track such failures and subsequently investigate each problematic image in more detail.

2.3.5 Calibration to Natural Systems

In the next step, the pipeline calibrates measured photometry to magnitudes in the appropriate natural system as follows. For each unsubtracted image, the mean magnitude of the selected calibration stars in the natural system appropriate to the image (from the catalog downloaded and converted according to the specifications in Section 2.3.2) is computed. Next, the mean *measured* magnitude of the same set of reference stars is computed for each aperture. The difference between the former and the latter yields a set of offsets (one for each aperture) to add to the measured magnitudes such that, in the current image, the average magnitude of the selected calibration stars matches that from the catalog. These offsets are also applied to the *measured* SN photometry from the image (and if it exists, the SN photometry from the associated galaxy-subtracted image). Standard techniques of error propagation are applied through these operations to determine the uncertainty in all derived natural system magnitudes, accounting for uncertainties in the calibration catalog and photometry.

This procedure is clearly sensitive to which calibration stars are used, and so several steps are employed in an attempt to make an optimal decision. First, calibration is performed on each image using all available calibration stars. Any calibration stars that are successfully measured in $< 40\%$ of images are removed and calibration is run again using the remaining calibration stars. Next, any images in which $< 40\%$ of the calibration stars are successfully measured are removed from further consideration. After these two preliminary quality cuts are performed, an iterative process is used to refine and improve the calibration. Each iteration consists of a decision that changes which calibration stars are used or which images are included and a recalibration based on that decision.

When run interactively, the pipeline provides the user with extensive information to consider when making this decision. In each iteration, the reference image is displayed with the current calibration stars and the SN identified. It also provides tables for each passband which include, for each calibration star: the median measured and calibration magnitudes as

[7] `https://idlastro.gsfc.nasa.gov/homepage.html`

well as the median of their differences, the standard deviation of the measured magnitudes, and the proportion of all images in the current passband for which the calibration star's magnitude was successfully measured. The user can remove certain calibration stars, or all that (in any passband) exceed a specific tolerance on the median magnitude difference. Other options and diagnostics are available, and thus an experienced user will develop certain decision-making patterns when performing interactive calibration, but further discussion is beyond the scope of this description.

The automated pipeline makes the decision as follows. Any image containing a reference star that differs by the greater of 3 standard deviations or 0.5 mag from the mean measured magnitude of that reference star in the relevant filter/system is removed and logged internally for later inspection. If no such discrepant images are identified, then the calibration star whose median difference between measured and reference magnitudes is most severe is removed, so long as the difference exceeds 0.05 mag. If neither of these two criteria is triggered, then the calibration process has converged and iteration exits successfully. However, if a point is reached where only two reference stars remain, the tolerance of 0.05 mag is incremented up by 0.05 mag and iteration continues. If the tolerance is incremented beyond 0.2 mag without iteration ending successfully, the calibration process exits with a warning.

The process described above tends to lead to robust results, but it is still possible for individual measurements to be afflicted by biases. Because of this, we visually inspect our results after automated calibration and in some cases interactively recalibrate and/or remove certain images if they are suspected of contamination or are of poor quality.

2.3.6 Landolt System Light Curves

The final stage of processing involves collecting each calibrated (natural system) magnitude measurement of the SN under consideration to form light curves (one for each combination of aperture and telescope system). Prior to transforming to the Landolt system, several steps are applied to these "raw" light curves. First, magnitudes in the *same* passbands that are temporally close (< 0.4 days apart) are averaged together. Next, magnitudes in *distinct* passbands that are similarly close in temporal proximity are grouped together so that they all have an epoch assigned as the average of their individual epochs. These steps result in a light curve for each telescope system used in observations, with magnitudes in the associated natural system.

Next, these light curves are transformed to the Landolt system by inverting the equations of Section 2.3.2 and using the appropriate colour terms from Table 2.1. Finally, the transformed light curves are combined into a final, standardised light curve which represents all observations of the SN.

2.3.7 Uncertainties

To quantify the uncertainties in results derived from our processing routine, we inject artificial stars of the same magnitude and PSF as the SN in each image and then reprocess the

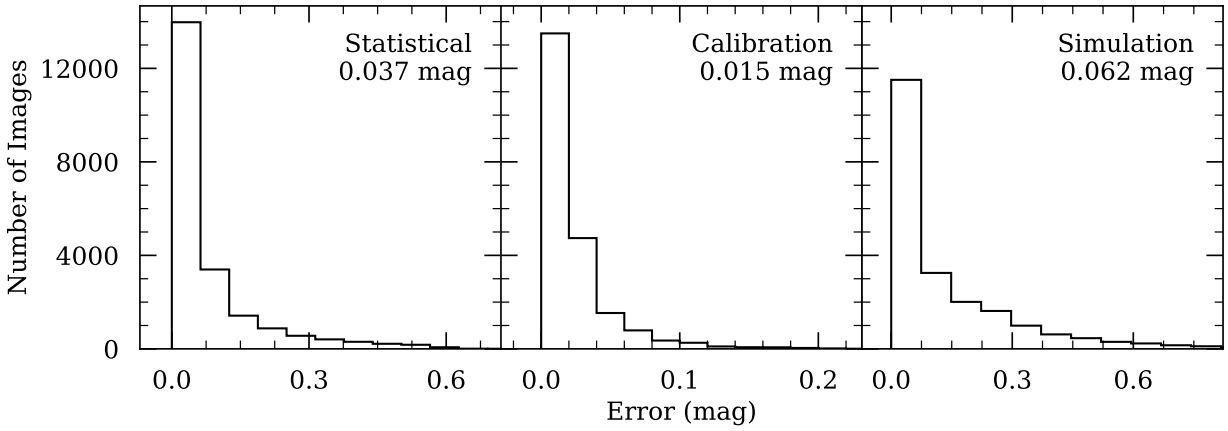

Figure 2.3: Distribution of uncertainties arising from statistical, calibration, and simulation sources. All magnitudes are instrumental magnitudes, and the median uncertainty from each source is printed.

images. We use a total of 30 artificial stars to surround the SN with five concentric, angularly offset hexagons of increasing size. The smallest has a "radius" of $\sim 25''$ (exactly 20 KAIT pixels) and each concentric hexagon increases this by the same additive factor. We assign the scatter in the magnitudes of the 30 recovered artificial stars to be the uncertainty in our measurement of the SN magnitude. This is then added in quadrature with the calibration and photometry uncertainties and propagated through all subsequent operations, leading to the final light curve.

This method has the advantage of being an (almost) end-to-end check of our processing, and it can still be used effectively when certain steps (namely, host-galaxy subtraction) are not necessary. We note that by treating uncertainties in this way, we are making the assumption that the derived magnitude and PSF of the SN are correct. If this assumption is not met, the artificial stars we inject into each image will not be an accurate representation of the profile of the SN, and thus we cannot be assured that the distribution in their recovered magnitudes is a reasonable approximation to that of the SN. Furthermore, errors will be substantially overestimated when an injected star overlaps with a true star in the image. When this happens (as verified by a visual inspection) we do not inject a star at this position and thus in some cases the uncertainty estimate is made with slightly fewer than 30 stars.

Altogether, the final uncertainty on each magnitude in our light curves is derived by propagating three sources of uncertainty through our calculations. These sources are (1) "statistical" (e.g., scatter in sky values, Poisson variations in observed brightness, uncertainty in sky brightness), (2) "calibration" (e.g., calibration catalog, derived colour terms), and (3) "simulation" (as described in the preceding paragraphs). In terms of instrumental magnitudes, we find median uncertainties from these sources of 0.037 mag, 0.015 mag, and 0.062 mag, respectively. We show the distribution of each in Figure 2.3.

2.3.8 Systematic Errors

In order to combine or compare photometric datasets from different telescopes, one must understand and account for systematic errors. In this section, we consider sources of possible systematic errors and quantify their impact on our final photometry. As three of the four telescope/detector configurations spanned by our dataset are already extensively considered by G10, our goal here is primarily to extend their findings to cover the fourth configuration, Nickel2.

2.3.8.1 Evolution of Colour Terms

The Nickel2 colour terms given in Table 2.1 are the average colour terms from observations of Landolt standards over many nights. Any evolution in the derived colour terms as a function of time introduces errors in the final photometry that are correlated with the colour of the SN and reference stars. To investivate this effect, we plot the Nickel2 colour terms as a function of time in Figure 2.4, but find no significant evidence for temporal dependence. This conclusion is in line with the findings of G10 for KAIT3, KAIT4, and Nickel1.

2.3.8.2 Evolution of Atmospheric Terms

For the same set of nights for which we compute the colour terms which constitute Figure 2.4, we also derive atmospheric correction terms. Because we source calibration stars from established catalogues (as outlined in Section 2.3.2), our derived atmospheric correction terms affect processing only indirectly (i.e., in the determination of colour terms). As such, we discuss them here only as a stability check. Figure 2.5 shows their evolution as a function of time. We do not find significant evidence for temporal dependence, which is consistent with the findings of G10 for KAIT3, KAIT4, and Nickel1. It is also worth noting that our derived terms ($k_B = 0.278$, $k_V = 0.157$, $k_R = 0.112$, and $k_I = 0.068$)) are similar to those derived for Nickel1 by G10 (0.277, 0.171, 0.120, and 0.078, respectively).

2.3.8.3 Combining KAIT and Nickel Observations

Another potential source of systematic error arises when combining observations from different configurations (e.g., KAIT4 and Nickel2). Any systematic differences between configurations introduces an error when observations from various systems are combined. To search for and investigate such differences, we compare the mean derived magnitude of each calibration star used in determining our final photometry for unique combinations of passband and system. In this investigation, we only consider instances where a calibration star was observed using two different systems. Figure 2.6 shows the distribution of differences in each passband for the common set of calibration stars between the KAIT4 and Nickel2 systems, which have the largest overlap. Similar distributions were constructed for all other

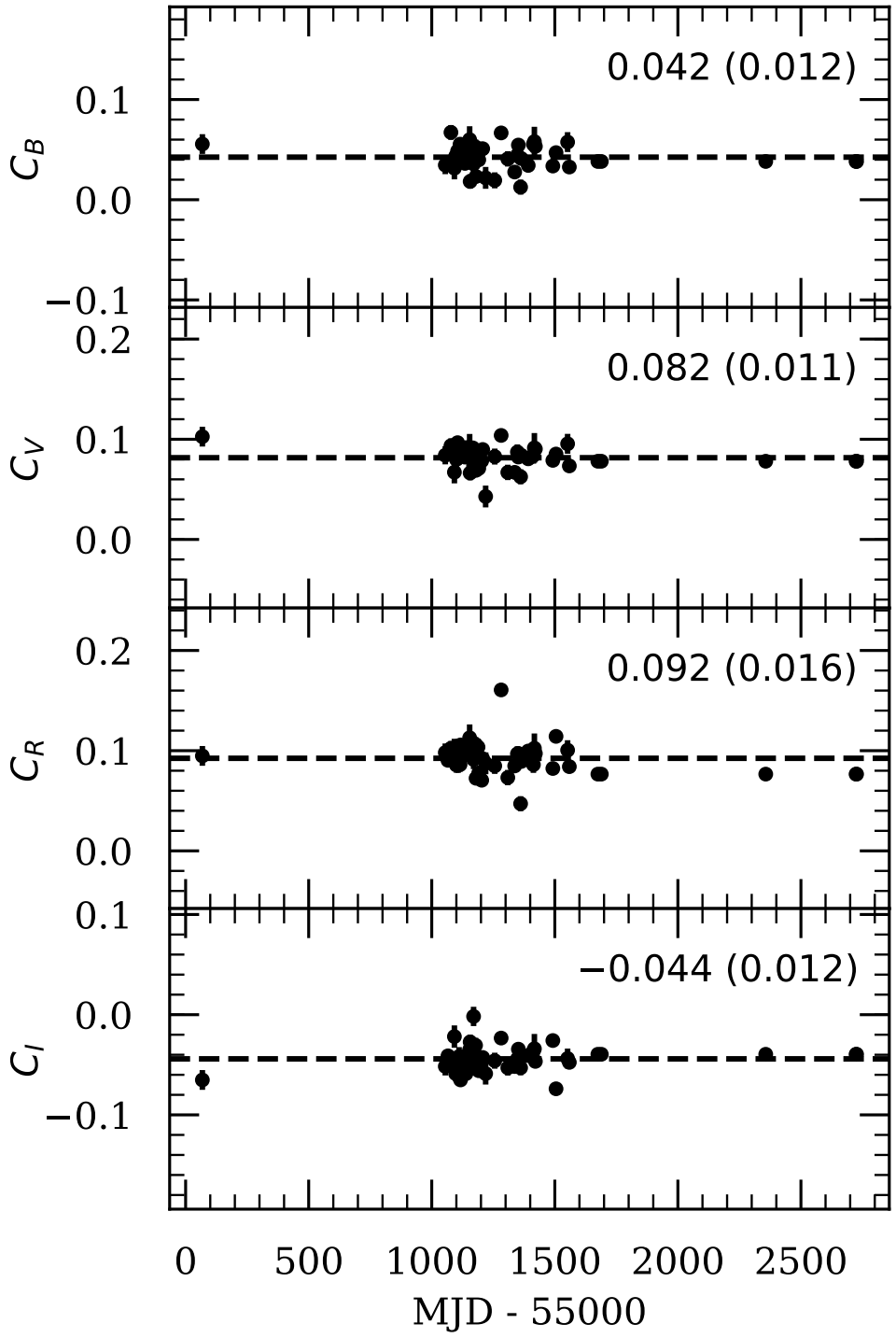

Figure 2.4: Nickel2 colour terms as a function of time. The mean and standard deviation in each passband are printed.

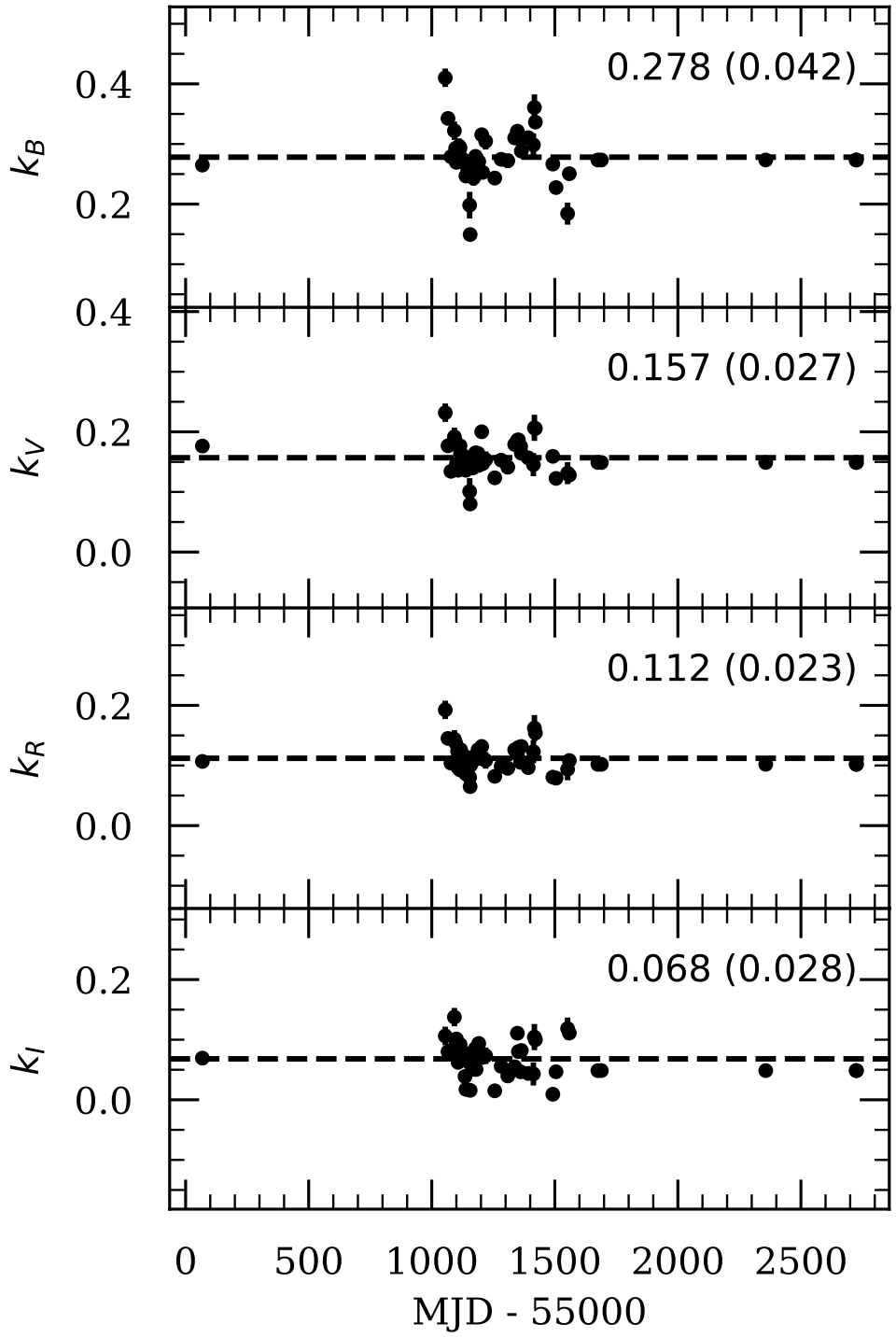

Figure 2.5: Same as Figure 2.4, except for atmospheric correction terms used to transform Nickel2 natural-system magnitudes to the Landolt system.

system combinations, and in all cases we find a median offset of $\lesssim 0.003$ mag[8] with scatter $\sigma \lesssim 0.03$ mag in each filter.

2.3.8.4 Galaxy Subtraction

When subtracting host-galaxy light, the finite signal-to-noise ratio (S/N) of the images used as templates can limit measurements of the magnitude of a SN, thereby introducing a correlated error between epochs of photometry. To investigate the severity of this effect, G10 stacked images to obtain a deeper set of template images with increased S/N for SN 2000cn, a SN Ia from their sample. By reprocessing their data with the new template images, G10 were able to probe the influence of host-galaxy templates derived from single images. Unsurprisingly, they found that the correlated error introduced by using a single image for a template is not negligible, but that it is appropriately accounted for by their error budget. As the modest differences between the Nickel1 and Nickel2 systems should not manifest any substantial differences with regard to galaxy subtraction in this manner, and because the error budget of G10 is similar to our own (as laid out in Section 2.3.7), we see no need for repetition of this test.

2.3.8.5 Total Systematic Error

Based on the preceding discussion, we assign a systematic uncertainty of 0.03 mag in $BVRI$ to our sample, consistent with G10. This uncertainty is not explicitly included in our photometry tables or light curve figures (e.g., Tables 2.2 & 2.6 and Figure 2.13), but must be accounted for when combining our dataset with others.

2.4 Results

In this section we present the results obtained by running our photometry pipeline on SNe Ia from LOSS images collected from 2009 through 2018, with several earlier SNe Ia also included. Basic information and references for each SN in our sample are provided in Table 2.3. The NASA/IPAC Extragalactic Database (NED)[9] and the TNS were used to source many of the given properties.

Figure 2.13 shows our light curves, each shifted such that time is measured relative to the time of maximum B-band brightness as determined by `MLCS2k2` (Jha et al. 2007) fits or Gaussian Process interpolations (Lochner et al. 2016) for peculiar SNe (see Sections 2.5.2.2 & 2.5.1, respectively). An example of our photometry is given in Table 2.2. In addition to leaving out the systematic 0.03 mag uncertainty derived in Section 2.3.8.5, we choose to provide light curves without considering corrections such as Milky Way (MW) extinction, K-corrections

[8]The only exception is the median I-band offset between Nickel1 and KAIT3, which is 0.008 mag.

[9]The NASA/IPAC Extragalactic Database (NED) is operated by the Jet Propulsion Laboratory, California Institute of Technology, under contract with the National Aeronautics and Space Administration (NASA).

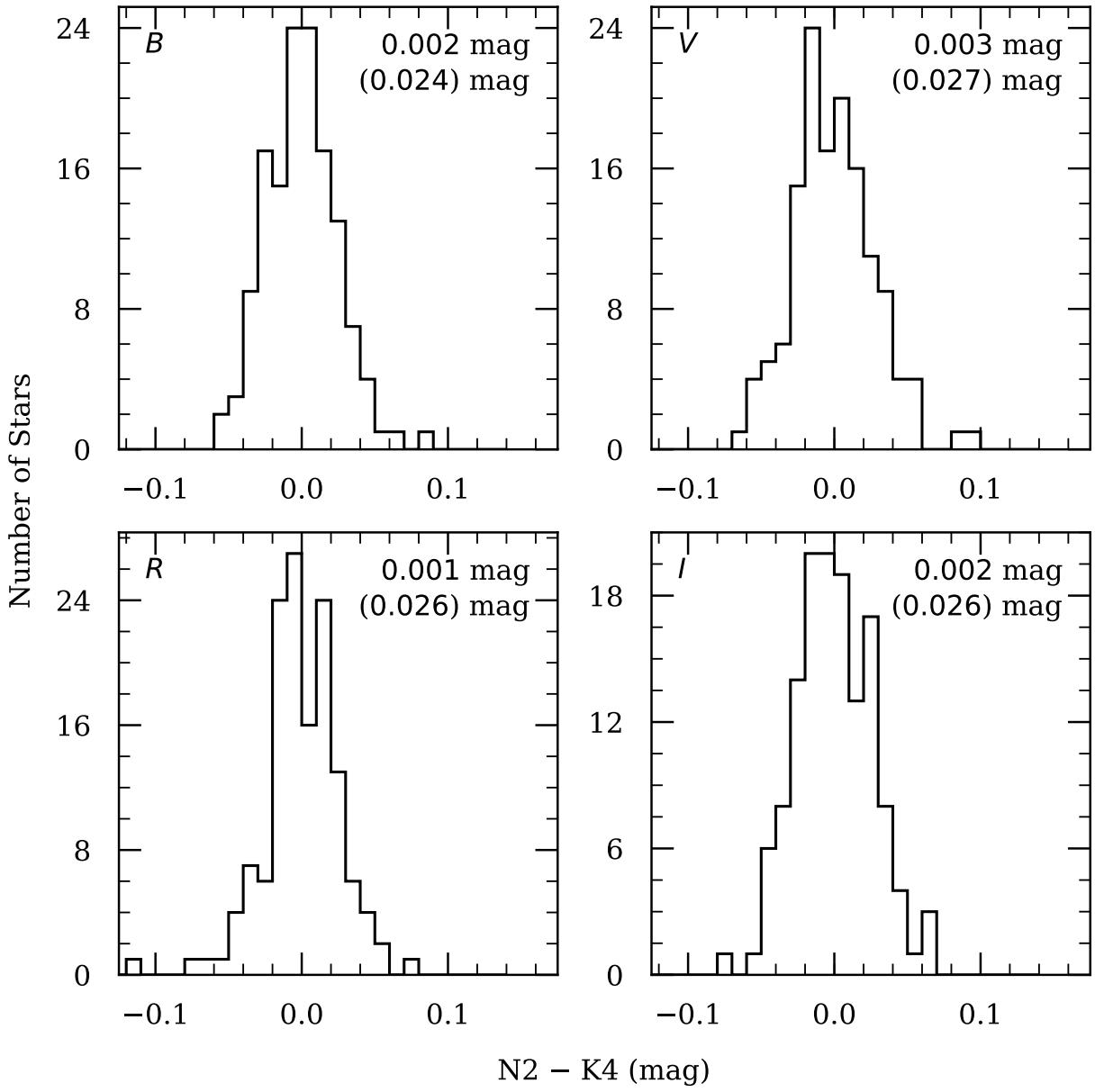

Figure 2.6: Distributions of the residuals of the mean derived magnitude of each calibration star used in determining final photometry for SNe in our dataset covered by the KAIT4 and Nickel2 systems. The distributions reveal negligible offset between these two systems in all bands with a scatter < 0.03 mag. The median and standard deviation of the residuals are printed for each passband.

Table 2.2: Photometry of SN 2008ds.

SN	MJD	B (mag)	V (mag)	R (mag)	I (mag)	*Clear* (mag)	System
2008ds	54645.47	...	...	...	...	15.700 ± 0.033	kait4
2008ds	54646.47	...	...	...	...	15.574 ± 0.024	kait4
2008ds	54647.46	15.613 ± 0.012	15.630 ± 0.010	15.593 ± 0.012	15.744 ± 0.018	15.501 ± 0.010	kait4
2008ds	54650.47	15.503 ± 0.014	15.487 ± 0.010	15.475 ± 0.013	15.766 ± 0.016	...	kait4
2008ds	54653.13	15.483 ± 0.009	15.474 ± 0.005	15.413 ± 0.006	15.756 ± 0.008	...	nickel1
2008ds	54653.44	15.492 ± 0.018	15.470 ± 0.010	15.435 ± 0.011	15.828 ± 0.017	...	kait4
2008ds	54655.13	15.570 ± 0.008	15.512 ± 0.006	15.451 ± 0.007	15.826 ± 0.009	...	nickel1
2008ds	54655.48	15.567 ± 0.016	15.507 ± 0.012	15.467 ± 0.015	15.925 ± 0.023	...	kait4
2008ds	54658.13	15.704 ± 0.008	15.606 ± 0.006	15.542 ± 0.006	15.962 ± 0.008	...	nickel1
2008ds	54662.16	15.995 ± 0.012	15.773 ± 0.005	...	...	...	nickel1

Note: First 10 epochs of $BVRI$ + unfiltered photometry of SN 2008ds. This table shows the form and content organisation of a much larger table that covers each epoch of photometry for each SN in our dataset. The full table is available online at `http://heracles.astro.berkeley.edu/sndb/info#DownloadDatasets(BSNIP,LOSS)`.

(Oke and Sandage 1968; Hamuy et al. 1993; Kim et al. 1996), or S-corrections (Stritzinger et al. 2002). This provides future studies the opportunity to decide which corrections to apply and full control over how they are applied. Because of the low redshift range of our dataset (see the right panel of Figure 2.7) and the similarity between systems, the K- and S-corrections will be quite small in any case. Though magnitudes in Figure 2.13 and Table 2.2 are given in the Landolt system, we also make our dataset available in natural-system magnitudes for those that would benefit from the reduced uncertainties (see Section 2.8.2). Our entire photometric dataset (Landolt and natural-system magnitudes) is available online from the Berkeley SuperNova DataBase[10] (SNDB; Silverman et al. 2012a; Shivvers et al. 2016).

2.4.1 The LOSS Sample

In order to accurately measure and exploit the correlation between light-curve width and luminosity for SNe Ia, thus allowing for precision measurements of cosmological parameters, densely sampled multicolour light curves which span pre- through post-maximum evolution are required. In Figure 2.8 we show the number of epochs of photometry for each SN in our sample versus the average cadence between epochs of photometry. The plot indicates that the majority of SNe in our sample have more than 10 epochs of observations with a cadence of fewer than 10 days, while a significant number of SNe were observed many more times at even higher frequency. These metrics confirm that on average, our light curves are well sampled and span a large range of photometric evolution.

[10] `http://heracles.astro.berkeley.edu/sndb/info#DownloadDatasets(BSNIP,LOSS)`

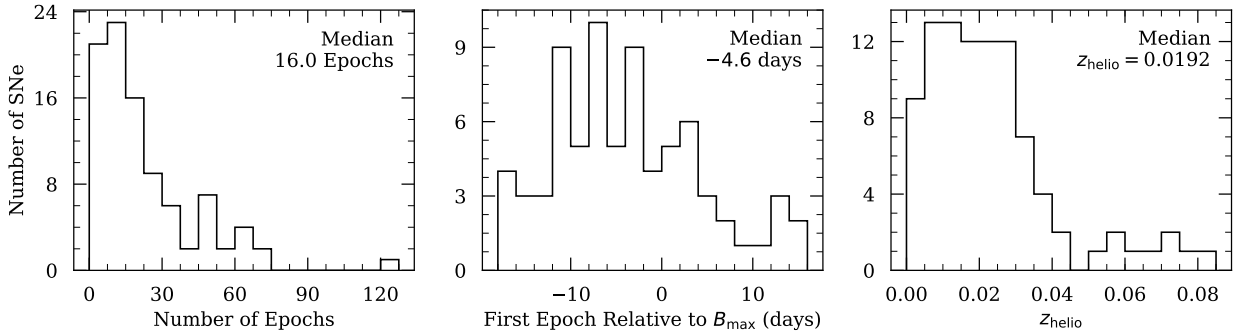

Figure 2.7: Distributions of dataset parameters. The left panel is the number of epochs of photometry as measured from V-band observations, centre is the first epoch of observation relative to time of maximum B-band light, and right is redshift.

The left panel of Figure 2.7 presents a histogram of the total number of photometry epochs for all SNe in our sample, and we find a median of 16 epochs. SN 2011dz has just one epoch of photometry and five objects (SNe 2006ev, 2009D, 2009hp, 2012E, 2012bh) have two epochs each, while SN 2013dy has 126 (the most), followed by SN 2012cg and then SN 2017fgc. We begin photometric follow-up observations for the typical SN in our sample ~ 4.6 days before maximum light in the B-band, with 52 SNe having data before maximum brightness. The centre panel of Figure 2.7 shows the distribution of first-observation epochs for our sample. The median redshift of our full sample is 0.0192, with a low of 0.0007 (SN 2014J) and a high of 0.0820 (SN 2017dws). We show the distribution of redshifts in the right panel of Figure 2.7. If we restrict to $z \geq 0.01$ (i.e., within the Hubble flow), our sample consists of 71 SNe with a median redshift of 0.0236.

2.4.2 Comparison with Published LOSS Reductions

For several of the SNe presented here, previous reductions of the photometry (usually performed with an earlier photometry pipeline, developed by G10) have been published. A comparison between these previous results and our own offers a useful efficacy check of our pipeline while avoiding the issues arising from comparisons between different telescopes or photometric systems. Wherever sufficient overlap between one of our light curves and that from a previous publication exists, we quantify the extent to which the datasets agree by computing the weighted mean residual. In some cases we further compare by considering the agreement between derived quantities such as the light-curve shape, $\Delta m_{15}(B)$, and the time of maximum brightness, $t_{B_{\max}}$. We emphasise that in general our results are derived from different sets of reference stars for calibration than those used to derive the results with which we compare, and that even when reference stars overlap, we may draw their magnitudes from different catalogs.

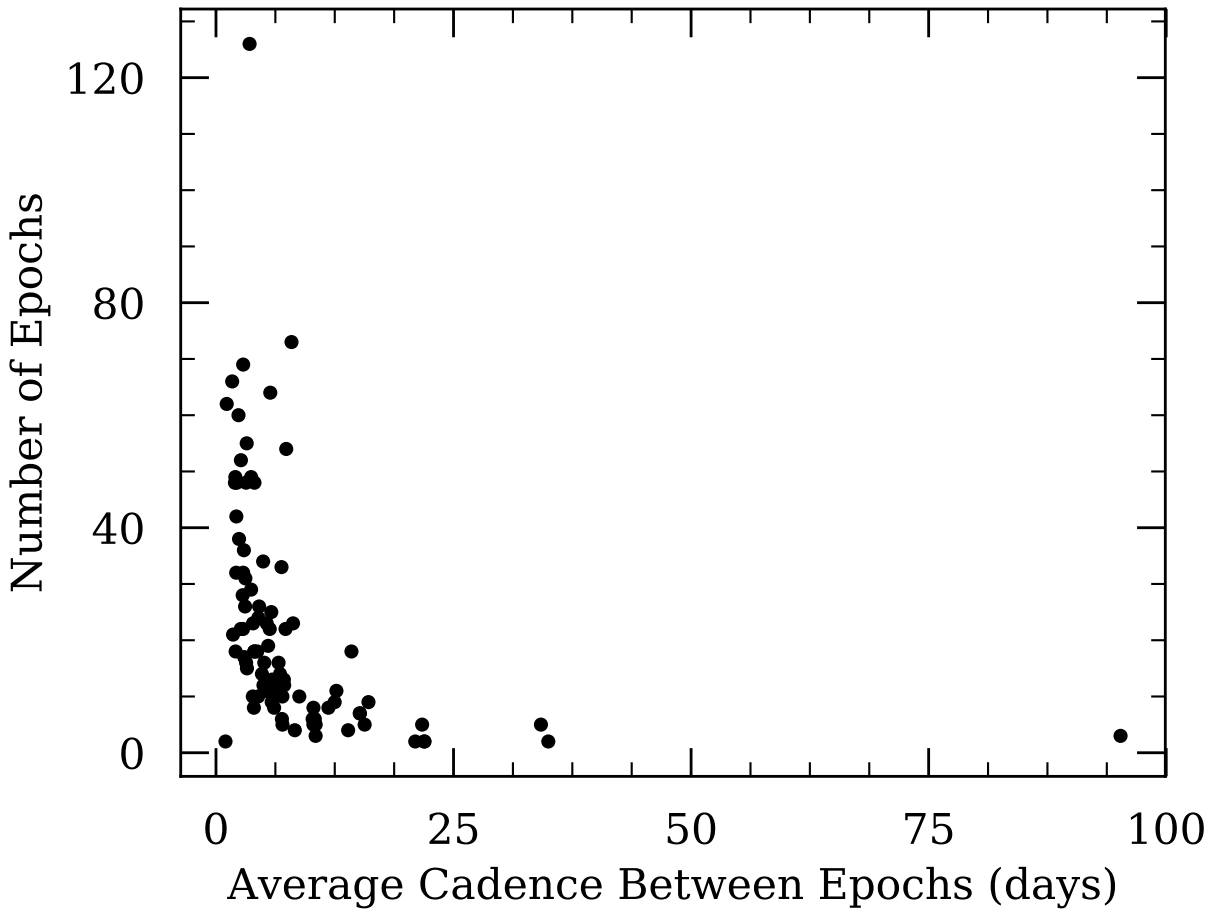

Figure 2.8: Scatterplot of the number of photometry epochs for each SN vs. the average cadence between epochs. The tight grouping with a lower average cadence and mid to high number of epochs indicates that our SNe are well sampled and cover a large portion of photometric evolution. The single SN with an average cadence in excess of 80 days is SN 2016ffh.

2.4.2.1 SN 2005hk

Phillips et al. (2007) published optical light curves from KAIT data for the Type Iax SN 2005hk. At the time of publication, no template images were available and so the authors acknowledged that their derived magnitudes for the SN, located $\sim 18.5''$ from the nucleus of its host galaxy, were probably affected by the background light. In the prevailing time, we have obtained template images of the host and used them to separate its flux from that of the SN. Comparing results, both of which were obtained using PSF-fitting photometry, we find agreement to within 0.090 mag in *BVRI*. It is worth noting that our measurements are generally fainter, especially when the SN is rising and declining. This suggests that host-galaxy subtraction is indeed necessary for this object. We also compare measurements of the light-curve shape parameter $\Delta m_{15}(B)$, and find strong agreement between our value (see Section 2.5.1 and Table 2.4) of 1.58 ± 0.05 mag and theirs of 1.56 ± 0.09 mag.

2.4.2.2 SN 2009dc

Our Nickel and KAIT images of the extremely slow-evolving SN 2009dc — a super-Chandrasekhar candidate (see Noebauer et al. 2016, for a summary of the properties of this subclass of thermonuclear SNe) — were initially processed and used to construct light curves by Silverman et al. (2011). In both our reduction and theirs, PSF-fitting photometry was employed and galaxy subtraction was not performed owing to the large separation between the SN and its host galaxy. We find agreement to better that 0.020 mag in *BVRI*. Furthermore, we derive $\Delta m_{15}(B) = 0.71 \pm 0.06$ mag, consistent with their result of $\Delta m_{15}(B) = 0.72 \pm 0.03$ mag.

2.4.2.3 SN 2009ig

Optical light curves of SN 2009ig were derived from KAIT data and published by Foley et al. (2012). Both our reduction procedure and theirs used PSF-fitting photometry after subtracting template images of the host galaxy. We find that our results agree to within 0.055 mag in *BVRI*. It is worth adding that SN 2009ig is in a field with very few stars available for comparison when calibrating to natural-system magnitudes — Foley et al. (2012) used only one star for comparison while we have used two. In light of these challenges, we are content with the similarity between our results, especially because we obtain a consistent value of $\Delta m_{15}(B)$[11]. As an added check, we reprocessed our data for SN 2009ig using the same calibration star as Foley et al. (2012) and find agreement to within ~ 0.025 mag in *BVRI*.

2.4.2.4 SN 2011by

KAIT *BVRI* photometry of SN 2011by was published by Silverman et al. (2013) and later studied in detail by Graham et al. (2015). In comparing our light curves (which have host-

[11]We find $\Delta m_{15}(B) = 0.85 \pm 0.12$ mag (the large uncertainty is mostly due to the uncertainty in the time of B maximum), while Foley et al. (2012) find $\Delta m_{15}(B) = 0.89 \pm 0.02$ mag.

galaxy light subtracted) to theirs (which do not), we find agreement to within ~ 0.05 mag. Furthermore, Silverman et al. (2013) found $B_{\rm max} = 12.89 \pm 0.03$ mag and $\Delta m_{15}(B) = 1.14 \pm 0.03$ mag, which are consistent with our results of $B_{\rm max} = 12.91 \pm 0.02$ mag and $\Delta m_{15}(B) = 1.09 \pm 0.10$ mag.

2.4.2.5 SN 2011fe

SN 2011fe/PTF11kly in M101 is perhaps the most extensively observed SN Ia to date (Nugent et al. 2011; Vinkó et al. 2012; Richmond and Smith 2012; Graham et al. 2015; Zhang et al. 2016). Photometry derived from KAIT data has been published by Graham et al. (2015) and Zhang et al. (2016), but we compare only with the latter. For the 20 epochs that overlap between our dataset and theirs, we find agreement of better than ~ 0.04 mag in *BVRI*.

2.4.2.6 SN 2012cg

SN 2012cg was discovered very young by LOSS, and KAIT photometry from the first ~ 2.5 weeks following discovery was published by Silverman et al. (2012b). Because of the small temporal overlap between this early-time dataset and the much more expansive set presented herein, and because we have obtained template images and used them to remove the host-galaxy light, it is not instructive to quantitatively compare between our dataset and theirs. We note, however, that we find a similar time of B-band maximum and that there is clear qualitative agreement between the two samples.

2.4.2.7 SN 2013dy

Zheng et al. (2013) published early-time KAIT photometry of SN 2013dy and used it to constrain the first-light time, while Pan et al. (2015a) published extensive optical light curves. We compare the 85 overlapping epochs of our dataset with those of Pan et al. (2015a), both of which were obtained using PSF-fitting photometry, and find agreement better than ~ 0.03 mag in *BVRI*.

2.4.2.8 SN 2013gy

KAIT B and V observations were averaged in flux space to create so-called BV.5-band photometry by Holmbo et al. (2019), who then used S-corrections to transform to the g band on the Pan-STARRS1 photometric system. Because of the difference between our choice of photometric system and theirs, we opt only to compare derived light-curve properties. Our result for the time of B-band maximum is within one day of theirs (consistent, given the uncertainties), and we find $\Delta m_{15}(B) = 1.247 \pm 0.072$ mag, nearly identical to their result of $\Delta m_{15}(B) = 1.234 \pm 0.060$ mag.

2.4.2.9 SN 2014J

SN 2014J in M82 has been extensively studied — unfiltered KAIT images were presented by Zheng et al. (2014) and used to constrain the explosion time, and Foley et al. (2014) published photometry from many sources, including a number of KAIT *BVRI* epochs. A comparison between our results and theirs reveals substantial ($\sim$ 0.2 mag) discrepancies. The origin of this disagreement stems from differences in our processing techniques — Foley et al. (2014) calibrated instrumental magnitudes against reference-star magnitudes *in the Landolt system* (thereby disregarding linear colour terms), while we have done calibrations with reference-star magnitudes *in the natural system* appropriate to the equipment before transforming to the Landolt system. When we reprocess our data using the former approach in conjunction with the reference stars used by Foley et al. (2014), we find agreement between our non-host-galaxy subtracted light curve and theirs to within 0.01 mag in *BVRI*. Our final light curve for SN 2014J reflects the latter approach (which is the default of our pipeline), and was derived using a different set of calibration stars after subtracting host-galaxy light.

2.4.2.10 SN 2016coj

SN 2016coj was discovered at a very early phase by LOSS, and Zheng et al. (2017) presented the first 40 days of our optical photometric, low- and high-resolution spectroscopic, and spectropolarimetric follow-up observations. Because our full photometric dataset encompasses a much broader time frame and Zheng et al. (2017) focused only on unfiltered photometry, a direct comparison is not possible. However, we note that our derived $\Delta m_{15}(B) = 1.33 \pm 0.03$ mag, $B_{\rm max} = 13.08 \pm 0.01$ mag, and $t_{B_{\rm max}} = 57547.15 \pm 0.19$ MJD are consistent with their preliminary reporting, based on photometry *without* host-galaxy subtraction, of 1.25 ± 0.12 mag, 13.1 ± 0.1 mag, and 57547.35 MJD, respectively.

2.4.2.11 Summary of Comparisons

We have compared the results of our photometry to the results derived from previous processing pipelines used by our group for ten SNe Ia. Of these, five (SNe 2009dc, 2009ig, 2011fe, 2013dy, and 2014J) can be directly compared in the sense that identical processing steps (e.g., whether galaxy subtraction was performed) were used. For this subsample, we find excellent ($\lesssim 0.05$ mag) agreement except for the cases of SN 2009ig (< 0.055 mag) and SN 2014J (~ 0.2 mag). However, we are able to attain much stronger agreement ($\lesssim 0.025$ mag and $\lesssim 0.010$ mag, respectively) if we employ the same calibration procedures used in the original processing. For the remaining five, we find consistent results in derived light-curve parameters, and more generally, good qualitative agreement in the shape of the light curves.

2.5 Discussion

The absolute peak brightness that a SN Ia attains has been shown to be strongly correlated with the "width" of its light curve (e.g., Phillips 1993). Thus, given a model for this correlation and a measurement of the light-curve width of a SN Ia, one can compute its intrinsic peak luminosity. By comparing this to its *observed* peak brightness, the distance to the SN Ia can be estimated. In this section, we examine the properties of the light curves in our sample in more detail. Specifically, in Section 2.5.1 we directly measure light-curve properties from interpolations, whereas in Section 2.5.2 we model our light curves with light-curve fitting tools.

2.5.1 Interpolated Light-Curve Properties

Perhaps the most ubiquitous parametrisation of the width (or decline rate) of a SN Ia light curve is $\Delta m_{15}(X)$, the difference in its magnitude at maximum light and 15 days later in passband X. We measure this quantity in B and V by interpolating the (filtered) light curves using Gaussian Processes, a technique that has proved useful in astronomical time series analysis due to its incorporation of uncertainty information and robustness to noisy or sparse data (Lochner et al. 2016).

For each SN in our sample where the photometry in B and/or V encompasses the maximum brightness in that band, we employ the following approach using tools from the `SNooPy`[12] package (Burns et al. 2011). First, we interpolate the light curve in each passband using Gaussian Processes, allowing us to determine the time at which that light curve peaks. With the phase information that this affords, the data are K-corrected using the spectral energy distribution (SED) templates of Hsiao et al. (2007). We further correct the data for MW extinction (Schlafly and Finkbeiner 2011) and then perform a second interpolation on the corrected data. From this interpolation we measure $t_{X_{\max}}, X_{\max}$, and $\Delta m_{15}(X)$ — the time of maximum brightness, maximum apparent magnitude, and light-curve width parameter (respectively) — in filters B and V. In measuring $\Delta m_{15}(X)$, we correct for the effect of time dilation. The final results of this fitting process are presented in Table 2.4.

2.5.2 Applying Light-Curve Fitters

While interpolation is viable for well-sampled light curves, those that are more sparsely sampled or which do not unambiguously constrain the maximum brightness cannot be reliably treated with this technique. Furthermore, interpolation completely disregards the effects of host-galaxy extinction, which must be accounted for when estimating distances.

Because of these limitations, we also employ two light-curve fitters to measure the properties of our sample. To the extent that the templates used by these fitters span the diversity in our dataset, this approach does not suffer from the same limitations as interpolation.

[12] `https://csp.obs.carnegiescience.edu/data/snpy/documentation/snoopy-manual-pdf`

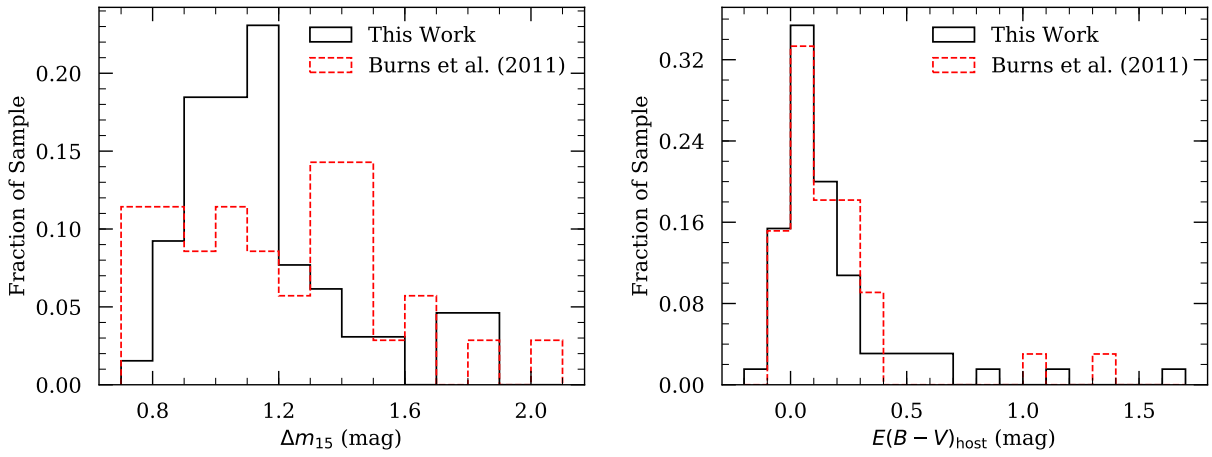

Figure 2.9: Distributions of Δm_{15} and $E(B-V)_{\rm host}$ from `SNooPy` $E(B-V)$ model fits to the light curves in our dataset appear in black. We include the corresponding distributions derived from Burns et al. (2011) in red.

2.5.2.1 SNooPy $E(B-V)$ Model

We use the so-called "EBV_model" in `SNooPy` to simultaneously fit the $BVRI$ light curves in our sample. In observed band X and SN rest-frame band Y, the model takes on the mathematical form

$$\begin{aligned} m_X(t-t_{\rm max}) = {} & T_Y\left(t_{\rm rel}, \Delta m_{15}\right) + M_Y(\Delta m_{15}) + \mu + \\ & R_X E(B-V)_{\rm gal} + R_Y E(B-V)_{\rm host} + \\ & K_{X,Y}\left(z, t_{\rm rel}, E(B-V)_{\rm host}, E(B-V)_{\rm gal}\right), \end{aligned} \tag{2.2}$$

where m is the observed magnitude, $t_{\rm max}$ is the time of B-band maximum, $t_{\rm rel} = (t' - t_{\rm max})/(1+z)$ is the rest-frame phase, M is the rest-frame absolute magnitude of the SN, μ is the distance modulus, $E(B-V)_{\rm gal}$ and $E(B-V)_{\rm host}$ are the reddening due to the Galactic foreground and host galaxy, respectively, R is the total-to-selective absorption, and K is the K-correction (which depends on the epoch and can depend on the host and Galactic extinction).

`SNooPy` generates the template, $T(t, \Delta m_{15})$, from the prescription of Prieto et al. (2006). As indicated, the light curve is parameterised by the decline-rate parameter, Δm_{15}, which is similar to $\Delta m_{15}(B)$. It is important to note, however, that these quantities are *not* identical, and may deviate from one another randomly and systematically (see Section 3.4.2 in Burns et al. 2011). The model assumes a peak B-band magnitude and $B-X$ colours based on the value of Δm_{15}, with six possible calibrations derived from CSP1a. We use calibration #6, which is derived from the best-observed SNe in the sample, less those that are heavily extinguished.

The template-fitting process with `SNooPy` consists of the following steps. First, an initial fit is made to determine the time of B-band maximum. This allows for initial K-corrections to be determined using the SED templates from Hsiao et al. (2007). The K-corrected data are then fit again, allowing colours to be computed as a function of time. Next, improved K-corrections are computed, warping the SED such that it matches the observed colours. Last, a final fit is performed using the improved K-corrections. The results from fitting are $t_{\max}, \Delta m_{15}, E(B-V)_{\rm host}$, and μ. We present these quantities for our dataset in Table 2.5. We also visualise the distributions of Δm_{15} and $E(B-V)_{\rm host}$ from our dataset in Figure 2.9, with the corresponding distributions from Burns et al. (2011) overlaid for comparison.

For Δm_{15}, we find a median value of 1.11 mag with a standard deviation of 0.26 mag, consistent with the respective values of 1.15 mag and 0.32 mag from the dataset of Burns et al. (2011). And for $E(B-V)_{\rm host}$, we find a median of 0.10 mag with a dispersion of 0.29 mag for our sample, similar to their values of 0.12 mag and 0.29 mag, respectively. We stress that comparing these parameters between our dataset and that of Burns et al. (2011) is only to provide a diagnostic view of how our sample is distributed relative to another from the literature — there is minimal overlap between the two samples, so we are *not* looking for a one-to-one correspondence.

Furthermore, we can use the fitted model for each light curve to calculate other parameters of interest, such as those derived from direct interpolation. This gives a method by which we can check for consistency in our results. For example, we expect the time of maximum brightness in a given band to be the same, regardless of whether it was calculated from an interpolation or a fitted model. We employ Kolmogorov-Smirnoff tests on our calculated times of maximum (where we have results from both interpolation and template fitting) to quantify the likelihood that those from interpolation are drawn from the same distribution as those from template fitting. In both cases ($t_{B_{\max}}$ and $t_{V_{\max}}$), we find p-values of unity, indicating that our expectation is met.

Applying such tests for $B_{\max}$ and $V_{\max}$ is less straightforward because of the presence of systematic offsets between results derived from interpolation and those derived from fitting `SNooPy`'s $E(B-V)$ model. While both methods provide peak magnitudes after performing K-corrections and correcting for MW reddening, only the $E(B-V)$ model fits account for host-galaxy reddening. With this caveat noted, it is still instructive to make comparisons, and in doing so we find p-values of 0.708 and 0.981 for $B_{\max}$ and $V_{\max}$, respectively. If we impose restrictions to make the comparison more legitimate — namely to use only those SNe in our sample that are not heavily extinguished by their hosts ($|E(B-V)_{\rm host}| < 0.1$ mag), that are spectroscopically normal (as given in Table 2.3), and for which `SNooPy` measures $\Delta m_{15} < 1.7$ mag — we find substantially improved agreement, with p-values of 0.956 and 1.000, respectively.

As noted above, Δm_{15} does not exactly correspond to $\Delta m_{15}(B)$. In comparing them, Burns et al. (2011) found a linear relationship of $\Delta m_{15}(B) = 0.89\Delta m_{15} + 0.13$. Performing an analogous comparison with our dataset subjected to the aforementioned light-curve shape restriction, we find $\Delta m_{15}(B) = (0.97 \pm 0.12)\Delta m_{15} + (0.02 \pm 0.14)$. Figure 2.10 shows our derived linear relationship within the context of our data.

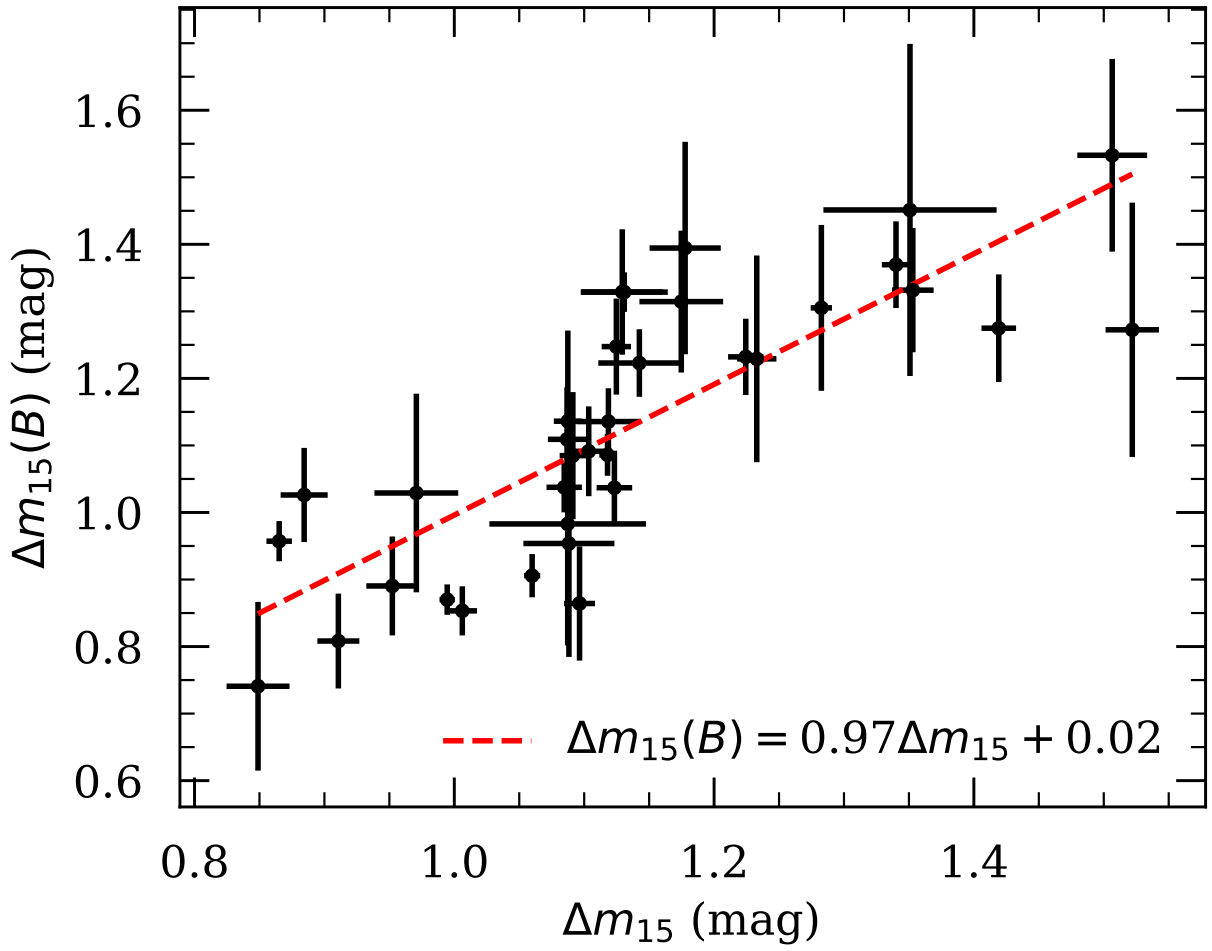

Figure 2.10: Comparison of the decline-rate parameter as measured from our Gaussian Process interpolations, $\Delta m_{15}(B)$, with that obtained directly from our `SNooPy` $E(B-V)$ model fits, Δm_{15}.

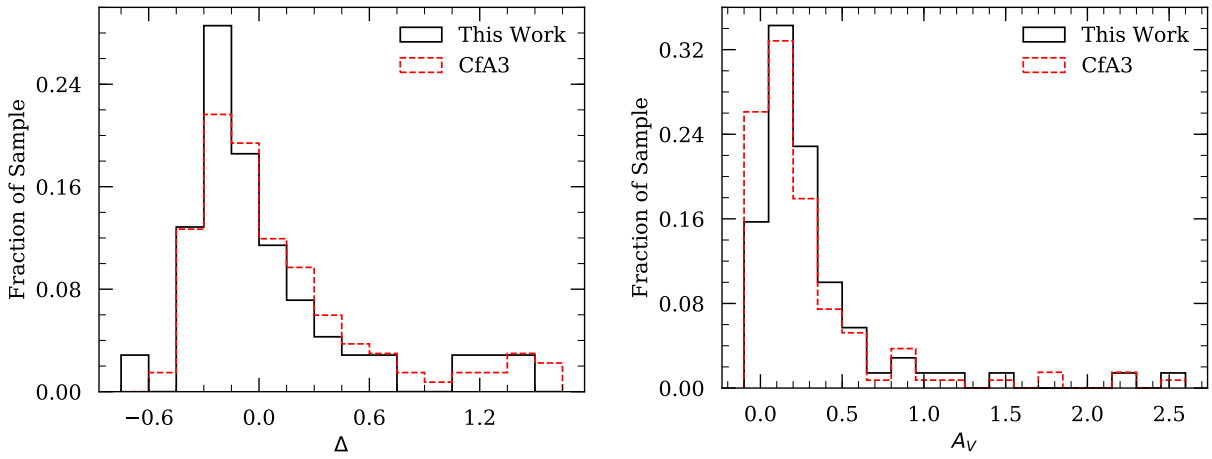

Figure 2.11: Distributions of Δ and A_V from `MLCS2k2` model fits to the light curves in our dataset appear in black. We include the corresponding distributions derived from CfA3 in red.

2.5.2.2 MLCS2k2

In addition to the methods described above, we have run `MLCS2k2.v007` (Jha et al. 2007) on our sample of light curves. `MLCS2k2` parameterises the absolute magnitude of a SN in terms of Δ, which quantifies how luminous a SN is relative to a fiducial value. By using a quadratic dependence on Δ, intrinsic variations in peak magnitude are modeled without introducing a parameter for intrinsic colour. In order to do this, `MLCS2k2` corrects for MW reddening and *attempts* to correct for reddening due to the host galaxy by employing a reddening law, R_V, to obtain the host-galaxy extinction parameter, A_V, after employing a prior on $E(B-V)$.

`MLCS2k2` yields four fitted parameters for each $BVRI$ light curve: the distance modulus (μ), the shape/luminosity parameter (Δ), the time of B-band maximum (t_0), and the host-galaxy extinction parameter (A_V). In running `MLCS2k2` on our dataset, we fix R_V to 1.7 and use the default host-reddening prior, which consists of a one-sided exponential with scale length $\tau_{E(B-V)} = 0.138$ mag. We use the SED templates of Hsiao et al. (2007), and following Hicken et al. (2009b) we use `MLCS2k2` model light curves trained using $R_V = 1.9$. We present the results of running `MLCS2k2.v007` on our sample in Table 2.5 and the distributions of Δ and A_V in Figure 2.11. We find a median and standard deviation for Δ of -0.11 and 0.46, and for A_V of 0.20 and 0.45. Comparing these to the corresponding parameters from CfA3 we find reasonable agreement, with -0.04 and 0.48, and 0.13 and 0.44, respectively. Our dataset only shares minimal overlap with that of CfA3, so these comparisons serve to reveal how our dataset is distributed relative to another low-z sample.

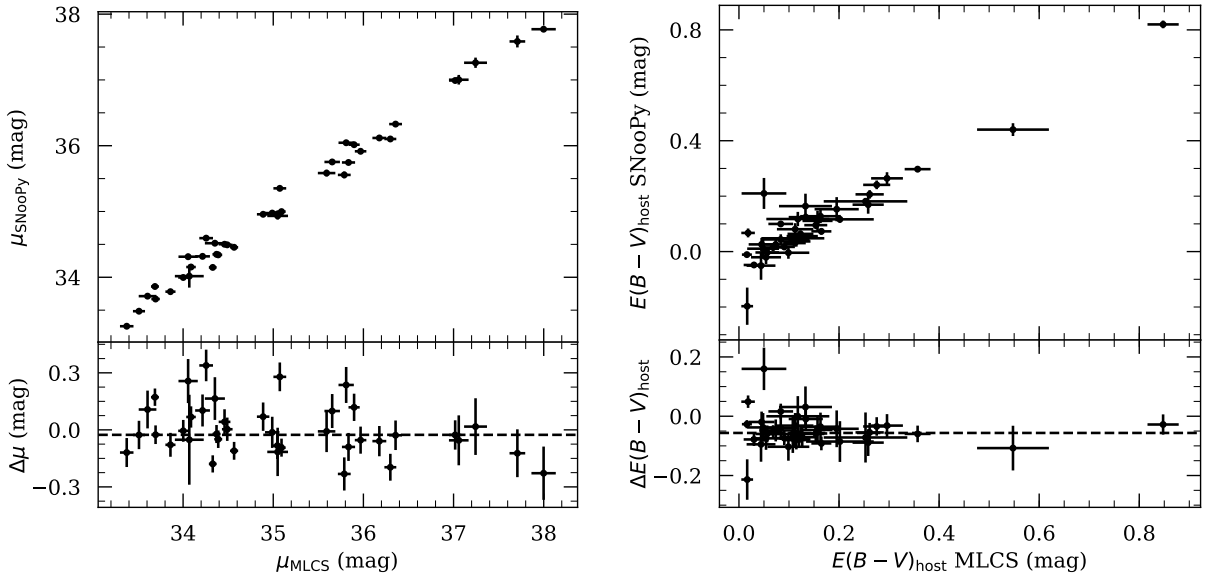

Figure 2.12: Comparison of the (scaled) distance modulus and host-galaxy reddening results from both light-curve fitters for the selected subset of our dataset.

2.5.3 Comparison of Light-Curve Fitter Results

To make any cosmological statements based on the results in the previous section is beyond the scope of this paper, as this would require a detailed study and justification of the utilised light-curve fitters and their parameters, amongst many other considerations. It is interesting and possible, however, to compare results from the two light-curve fitters we employ to check for consistency. As the principal quantity of interest when fitting the light curves of SNe Ia is distance, we will focus our comparison on the derived distance moduli.

The left plot in Figure 2.12 compares the distance moduli from `SNooPy` and `MLCS2k2` after correcting to put the measurements on the same scale (so that *relative* distance moduli are compared, independent from assumptions about the Hubble constant). This correction consists of adding an offset to the distance moduli from each fitter such that the value of H_0 measured from each set of results yields 65 km s^{-1} Mpc^{-1}. We perform this comparison only for spectroscopically normal SNe Ia in our sample for which `SNooPy` finds $\Delta m_{15} < 1.7$ mag and for which $z > 0.01$. Of course, further restrictions should be placed when selecting a sample for cosmological purposes, but our selection is reasonable for performing a general comparison. We find strong agreement between the two sets of corrected distance moduli — a Kolmogorov-Smirnoff test gives a p-value of 1.000. The median residual is -0.026 mag with a statistical dispersion of 0.135 mag.

If we were to ensure consistency in choosing the parameters for each light-curve fitter, the residuals would almost certainly decrease. In particular, when fitting with `MLCS2k2`, we place

an exponentially decaying prior on A_V, but no such prior was imposed with `SNooPy`. This difference may well manifest in statistically and systematically different results for host-galaxy reddening and distance moduli between the two fitters. We compare host-galaxy reddening results in the right panel of Figure 2.12, where for `MLCS2k2` we have converted to reddening using $E(B-V)_{\rm host} = A_V/R_V$, with $R_V = 1.7$. The agreement is reasonable, with a median residual of -0.056 mag and statistical uncertainty of 0.055 mag. Furthermore, the facts that the median residual (`SNooPy` minus `MLCS2k2`) is negative and that the disagreement is most severe for small $E(B-V)_{\rm host}$ are consistent with what one might expect given the prior imposed by `MLCS2k2`.

2.6 Conclusion

In this paper we present *BVRI* (along with some unfiltered) light curves of 93 SNe Ia derived from images collected by the LOSS follow-up program primarily over the interval from 2009–2018, but with several instances as early as 2005. Careful and consistent observational and processing techniques ensure that our data is prepared in a homogeneous fashion. We estimate the systematic uncertainty in our dataset to be 0.03 mag in *BVRI*, and we encourage the community to incorporate our light curves in future studies.

In cases where our results overlap with previous reductions of LOSS data, we provide a set of comparisons as a consistency check. In general, we find good agreement, giving us confidence in the quality of our processing and analysis. When combined with the light curves of G10, the resulting dataset spans 20 years of observations of 258 SNe Ia from the same two telescopes.

We study the properties of the light curves in our dataset, with particular focus on the parameters used in various width-luminosity relationships. Using direct interpolations, we measured $\Delta m_{15}(B)$ and $\Delta m_{15}(V)$. We also apply the light-curve fitters `SNooPy` and `MLCS2k2.v007` to measure Δm_{15} and Δ, respectively. We compare results derived from these methods, and find an acceptable degree of agreement given the differences in starting assumptions.

A consideration of the photometric dataset presented here alongside spectra from the Berkeley Supernova Ia Program (BSNIP) database will enable further utility. Our dataset overlaps with 13 SNe from the first BSNIP data release (Silverman et al. 2012a), with an average of 4.5 spectra each. Furthermore we expect significant overlap between the SNe in our dataset and our upcoming second BSNIP data release of $\sim$ 700 spectra from $\sim$ 250 SNe Ia observed over a similar temporal range (Stahl et al. 2020b).

2.7 Sample Information

Table 2.3: SN Ia sample.

SN Name	R.A.[a] α(2000)	Decl.[a] δ(2000)	Discovery[a] Date (UT)	Discovery Reference	Spectroscopic[b] Reference	Type[c]	Host[a] Galaxy	$z_{\rm helio}$[d]	$E(B-V)_{\rm MW}$[e] (mag)	E[f] ($''$)	N[f] ($''$)	Host Subtr.[g]
2005hk	6.96196	−1.19792	30 Oct 2005	IAUC 8625	CBET 269, Ph07	Iax	UGC 272	0.013	0.020	16.9	7.5	Y
2005ki	160.11758	9.20233	18 Nov 2005	CBET 294	CBET 296	Ia	NGC 3332	0.019	0.027	−2.2	71.2	N
2006ev	322.74692	13.98922	12 Sep 2006	IAUC 8747	CBET 622	Ia	UGC 11758	0.029	0.077	23.9	11.3	Y
2006mq	121.55162	−27.56261	22 Oct 2006	CBET 721	CBET 724	Ia	ESO 494–G26	0.003	0.362	17.3	−123.1	N
2007F	195.81283	50.61881	11 Jan 2007	CBET 803	CBET 805	Ia	UGC 8162	0.024	0.015	−9.8	−7.0	Y
2007bd	127.88867	−1.19944	4 Apr 2007	CBET 914	CBET 915	Ia	UGC 4455	0.031	0.029	6.0	−6.2	Y
2007bm	171.25958	−9.79828	20 Apr 2007	CBET 936	CBET 939	Ia	NGC 3672	0.006	0.035	−2.5	−10.4	Y
2007fb	359.21821	5.50883	3 Jul 2007	CBET 992	CBET 993	Ia	UGC 12859	0.018	0.048	12.2	1.5	Y
2007fs	330.4185	−21.50822	15 Jul 2007	CBET 1002	CBET 1003	Ia	ESO 601–G5	0.017	0.029	34.5	10.6	Y
2007if	17.71404	15.46108	16 Aug 2007	CBET 1059	CBET 1059	SC	Anon.	$0.074^{\pm}$	0.071	...	...	N
2007jg	52.46175	0.05683	14 Sep 2007	CBET 1076	CBET 1076	Ia	SDSS J032950.83 + 000316.0[†]	0.037	0.091	−0.1	8.6	Y
2007kk	55.59692	39.24178	28 Sep 2007	CBET 1096	CBET 1097	Ia	UGC 2828	0.041	0.196	−9.1	−9.9	Y
2008Y	169.87737	54.46283	6 Feb 2008	CBET 1240	CBET 1246	Ia	MCG +09–19–39	0.070	0.011	−2.3	7.1	Y
2008dh	8.79717	23.25419	8 Jun 2008	CBET 1409	CBET 1409	Ia	PGC 1684149[†]	0.037	0.026	12.2	−3.0	Y
2008ds	7.46179	31.39275	28 Jun 2008	CBET 1419	CBET 1419	Ia-pec	UGC 299	0.021	0.055	−33.0	−2.2	Y
2008eg	27.90112	19.10469	20 Jul 2008	CBET 1444	CBET 1444	Ia	UGC 1324	0.034	0.057	0.3	4.3	Y
2008ek	241.38821	17.59256	28 Jul 2008	CBET 1452	CBET 1454	Ia	IC 1181	0.033	0.038	−9.7	−4.1	Y
2008eo	10.46683	32.99033	3 Aug 2008	CBET 1459	CBET 1465	Ia	UGC 442	0.016	0.070	4.4	−3.5	Y
2008eq	255.03	23.13239	2 Aug 2008	CBET 1460	CBET 1465	Ia	PGC 214560[†]	0.057	0.063	4.1	3.6	Y
2008fk	38.52108	1.39514	2 Sep 2008	CBET 1494	CBET 1499	Ia	2MASX J02340513+0123408[†]	0.072	0.020	−1.2	1.9	Y
2008fu	45.61875	−24.45597	25 Sep 2008	CBET 1517	CBET 1519	Ia	ESO 480–IG21	0.052	0.019	−2.6	−0.5	Y
2008gg	21.346	−18.17244	9 Oct 2008	CBET 1538	CBET 1540	Ia	NGC 539	0.032	0.021	18.7	−30.9	N
2008gl	20.22842	4.80531	20 Oct 2008	CBET 1545	CBET 1547	Ia	UGC 881	0.034	0.024	20.2	14.3	Y
2008go	332.68679	−20.78811	22 Oct 2008	CBET 1553	CBET 1554	Ia	Anon.[†]	0.062	0.032	11.9	8.8	N
2008gp	50.75304	1.36189	27 Oct 2008	CBET 1555	CBET 1558	Ia	MCG +00–9–74	0.033	0.104	10.9	−14.0	Y
2008ha	353.71954	18.2265	7 Nov 2008	CBET 1567	CBET 1576	Iax	UGC 12682	0.005	0.068	−11.5	−2.6	Y
2008hs	36.37342	41.84308	1 Dec 2008	CBET 1598	CBET 1599	Ia	NGC 910	0.017	0.049	31.7	67.7	N
2009D	58.59512	−19.18172	2 Jan 2009	CBET 1647	CBET 1647	Ia	MCG –03–10–52	0.025	0.046	−26.1	30.9	N
2009al	162.84196	8.57853	26 Feb 2009	CBET 1705	CBET 1708	Ia	NGC 3425[†]	0.022	0.021	−51.3	41.0	N
2009an	185.69779	65.85117	27 Feb 2009	CBET 1707	CBET 1709	Ia	NGC 4332	0.009	0.016	4.4	26.6	Y
2009dc	237.8005	25.70778	9 Apr 2009	CBET 1762	CBET 1776	SC	UGC 10064	0.021	0.060	−15.7	21.1	N
2009ee	170.35542	34.33981	9 May 2009	CBET 1795	CBET 1802	Ia	IC 2738	0.035	0.021	27.7	−60.7	N
2009eq	280.03458	40.12681	11 May 2009	CBET 1805	CBET 1817	Ia-pec	NGC 6686	0.024	0.053	14.7	−39.0	N
2009eu	247.17137	39.55347	21 May 2009	CBET 1813	CBET 1817	Ia	NGC 6166	0.030	0.010	30.6	6.9	Y
2009fv	247.43425	40.81161	2 Jun 2009	CBET 1834	CBET 1846	Ia	NGC 6173	0.029	0.005	−7.7	0.0	Y
2009hn	38.00129	1.24819	24 Jul 2009	CBET 1886	CBET 1889	Ia	UGC 2005	0.022	0.021	38.1	6.0	Y
2009hp	44.59983	6.59308	26 Jul 2009	CBET 1888	CBET 1889	Ia	MCG +01–08–30	0.021	0.198	−9.2	4.6	Y
2009hs	268.96221	62.59975	28 Jul 2009	CBET 1892	CBET 1909	91bg-like	NGC 6521	0.027	0.035	17.2	−45.0	N
2009ig	39.54837	−1.31253	20 Aug 2009	CBET 1918	CBET 1918	Ia	NGC 1015	0.009	0.028	0.7	22.2	Y
2009kq	129.06288	28.06714	5 Nov 2009	CBET 2005	ATEL 2291	Ia	MCG +05–21–1	0.012	0.035	−4.2	24.5	Y
2010ao	205.92079	3.90003	18 Mar 2010	CBET 2211	CBET 2223	Ia	UGC 8686	0.023	0.023	11.8	14.5	Y
2010hs	36.41308	24.76489	12 Sep 2010	CBET 2454	CBET 2461	Ia	PGC 1715790[†]	$0.076^{\mp}$	0.100	−93.4	−46.4	N
2010ii	339.55492	35.49167	30 Sep 2010	CBET 2474	CBET 2474	Ia	NGC 7342	0.027	0.075	0.4	−25.9	Y
2010ju	85.48329	18.4975	14 Nov 2010	CBET 2549	CBET 2550	Ia	UGC 3341	0.015	0.361	6.3	18.5	Y
2011M	75.17312	62.24406	19 Jan 2011	CBET 2640	CBET 2640	Ia	UGC 3218	0.017	0.352	−15.1	0.1	Y
2011bd	266.77633	57.30131	24 Mar 2011	CBET 2685	CBET 2685	Ia	NGC 6473	$0.028^{\ddagger}$	0.041	3.3	−31.0	Y
2011by	178.93983	55.32606	26 Apr 2011	CBET 2708	CBET 2708	Ia	NGC 3972	0.003	0.012	4.0	19.1	Y
2011df	291.89017	54.38647	21 May 2011	CBET 2729	CBET 2729	Ia	NGC 6801	0.014	0.112	−19.0	48.9	Y
2011dl	244.52071	21.55111	17 Jun 2011	CBET 2744	CBET 2744	Ia	UGC 10321	$0.026^{\ddagger}$	0.067	−18.6	−35.0	N

Table 2.3 continued

SN Name	R.A.[a] α(2000)	Decl.[a] δ(2000)	Discovery[a] Date (UT)	Discovery Reference	Spectroscopic[b] Reference	Type[c]	Host[a] Galaxy	$z_{\rm helio}$[d]	$E(B-V)_{\rm MW}$[e] (mag)	E[f] ($''$)	N[f] ($''$)	Host Subtr.[g]
2011dz	243.18675	28.28422	26 Jun 2011	CBET 2761	CBET 2761	Ia	UGC 10273	0.025	0.044	−2.4	−61.8	Y
2011ek	36.45371	18.53333	4 Aug 2011	CBET 2783	CBET 2783	Ia	NGC 918	0.005	0.307	−27.7	133.5	Y
2011fe	210.77421	54.27372	24 Aug 2011	CBET 2792	CBET 2792	Ia	M101‡	0.001	0.008	−59.3	−270.1	Y
2011fs	334.33133	35.58056	15 Sep 2011	CBET 2825	CBET 2825	Ia	UGC 11975	0.021	0.101	−2.7	33.8	N
2012E	38.34496	9.58489	14 Jan 2012	CBET 2981	CBET 2981	Ia	NGC 975	0.020	0.063	0.6	−60.5	N
2012Z	50.52229	−15.38767	29 Jan 2012	CBET 3014	CBET 3014	Iax	NGC 1309	0.007	0.034	−17.5	44.6	N
2012bh	183.40546	46.48347	11 Mar 2012	CBET 3066	CBET 3066	Ia	UGC 7228	0.025	0.016	5.2	−37.8	N
2012cg	186.80346	9.42033	17 May 2012	CBET 3111	CBET 3111	Ia	NGC 4424	0.001	0.018	18.1	−1.2	Y
2012dn	305.90108	−28.27872	8 Jul 2012	CBET 3174	CBET 3174	SC	PGC 64605‡	0.010	0.052	...	...	Y
2012ea	266.29333	18.14078	8 Aug 2012	CBET 3199	CBET 3199	91bg-like	NGC 6430	0.010	0.055	−55.2	6.6	N
2012gl	153.20967	12.68242	29 Oct 2012	CBET 3302	CBET 3302	Ia	NGC 3153	0.009	0.036	−2.6	56.7	N
2013bs	259.34179	41.06672	18 Apr 2013	CBET 3494	CBET 3494	Ia	NGC 6343	0.028	0.025	65.1	50.4	N
2013dh	232.50454	12.98692	12 Jun 2013	CBET 3561	CBET 3561	91T-like	NGC 5936	0.013	0.033	3.8	−8.7	Y
2013dr	259.87608	47.70128	1 Jul 2013	CBET 3576	CBET 3576	Ia	PGC 60077‡	0.017	0.021	−8.7	−4.3	Y
2013dy	334.57333	40.56933	10 Jul 2013	CBET 3588	CBET 3588	Ia	NGC 7250	0.004	0.132	−2.3	25.0	Y
2013ex	83.19425	−14.04594	19 Aug 2013	CBET 3635	CBET 3635	Ia	NGC 1954	0.010	0.123	−24.9	60.6	N
2013fa	310.97321	12.51436	25 Aug 2013	CBET 3641	CBET 3641	Ia	NGC 6956	0.016	0.086	−2.1	8.8	Y
2013fw	318.43654	13.57592	21 Oct 2013	CBET 3681	CBET 3681	Ia	NGC 7042	0.017	0.067	−15.9	3.6	Y
2013gh	330.591	−18.91678	8 Aug 2013	CBET 3706	CBET 3706	Ia	NGC 7183	0.009	0.025	3.1	−1.0	Y
2013gq	124.47275	23.46958	25 Mar 2013	CBET 3730	CBET 3730	Ia	NGC 2554	0.014	0.049	−0.4	−9.2	Y
2013gy	55.57033	−4.72181	6 Dec 2013	CBET 3743	CBET 3743	Ia	NGC 1418	0.014	0.050	10.8	32.2	N
2014J	148.92558	69.67389	21 Jan 2014	CBET 3792	CBET 3792	Ia	NGC 3034	0.001	0.136	−55.2	−19.8	Y
2014ai	139.93404	33.76378	21 Mar 2014	CBET 3838	CBET 3838	Ia	NGC 2832	0.023	0.015	−33.5	50.5	N
2014ao	128.63883	−2.54336	17 Apr 2014	CBET 3855	CBET 3855	Ia	NGC 2615	0.014	0.031	−0.4	12.4	Y
2014bj	290.66312	43.89081	22 May 2014	CBET 3893	CBET 3893	Ia	Anon.	0.005‡	0.091	...	...	N
2014dt	185.48987	4.47181	29 Oct 2014	CBET 4011	CBET 4011	Iax	NGC 4303	0.005	0.019	39.9	−6.6	Y
2015N	325.82037	43.57989	6 Jul 2015	CBET 4124	CBET 4124	Ia	UGC 11797	0.019	0.456	−36.1	12.9	Y
2016aew	212.86037	1.28596	12 Feb 2016	TNSTR–2016–106	TNSCR–2016–114	Ia	IC 0986	0.025	0.033	3.9	−2.0	Y
2016coj	182.02833	65.17729	28 May 2016	TNSTR–2016–384	TNSCR–2016–386	Ia	NGC 4125	0.005	0.016	4.9	11.3	Y
2016fbk	26.02737	34.38283	16 Aug 2016	TNSTR–2016–568	TNSCR–2016–572	Ia	UGC 01212	0.036	0.042	−19.6	−16.1	Y
2016ffh	227.95617	46.25089	17 Aug 2016	TNSTR–2016–583	TNSCR–2016–589	Ia	CGCG 249–011	0.018	0.024	11.4	−10.7	Y
2016gcl	354.48592	27.27715	8 Sep 2016	TNSTR–2016–644	TNSCR–2016–655	91T-like	AGC 331536	0.028	0.063	−2.7	−1.5	Y
2016gdt	328.09396	3.42181	8 Sep 2016	TNSTR–2016–652	TNSCR–2016–666	91bg-like	IC 1407	0.029	0.072	−13.3	−19.3	N
2016hvl	101.009	12.39662	4 Nov 2016	TNSTR–2016–884	TNSCR–2016–892	Ia	UGC 3524	0.013	0.377	22.9	−19.2	N
2017cfd	130.20479	73.48754	16 Mar 2017	TNSTR–2017–315	TNSCR–2017–325	Ia	IC 511	0.012	0.019	−5.5	3.1	Y
2017drh	263.10854	7.0632	3 May 2017	TNSTR–2017–513	TNSCR–2017–516	Ia	NGC 6384	0.006	0.106	26.1	10.5	Y
2017dws	235.05904	11.34486	3 May 2017	TNSTR–2017–528	TNSCR–2017–534	Ia	Anon.	0.082‡	0.035	...	...	Y
2017erp	227.31171	−11.33422	13 Jun 2017	TNSTR–2017–647	TNSCR–2017–655	Ia	NGC 5861	0.006	0.093	−18.8	−45.2	N
2017fgc	20.06017	3.40277	11 Jul 2017	TNSTR–2017–753	TNSCR–2017–757	Ia	NGC 0474	0.008	0.029	116.0	−45.4	N
2017glx	295.91787	56.11008	3 Sep 2017	TNSTR–2017–963	TNSCR–2017–970	91T-like	NGC 6824	0.011	0.107	−3.4	2.2	Y
2017hbi	38.13154	35.4836	2 Oct 2017	TNSTR–2017–1066	TNSCR–2017–1074	Ia	Anon.	0.040‡	0.061	...	...	N
2018aoz	177.75762	−28.74406	2 Apr 2018	TNSTR–2018–428	TNSCR–2018–433	Ia	NGC 3923	0.006	0.072	1.8	223.1	N
2018dem	317.99387	−0.2181	8 Jul 2018	TNSTR–2018–947	TNSCR–2018–1219	Ia	SDSS J211158.77–001309.9	0.060	0.072	−3.6	4.8	Y
2018gv	121.39421	−11.43786	15 Jan 2018	TNSTR–2018–57	TNSCR–2018–75	Ia	NGC 2525	0.005	0.050	−50.4	−39.0	Y

[a] Basic information for each SN, including its J2000 right ascension and declination (in decimal degrees), its host galaxy, and its discovery date, were sourced from TNS. However, host galaxies marked with a "†" symbol were obtained from Lennarz et al. (2012a), while those with a "‡" are from the given discovery reference.

[b] Spectroscopic classification reference. Ph07 refers to Phillips et al. (2007).

[c] Spectroscopic type as classified in the spectroscopic reference. Super-Chandrasekhar candidates are labeled with "SC".

[d] Host-galaxy heliocentric redshifts are from NED unless otherwise indicated. Those marked with a "‡" symbol were obtained from their spectroscopic references, and "±" refers to Scalzo et al. (2010) and "∓" to Lennarz et al. (2012a).

[e] Extinction is calculated at the SN position using the dust maps of Schlegel et al. (1998) subject to the recalibration of Schlafly and Finkbeiner (2011).

[f] Offsets from host-galaxy nuclei are computed using the host location as given by NED (if available) for all SNe except SN 2010hs, whose host coordinates are from the catalog of Lennarz et al. (2012a).

[g] Indicates whether the SN had its host galaxy subtracted (Y) or not (N).

2.8 Light Curves

2.8.1 Light-Curve Properties

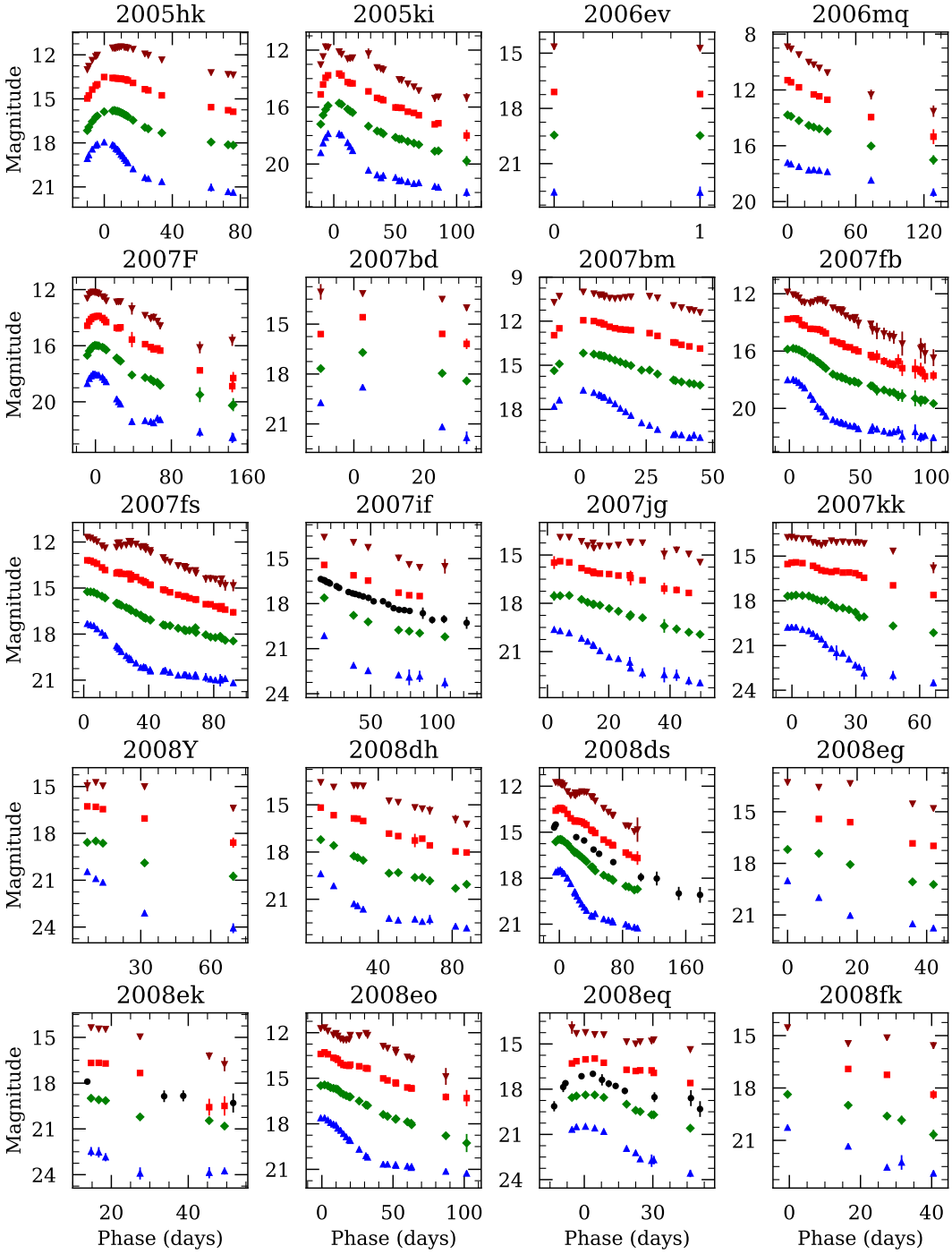

Figure 2.13: Observed *BVRI* and unfiltered light curves of our SN Ia sample. Blue up-triangles are $B + 2$, green diamonds are V, red squares are $R - 2$, dark red down-triangles are $I - 4$, and black circles are *Clear*-1. In most cases the error bars are smaller than the points themselves. All dates have been shifted relative to the time of maximum B-band brightness, if determined, and relative to the time of the first epoch otherwise.

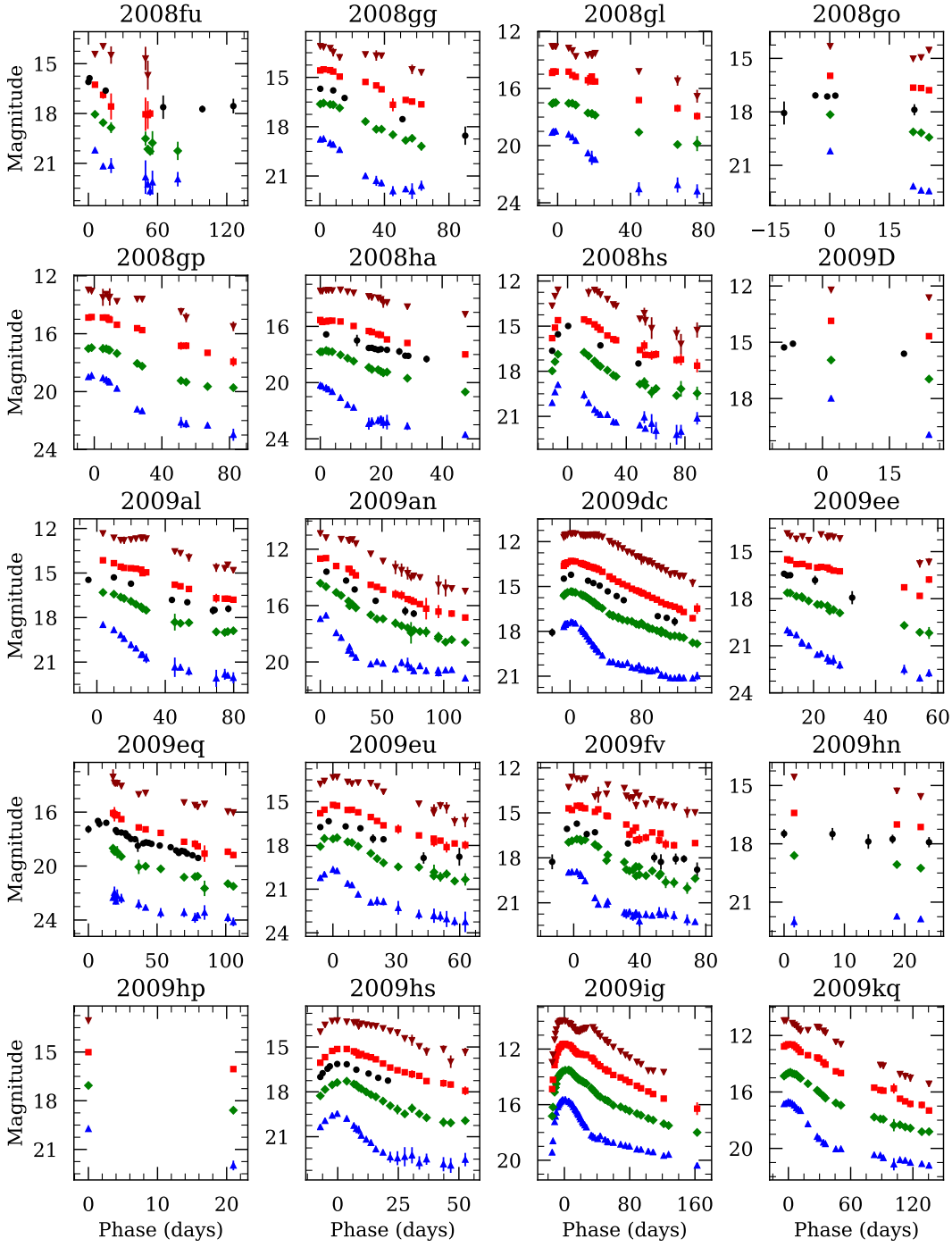

Figure 2.13: Observed *BVRI* and unfiltered light curves of our SN Ia sample. Blue up-triangles are $B + 2$, green diamonds are V, red squares are $R - 2$, dark red down-triangles are $I - 4$, and black circles are *Clear*-1. In most cases the error bars are smaller than the points themselves. All dates have been shifted relative to the time of maximum B-band brightness, if determined, and relative to the time of the first epoch otherwise.

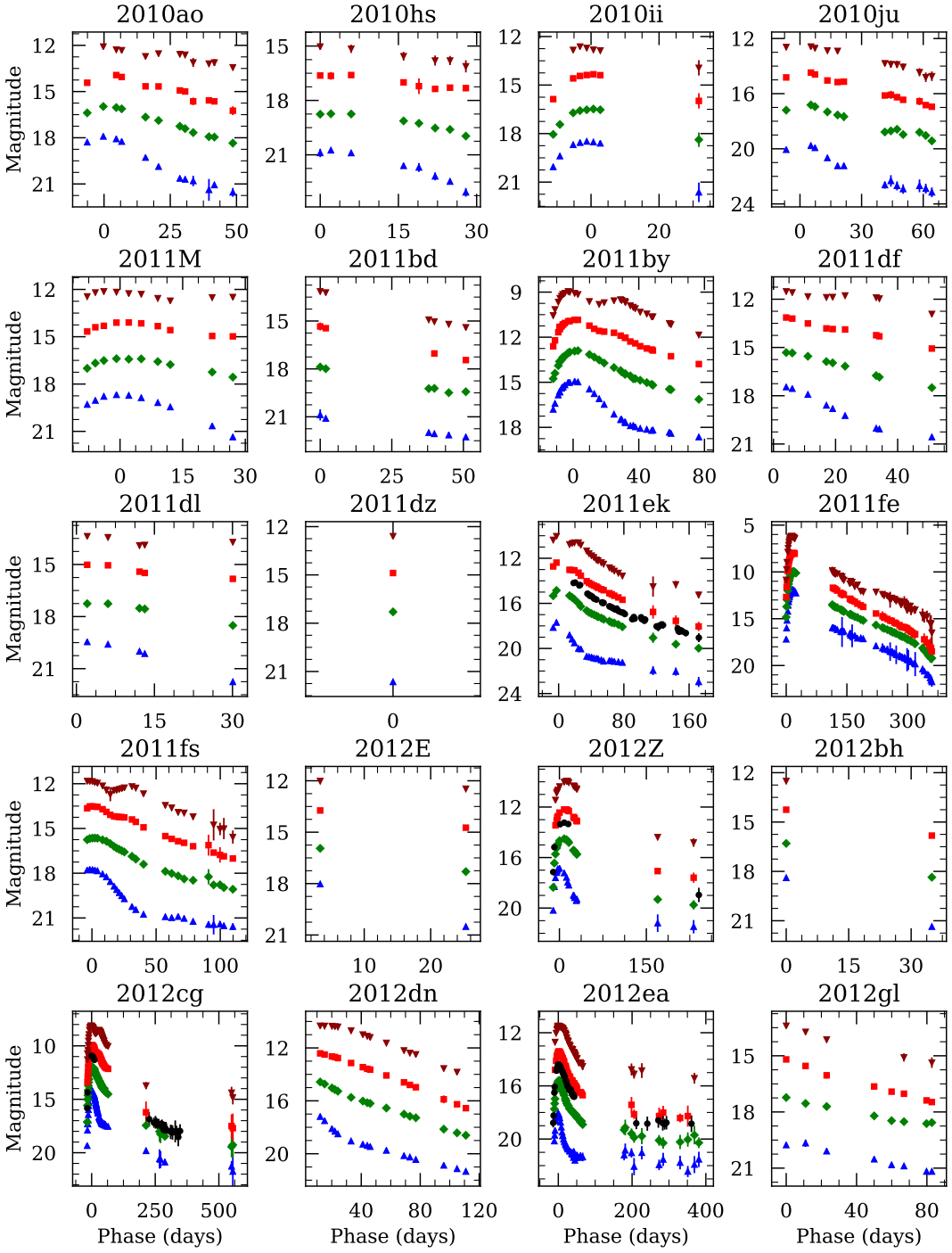

Figure 2.13: Observed *BVRI* and unfiltered light curves of our SN Ia sample. Blue up-triangles are $B + 2$, green diamonds are V, red squares are $R - 2$, dark red down-triangles are $I - 4$, and black circles are *Clear*-1. In most cases the error bars are smaller than the points themselves. All dates have been shifted relative to the time of maximum B-band brightness, if determined, and relative to the time of the first epoch otherwise.

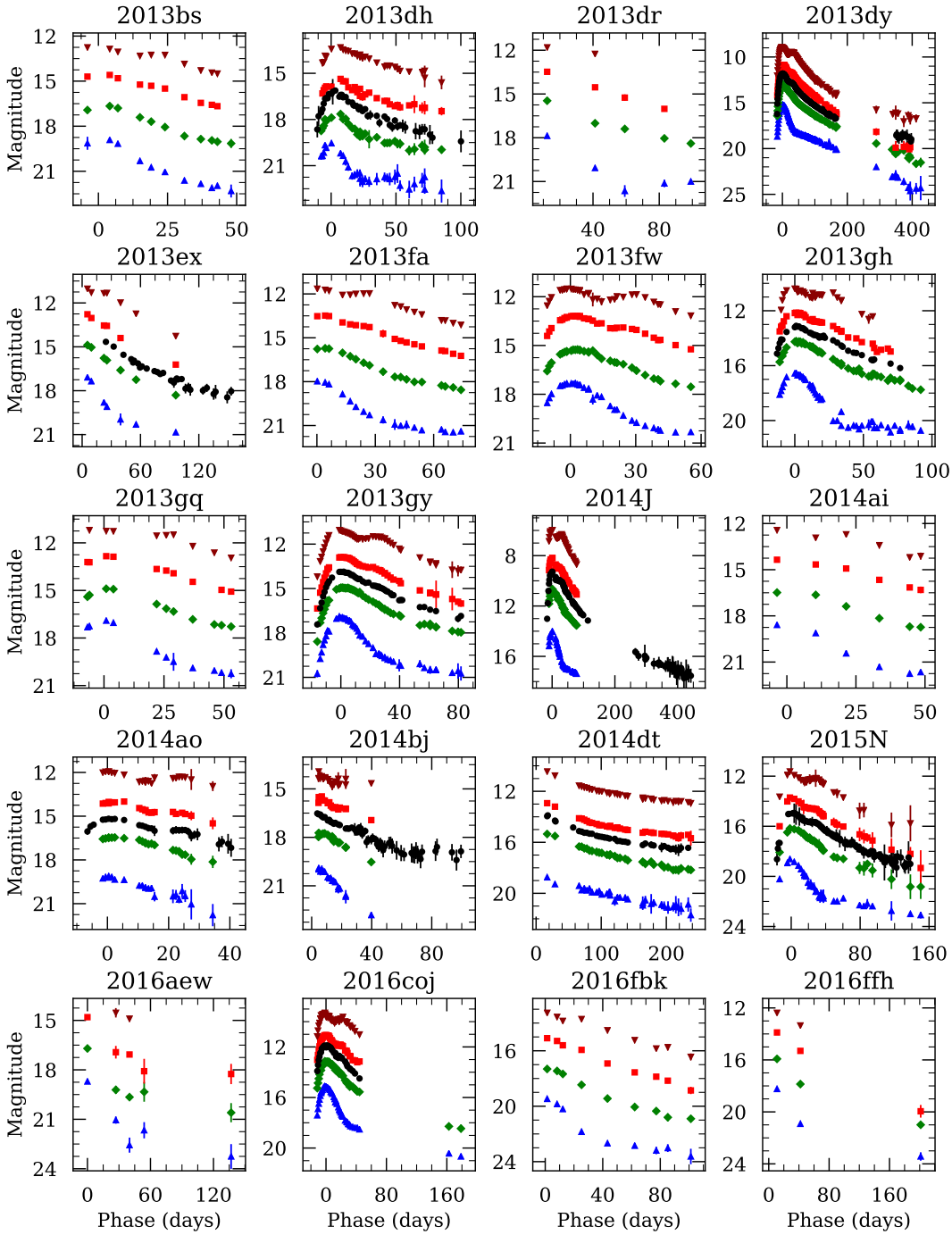

Figure 2.13: Observed *BVRI* and unfiltered light curves of our SN Ia sample. Blue up-triangles are $B + 2$, green diamonds are V, red squares are $R - 2$, dark red down-triangles are $I - 4$, and black circles are *Clear*-1. In most cases the error bars are smaller than the points themselves. All dates have been shifted relative to the time of maximum B-band brightness, if determined, and relative to the time of the first epoch otherwise.

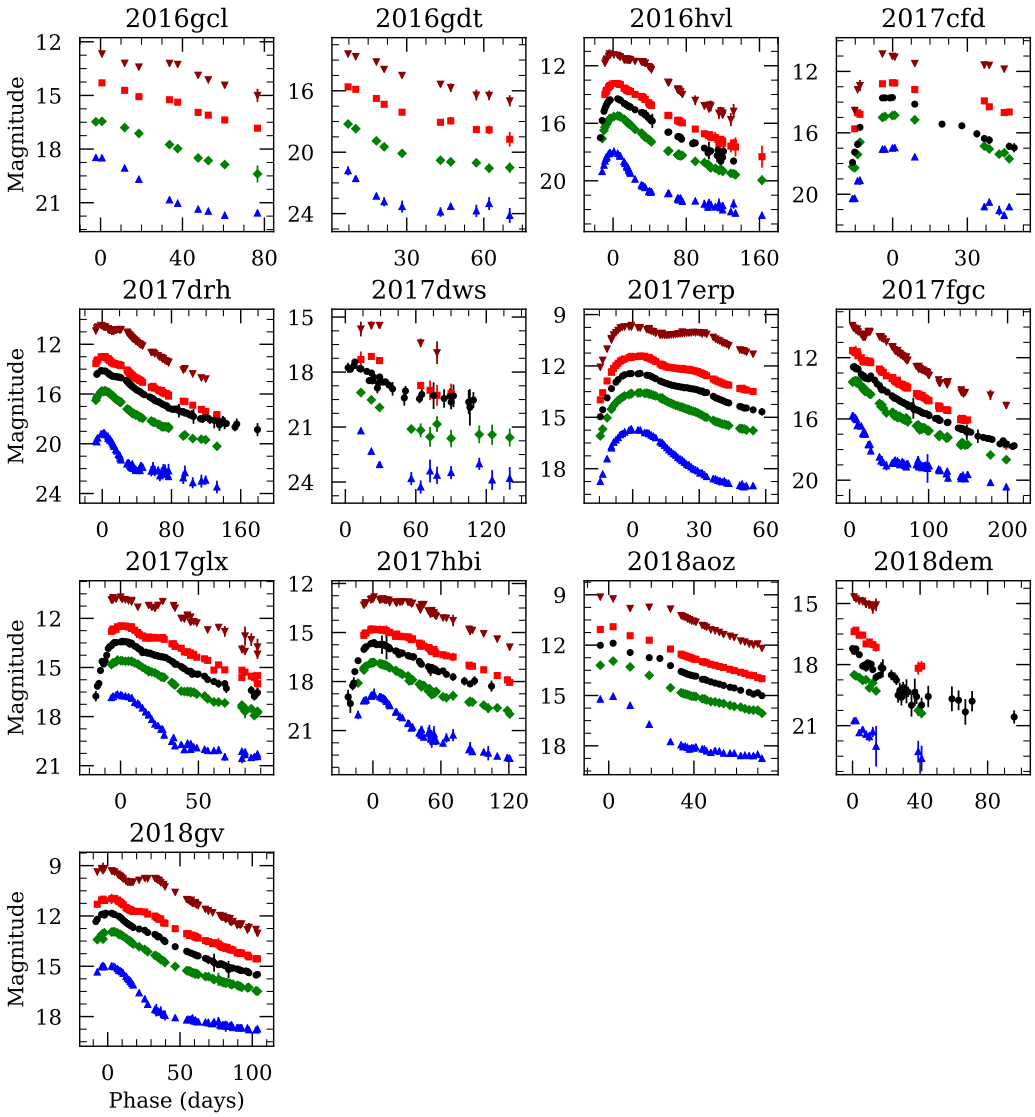

Figure 2.13: Observed *BVRI* and unfiltered light curves of our SN Ia sample. Blue up-triangles are $B + 2$, green diamonds are V, red squares are $R - 2$, dark red down-triangles are $I - 4$, and black circles are *Clear*-1. In most cases the error bars are smaller than the points themselves. All dates have been shifted relative to the time of maximum B-band brightness, if determined, and relative to the time of the first epoch otherwise.

Table 2.4: Light-curve properties derived from Gaussian Process interpolation.

SN	$t_{B_{\max}}$ (MJD)	$B_{\max}$ (mag)	$\Delta m_{15}(B)$ (mag)	$t_{V_{\max}}$ (MJD)	$V_{\max}$ (mag)	$\Delta m_{15}(V)$ (mag)	$(B-V)_{B_{\max}}$ (mag)
2005hk	53684.32 ± 0.29	15.850 ± 0.022	1.580 ± 0.053	53688.11 ± 0.56	15.703 ± 0.018	0.799 ± 0.039	0.069 ± 0.029
2005ki	53704.67 ± 0.40	15.572 ± 0.042	1.275 ± 0.080	53705.97 ± 0.56	15.534 ± 0.043	0.826 ± 0.067	0.021 ± 0.060
2007F	54122.32 ± 0.45	15.975 ± 0.016	0.864 ± 0.085	54124.03 ± 0.54	15.928 ± 0.011	0.550 ± 0.069	0.029 ± 0.020
2007bd	54210.22 ± 1.87	16.680 ± 0.051	1.451 ± 0.248	54212.58 ± 1.74	16.552 ± 0.074	0.891 ± 0.177	0.095 ± 0.090
2007bm	54224.46 ± 0.50	14.548 ± 0.022	1.232 ± 0.057	54225.66 ± 0.39	14.057 ± 0.011	0.690 ± 0.025	0.481 ± 0.025
2007fb	54287.92 ± 0.62	15.792 ± 0.021	1.332 ± 0.093	54288.90 ± 0.65	15.668 ± 0.024	0.726 ± 0.049	0.119 ± 0.032
2007kk	54382.76 ± 1.41	16.953 ± 0.024	0.954 ± 0.169	54385.52 ± 0.98	16.993 ± 0.017	0.559 ± 0.063	-0.064 ± 0.030
2008ds	54651.90 ± 0.24	15.263 ± 0.009	0.957 ± 0.030	54652.49 ± 0.25	15.303 ± 0.004	0.617 ± 0.019	-0.042 ± 0.010
2008eo	54688.14 ± 0.81	15.311 ± 0.020	1.026 ± 0.070	54689.74 ± 0.30	15.220 ± 0.006	0.675 ± 0.016	0.074 ± 0.021
2008eq	54689.54 ± 0.93	18.222 ± 0.027	1.029 ± 0.148	54691.77 ± 1.22	18.141 ± 0.029	0.576 ± 0.092	0.064 ± 0.040
2008gg	54749.80 ± 1.50	16.677 ± 0.033	0.983 ± 0.181	54752.39 ± 1.20	16.523 ± 0.029	0.570 ± 0.130	0.130 ± 0.044
2008gl	54767.98 ± 0.83	16.882 ± 0.043	1.394 ± 0.158	54769.51 ± 1.32	16.870 ± 0.039	0.704 ± 0.101	0.005 ± 0.058
2008gp	54779.28 ± 0.85	16.484 ± 0.037	1.136 ± 0.135	54780.97 ± 1.16	16.610 ± 0.038	0.631 ± 0.108	-0.136 ± 0.053
2008hs	54812.80 ± 0.52	15.932 ± 0.106	1.991 ± 0.160	54814.38 ± 0.54	15.769 ± 0.123	1.228 ± 0.161	0.129 ± 0.162
2009dc	54946.34 ± 0.80	15.148 ± 0.014	0.713 ± 0.060	54946.85 ± 0.85	15.166 ± 0.015	0.294 ± 0.035	-0.020 ± 0.021
2009eu	54984.59 ± 0.50	17.690 ± 0.054	1.816 ± 0.132	54986.86 ± 0.68	17.464 ± 0.041	1.006 ± 0.091	0.179 ± 0.068
2009fv	54994.47 ± 0.40	16.887 ± 0.024	1.670 ± 0.090	54998.15 ± 1.33	16.775 ± 0.022	0.767 ± 0.123	0.069 ± 0.032
2009hs	55048.55 ± 0.34	17.376 ± 0.041	2.090 ± 0.109	55051.00 ± 0.32	17.170 ± 0.030	1.186 ± 0.058	0.136 ± 0.051
2009ig	55079.70 ± 1.11	13.560 ± 0.032	0.850 ± 0.124	55082.78 ± 0.44	13.427 ± 0.013	0.682 ± 0.023	0.095 ± 0.034
2009kq	55155.05 ± 0.39	14.591 ± 0.014	1.091 ± 0.067	55156.49 ± 0.24	14.540 ± 0.010	0.658 ± 0.023	0.037 ± 0.017
2010ao	55289.32 ± 0.57	15.857 ± 0.037	1.329 ± 0.094	55290.55 ± 0.59	15.921 ± 0.024	0.693 ± 0.053	-0.073 ± 0.045
2010ii	55480.46 ± 0.21	16.207 ± 0.011	1.034 ± 0.317	55481.61 ± 0.47	16.248 ± 0.012	0.769 ± 0.241	-0.052 ± 0.016
2010ju	55525.65 ± 1.04	16.136 ± 0.073	1.315 ± 0.106	55526.39 ± 1.01	15.628 ± 0.056	0.715 ± 0.053	0.505 ± 0.092
2011M	55593.45 ± 0.26	15.225 ± 0.014	1.136 ± 0.050	55595.27 ± 0.32	15.228 ± 0.013	0.649 ± 0.050	-0.023 ± 0.019
2011by	55690.56 ± 0.68	12.906 ± 0.018	1.085 ± 0.095	55692.59 ± 0.62	12.874 ± 0.015	0.695 ± 0.052	0.014 ± 0.024
2011ek	55789.58 ± 0.85	14.504 ± 0.123	1.272 ± 0.190	55790.80 ± 0.67	13.715 ± 0.061	0.795 ± 0.092	0.775 ± 0.137
2011fs	55832.32 ± 0.69	15.357 ± 0.009	0.808 ± 0.071	55835.04 ± 0.57	15.313 ± 0.008	0.565 ± 0.035	0.018 ± 0.012
2012Z	55965.90 ± 0.38	14.662 ± 0.026	1.199 ± 0.074	55973.93 ± 0.86	14.377 ± 0.016	0.790 ± 0.066	0.105 ± 0.030
2012cg	56081.36 ± 0.26	12.115 ± 0.012	0.906 ± 0.032	56083.25 ± 0.24	11.952 ± 0.005	0.631 ± 0.013	0.144 ± 0.013
2012ea	56157.89 ± 0.11	15.848 ± 0.009	1.945 ± 0.028	56160.18 ± 0.14	15.403 ± 0.007	1.224 ± 0.018	0.387 ± 0.012
2013bs	56406.88 ± 1.68	16.697 ± 0.090	1.533 ± 0.144	56409.11 ± 0.71	16.589 ± 0.038	0.903 ± 0.049	0.073 ± 0.098
2013dh	56463.02 ± 0.62	17.507 ± 0.069	1.554 ± 0.155	56467.07 ± 0.54	17.524 ± 0.048	1.014 ± 0.071	-0.151 ± 0.084
2013dy	56500.40 ± 0.19	12.697 ± 0.008	0.870 ± 0.023	56501.84 ± 0.34	12.578 ± 0.005	0.609 ± 0.021	0.109 ± 0.010
2013fw	56601.14 ± 0.26	15.078 ± 0.006	1.038 ± 0.037	56603.53 ± 0.29	15.059 ± 0.006	0.630 ± 0.021	-0.010 ± 0.008
2013gh	56527.13 ± 0.41	14.434 ± 0.028	1.223 ± 0.050	56529.24 ± 0.49	14.180 ± 0.011	0.606 ± 0.029	0.225 ± 0.030
2013gq	56384.64 ± 0.66	14.738 ± 0.029	1.229 ± 0.154	56386.45 ± 0.77	14.753 ± 0.019	0.645 ± 0.072	-0.035 ± 0.035
2013gy	56647.80 ± 0.65	14.751 ± 0.025	1.247 ± 0.072	56650.05 ± 0.55	14.803 ± 0.006	0.644 ± 0.034	-0.071 ± 0.025
2014J	56688.93 ± 0.65	11.452 ± 0.020	0.890 ± 0.074	56689.71 ± 0.50	10.237 ± 0.017	0.553 ± 0.033	1.211 ± 0.026
2015N	57222.81 ± 0.27	14.853 ± 0.025	1.109 ± 0.078	57225.28 ± 0.79	14.768 ± 0.032	0.628 ± 0.054	0.040 ± 0.041
2016coj	57547.15 ± 0.19	13.082 ± 0.007	1.329 ± 0.030	57547.89 ± 0.18	13.088 ± 0.007	0.681 ± 0.018	-0.010 ± 0.010
2016gcl	57647.90 ± 1.63	16.227 ± 0.023	0.741 ± 0.126	57650.42 ± 1.18	16.251 ± 0.016	0.543 ± 0.069	-0.044 ± 0.028
2016hvl	57709.70 ± 0.47	14.392 ± 0.022	1.037 ± 0.055	57713.43 ± 0.67	14.282 ± 0.011	0.619 ± 0.028	0.058 ± 0.025
2017drh	57891.14 ± 0.44	16.691 ± 0.022	1.370 ± 0.065	57891.98 ± 0.48	15.396 ± 0.010	0.720 ± 0.032	1.291 ± 0.024
2017erp	57934.53 ± 0.22	13.336 ± 0.008	1.086 ± 0.031	57937.21 ± 0.35	13.275 ± 0.007	0.667 ± 0.020	0.036 ± 0.010
2017glx	58007.78 ± 0.25	14.228 ± 0.009	0.780 ± 0.026	58009.73 ± 0.87	14.250 ± 0.007	0.493 ± 0.045	-0.037 ± 0.011
2017hbi	58045.80 ± 0.61	16.580 ± 0.019	0.710 ± 0.074	58045.64 ± 0.76	16.671 ± 0.014	0.310 ± 0.045	-0.091 ± 0.024
2018aoz	58222.46 ± 0.58	12.761 ± 0.030	1.305 ± 0.124	58223.38 ± 0.46	12.730 ± 0.018	0.779 ± 0.077	0.025 ± 0.035
2018gv	58149.38 ± 0.31	12.751 ± 0.015	0.853 ± 0.037	58153.39 ± 0.32	12.788 ± 0.007	0.740 ± 0.017	-0.125 ± 0.017

Note: Only those SNe from our sample where the fitting process described in Section 2.5.1 succeeded appear here.

Table 2.5: Results of SNooPy and MLCS2k2 fitting.

	SNooPy $E(B-V)$ Fitted Parameters				MLCS2k2 Fitted Parameters			
SN	$t_{\max}$ (MJD)	Δm_{15} (mag)	$E(B-V)_{\rm host}$ (mag)	μ (mag)	t_0 (MJD)	Δ	A_V (mag)	μ (mag)
2005ki	53705.23 ± 0.06	1.419 ± 0.013	-0.011 ± 0.009	34.666 ± 0.013	53705.21 ± 0.11	0.373 ± 0.052	0.027 ± 0.017	34.719 ± 0.065
2007F	54123.83 ± 0.09	1.096 ± 0.012	0.041 ± 0.010	35.163 ± 0.011	54123.13 ± 0.10	-0.179 ± 0.033	0.204 ± 0.036	35.351 ± 0.046
2007bd	54207.12 ± 0.50	1.351 ± 0.067	0.010 ± 0.037	35.748 ± 0.050	54206.65 ± 0.23	0.209 ± 0.103	0.082 ± 0.054	35.851 ± 0.097
2007bm	54225.02 ± 0.15	1.224 ± 0.014	0.588 ± 0.011	32.635 ± 0.019	54223.94 ± 0.08	0.057 ± 0.038	1.109 ± 0.036	32.389 ± 0.048
2007fb	54287.48 ± 0.16	1.353 ± 0.016	0.100 ± 0.009	34.657 ± 0.017	54286.73 ± 0.31	0.285 ± 0.055	0.142 ± 0.042	34.749 ± 0.059
2007fs	54293.70 ± 0.42	0.879 ± 0.015	0.015 ± 0.013	34.505 ± 0.014	54295.17 ± 0.35	-0.161 ± 0.028	0.116 ± 0.032	34.649 ± 0.044
2007if	54338.39 ± 0.86	0.768 ± 0.029	0.034 ± 0.026	36.133 ± 0.033	54343.02 ± 1.17	-0.350 ± 0.062	0.384 ± 0.068	36.245 ± 0.123
2007jg	54365.35 ± 0.47	1.199 ± 0.022	-0.021 ± 0.024	36.493 ± 0.032	54364.35 ± 0.55	-0.025 ± 0.060	0.092 ± 0.051	36.616 ± 0.071
2007kk	54383.83 ± 0.26	1.088 ± 0.035	-0.004 ± 0.022	36.267 ± 0.025	54382.59 ± 0.44	-0.340 ± 0.040	0.168 ± 0.071	36.558 ± 0.066
2008Y	54499.62 ± 1.52	0.939 ± 0.126	0.164 ± 0.045	37.425 ± 0.078	54498.33 ± 1.66	-0.110 ± 0.112	0.226 ± 0.090	37.503 ± 0.127
2008dh	54625.56 ± 0.67	0.924 ± 0.035	0.026 ± 0.024	36.282 ± 0.020	54626.31 ± 0.66	-0.124 ± 0.052	0.077 ± 0.044	36.436 ± 0.077
2008ds	54651.45 ± 0.15	0.865 ± 0.010	-0.013 ± 0.007	34.746 ± 0.011	54652.06 ± 0.18	-0.270 ± 0.023	0.045 ± 0.027	34.975 ± 0.039
2008ek	54668.63 ± 2.52	1.813 ± 0.033	0.669 ± 0.145	36.434 ± 0.096	54662.46 ± 1.63	1.213 ± 0.141	0.220 ± 0.135	35.997 ± 0.120
2008eo	54686.91 ± 0.38	0.884 ± 0.018	0.095 ± 0.015	34.513 ± 0.015	54688.23 ± 0.30	-0.197 ± 0.028	0.261 ± 0.039	34.630 ± 0.045
2008eq	54689.59 ± 0.28	0.971 ± 0.032	0.207 ± 0.015	37.155 ± 0.036	54689.46 ± 0.34	-0.227 ± 0.053	0.444 ± 0.048	37.277 ± 0.068
2008fk	54722.03 ± 1.02	1.263 ± 0.074	-0.197 ± 0.067	37.749 ± 0.091	54719.62 ± 0.99	-0.229 ± 0.084	0.028 ± 0.020	37.967 ± 0.087
2008gg	54750.61 ± 0.58	1.087 ± 0.060	0.111 ± 0.036	35.720 ± 0.050	54749.06 ± 0.72	-0.350 ± 0.046	0.267 ± 0.051	36.047 ± 0.071
2008gl	54766.97 ± 0.27	1.178 ± 0.027	0.124 ± 0.012	35.917 ± 0.024	54767.32 ± 0.37	0.189 ± 0.109	0.227 ± 0.058	35.913 ± 0.086
2008go	54765.09 ± 1.09	1.158 ± 0.101	0.081 ± 0.022	37.167 ± 0.073	54764.78 ± 0.65	0.002 ± 0.118	0.191 ± 0.062	37.317 ± 0.109
2008gp	54779.01 ± 0.08	1.087 ± 0.011	-0.048 ± 0.008	35.909 ± 0.009	54778.92 ± 0.35	-0.106 ± 0.064	0.051 ± 0.035	36.094 ± 0.073
2008hs	54813.07 ± 0.11	1.720 ± 0.012	0.103 ± 0.017	34.836 ± 0.033	54812.83 ± 0.08	1.181 ± 0.042	0.011 ± 0.010	34.297 ± 0.058
2009D	54841.02 ± 0.54	0.932 ± 0.041	0.026 ± 0.017	35.140 ± 0.018	54841.93 ± 1.47	-0.138 ± 0.108	0.125 ± 0.056	35.248 ± 0.080
2009al	54896.75 ± 0.35	1.106 ± 0.029	0.264 ± 0.022	35.127 ± 0.023	54894.38 ± 0.79	-0.264 ± 0.043	0.503 ± 0.054	35.305 ± 0.066
2009dc	...	...	...	...	54945.34 ± 0.16	-0.693 ± 0.017	0.348 ± 0.031	34.687 ± 0.037
2009ee	54951.64 ± 0.80	1.273 ± 0.021	0.210 ± 0.056	36.209 ± 0.042	54949.75 ± 0.71	0.466 ± 0.086	0.085 ± 0.076	36.068 ± 0.085
2009eu	54984.30 ± 0.12	1.787 ± 0.013	0.279 ± 0.021	35.924 ± 0.025	54984.38 ± 0.20	1.199 ± 0.058	0.056 ± 0.046	35.606 ± 0.063
2009hs	55048.76 ± 0.11	1.798 ± 0.013	0.269 ± 0.025	35.728 ± 0.024	55048.51 ± 0.13	1.259 ± 0.034	0.018 ± 0.012	35.404 ± 0.048
2009ig	...	...	...	...	55079.47 ± 0.09	-0.354 ± 0.023	0.123 ± 0.029	33.167 ± 0.039
2009kq	55154.71 ± 0.15	1.103 ± 0.018	0.017 ± 0.011	33.834 ± 0.014	55154.69 ± 0.20	-0.062 ± 0.035	0.154 ± 0.036	33.954 ± 0.047
2010ao	55288.84 ± 0.30	1.129 ± 0.031	0.037 ± 0.019	35.122 ± 0.028	55288.75 ± 0.26	0.009 ± 0.056	0.195 ± 0.048	35.147 ± 0.069
2010ii	...	...	...	...	55481.48 ± 0.19	0.315 ± 0.116	0.031 ± 0.022	35.457 ± 0.096
2010ju	55524.52 ± 0.29	1.175 ± 0.032	0.440 ± 0.023	34.477 ± 0.044	55524.07 ± 0.23	-0.044 ± 0.070	0.931 ± 0.122	34.315 ± 0.107
2011M	55593.49 ± 0.12	1.119 ± 0.025	0.048 ± 0.012	34.482 ± 0.019	55593.14 ± 0.15	-0.008 ± 0.060	0.183 ± 0.107	34.475 ± 0.082
2011by	55690.78 ± 0.09	1.091 ± 0.010	0.094 ± 0.011	32.077 ± 0.011	55690.33 ± 0.09	-0.037 ± 0.029	0.300 ± 0.028	32.071 ± 0.042
2011df	55715.10 ± 0.30	0.943 ± 0.019	0.056 ± 0.010	34.161 ± 0.013	55716.02 ± 0.41	-0.162 ± 0.038	0.215 ± 0.053	34.261 ± 0.056
2011dl	55738.35 ± 0.50	1.089 ± 0.046	0.169 ± 0.033	36.079 ± 0.031	55736.95 ± 0.77	-0.278 ± 0.060	0.439 ± 0.053	36.228 ± 0.064
2011ek	55789.74 ± 0.10	1.522 ± 0.021	0.503 ± 0.012	32.250 ± 0.026	55789.14 ± 0.15	0.562 ± 0.073	0.979 ± 0.101	31.821 ± 0.090
2011fe	55815.22 ± 0.06	1.096 ± 0.005	-0.006 ± 0.005	29.228 ± 0.006	...	...	...	...
2011fs	55833.25 ± 0.19	0.911 ± 0.016	0.064 ± 0.012	34.620 ± 0.013	55832.95 ± 0.26	-0.310 ± 0.026	0.209 ± 0.044	34.825 ± 0.045
2012E	55949.73 ± 0.79	1.343 ± 0.051	0.117 ± 0.026	34.682 ± 0.018	55948.57 ± 1.67	0.343 ± 0.162	0.200 ± 0.107	34.612 ± 0.111
2012cg	56082.40 ± 0.06	1.060 ± 0.006	0.173 ± 0.007	31.054 ± 0.006	56081.62 ± 0.06	-0.254 ± 0.021	0.543 ± 0.026	31.120 ± 0.035
2012dn	56132.44 ± 0.00	0.940 ± 0.028	0.458 ± 0.025	32.725 ± 0.023	56134.14 ± 0.57	-0.181 ± 0.050	0.841 ± 0.044	32.744 ± 0.076

Table 2.5 continued

	SNooPy $E(B-V)$ Fitted Parameters				MLCS2k2 Fitted Parameters			
SN	$t_{\max}$ (MJD)	Δm_{15} (mag)	$E(B-V)_{\rm host}$ (mag)	μ (mag)	t_0 (MJD)	Δ	A_V (mag)	μ (mag)
2012ea	56158.17 ± 0.06	1.821 ± 0.000	0.389 ± 0.009	33.883 ± 0.009	56158.11 ± 0.07	1.396 ± 0.022	0.048 ± 0.029	33.496 ± 0.034
2013bs	56406.52 ± 0.22	1.507 ± 0.027	0.067 ± 0.016	35.516 ± 0.026	56406.38 ± 0.23	0.686 ± 0.062	0.031 ± 0.023	35.332 ± 0.071
2013dr	56486.38 ± 1.02	0.987 ± 0.089	0.153 ± 0.044	34.181 ± 0.174	56486.04 ± 1.44	-0.217 ± 0.080	0.332 ± 0.075	34.328 ± 0.160
2013dy	56501.48 ± 0.07	0.995 ± 0.006	0.123 ± 0.005	31.773 ± 0.008	56500.13 ± 0.06	-0.325 ± 0.016	0.420 ± 0.046	31.923 ± 0.040
2013ex	56529.48 ± 0.40	1.013 ± 0.030	0.044 ± 0.019	33.648 ± 0.033	56530.06 ± 0.60	-0.066 ± 0.051	0.142 ± 0.061	33.770 ± 0.067
2013fa	56536.19 ± 0.23	1.140 ± 0.023	0.297 ± 0.011	34.320 ± 0.018	56535.17 ± 0.46	-0.114 ± 0.037	0.607 ± 0.044	34.347 ± 0.053
2013fw	56601.68 ± 0.10	1.085 ± 0.014	0.031 ± 0.009	34.314 ± 0.014	56600.81 ± 0.09	-0.277 ± 0.027	0.189 ± 0.038	34.588 ± 0.043
2013gh	56529.10 ± 0.32	1.142 ± 0.032	0.366 ± 0.021	33.146 ± 0.028	56528.32 ± 0.08	0.112 ± 0.036	0.798 ± 0.034	32.808 ± 0.046
2013gq	56385.29 ± 0.18	1.233 ± 0.015	-0.003 ± 0.016	33.946 ± 0.029	56384.22 ± 0.17	0.008 ± 0.043	0.096 ± 0.040	34.119 ± 0.056
2013gy	56649.21 ± 0.12	1.125 ± 0.011	0.073 ± 0.012	34.024 ± 0.012	56648.36 ± 0.07	0.026 ± 0.032	0.280 ± 0.034	33.947 ± 0.044
2014J	56690.04 ± 0.13	0.952 ± 0.020	1.179 ± 0.014	28.415 ± 0.025	56689.20 ± 0.09	-0.219 ± 0.025	2.194 ± 0.048	27.865 ± 0.047
2014ai	56745.96 ± 0.23	1.490 ± 0.058	0.128 ± 0.025	35.097 ± 0.054	56744.75 ± 0.51	0.191 ± 0.124	0.277 ± 0.069	35.308 ± 0.115
2014ao	56766.17 ± 0.34	0.977 ± 0.032	0.820 ± 0.014	34.759 ± 0.033	56765.77 ± 0.61	-0.204 ± 0.088	1.441 ± 0.053	34.515 ± 0.076
2014bj	56796.73 ± 0.55	1.108 ± 0.038	0.044 ± 0.021	36.632 ± 0.024	56795.74 ± 0.65	-0.168 ± 0.071	0.169 ± 0.062	36.824 ± 0.078
2015N	57223.19 ± 0.15	1.087 ± 0.015	0.181 ± 0.012	33.877 ± 0.017	57222.89 ± 0.21	-0.134 ± 0.045	0.430 ± 0.142	33.865 ± 0.098
2016coj	57547.89 ± 0.23	1.131 ± 0.034	0.121 ± 0.018	32.306 ± 0.026	57547.83 ± 0.06	0.613 ± 0.033	0.024 ± 0.017	31.969 ± 0.042
2016fbk	57624.94 ± 0.41	0.993 ± 0.034	0.241 ± 0.016	36.180 ± 0.036	57625.09 ± 0.51	-0.046 ± 0.049	0.468 ± 0.046	36.156 ± 0.062
2016gcl	57649.84 ± 0.53	0.849 ± 0.024	0.025 ± 0.032	35.608 ± 0.056	57649.62 ± 0.38	-0.366 ± 0.029	0.126 ± 0.041	35.852 ± 0.050
2016gdt	57641.53 ± 1.08	1.822 ± 0.001	0.677 ± 0.064	35.832 ± 0.051	57640.11 ± 0.91	1.499 ± 0.077	0.147 ± 0.103	35.492 ± 0.076
2016hvl	57711.00 ± 0.12	1.123 ± 0.014	0.116 ± 0.012	33.420 ± 0.014	57709.48 ± 0.11	-0.281 ± 0.026	0.343 ± 0.115	33.634 ± 0.075
2017cfd	...	...	...	...	57844.39 ± 0.13	0.093 ± 0.048	0.504 ± 0.041	33.693 ± 0.058
2017drh	57890.60 ± 0.09	1.340 ± 0.011	1.601 ± 0.014	32.687 ± 0.013	57889.72 ± 0.10	0.112 ± 0.036	2.558 ± 0.045	32.169 ± 0.053
2017dws	57867.60 ± 1.20	0.882 ± 0.030	-0.051 ± 0.051	37.935 ± 0.038	57869.18 ± 1.29	-0.339 ± 0.091	0.075 ± 0.049	38.258 ± 0.135
2017erp	57935.15 ± 0.06	1.118 ± 0.006	0.099 ± 0.006	32.405 ± 0.006	57933.88 ± 0.06	-0.234 ± 0.021	0.444 ± 0.039	32.503 ± 0.039
2017fgc	57955.52 ± 0.38	0.840 ± 0.008	0.081 ± 0.016	32.775 ± 0.035	57955.78 ± 0.41	-0.324 ± 0.026	0.305 ± 0.033	32.866 ± 0.049
2017glx	...	...	...	...	58009.16 ± 0.16	-0.196 ± 0.025	0.174 ± 0.044	33.684 ± 0.044
2017hbi	...	...	...	...	58044.44 ± 0.14	-0.692 ± 0.017	0.186 ± 0.035	36.347 ± 0.041
2018aoz	58221.43 ± 0.14	1.283 ± 0.008	-0.079 ± 0.011	32.001 ± 0.014	58221.27 ± 0.19	0.187 ± 0.040	0.018 ± 0.012	32.107 ± 0.053
2018gv	58150.11 ± 0.08	1.006 ± 0.011	-0.046 ± 0.006	32.164 ± 0.013	58149.59 ± 0.11	-0.169 ± 0.024	0.035 ± 0.020	32.363 ± 0.038

Note: Only those SNe from our sample where the fitting process described in Sections 2.5.2.1 or 2.5.2.2 succeeded appear here.

2.8.2 Natural-System Light Curves

SN light curves have long been released on the Landolt system (e.g., CfA1, CfA2, G10), thus allowing for easy comparison between datasets from different telescopes. Indeed, we analysed our light curves only after transforming to the Landolt system — a decision motivated largely by the fact that our dataset is derived from observations collected with four distinct telescope/CCD/filter combinations. However, there are instances where natural-system light curves are more attractive. Since the stellar SEDs that are used to derive colour terms do not accurately reflect those of SNe Ia, SN photometry transformed using such colour terms will not necessarily be on the Landolt system. Conventionally, second-order "S-corrections" are performed to properly account for the SN SED by using a selected spectral series (Stritzinger et al. 2002), but many groups are now releasing their low-z SN Ia photometry datasets in the natural systems of their telescopes along with the transmission curves of their photometry systems (e.g., CfA3, CfA4, CSP1-3). Thus, given a spectral series (e.g., Hsiao et al. 2007) and transmission functions, one can transform photometry from one system to another without the need for colour corrections. In turn, this should provide less scatter in SN flux measurements.

The aforementioned benefits motivate us to release our photometric dataset (see Section 6.4) in the relevant natural systems in addition to the Landolt system. A table of natural-system magnitudes analogous to Table 2.2 is available for our entire dataset, with a sample given in Table 2.6. We reiterate that owing to changes in the observing equipment, there are four transmission curves (KAIT3, KAIT4, Nickel1, Nickel2) for each bandpass. Any analysis of the dataset as a whole should therefore be done either on the Landolt system or after transforming all of the data to a common system (see Appendix A of Ganeshalingam et al. 2013). Transmission curves for all filter and system combinations covered by our dataset are archived with the journal and available online in our SNDB.

Table 2.6: Natural-System Photometry of SN 2008ds.

SN	MJD	B (mag)	V (mag)	R (mag)	I (mag)	*Clear* (mag)	System
2008ds	54645.47	...	...	...	...	15.700 ± 0.033	kait4
2008ds	54646.47	...	...	...	...	15.574 ± 0.024	kait4
2008ds	54647.46	15.615 ± 0.012	15.629 ± 0.010	15.597 ± 0.011	15.742 ± 0.018	15.501 ± 0.010	kait4
2008ds	54650.47	15.501 ± 0.014	15.488 ± 0.010	15.476 ± 0.012	15.762 ± 0.015	...	kait4
2008ds	54653.13	15.482 ± 0.009	15.474 ± 0.005	15.418 ± 0.005	15.768 ± 0.008	...	nickel1
2008ds	54653.44	15.489 ± 0.018	15.471 ± 0.010	15.439 ± 0.010	15.823 ± 0.016	...	kait4
2008ds	54655.13	15.565 ± 0.008	15.515 ± 0.006	15.456 ± 0.006	15.840 ± 0.009	...	nickel1
2008ds	54655.48	15.559 ± 0.016	15.510 ± 0.012	15.471 ± 0.013	15.919 ± 0.022	...	kait4
2008ds	54658.13	15.695 ± 0.008	15.611 ± 0.006	15.548 ± 0.005	15.978 ± 0.008	...	nickel1
2008ds	54662.16	15.975 ± 0.011	15.785 ± 0.005	...	...	...	nickel1

Note: First 10 epochs of natural-system $BVRI$ + unfiltered photometry of SN 2008ds. This table shows the form and content organisation of a much larger table that covers each epoch of photometry for each SN in our dataset. The full table is available online at `http://heracles.astro.berkeley.edu/sndb/info#DownloadDatasets(BSNIP,LOSS)`.

Chapter 3

Berkeley Supernova Ia Program: Data Release of 637 Spectra from 247 Type Ia Supernovae

A version of this chapter was originally published in *The Monthly Notices of the Royal Astronomical Society* (Stahl et al. 2020b).

Chapter Abstract

We present 637 low-redshift optical spectra collected by the Berkeley Supernova Ia Program (BSNIP) between 2009 and 2018, almost entirely with the Kast double spectrograph on the Shane 3 m telescope at Lick Observatory. We describe our automated spectral classification scheme and arrive at a final set of 626 spectra (of 242 objects) that are unambiguously classified as belonging to Type Ia supernovae (SNe Ia). Of these, 70 spectra of 30 objects are classified as spectroscopically peculiar (i.e., not matching the spectral signatures of "normal" SNe Ia) and 79 SNe Ia (covered by 328 spectra) have complementary photometric coverage. The median SN in our final set has one epoch of spectroscopy, has a redshift of 0.0208 (with a low of 0.0007 and high of 0.1921), and is first observed spectroscopically 1.1 days after maximum light. The constituent spectra are of high quality, with a median signal-to-noise ratio of 31.8 pixel^{-1}, and have broad wavelength coverage, with $\sim$ 95% covering at least 3700–9800 Å. We analyze our dataset, focusing on quantitative measurements (e.g., velocities, pseudo-equivalent widths) of the evolution of prominent spectral features in the available early-time and late-time spectra. The data are available to the community, and we encourage future studies to incorporate our spectra in their analyses.

3.1 Introduction

Supernovae (SNe) have proven themselves to be powerful probes of the dynamic nature of the Universe on scales ranging from stellar to cosmological. The class of objects known as Type Ia supernovae (SNe Ia), which result from the thermonuclear explosions of carbon-oxygen white dwarfs in binary systems (e.g., Hoyle and Fowler 1960; Colgate and McKee 1969; Nomoto et al. 1984), have been of particular interest to astrophysicists for many years.

Despite intensive study, many important details of SNe Ia remain poorly understood, if at all (for a review, see Howell 2011). How do differences in initial conditions lead to the variation in properties observed among SNe Ia? What are the physical details of the explosion mechanism(s)? Are the progenitor systems "single-degenerate" (Whelan and Iben 1973) or "double-degenerate" (Webbink 1984; Iben and Tutukov 1984), and how do they contribute to the observed variance in SN Ia attributes? To answer these and other questions, numerous observations of SNe Ia will undoubtedly be required — preferably obtained and reduced in a thorough and consistent manner.

Despite these outstanding questions regarding SNe Ia as astrophysical objects, they are highly prized for their large and *relatively* homogeneous optical spectra and luminosities at peak brightness, though some differences do exist (e.g., Filippenko 1997, and references therein). To the extent that their peak luminosities are "standardisable," SNe Ia are excellent cosmological distance indicators. Accordingly, much effort has been expended in developing methods to better calibrate relationships between various observables and peak luminosity. The "Phillips relation" identifies a correlation between luminosity at peak brightness and light-curve decline rate for most SNe Ia (Phillips 1993). By making use of optical colours, Riess et al. (1996) have devised a method that yields further improvements, including the determination of the extinction caused by dust in the host galaxy of a SN Ia. Distance measurements derived using such methods led to the discovery of the accelerating expansion of the Universe (Riess et al. 1998; Perlmutter et al. 1999), which revolutionised the field of cosmology. Indeed, the nature of the dark energy that gives rise to the acceleration is currently one of the most important questions in physics.

SNe Ia have since been used to place increasingly stringent constraints on cosmological parameters (Astier et al. 2006; Riess et al. 2007; Hicken et al. 2009b; Suzuki et al. 2012; Betoule et al. 2014; Jones et al. 2018; Scolnic et al. 2018) and continue to provide precise measurements of the Hubble constant (Riess et al. 2016, 2019; Dhawan et al. 2018). As spectra must contain more information than light curves, many have searched for and identified spectroscopic parameters to make SN Ia distance measurements more precise (Bailey et al. 2009; Wang et al. 2009; Blondin et al. 2011; Silverman et al. 2012c; Fakhouri et al. 2015; Zheng et al. 2018a). In addition, Foley and Kasen (2011) found that the intrinsic colour of SNe Ia at peak brightness depends on the velocity of their ejecta, and Wang et al. (2013) have shown that the latter has a significant connection to SN Ia birthplace environments — and hence progenitor stars. It is likely that future increases in distance measurement precision will make use of spectroscopic parameters, motivating the need for extensive, consistent samples of SN Ia spectra.

The Berkeley Supernova Ia Program (BSNIP) is a large-scale effort to study the properties of SNe Ia at low redshift ($z \lesssim 0.05$), primarily via optical spectroscopy (Silverman et al. 2012a, henceforth S12a) and photometry (Ganeshalingam et al. 2010; Stahl et al. 2019, henceforth G10 and S19, respectively). The spectra presented in this data-release paper are complementary to those published by S12a, and extend the BSNIP SN Ia spectral dataset to cover the period from 1989 through 2018. Our strategy is generally to observe as many SNe Ia as possible, with particular effort invested in obtaining frequent spectral coverage of peculiar objects. Furthermore, we strive for spectral coverage of all objects that our group is also observing photometrically (consequently, there is considerable overlap in SNe Ia between the spectra presented herein and the photometric dataset released by S19), and we aim to provide prompt spectroscopic classifications of all SNe discovered by the 0.76-m Katzman Automatic Imaging Telescope at Lick Observatory (KAIT; Filippenko et al. 2001). Our spectra are obtained and reduced in a controlled and consistent manner, thereby eliminating many of the systematic differences that manifest when distinct datasets are collected into one sample.

In this data release, we present and characterise 637 optical spectra of 247 distinct objects collected by the BSNIP between the beginning of 2009 and the end of 2018. The spectra were obtained with the Shane 3 m telescope at Lick Observatory and the Keck-I 10 m telescope at the W. M. Keck Observatory. Of the full set of spectra, 546 are published here for the first time. When we combine our spectral dataset with that presented by S12a, we obtain a sample of nearly 2000 spectra of low-redshift SNe Ia, all of which have been observed and reduced in a consistent manner. We organise the remainder of this paper as follows. Section 6.2 describes the organisation, observation, and reduction strategies employed in assembling our dataset. In Section 3.3 we detail our spectral classification scheme, and we study its results and derive final object classifications. We present our final spectroscopic dataset and explore its early-time and late-time evolution in Section 6.4, and we conclude with Section 6.5.

3.2 Data

3.2.1 Data Management and Selection

All BSNIP spectroscopy, along with useful metadata for those observations and the SNe in them (e.g., observer, reducer, host galaxy, redshift, etc.), are catalogued in our UC Berkeley SuperNova DataBase[1] (SNDB; S12a, Shivvers et al. 2016) after the data are processed and reduced (see Section 3.2.3 for a summary of our data-processing techniques). Therefore, to collect the dataset presented herein we simply query the private (prepublication) portion of our SNDB for all spectra observed between 1 January 2009 and 31 December 2018 for

[1] `http://heracles.astro.berkeley.edu/sndb/`

objects spectroscopically classified[2] as SNe Ia.

This results in 744 matches, which we then filter by (i) selecting only those spectra with an average signal-to-noise ratio (SNR) greater than 5 pixel^{-1} (yielding 714 matches above this quality threshold) and (ii) retaining only those with a wavelength coverage of at least 3700–7000 Å (yielding 648 matches with sufficient spectral coverage for our subsequent analyses). Finally, we remove several of the remaining spectra, including any that are from SNe discovered earlier than 1 January 2008 (to avoid presenting only late-time spectra of an object at the early end of our selection range), to obtain the aforementioned set of 637 spectra. Following publication, all previously unpublished spectra will be transferred to the publicly accessible portion of the SNDB. We list basic SN-level information in Table 3.6 and spectrum-level information in Table 3.1, with many of the properties sourced from the Transient Name Server (TNS)[3] or the NASA/IPAC Extragalactic Database (NED)[4]. Representative SN Ia spectra from our sample showing low, medium, and high SNRs are given in Figure 3.1. The SNR of the central spectrum in the figure is similar to the mean SNR for our entire sample (as discussed in Section 3.4.1), and is thus indicative of the high quality of the spectra presented herein.

3.2.2 Observations

The vast majority of the spectra in our dataset (579/637) were obtained using the Kast double spectrograph (Miller and Stone 1993) mounted on the Shane 3 m telescope at the Lick Observatory. The remaining observations (58/637) were made with the Low Resolution Imaging Spectrometer (LRIS; Oke et al. 1995) at the W. M. Keck Observatory. The seeing at these locations averages $\sim 2''$ and $\sim 1''$, respectively. Most spectra presented here were obtained with the long slit at or near the parallactic angle so as to reduce the differential light loss caused by atmospheric dispersion (Filippenko 1982); however, this was not necessary with LRIS, as it is equipped with an atmospheric dispersion corrector. The specific details of our observing strategy are thoroughly documented by S12a, so here we mention only relevant changes to the aforementioned instruments.

On 18 September 2016, the Kast red-side CCD was replaced with a Hamamatsu 1024 × 4096 pixel device with 15 μm pixels, yielding a spatial scale of $0\farcs43$ pixel^{-1}. Compared to the previous red-side CCD, the new detector features significantly reduced readout noise and better quantum efficiency for wavelengths greater than 5000 Å. Most (483/579) Kast spectra presented herein were taken prior to this upgrade.

In May and June of 2009, the LRIS red-channel CCD was replaced with a mosaic of two 2k × 4k pixel Lawrence Berkeley National Lab (LBNL) CCDs with a spatial scale of $0\farcs135$

[2]We source spectroscopic classifications primarily from the Central Bureau of Electronic Telegrams (CBETs) and the International Astronomical Union Circulars (IAUCs).

[3]`https://wis-tns.weizmann.ac.il`

[4]The NASA/IPAC Extragalactic Database (NED) is operated by the Jet Propulsion Laboratory, California Institute of Technology, under contract with the National Aeronautics and Space Administration (NASA).

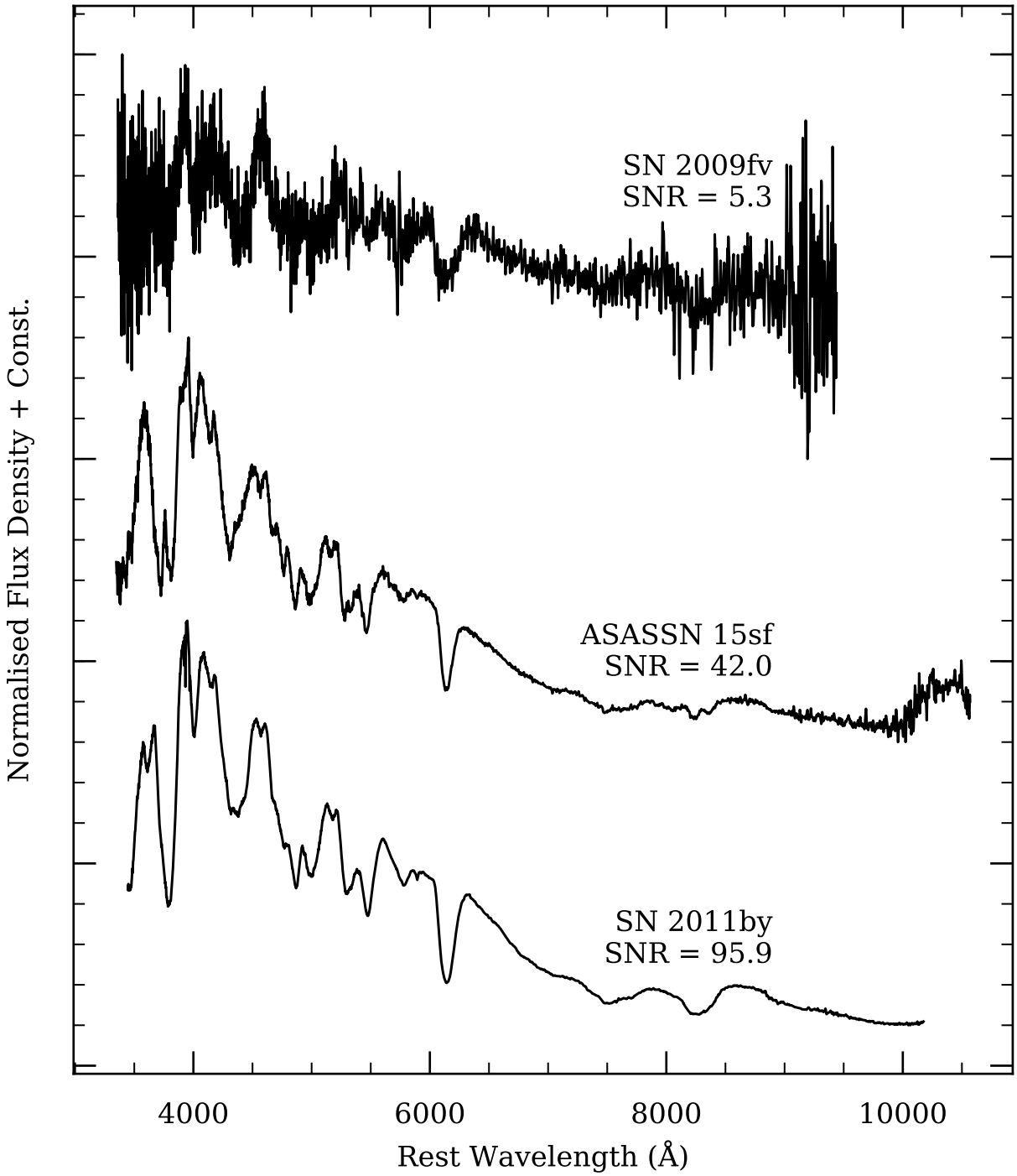

Figure 3.1: Representative SN Ia spectra from our sample showing low, medium, and high SNRs (progressing downward). The spectra have been deredshifted and normalised to a range of unity, and all are at 4 ± 1 days relative to to their SN's light-curve-determined time of maximum brightness.

Table 3.1: SN Ia spectral information.

SN Name	UT Date[a] (Y-M-D)	t_{LC}[b]	Instr.[c]	Wavelength Range (Å)	Res.[d] (Å)	P.A.[e] (°)	Airmass[f]	Exposure Time (s)	SNR	Reference[g]
SN 2008hm	2008−12−31.311	26.5	1	3452−10700	4.3/10.5	110.7	1.12	1800	31.7	...
SN 2008hv	2008−12−31.378	14.3	1	3452−10700	4.7/11.9	138.8	1.32	1200	61.1	...
SN 2008hy	2009−01−05.155	32.9	1	3400−10700	4.9/9.8	35.7	1.31	1200	24.9	...
SN 2009D	2009−01−05.184	−5.6	1	3390−10700	5.0/12.2	161.1	1.86	1200	8.3	...
SN 2009Y	2009−02−19.665	5.7	2	3270−9270	2.1/6.7	183.0	1.29	180	95.1	...
SN 2009Y	2009−03−29.532	43.2	1	3410−10100	5.3/11.3	203.8	2.32	1500	9.6	...
SN 2009Y	2009−04−18.416	62.9	1	3454−9900	4.3/10.5	181.7	1.76	1800	31.8	...
SN 2009V	2009−02−19.605	...	2	3388−9270	4.5/5.9	95.0	1.68	450	7.5	...
SN 2009ae	2009−02−19.677	...	2	3270−9270	4.5/5.4	85.0	1.02	300	39.6	...
SN 2009an	2009−03−29.507	21.1	1	3410−10100	4.5/12.1	107.2	1.42	1500	34.1	...

Abridged table of SN Ia spectral information (the full table is available online at `http://heracles.astro.berkeley.edu/sndb/info#DownloadDatasets(BSNIP,LOSS)`).
[a]Each UT date is specified for the temporal midpoint of the associated observation.
[b]Phases are in rest-frame days as computed from the appropriate redshift and photometry references from Table 3.6.
[c]Instruments (Instr.) are as follows: (1) Kast (Shane 3 m) and (2) LRIS (Keck-I 10 m).
[d]Spectral resolution (Res.) are for the blue and red components, respectively. See Section 2 of S12a for more information.
[e]Observed slit position angle (P.A.) for each observation.
[f]Each airmass is specified for the temporal midpoint of the associated observation.
[g]References to previous publications including the noted spectra are as follows: (1) Silverman et al. (2011), (2) Foley et al. (2012), (3) Foley et al. (2013a), (4) Silverman et al. (2013), (5) Mazzali et al. (2015), (6) Silverman et al. (2012b), (7) Childress et al. (2013), (8) Zheng et al. (2013), (9) Pan et al. (2015a), (10) Foley et al. (2015), (11) Foley et al. (2016), (12) Zheng et al. (2017), and (13) Xuhui et al. (2019, in prep.).

pixel^{-1}. The mosaic features smaller pixels and higher quantum efficiency in the red than the original CCD (Rockosi et al. 2010). Nearly all (52/58 since 1 July 2009) LRIS spectra were taken using this upgraded configuration.

3.2.3 Data Reduction

An important attribute of our sample is the consistency with which the data have been reduced. Regardless of instrument, the same general procedures are followed for all spectral reductions, and just five individuals are responsible for reducing the majority ($> 88\%$) of our dataset. In the following paragraph, we briefly summarise the principal steps in our reduction strategy (see S12a for a more comprehensive discussion), which are implemented using `IRAF`[5] routines and publicly available `Python` and `IDL` programs[6].

First, standard preparation steps including bias removal, cosmic ray rejection, and flat-field correction are performed. Following extraction, one-dimensional spectra are wavelength-calibrated using comparison-lamp spectra typically taken in the afternoon prior to each ob-

[5]IRAF is distributed by the National Optical Astronomy Observatory, which is operated by AURA, Inc., under a cooperative agreement with the U.S. National Science Foundation (NSF).

[6]Kast and LRIS data are currently reduced with `KastShiv` (Shivvers et al. 2016) and `LPipe` (Perley 2019), respectively. Prior to October 2016, a number of LRIS spectra were reduced with purpose-built routines from the Carnegie `Python` (`CarPy`) Distribution (Kelson et al. 2000; Kelson 2003).

serving run. The spectra are then flux-calibrated using spectra (taken during each observing run with the appropriate instrumental setup) of bright spectrophotometric standard stars at similar airmasses. Finally, atmospheric (telluric) absorption features are removed and overlapping (i.e., red- and blue-side spectra from Kast or LRIS) are combined by scaling one so that it matches the other[7] over the common wavelength range. We consider spectra at this stage to be "science ready."

3.3 Classification

Optical spectra are widely used to classify SNe as belonging to one of several distinct types, and possibly subtypes (e.g., Filippenko 1997). We perform such classification in an automated fashion using the SuperNova IDentification code (`SNID`, Blondin and Tonry 2007) with tightly controlled tolerances. `SNID` classifies SNe by cross-correlating an input spectrum against a large library of template spectra (Tonry and Davis 1979). In the following sections we detail our spectral classification procedure, present results, and discuss verifications of these results.

3.3.1 `SNID` Classification Procedure

Using a classification scheme similar to that employed by S12a, we attempt to determine the type, subtype, redshift, and age from each spectrum in our sample via consecutive `SNID` runs that adhere to the specifications outlined in the following sections.

3.3.1.1 `SNID` Type

We first attempt to determine the type of a SN from its spectrum by executing a `SNID` run and requiring an $r$lap[8] value of at least 10. If the host-galaxy redshift of the SN is listed in Table 3.6, then we force `SNID` to use this redshift by invoking the *forcez* keyword — otherwise `SNID` will attempt to find the redshift simultaneously. In order for type determination to be considered successful, we require that the fraction of "good"[9] correlations corresponding to the proposed type be $> 50\%$ and that the best-matching "good" template be of the same type. If no type is determined by this approach, we relax the minimum $r$lap value to 5 and repeat the procedure. If a type is determined at this stage, we proceed to subtype determination.

[7]For Kast spectra, the blue side is scaled to match the red side, while for LRIS spectra, whichever side shows the lower transmission level is scaled upward.

[8]The $r$lap is a measure of quality used by `SNID` — higher values correspond to classifications that are more trustworthy.

[9]In SNID, a template is graded "good" when its strongest correlation with the input spectrum occurs at a redshift that differs by less than 0.02 from the forced (or simultaneously fit) redshift of the input spectrum.

3.3.1.2 SNID Subtype

In the subtype-determination run, we again force SNID to use the redshift of the SN if it is available (and find it simultaneously otherwise). We also force SNID to use only templates that match the previously found type. Again, we attempt a SNID run with a minimum $r$lap value of 10, and relax this to 5 if the first run is unsuccessful. In the case of subtype determination, success is achieved if the fraction of "good" correlations corresponding to a subtype is $> 50\%$ and the best-matching "good" template is of the same subtype.

3.3.1.3 SNID Redshift

We use SNID to determine the redshift from a spectrum by executing a SNID run that requires all templates to be of the subtype found previously (or type, if the subtype was not successfully determined). We use no external redshift information, even if it appears in Table 3.6, but we do restrict the range of template redshifts to lie within $0 < z < 0.3$. We calculate the redshift as the median of all "good" template redshift values, and the redshift uncertainty is taken to be the standard deviation of these values. If the redshift and subtype are determined, then we attempt to find the rest-frame phase relative to maximum light (henceforth referred to as "age") from the spectrum.

3.3.1.4 SNID Age

We attempt to determine the age of a SN spectrum by executing a SNID run that uses only templates of the subtype determined previously and that requires SNID to use the known redshift, or the redshift determined previously if it was not known. The age (henceforth, t_{SNID}) is calculated as the median of only the "good" template ages that have an $r$lap value of at least 75% of the largest achieved $r$lap value. The age uncertainty is the standard deviation of these ages. Furthermore, we require that the age uncertainty be less than the larger of 4 days or 20% of the determined age.

3.3.2 Classification Results and Verifications

Of the 637 spectra selected for characterisation, our SNID routine successfully determines the type in 608 instances, the subtype in 506, the redshift in 605, and the age in 406. We present the results derived from performing our SNID classification procedure in Table 3.2, and we discuss and examine them in the following subsections.

3.3.2.1 Types and Subtypes

To study the robustness of our SNID-determined types and subtypes, we look for distinctions we can draw between spectra that were successfully classified versus those that were not. In particular, we investigate whether there is a significant difference between success and failure

Table 3.2: `SNID` classification results.

	Classification Results				Best-Matching `SNID` Template				
SN	Type	Subtype	$z_{\rm SNID}$	$t_{\rm SNID}{}^a$	Name	Subtype	$r$lap	z	t^a
SN 2008hm	Ia	...	0.0195 ± 0.0046	...	sn99aa	Ia-99aa	17.5	0.0321	34.1
SN 2008hv	Ia	Ia-norm	0.0114 ± 0.0037	18.9 ± ...	sn04ey	Ia-norm	31.2	0.0114	18.9
SN 2008hy	Ia	...	0.0076 ± 0.0038	...	sn91T	Ia-91T	23.4	0.0054	46.6
SN 2009D	Ia	Ia-norm	0.0214 ± 0.0063	-10.6 ± 2.8	sn90N	Ia-norm	16.7	0.0301	−6.4
SN 2009Y	Ia	Ia-norm	0.0014 ± 0.0060	5.9 ± 3.2	sn02bo	Ia-norm	14.0	0.0041	5.5
SN 2009Y	Ia	Ia-norm	0.0085 ± 0.0023	44.5 ± 5.7	sn02bo	Ia-norm	14.0	0.0070	44.5
SN 2009Y	Ia	Ia-norm	0.0116 ± 0.0031	72.5 ± 9.7	sn02bo	Ia-norm	14.1	0.0091	72.5
SN 2009V	Ia	Ia-norm	0.0933 ± 0.0044	11.2 ± 0.5	sn94ae	Ia-norm	15.6	0.0938	11.3
SN 2009ae	Ia	Ia-norm	0.0307 ± 0.0043	18.2 ± 3.4	sn02bo	Ia-norm	17.2	0.0345	17.8
SN 2009an	Ia	Ia-norm	0.0078 ± 0.0030	...	sn02eu	Ia-norm	14.5	0.0065	33.4

Abridged table of `SNID` classifications (the full table is available online at `http://heracles.astro.berkeley.edu/sndb/info#DownloadDatasets(BSNIP,LOSS)`).

[a]Spectral ages (phases) are in rest-frame days relative to the time of the associated SN's maximum brightness. Age uncertainties marked with "..." correspond to cases where only one template was a "good" match.

that is codified by (i) the average SNR of a spectrum, or (ii) the phase in a SN's temporal evolution during which that spectrum was observed.

The median SNR of the spectra for which `SNID` successfully determines a type (subtype) is 32.7 pixel^{-1} (33.4 pixel^{-1}), while for those where it failed the median is 14.3 pixel^{-1} (26.4 pixel^{-1}). For the case of determining the type, this presents a compelling argument — spectra for which the type is classified are generally of higher quality (as assessed by the SNR) than those that are not. Although the gap in median SNR between the successful and failed subsets is notably less pronounced for the case of determining the subtype, we must make a concession for the fact (as stated in Section 3.3.1.1) that the entire population, for which an attempt is made to determine subtype, is drawn *only* from those where the type has been successfully determined (and hence whose aggregate SNR is higher, as discussed above). With this important caveat noted, it would appear that the gap in SNR between successful and failed subtype classifications is indeed meaningful — those SNe for which the subtype is not successfully determined have a median SNR that is ~ 9 times below that of the entire population, relative to the median SNR for those for which the subtype is determined.

Next, we examine how the difference in rest-frame days between when a spectrum was observed and when the SN in that spectrum reached maximum brightness as determined from its light curve (i.e., the phase) may influence `SNID`'s success rate with regard to (sub)type classification. We find that the median phase in cases where `SNID` successfully identifies a type (subtype) is 19.4 days (16.5 days), while in cases where it fails the median is 65.3 days (40.7 days). Owing to the much sparser coverage of `SNID` spectral templates at late phases (see, e.g., Figure 6 of S12a), it makes sense for the failure rate to be larger for spectra at late phases. In addition, spectra at earlier phases tend to have higher SNRs than do those

at later phases[10] because SNe Ia fade throughout their post-maximum evolution. As we have seen above, the SNR of a spectrum plays a substantive role the outcome of (sub)type classification. We find it reasonable, then, that the median phase is earlier for successes than it is for failures. Furthermore, while the caveat from the preceding paragraph regarding the population for which subtype-determination is attempted is still relevant, it is similarly overcome — the difference between the median phase of those for which the subtype is not successfully determined (40.7 days) and that of the entire population (19.4 days) is ~ 7 times larger than the associated difference for those whose subtype is determined (16.5 days).

3.3.2.2 Redshifts

We investigate our `SNID`-determined redshifts by comparing them to the corresponding host-galaxy redshifts, when they are available, as shown in Figure 3.2. From the 563 spectra in our sample for which (i) `SNID` determined a redshift, (ii) `SNID` determined the spectrum was of a SN Ia (independent of the subtype classification), and (iii) a redshift is listed in Table 3.6, we find a median residual of 0.0002 with a standard deviation of 0.0039. Furthermore, we calculate the normalised median absolute deviation (Ilbert et al. 2006), defined as

$$\sigma \equiv 1.48 \times \text{median} \left[\frac{|z_{\text{SNID}} - z_{\text{gal}}|}{1 + z_{\text{gal}}} \right], \tag{3.1}$$

and find a value 0.003, similar to S12a who found 0.002 for their dataset. Of the spectra used for comparison, 446 have a redshift residual within one standard deviation of the median, 522 are within two standard deviations, and 553 are within three.

3.3.2.3 Phases

Next we compare `SNID`-determined phases to those calculated (in rest-frame days) relative to light-curve-determined times of maxima (henceforth, t_{LC}), when available (see Table 3.1 for t_{LC} values and Table 3.6 for references on the times of maximum brightness used to compute them). We perform this comparison for all spectra with the requisite information which `SNID` classified as belonging to a SN Ia (for a total of 219 spectra), and the result is shown in Figure 3.3. There is a rather tight correlation for $t_{\text{SNID}} \lesssim 100$ days, but beyond this point the `SNID`-determined ages systematically underestimate the true (i.e., light-curve-derived) phases. This is not unexpected given the dearth of template spectra available at late phases (as discussed in Section 3.3.2.1) and is consistent with the results of previous studies (e.g., Figure 7 of S12a).

If we further restrict the subset used for phase comparison to cover only the earlier, more rapidly evolving stages of spectroscopic evolution [namely, only those for which the (rest-frame) light-curve-determined phase is < 50 days and the `SNID`-determined phase is < 30 days], we are left with 127 spectra. The median residual for this subset is ~ 0.4 days

[10] If we divide our sample into two groups based on phase (< 20 days, > 20 days), the median SNR of the early-time subset is 57.6 pixel^{-1}, while for the late-time subset it is 32.4 pixel^{-1}.

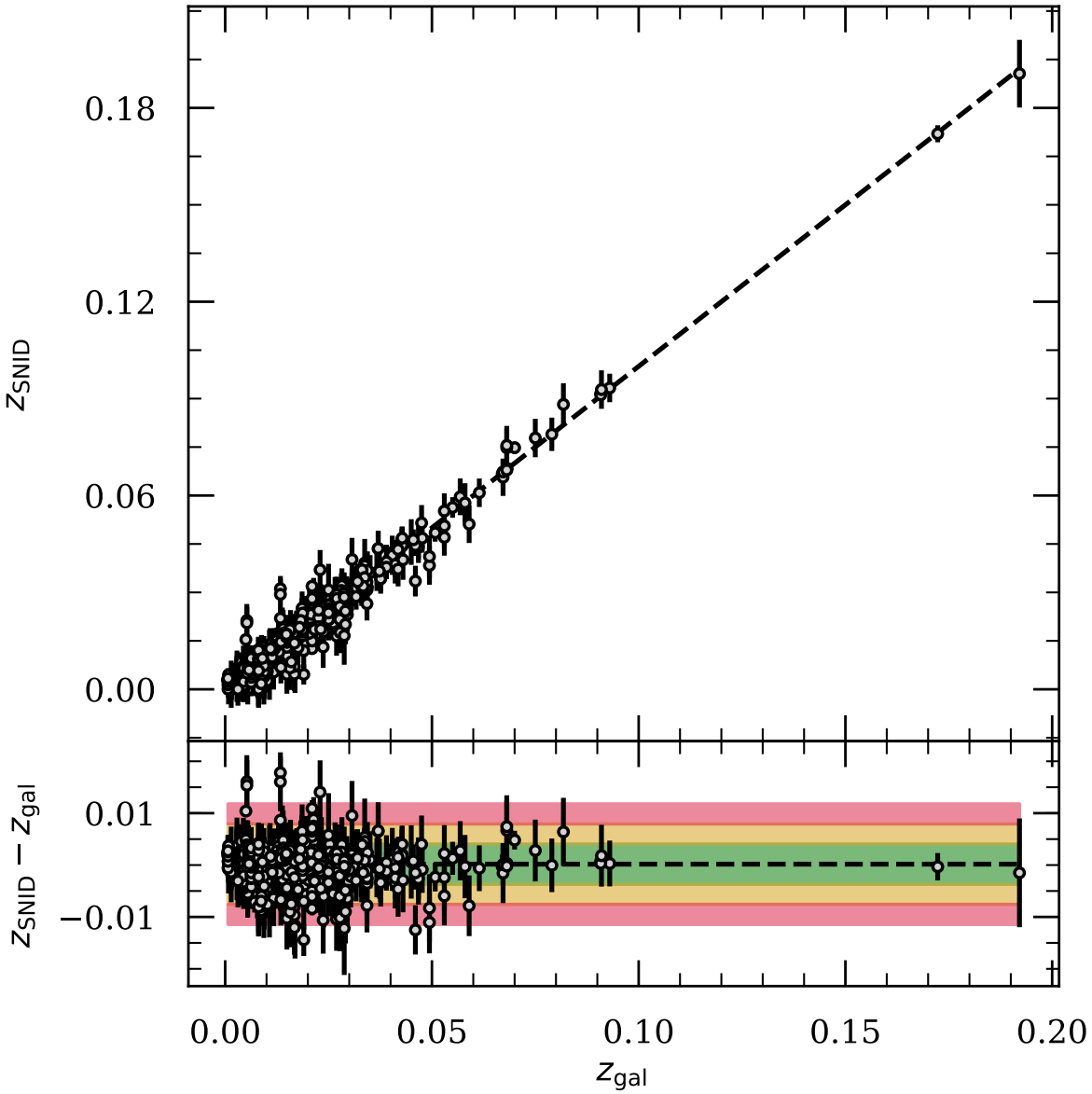

Figure 3.2: SNID-determined redshifts versus host-galaxy redshifts, with residuals in the lower panel. The dashed line in the top panel shows the one-to-one correspondence for z_{gal}, and in the bottom panel it indicates the median residual. The green, yellow, and red regions in the lower panel correspond to the 1σ, 2σ, and 3σ bounds about the median residual, respectively. We note that the typical uncertainties for z_{gal} (which are omitted from the figure) are $\sim 1/4$ of those for z_{SNID}.

with a standard deviation of $\sim$ 3.9 days. Of this subset, 95 spectra have a residual that lies within 1σ of the median, 116 are within 2σ, and 125 are within 3σ. We find that for very early phases ($t_{\rm LC} \lesssim -10$ days), SNID-determined phases tend to be an overestimate (as can be seen in the inset panel of Figure 3.3). As with SNID's tendency to underestimate the phase of late-time spectra, the dominant cause of the noted early-phase overestimate can be attributed to the paucity of template spectra at similar phases.

3.3.3 Object Classifications

Many of the SNe in our sample have multiple spectra, and therefore we must combine the classification information derived for each spectrum to obtain a final classification for each object. To determine the type of an object with multiple spectra, we choose the most frequently occurring type in that object's spectral classifications. In cases with a tie between two possible type characterisations, we use the type of the spectrum whose best-matching SNID template has the larger $r$lap value. To account for the uncertainty surrounding such classifications, we add a "*" to the type. We follow a similar procedure for determining the subtype of each object, except that in cases where there is a tie for the most frequent subtype, we do not classify the subtype. The final (sub)type derived from this methodology is listed for each SN in our sample in Table 3.6. Altogether, 242 objects are unambiguously classified as SNe Ia and one is given the classification of "Ia*". The remaining four objects are discussed in the following section.

3.3.4 Objects Not Classified as SNe Ia

There are four objects (SN 2009eq, LSQ 12fhe, SN 2013gh, and SN 2013fw) in our dataset for which the aforementioned classification method either fails to classify the object at all, or classifies it as something other than a SN Ia. We examine and briefly discuss each of these objects below.

3.3.4.1 SN 2009eq

Of the three spectra of SN 2009eq included in our dataset, two (taken 3 d and 20 d after our first spectrum) are classified as belonging to a SN Ic, and the remaining one (our first observation of the object) is not successfully classified at all. After visual inspection of the three spectra by multiple coauthors, we override the SNID-determined type in favour of "Ia*" — the spectra appear to be consistent with that of a SN Ia, and particularly a SN 1991bg-like (Filippenko et al. 1992a; Leibundgut et al. 1993) object evolving within one month of maximum brightness. However, given that our SNID-based classification scheme does not come to the same conclusion, we cannot unambiguously give a "Ia" classification *from our dataset alone*. It is also worth noting that our determination that SN 2009eq is a SN 1991bg-like object is consistent with its initial classification (Foley et al. 2009).

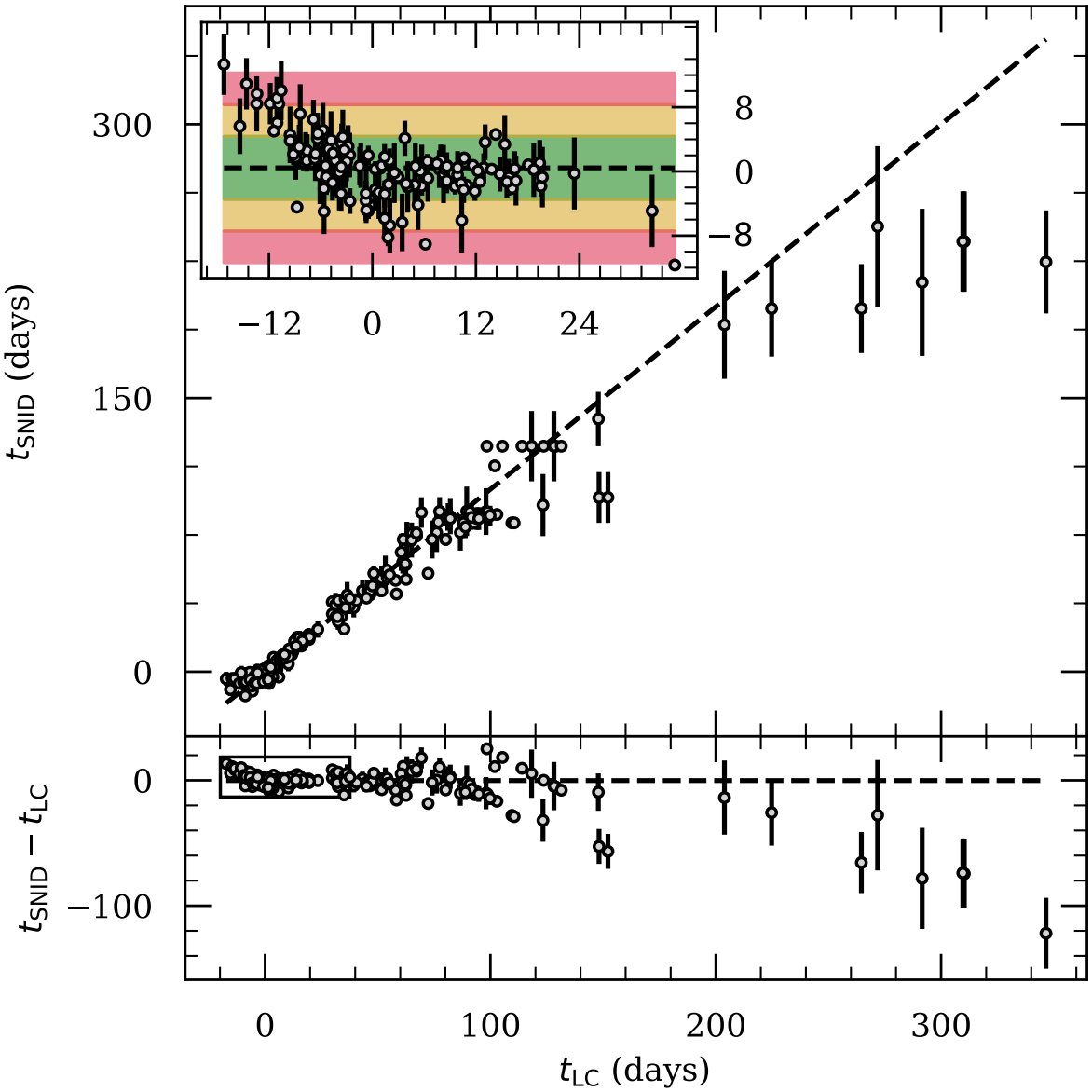

Figure 3.3: SNID-determined phases versus those derived from light-curve maxima and listed in Table 3.1. Residuals are shown in the lower panel. The dashed line in the top panel indicates the one-to-one correspondence for t_{LC}, and in the bottom panel it shows the median residual. The inset panel displays the residuals from the subset of our sample for which $t_{\mathrm{SNID}} \leq 30$ days and $t_{\mathrm{LC}} \leq 50$ days, in addition to the conditions used to select the initial sample. The green, yellow, and red regions correspond to the 1σ, 2σ, and 3σ bounds about the median residual, respectively.

3.3.4.2 LSQ 12fhe

Our classification scheme deems the single spectrum of LSQ 12fhe in our dataset to be of a SN Ic, contradicting the object's initial classification as a SN Ia of the SN 1991T-like (Filippenko et al. 1992b; Phillips et al. 1992) subtype (Hadjiyska et al. 2012). Looking more closely at our `SNID` classification, we see that the SN Ic classification was favoured by just one more template than for a SN Ia. After visual inspection by multiple coauthors, we reach a consensus that the object is definitely a SN Ia, and most likely of the SN 1991T-like subtype (consistent with the initial classification). Accordingly, we override our `SNID`-determined type to be "Ia*" — this reflects its true classification but accounts for the fact that our classification scheme does not reach the correct conclusion.

3.3.4.3 SN 2013gh

SN 2013gh is covered by three spectra in our dataset (with light-curve-determined phases of -12, 70, and 392 days). The first spectrum is unambiguously determined to be of a SN Ia (with an undetermined age), while the second is assigned as a SN Ic (with an age of 1.5 days), and the third is undetermined (not surprising given `SNID`'s lack of late-phase templates, as previously discussed). In light of (i) the visually obvious SN Ia determination from the first spectrum, (ii) the completely incorrect `SNID`-determined phase of the second spectrum, and (iii) the multiple-coauthor consensus that the second spectrum is consistent with that of a SN Ia at the appropriate phase, we again override our `SNID`-determined type in favour of "Ia*".

3.3.4.4 SN 2013fw

The single spectrum of SN 2013fw in our dataset is at a very late phase (> 300 days), and thus it is unsurprising, given `SNID`'s lack of suitable templates (as discussed in Section 3.3.2.1), that our classification scheme does not succeed. We thus defer to the existing object classification (Jin et al. 2013), and assign its type as "Ia*" — it is a SN Ia but we cannot conclusively confirm or refute the classification using our dataset alone.

3.4 Results

In this section we present and study our low-redshift SN Ia spectral dataset derived from observations totaling more than 275 hr of telescope time. Of our initial selection (from Section 3.2.1), 242 objects (covered by a total of 626 spectra) are unambiguously classified as SNe Ia by the methodology described in the preceding section. In the discussion that follows, we consider only this selection of spectra. We provide plots and file access for all spectra described in this work electronically via our SNDB.

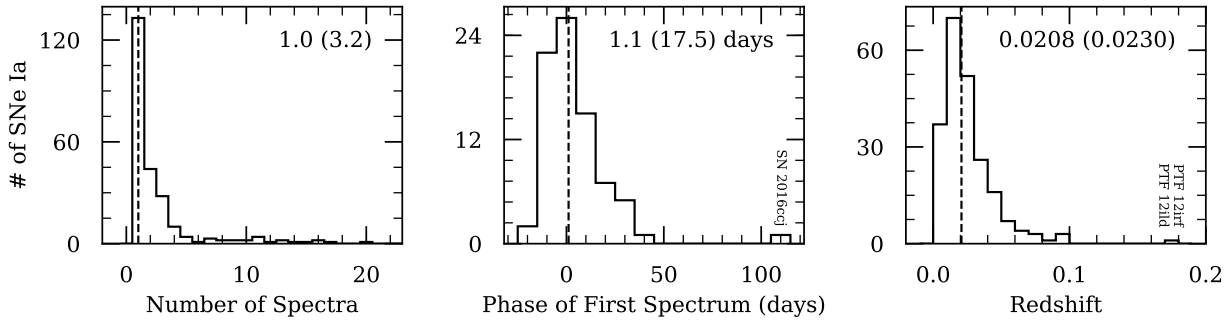

Figure 3.4: Distributions of SN-level parameters, with the associated median (standard deviation) values included. The left panel is the number of spectra, centre is the light-curve-determined rest-frame phase of the first observed spectrum, and right is redshift. The SNe responsible for the outlying bins in the centre and right panels are labeled.

3.4.1 Sample Characteristics

Our dataset averages 2.6 spectra per SN Ia (with a median of 1), similar to the ~ 2.2 spectra per object S12a found for their dataset and reflective of BSNIP's emphasis on maximising the number of objects studied spectroscopically rather than the number of spectra per object. SN 2016coj has the most spectra of any object in our sample with 20, followed by SN 2011fe with 17. Figure 3.4 shows the full distribution of the number of spectra per SN Ia. Of the 242 SNe Ia in our sample, 109 are covered by at least two spectra. For the 79 SNe in our sample that have a light-curve-determined time of maximum brightness (as noted in Table 3.6), we find a median (rest-frame) phase of the first spectrum of 1.1 days, as shown in the centre panel of Figure 3.4. Of this subsample with phase information, 38 SNe have a spectrum observed before the time of maximum brightness and 69 have one within 20 days of maximum. We show the redshift distribution of the objects in our sample in the right panel of Figure 3.4. Aside from two SNe with redshifts of near (but below) 0.2, all have $z < 0.1$ and 201 (of the 221 with a redshift listed in Table 3.6) have $z \leq 0.05$. We find a median redshift of 0.0208 for the full sample, and for the 184 SNe with $z \geq 0.01$ (i.e., within the Hubble flow) we find a median of 0.0230.

We show the distribution of average SNRs for the spectra in our dataset in the left panel of Figure 3.5. The median is 31.8 pixel^{-1} (with a mean of 38.3 pixel^{-1}), and 574/626 spectra have SNR > 10 pixel^{-1}. By design (see Section 3.2.1), we find a minimum SNR of ~ 5 pixel^{-1}. As shown in the centre panel of Figure 3.5, we find the median (light-curve-determined rest-frame) phase for the spectra with such information to be 19.4 days. The spectrum with the earliest phase belongs to SN 2011fe at -17.2 days, followed by two spectra of SN 2012cg with phases of -16.4 days and -15.4 days. The spectrum with the latest phase belongs to SN 2013dy at 422 days, followed by one from SN 2011fe at 379 days. Our dataset includes 15 spectra at phases of at least 160 days. We find that 168 of the 328

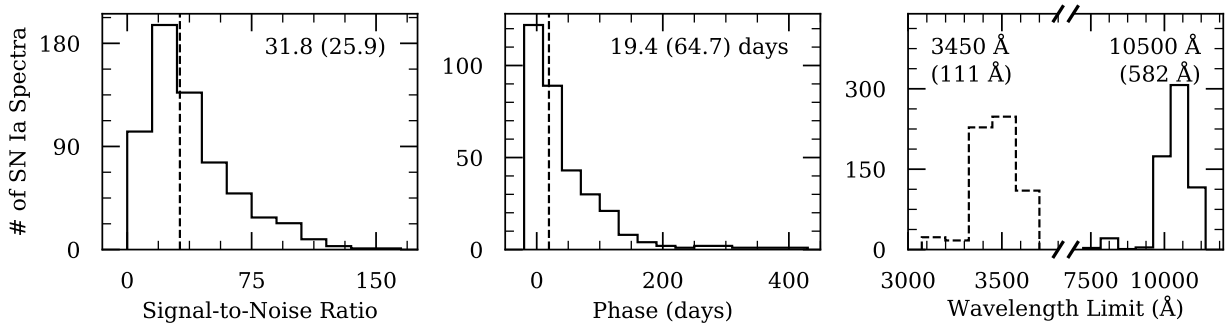

Figure 3.5: Distributions of spectrum-level parameters, with the associated median (standard deviation) values included. The left panel shows the SNR, centre is the light-curve-determined rest-frame phase, and right is the blue and red wavelength limits.

spectra in our sample which have light-curve-determined phases correspond to earlier than 20 days in the post-maximum evolution of their SN. The distributions of the wavelengths of the blue and red ends of our spectra are shown in the right panel of Figure 3.5. We find a median blue (red) wavelength limit of 3450 Å (10,500 Å), and 592 of our spectra cover at least 3700–9800 Å.

3.4.2 Early-time Spectra

A number of prior SN Ia analyses (e.g., Riess et al. 1997b; Folatelli 2004; Foley et al. 2005a; Branch et al. 2006; Garavini et al. 2007; Wang et al. 2009; Blondin et al. 2012; Silverman et al. 2012d; Folatelli et al. 2013; Childress et al. 2014; Zhao et al. 2015) have studied SN Ia optical spectra in terms of multiple "features" — each typically a blend of many spectral transitions, but distinctive enough to be considered in aggregate as a single major absorption feature complex. Of principal interest are assessments of (i) the expansion velocities of such features, and (ii) quantities that probe the relative strengths of the features, often assessed through pseudo-equivalent width (pEW) measurements.

Providing a tracer of explosion kinetic energy, the expansion velocities of SN Ia ejecta have been extensively studied — especially during the characteristic decline through the near-maximum evolution (e.g., Benetti et al. 2005; Wang et al. 2009). Silverman et al. (2012d, henceforth S12b) find velocities within a few days of maximum brightness that are consistent with the notion that SN Ia ejecta are layered — features of O I, Si II, and S II tend to have lower velocities (and are thus found in the inner, more slowly expanding layers), while those of Ca II have the highest velocities (and are therefore associated with the outer, more rapidly expanding layers). These findings are consistent with our own (see Section 3.4.2.2). Together with probes of feature strength (e.g., pEW measurements), expansion velocities can be used to quantify the degree of homogeneity between spectra of different SNe Ia (and hence SNe themselves) at similar epochs, as well as describe the expected temporal evolution

Table 3.3: Spectral features.

Feature	Rest Wavelength (Å)	Blue Boundary (Å)	Red Boundary (Å)
Ca II H&K	3945.28	3400–3800	3800–4100
Si II λ4000	4129.73	3850–4000	4000–4150
Mg II	...[a]	4000–4150	4350–4700
Fe II	...[a]	4350–4700	5050–5550
S II "W"	5624.32	5100–5300	5450–5700
Si II λ5972	5971.85	5400–5700	5750–6000
Si II λ6355	6355.21	5750–6060	6200–6600
O I triplet	7773.37	6800–7450	7600–8000
Ca II near-IR triplet	8578.75	7500–8100	8200–8900

Note: Spectral features and boundaries, as adapted from S12b.
[a]A single reference wavelength is not useful for this feature because it is a blend of too many spectral lines. Hence, we do not compute expansion velocities for this feature.

of spectral features (Folatelli 2004). Feature-strength measurements from SN Ia spectra are further prized for the prospect that they might correlate with luminosity (e.g., Nugent et al. 1995; Silverman et al. 2012c).

Following S12b, we measure the expansion velocities, pEWs, and fluxes at the endpoints of nine features in the spectra from our sample which have a light-curve-determined rest-frame phase of < 20 days[11]. While some studies consider high-velocity and photospheric components for certain features (typically by fitting a series of Gaussians to the absorption profile; e.g., Silverman et al. 2015; Pan et al. 2015b; Zhao et al. 2016), we do not draw such a distinction in the following analysis (so as to remain consistent with the methodology of S12b). Our selected features, each labeled by the ion or spectral transition line most dominant in the absorption, are listed in Table 3.3 along with their rest wavelengths.

Because SN Ia spectra — and hence the aforementioned features — undergo temporal evolution for an individual SN Ia and exhibit variation over many SNe Ia (even when comparing similar epochs), the endpoints of each feature must be determined on a spectrum-by-spectrum basis. To this end we have developed `respext`[12], a `Python` package for automated SN Ia spectral feature analysis that is an object-oriented and extensively modified refactorisation (or *redux*) of the `spextractor`[13] package. Given an input spectrum, the

[11]Two pairs of the selected features (Si II λ4000, Mg II; and S II "W", Si II λ5972) become significantly blended at the late end of this range, so we therefore only measure these features for $t_{\rm LC} \leq 10$ days.

[12]`https://github.com/benstahl92/respext`

[13]`https://github.com/astrobarn/spextractor`

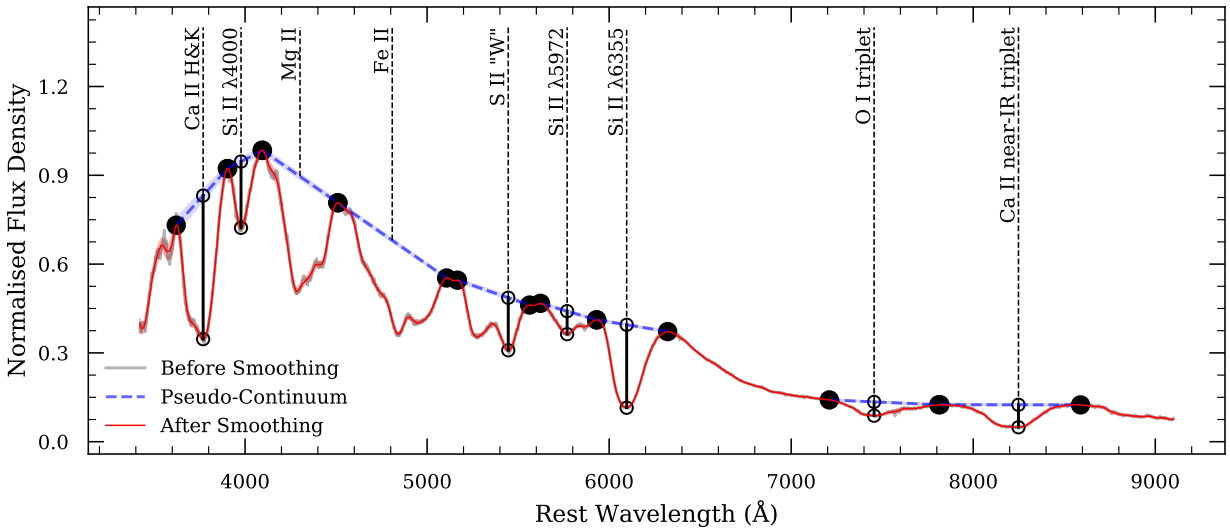

Figure 3.6: Spectrum of SN 2016coj at roughly 0.5 day before maximum brightness after processing with `respext`. The Galactic reddening-corrected and deredshifted (but otherwise unprocessed) original spectrum appears in grey, while the smoothed spectrum is in red. Large black dots represent the identified feature boundaries which define the pseudo-continuum (in blue). Smaller black circles indicate absorption minima and the pseudo-continuum fluxes at their locations.

program smooths[14] it using a Savitzky-Golay filter (Savitzky and Golay 1964) and then automatically (or if necessary, manually) selects absorption-feature boundaries, from which pseudo-continua are derived. It then measures the pEWs, expansion velocities, and boundaries of those features. Figure 3.6 shows the result of this procedure when applied to a spectrum of SN 2016coj near maximum brightness. In the following subsections, we describe our measurement procedure in detail and present our results.

3.4.2.1 Pseudo-continua and Pseudo-equivalent Widths

After taking steps to standardise[15] an input spectrum, the first task is to determine the edges of each of its features. We do this by means of a two-step process: (i) we compute the derivative of the smoothed spectrum and identify the wavelengths corresponding to where it changes from positive to negative (i.e., the wavelengths of local maxima); (ii) of

[14] In tests, we have found negligible difference between measurements conducted with and without smoothing. Smoothing does, however, allow us to study spectra whose SNRs would otherwise make their measurement unreliable.

[15] The steps performed to homogenise input spectra include correcting for Milky Way (MW) reddening using the values given in Table 3.6 and assuming the extinction law of Cardelli et al. (1989) as modified by O'Donnell (1994), deredshifting (again using values from Table 3.6), flux-normalising, and smoothing.

Table 3.4: SN Ia spectral feature measurements near maximum brightness.

SN	Feature	$t_{\rm LC}{}^a$	$F_{\rm b}^b$	$F_{\rm r}^b$	pEW^c	v^d
SN 2008hv	Ca II H&K	14.29	2.66 ± 0.17	4.04 ± 0.11	62.7 ± 5.2	-11.74 ± 0.16
SN 2009D	Ca II H&K	-5.61	6.67 ± 0.74	7.29 ± 0.50	120.1 ± 6.3	-20.01 ± 0.16
SN 2009Y	Ca II H&K	5.72	8.75 ± 0.14	16.24 ± 0.25	114.7 ± 2.4	-17.87 ± 0.16
SN 2009bv	Ca II H&K	12.46	0.86 ± 0.04	1.24 ± 0.04	83.0 ± 3.5	-12.14 ± 0.16
SN 2009cz	Ca II H&K	-3.03	6.51 ± 0.16	6.75 ± 0.11	117.1 ± 2.7	-19.59 ± 0.16
SN 2009dc	Ca II H&K	-5.74	7.15 ± 0.11	6.97 ± 0.34	40.4 ± 4.7	-16.16 ± 0.16
SN 2009ds	Ca II H&K	8.62	12.71 ± 0.42	15.66 ± 0.31	80.5 ± 2.9	-12.61 ± 0.16
SN 2009eu	Ca II H&K	-4.80	0.42 ± 0.02	0.58 ± 0.02	100.5 ± 3.5	-18.79 ± 0.16
SN 2009fw	Ca II H&K	5.30	0.31 ± 0.11	0.43 ± 0.09	68.5 ± 14.5	-19.88 ± 0.16
SN 2009fw	Ca II H&K	6.44	0.53 ± 0.05	1.26 ± 0.05	77.9 ± 5.4	-19.10 ± 0.16

Abridged table of SN Ia spectral feature measurements (the full table is available online at `http://heracles.astro.berkeley.edu/sndb/info#DownloadDatasets(BSNIP,LOSS)`).
[a]Phases are in rest-frame days as given in Table 3.1.
[b]Fluxes at feature boundaries are in units of 10^{-15} erg s^{-1} cm^{-2} Å^{-1}.
[c]Pseudo-equivalent widths are in units of Å.
[d]Expansion velocities are in units of 10^3 km s^{-1} and are *blueshifts*.

these identified wavelengths, the one corresponding to the maximum flux of the smoothed spectrum within the blue (red) edge boundary (as given in Table 3.3) is used to define the blue (red) edge of the absorption feature. Owing to the fact that the blue end of the O I triplet rarely reaches a local maximum, we follow S12b by modifying our procedure to identify where the derivative passes through -2.0×10^{-18} erg s^{-1} cm^{-2} Å^{-2} (moving in the positive direction). We visually inspect all feature boundaries derived from this procedure, and infrequently override them by manually selecting boundary points when the original ones are not correct. The uncertainty in the flux at the boundary points is assigned as the root-mean-square error (RMSE) between the input and smoothed fluxes within a range identical to the width of the smoothing window centred at the identified boundary wavelengths. We list all measured feature-boundary fluxes (and their uncertainties) in Table 3.4.

If the blue and red boundaries of a feature are successfully determined, we define the pseudo-continuum by connecting the boundary points with a line. The lower (upper) uncertainty of the pseudo-continuum is derived by connecting a line between the boundary points, with their fluxes reduced (increased) by their uncertainties. Once the pseudo-continuum is determined, we calculate the pEW (e.g., Garavini et al. 2007, S12b),

$$\mathrm{pEW} = \sum_{i=0}^{N-1} \Delta\lambda_i \left(1 - \frac{f(\lambda_i)}{f_c(\lambda_i)}\right), \tag{3.2}$$

where N is the number of pixels between the blue and red boundaries of the feature (which

also define the pseudo-continuum as discussed above), λ_i ($\Delta\lambda_i$) is the wavelength (width) of the ith pixel, and $f(\lambda_i)$ [$f_c(\lambda_i)$] is the spectrum [pseudo-continuum] flux at λ_i. The uncertainty in our measurement of the pEW is calculated using standard techniques of error propagation using both the uncertainty of the pseudo-continuum (as described above) and the uncertainty in the spectrum flux at each pixel (derived using the RMSE as done for feature boundaries, also described above).

Table 3.4 includes a column containing all measured pEWs, and we visualise their temporal evolution in Figure 3.7. In the same figure, we compare the aggregate pEW evolution for each feature in our dataset to those derived from the dataset of S12b. Given that this comparison is for measurements made between different (but similarly targeted, observed, and reduced) spectra from different SNe Ia, we find the level of consistency satisfactory. Indeed, the same evolutionary trends clearly manifest themselves in both datasets — we mention some of the more noteworthy observations in the following paragraphs.

Both the Ca II H&K feature and Ca II near-infrared (IR) triplet exhibit relatively large pEWs for $t_{\rm LC} \lesssim -5$ days, but while the former has a pEW that slowly declines through its evolution beyond this point (with noticeably reducing scatter), the pEW of the latter markedly grows. These features, together with the Fe II complex (which seems to grow quadratically for $t_{\rm LC} \gtrsim -8$ days), have the largest pEWs of all features measured (and are thus in the last row of Figure 3.7).

The Mg II feature pEW measurements show a modestly increasing trend and have relatively small scatter compared to those for the Si II λ6355 feature and O I triplet (all three displayed in the central row of Figure 3.7 owing to their similar range of values). The O I triplet's mean pEW evolution appears to consist of several distinct stages: there is an increase for $t_{\rm LC} \lesssim 5$ days, at which point the evolution reaches a broad peak of ~ 120 Å, and then there is a stage of decrease. The mean pEW evolution of the S II "W" feature follows a similar trend, except that the peak of ~ 80 Å occurs a few days earlier and is more sharply defined.

Si II λ6355, the most characteristic spectral feature of SNe Ia near maximum brightness, shows relatively flat pEW evolution (~ 100 Å) for $t_{\rm LC} \lesssim 10$ days, after which our measurements are consistent with a "hint of sharp upturn" as was noted by S12b, and which is likely due to blending with Si II λ5972 at such epochs. Similarly, the Si II λ5972 feature exhibits relatively constant (if slightly increasing) pEW evolution until $t_{\rm LC} \approx 5$ days, at which phase there is an uptick, likely due to blending with the Na I D line (from the MW, and owing to their low redshifts, possibly from the host galaxies of the SNe). The Si II λ4000 feature has the lowest aggregate pEWs in our sample (hence its position in the first row of Figure 3.7, along with the measurements for Si II λ5972 and S II "W"), and shows evidence for a slight trend of increasing pEW.

3.4.2.2 Expansion Velocities

With feature boundaries determined according to Section 3.4.2.1, we identify the absorption minimum (wavelength and flux) in each feature by fitting the smoothed flux (within each

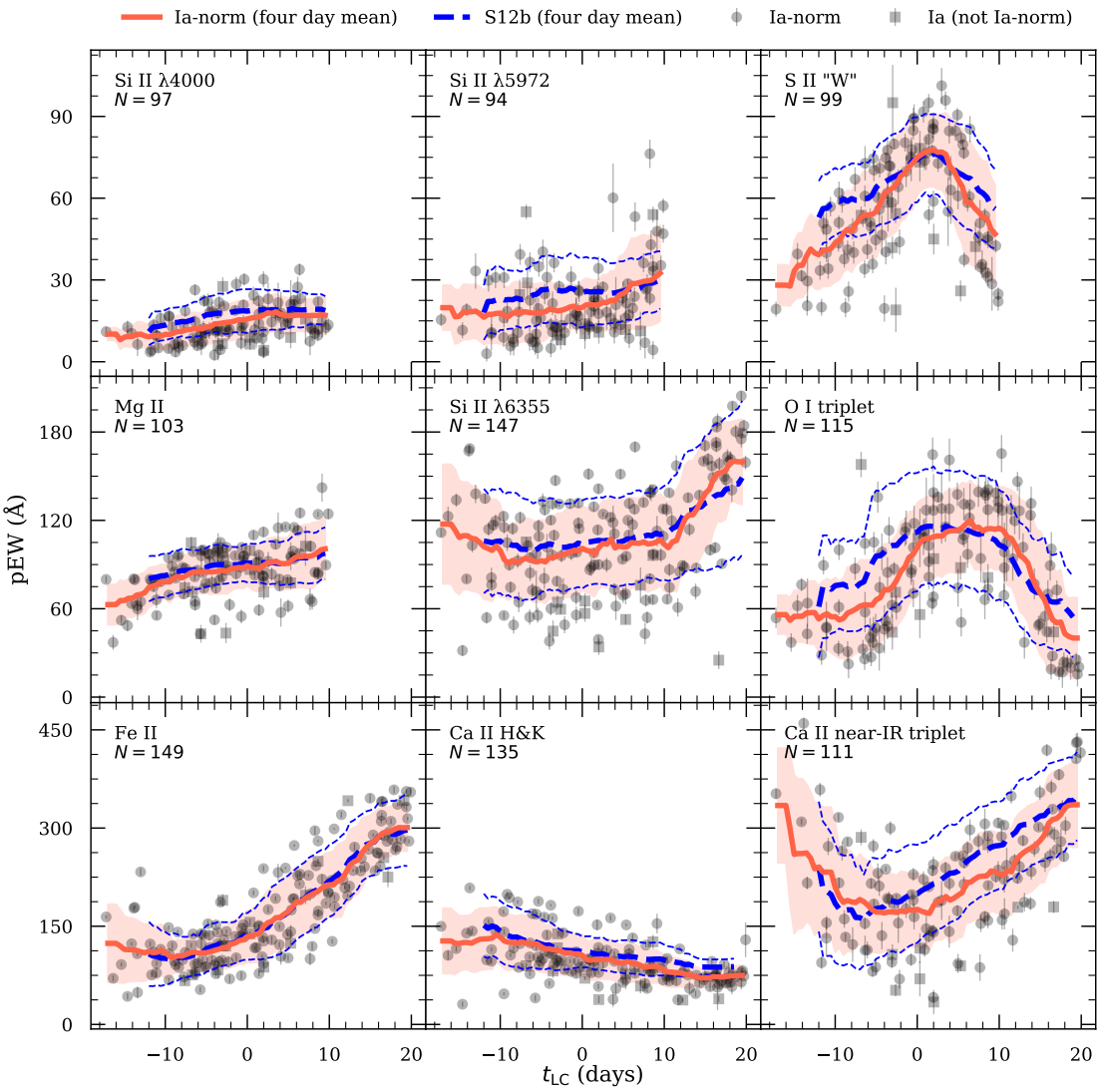

Figure 3.7: Evolution of pEWs for the features noted in Table 3.3, grouped by pEW magnitude. Grey circles are measured pEWs for spectra belonging to SNe classified as "Ia-norm" according to the prescription of Section 3.3, and grey squares are those for SNe classified as "Ia" of any subtype (except "Ia-norm") or "Ia" with no subtype determined. The red line and filled region represent the mean and standard deviation (respectively) of all "Ia-norm" measurements within four days of each half-day increment in the evolution, and the dashed blue lines represent the corresponding descriptors derived from the dataset of S12b. The feature and number of "Ia-norm" measurements for it are included in each panel.

feature boundary) with a cubic spline and computing the minimum. We do this for all features with identified boundaries except for Mg II and Fe II, which are composites of so many blended lines that there is ambiguity when choosing a reference wavelength against which to measure expansion velocities. The S II "W" feature has two broad absorptions, so for consistency — both internally and with the results described by S12b — we always measure the minimum of the redder of the two features (even if the bluer component has a deeper absorption). As with measurements of feature boundaries, we perform a visual inspection, and in cases where the spline fit does not accurately reflect the true flux minimum we manually adjust the range over which the spline is fit in order to more faithfully capture the signal. Following S12b, we impose a 2 Å uncertainty on the wavelength of the feature minimum (and do not explicitly account for systematic uncertainties due to the spectral resolution).

To calculate the expansion velocity of a feature, v, we use the wavelength of its flux minimum (as determined above) and the appropriate rest wavelength (as given in Table 3.3) with the relativistic Doppler equation. The uncertainty in the expansion velocity is obtained by propagating the wavelength uncertainty (as described above). We present all of our velocity measurements in Table 3.4. We emphasise that they are derived from *blueshifted* spectral features (and hence appear as negative number in the table). All velocity measurements are shown in Figure 3.8, and the aggregate results are compared to those derived from the dataset of S12b. As with the pEW comparison, we find clear qualitative consistency in evolutionary trends (especially given some allowance for biases due to low-number statistics at the earliest epochs).

Similar to S12b, we find the highest expansion velocities from the two Ca II features we investigated. The features exhibit similar evolution, with velocities in excess of $25,000$ km s^{-1} (and as high as $\sim 30,000$ km s^{-1}) for $t \lesssim -5$ days, followed by a rapid decline to relative constancy (slightly decreasing for Ca II H&K) at $\sim 12,000$ km s^{-1} for $t \gtrsim 0$ days.

All three features of Si II show a similar evolutionary track of modest decline, albeit with different scales. The largest velocities are claimed by Si II λ6355, followed by Si II λ5972 (both of which converge to a steady velocity of $\sim 11,000$ km s^{-1} for $t \gtrsim 0$ days), and finally Si II λ4000 (which continues to decline throughout the evolution). The velocity of the S II "W" feature shows a very similar evolution to that of Si II λ4000, but with a bit more scatter and a slightly steeper decline.

The expansion velocities of the O I triplet cover a similar range of values to those of the Si II "W" feature, but with a significantly larger degree of scatter (especially for later epochs). This is unsurprising: the O I triplet is a broad feature, and thus when it becomes weak (as it does at later phases, as shown in Figure 3.7) the exact location of the minimum is more challenging to robustly determine. It is difficult to quantify the extent to which this mechanism introduces scatter relative to what may be intrinsic, but after visually inspecting the results, we find the derived minima to be reasonable.

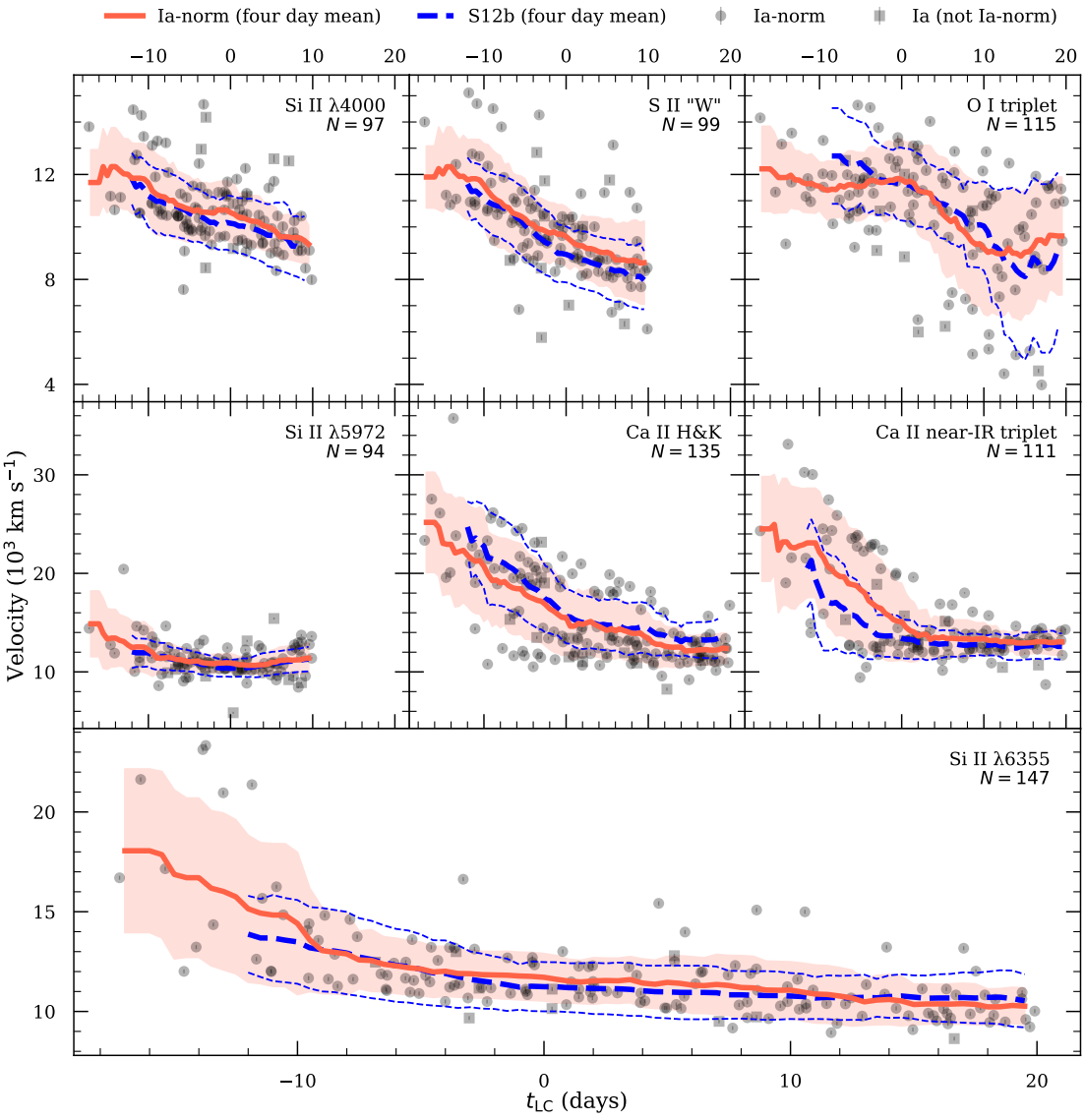

Figure 3.8: Same as Figure 3.7, but for expansion velocities. Though we show positive velocity scales, we reiterate that the velocities correspond to *blueshifts*.

3.4.3 Late-time Spectra

As a SN Ia reaches the so-called nebular phase in its evolution (starting $t \gtrsim 100$ days after maximum light, and fully for $t \gtrsim 160$ days), the density of the ejecta diminishes to the point of becoming optically thin, thereby allowing light from deep within the interior to escape. This results in broad emission lines (due mostly to iron-group elements) in the late-time optical spectra of SNe Ia, which may encode important physical and geometric details of the explosion mechanism(s) (Maeda et al. 2010b; Maguire et al. 2018). In particular, many studies of late-time SN Ia spectra have considered three broad emission features centred near 4701, 6155, and 7378 Å, which are attributed to blends of various lines of [Fe III], [Fe II], and [Ni II], respectively (Mazzali et al. 1998; Maeda et al. 2010a; Blondin et al. 2012; Silverman et al. 2013; Maguire et al. 2018).

Of the spectra in our dataset having light-curve-determined phases, there are 15 (spanning 7 SNe Ia) for which $t_{\rm LC} \geq 160$ days. Though this is not a sufficiently large sample to perform a stand-alone study (and because a subset of these spectra have already been considered in other works; see the references listed in Table 3.1), we perform only a brief analysis focusing on the velocity shift of the [Fe III] λ4701 feature and the mean velocity shift of the two remaining features (which, for consistency with the aforementioned studies, we refer to as the "nebular velocity"). We describe our methodology and measurements in the following subsections.

3.4.3.1 Methodology

We measure velocities of the listed features in our nebular spectra using tools from our `respext` package. Again, we preprocess spectra by correcting for Galactic extinction and then deredshifting, flux-normalising, and smoothing. Emission peaks are identified by eye and then, following the approach described in Section 3.4.2.2, we fit a cubic spline to the smoothed spectrum in the vicinity of the peak, allowing us to derive the wavelength at which the flux is maximal. Consistent with our treatment of early-time spectra, we impose a uniform 2 Å uncertainty on all wavelengths determined by this method. The velocity of the feature is then obtained using the relativistic Doppler equation. Our results are summarised in Table 3.5.

3.4.3.2 [Fe iii] λ4701 Velocities

We present our measurements of the velocity shifts of the [Fe III] λ4701 feature in the top panel of Figure 3.9. Similar to Silverman et al. (2013), we find evidence for a slow decrease in blueshift (i.e., a velocity *increase*) in the nebular-phase evolution. For the three SNe Ia in our sample having multiple nebular-phase spectra with nonnegligible temporal separation (SN 2011fe, SN 2011by, and SN 2014J), we find average velocity increase rates of 15, 11, and 5 km $\rm s^{-1}$ $\rm d^{-1}$ (respectively).

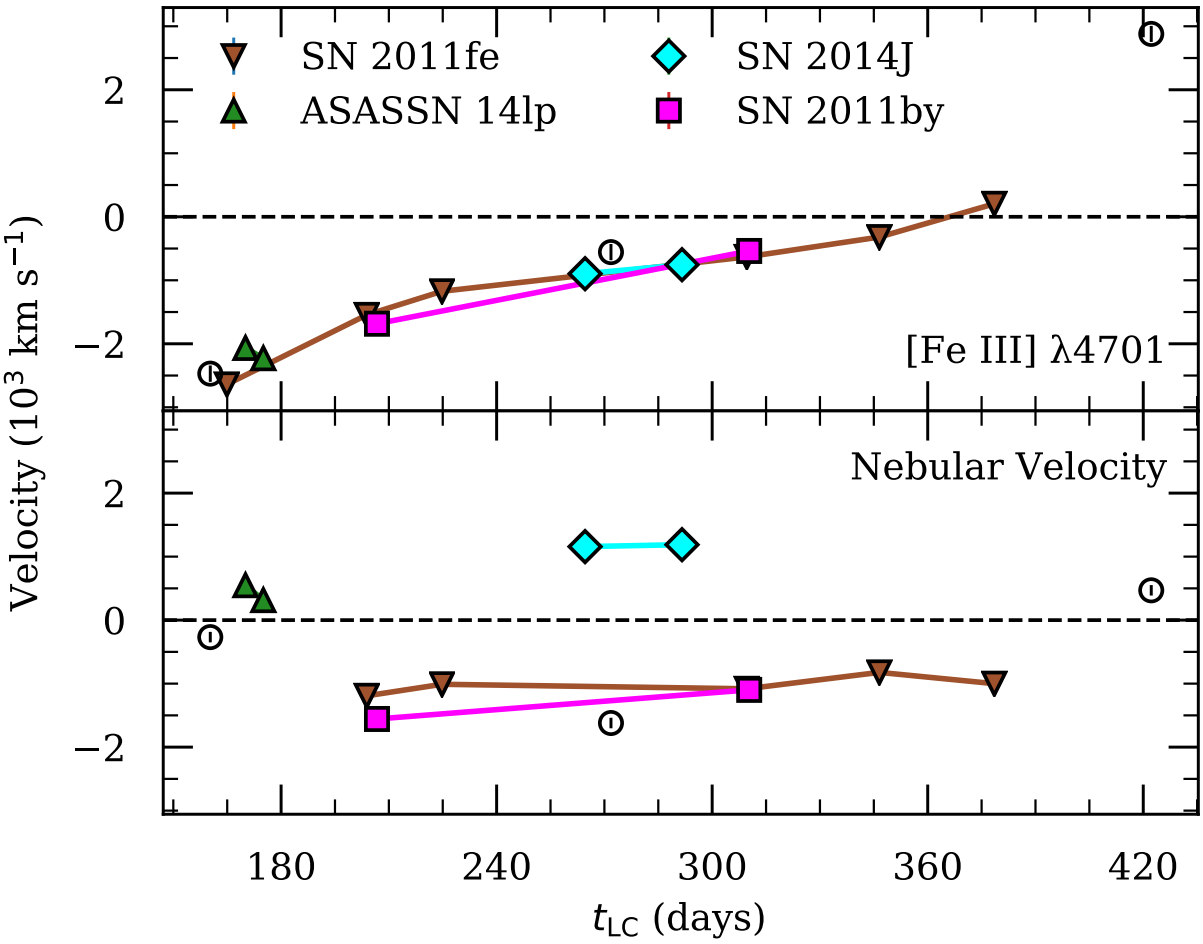

Figure 3.9: Measured velocity shifts from the nebular spectra in our sample. The top panel shows the velocity shifts for the [Fe III] λ4701 feature, while the bottom shows the nebular velocities (as discussed in Section 3.4.3.3). SNe Ia with multiple nebular spectra are marked as indicated in the legend and connected by lines. The error bars, which do not account for systematic uncertainties from the resolution of our spectra, are typically smaller than the markers. For a typical resolution of ~ 10 Å, the omitted systematic uncertainty amounts to ~ 500 km s^{-1}.

Table 3.5: Late-time SN Ia spectral feature measurements.

SN Name	$t_{\rm LC}$[a]	Velocity[b] [Fe III] λ4701	Velocity[b] [Fe II] λ7155	Velocity[b] [Ni II] λ7378
SN 2009ig	160.3	-2.47 ± 0.13	0.83 ± 0.08	-1.36 ± 0.08
SN 2011by	206.7	-1.68 ± 0.13	-1.38 ± 0.08	-1.73 ± 0.08
SN 2011by	310.3	-0.54 ± 0.13	-1.05 ± 0.08	-1.15 ± 0.08
SN 2011fe	164.9	-2.64 ± 0.13	-1.37 ± 0.08	...
SN 2011fe	203.9	-1.54 ± 0.13	-1.26 ± 0.08	-1.12 ± 0.08
SN 2011fe	224.8	-1.17 ± 0.13	-0.93 ± 0.08	-1.09 ± 0.08
SN 2011fe	309.6	-0.63 ± 0.13	-1.22 ± 0.08	-0.94 ± 0.08
SN 2011fe	346.5	-0.32 ± 0.13	-0.76 ± 0.08	-0.89 ± 0.08
SN 2011fe	378.5	0.20 ± 0.13	-1.10 ± 0.08	-0.90 ± 0.08
SN 2013dy	422.2	2.88 ± 0.13	0.55 ± 0.08	0.39 ± 0.08
SN 2013gy	271.8	-0.56 ± 0.13	-0.29 ± 0.08	-2.95 ± 0.08
SN 2014J	264.6	-0.90 ± 0.13	0.86 ± 0.08	1.45 ± 0.08
SN 2014J	291.6	-0.75 ± 0.13	1.00 ± 0.08	1.38 ± 0.08
ASASSN 14lp	170.1	-2.07 ± 0.13	0.57 ± 0.08	0.53 ± 0.08
ASASSN 14lp	175.1	-2.23 ± 0.13	0.44 ± 0.08	0.19 ± 0.08

[a]Spectral phases are in rest-frame days as given in Table 3.1.
[b]Velocities are in units of 10^3 km s^{-1}. Negative values are blueshifted. Systematic uncertainties associated with the resolution of the spectra are not included.

3.4.3.3 Nebular Velocities

As with Maeda et al. (2010a), Blondin et al. (2012), and Silverman et al. (2013), we derive nebular velocities as the arithmetic mean of the [Fe II] λ7155 and [Ni II] λ7378 feature velocities. Whereas previous studies have determined the uncertainty in the nebular velocity as the difference between the constituent velocities (Maeda et al. 2010a), or half of this difference (Silverman et al. 2013), we derive it from direct propagation of uncertainties. We present our nebular velocity measurements in the bottom panel of Figure 3.9. In contrast to the slow (but noticeable) increasing trend in the [Fe III] λ4701 velocities, we find an even weaker trend in nebular velocities. For the previously mentioned set of three SNe Ia with multiple nebular spectra, we find average velocity increase rates of just 2, 4, and 1 km s^{-1} d^{-1} — consistent with the assertion made by Silverman et al. (2013) that a single measurement of the nebular velocity of a given SN Ia is sufficient to describe that SN throughout its nebular-phase evolution.

3.5 Conclusion

In this paper we present 637 optical spectra collected by the Berkeley Supernova Ia Program using the Kast double spectrograph at Lick Observatory and LRIS at the W. M. Keck Observatory between 2009 and 2018. Careful observation and processing techniques perfected over the last 20+ years are employed to prepare the spectra in a manner that is (i) self-consistent and (ii) consistent with earlier BSNIP spectral data releases (S12a).

We employ a robust automated spectral classification procedure that uses `SNID` to derive the type, subtype, redshift, and rest-frame phase of the spectra in our dataset, achieving a successful result in the majority of cases. Furthermore, we perform a study of the results and conclude that failures preferentially occur for late-phase spectra (where the temporal coverage of `SNID` is sparse) and for spectra with lower SNRs (and which are thus of lower quality). Where independent measurements (i.e., host-galaxy redshifts, and light-curve-derived rest-frame phases) are available, we compare them to `SNID`-based predictions. The redshifts show negligible difference in aggregate and have relatively small scatter, while the phases have a larger — but still reasonable — scatter (especially when a more temporally restrictive subset is selected). After combining the classifications in cases where multiple spectra are available for a given object, we address the several cases in which a selected object was not classified as a SN Ia. Ultimately, we obtain a final sample of 626 spectra from 242 low-redshift SNe Ia.

We study the early-time and late-time properties of our dataset, with emphasis on measurements of the most prominent features in SN Ia spectra at such phases. In particular, we measure the expansion velocities, pEWs, and fluxes at the boundaries of nine absorption-feature complexes from the subset of our spectra that were observed within 20 days of maximum light. When we compare with the analogous set of measurements performed on an earlier set of BSNIP spectra (S12b), we find clear evidence for the same evolutionary behaviours in the features. Similarly, we measure the velocity shifts of three emission features from the subset of our spectra that were observed more than 160 days after maximum light. With just 15 such nebular spectra, our sample is too small to merit a stand-alone study, but we do find clear manifestations of the evolutionary behaviours noted by more comprehensive studies.

When our dataset is combined with that described by S12a, the BSNIP low-redshift SN Ia spectral dataset reaches nearly 2000 optical spectra, all of which have been handled consistently through all phases of observing and processing. Further utility will be unlocked by considering the aforementioned spectral dataset in conjunction with its companion photometric dataset of more than 250 SNe Ia from the Lick Observatory Supernova Search follow-up program (see G10 and S19, for the photometric datasets covering 1998–2008 and 2009–2018, respectively). In a future study, we will leverage these datasets to explore the extent to which photometrically derived parameters can be reconstructed from SN Ia spectra (Stahl et al. 2020a).

3.6 Sample Information

Table 3.6: SN Ia information.

SN Name	Discovery Date (UT)	R.A. α(2000)	Decl. δ(2000)	$z_{\rm helio}$[a]	$E(B-V)_{\rm MW}$[b] (mag)	SNID[c] (sub)type	# of Spectra	First[d] Epoch	Last[d] Epoch	$\rm MJD_{max}$[e] Reference
SN 2008hm	2008−11−25	51.7954	46.9443	0.0197	0.381	Ia	1	26.5	...	2
SN 2008hv	2008−12−02	136.8920	3.3923	0.0125	0.027	Ia-norm	1	14.3	...	2
SN 2008hy	2008−12−06	56.2852	76.6654	0.0085	0.203	Ia	1	32.9	...	2
SN 2009D	2009−01−02	58.5951	−19.1817	0.0250	0.046	Ia-norm	1	−5.6	...	1
SN 2009Y	2009−02−01	220.5990	−17.2468	0.0094	0.087	Ia-norm	3	5.7	62.9	2
SN 2009V	2009−02−02	153.2030	43.1832	0.0930†(c)	0.012	Ia-norm	1	...	...	...
SN 2009ae	2009−02−15	249.8700	21.3154	0.0311	0.049	Ia-norm	1	...	...	...
SN 2009an	2009−02−27	185.6980	65.8512	0.0092	0.016	Ia-norm	2	21.1	40.7	2
SN 2009bp	2009−03−17	211.9570	36.6436	...	0.004	Ia	1	...	...	...
SN 2009bs	2009−03−21	201.7340	52.7549	0.0298	0.011	Ia-91bg	2	...	...	...
SN 2009bv	2009−03−27	196.8350	35.7844	0.0367	0.008	Ia-norm	1	12.5	...	2
SN 2009cz	2009−04−06	138.7500	29.7353	0.0211	0.022	Ia	1	−3.0	...	4
SN 2009dc	2009−04−09	237.8010	25.7078	0.0214	0.060	Ia-norm	8	−5.7	109.5	1
SN 2009do	2009−04−22	188.7430	50.8512	0.0397	0.013	Ia-norm	1	23.4	...	2
SN 2009ds	2009−04−28	177.2670	−9.7291	0.0193	0.033	Ia-norm	1	8.6	...	2
SN 2009en	2009−05−08	221.5940	13.0242	0.0467	0.020	Ia-norm	2	...	...	...
SN 2009ep	2009−05−11	208.0440	2.3242	0.0237	0.025	Ia-norm	2	...	...	...
SN 2009eq	2009−05−11	280.0350	40.1268	0.0236	0.053	Ia*	3	...	...	...
SN 2009ew	2009−05−16	249.7490	17.9828	...	0.062	Ia-norm	2	...	...	...
SN 2009eu	2009−05−21	247.1710	39.5535	0.0304	0.010	Ia-norm	1	−4.8	...	1
SN 2009ft	2009−05−23	216.0250	7.7695	0.0568	0.021	Ia-norm	1	...	...	...
SN 2009fx	2009−05−29	253.2970	23.9653	0.0477	0.049	Ia-norm	1	...	...	...
SN 2009fl	2009−05−30	246.2920	40.8891	0.0294	0.007	Ia-norm	2	...	...	...
SN 2009fu	2009−06−01	33.0375	44.5653	0.0171	0.076	Ia-norm	1	...	...	...
SN 2009fy	2009−06−01	351.0210	16.6641	0.0410	0.028	Ia-norm	2	...	...	...
SN 2009fv	2009−06−02	247.4340	40.8116	0.0293	0.005	Ia-norm	3	3.8	16.4	1
SN 2009gq	2009−06−02	333.7200	17.5131	0.0670†(c)	0.037	Ia-norm	1	...	...	...
SN 2009fw	2009−06−06	308.0770	−19.7332	0.0282	0.050	Ia-norm	4	5.3	17.9	2
SN 2009gf	2009−06−15	213.9050	14.2802	0.0185	0.022	Ia-norm	3	...	...	...
SN 2009gs	2009−06−15	319.7060	−5.9530	...	0.102	Ia-norm	3	...	...	...
SN 2009he	2009−07−03	245.5510	57.2729	0.0306	0.008	Ia-91bg	1	...	...	...
SN 2009hi	2009−07−10	350.9840	16.7749	0.0411	0.026	Ia-norm	3	...	...	...
SN 2009hk	2009−07−11	309.6560	−25.1156	0.0180†(c)	0.038	Ia	1	...	...	...
SN 2009hl	2009−07−11	262.7920	36.4278	0.0494†(d)	0.030	Ia-norm	2	...	...	...
SN 2009hn	2009−07−24	38.0013	1.2482	0.0220	0.021	Ia-norm	1	...	...	...
SN 2009ho	2009−07−25	37.1389	37.9511	...	0.049	Ia	1	...	...	...
SN 2009hp	2009−07−26	44.5998	6.5931	0.0211	0.198	Ia-norm	1	...	...	...
SN 2009hs	2009−07−28	268.9620	62.5998	0.0275	0.035	Ia	1	8.6	...	1
SN 2009hr	2009−07−29	10.1422	3.5414	0.0170†(c)	0.022	Ia-norm	1	...	...	...
PTF 09dlc	2009−08−17	326.6250	6.4192	0.0672†(p)	0.047	Ia-norm	2	−2.3	18.2	5
SN 2009jb	2009−08−17	260.9240	30.4971	0.0237†(p)	0.037	Ia-norm	3	...	...	...
PTF 09dnp	2009−08−18	229.8520	49.4990	0.0376†(p)	0.016	Ia-norm	2	...	...	...
SN 2009ig	2009−08−20	39.5484	−1.3125	0.0088	0.028	Ia-norm	16	−13.8	160.3	1
SN 2009ih	2009−08−21	238.8790	41.9483	0.0329	0.015	Ia-91bg	1	...	...	...
SN 2009ix	2009−09−08	49.4709	40.9589	...	0.128	Ia-norm	2	...	...	...
SN 2009jg	2009−09−22	265.1430	18.7137	...	0.062	Ia-norm	1	...	...	...
SN 2009jr	2009−10−08	306.6080	2.9092	0.0165	0.116	Ia-99aa	2	−3.6	5.3	2
SN 2009jp	2009−10−09	349.4280	13.9569	0.0550†(c)	0.040	Ia-norm	1	...	...	...
SN 2009kk	2009−10−15	57.4345	−3.2644	0.0129	0.118	Ia-norm	2	−0.4	19.4	2
SN 2009ko	2009−10−28	120.4930	15.0596	0.0162	0.028	Ia-norm	2	...	...	...
SN 2009kq	2009−11−05	129.0630	28.0671	0.0117	0.035	Ia-norm	4	−9.2	28.4	1
SN 2009lg	2009−11−10	354.7080	28.2651	0.0580	0.165	Ia-norm	1	...	...	...
SN 2009le	2009−11−16	32.3214	−23.4124	0.0178	0.014	Ia-norm	1	17.5	...	2
SN 2009li	2009−11−16	5.7142	6.9699	0.0404	0.023	Ia-norm	1	...	...	...
SN 2009lv	2009−11−19	4.1107	22.4361	...	0.059	Ia-norm	2	...	...	...
SN 2009lu	2009−11−20	163.5870	−4.3442	0.0215	0.026	Ia-norm	1	...	...	...
SN 2009lr	2009−11−23	348.5600	−2.7533	...	0.041	Ia	2	...	...	...
SN 2009me	2009−12−03	182.4160	43.6750	...	0.012	Ia-norm	2	...	...	...
SN 2009mj	2009−12−10	103.3010	44.0713	0.0196	0.092	Iax	1	...	...	...
SN 2009mh	2009−12−12	175.9830	10.7820	0.0197	0.038	Ia	1	...	...	...
SN 2009mv	2009−12−16	108.9160	35.2412	...	0.053	Ia-norm	1	...	...	...
SN 2009nr	2009−12−22	197.7460	11.4915	0.0112	0.022	Ia-norm	3	11.6	129.3	6

Table 3.6 continued

SN Name	Discovery Date (UT)	R.A. α(2000)	Decl. δ(2000)	$z_{\rm helio}$[a]	$E(B-V)_{\rm MW}$[b] (mag)	SNID[c] (sub)type	# of Spectra	First[d] Epoch	Last[d] Epoch	$\rm MJD_{max}$[e] Reference
SN 2009mz	2009−12−26	210.8530	−6.0587	0.0086	0.024	Ia-norm	2	...	...	...
SN 2009na	2009−12−26	161.7560	26.5439	0.0210	0.028	Ia-norm	3	3.0	39.4	2
SN 2009nq	2009−12−28	348.8210	19.0229	0.0158	0.125	Ia-norm	1	...	...	...
SN 2009nk	2009−12−29	212.7450	6.3633	0.0196	0.023	Ia-norm	2	...	...	...
SN 2010A	2010−01−04	38.1644	0.6195	0.0207	0.025	Ia-99aa	1	...	...	...
SN 2010B	2010−01−07	208.5370	60.6804	0.0102	0.011	Ia-norm	4	...	...	...
SN 2010N	2010−01−12	197.2720	17.0729	0.0210†(c)	0.019	Ia-norm	2	...	...	...
SN 2010H	2010−01−16	121.6020	1.0359	0.0154	0.026	Ia-norm	3	...	...	...
SN 2010V	2010−02−04	217.1600	30.6360	0.0129†(d)	0.019	Ia-norm	3	...	...	...
SN 2010Y	2010−02−08	162.7660	65.7797	0.0109	0.011	Ia-norm	4	−6.4	22.3	2
SN 2010p1	2010−02−12	160.6750	58.8438	0.0313	0.007	Ia-norm	2	...	...	...
SN 2010ag	2010−03−05	255.9730	31.5017	0.0337	0.026	Ia	3	0.3	58.3	2
SN 2010ai	2010−03−08	194.8500	27.9964	0.0193†(d)	0.008	Ia-norm	1	−6.4	...	2
SN 2010an	2010−03−11	244.4190	35.0028	0.0295	0.020	Ia-norm	3	...	...	...
SN 2010au	2010−03−15	138.1520	34.8547	0.0615	0.018	Ia-norm	2	...	...	...
SN 2010ax	2010−03−15	220.4730	10.7504	0.0508	0.024	Ia-norm	1	...	...	...
SN 2010ao	2010−03−18	205.9210	3.9000	0.0228	0.023	Ia-norm	1	−11.1	...	1
SN 2010at	2010−03−19	181.2480	76.1312	0.0418	0.073	Ia	1	...	...	...
SN 2010ba	2010−03−21	179.5860	15.3363	...	0.037	Ia-norm	3	...	...	...
SN 2010bn	2010−04−05	176.2320	−5.0789	0.0530†(c)	0.019	Ia-norm	1	...	...	...
SN 2010bu	2010−04−09	235.7430	2.2813	0.0390†(c)	0.064	Ia-norm	2	...	...	...
SN 2010cp	2010−05−09	195.1080	−15.2889	0.0164	0.049	Ia-91bg	1	...	...	...
SN 2010cs	2010−05−12	221.9820	19.0549	0.0419	0.029	Ia-norm	1	...	...	...
SN 2010cr	2010−05−15	202.3540	11.7962	0.0216	0.030	Ia-norm	2	8.2	15.0	2
SN 2010dl	2010−05−24	323.7540	−0.5133	0.0300	0.033	Ia-norm	1	18.1	...	2
SN 2010eb	2010−06−12	20.4074	5.2944	0.0076	0.026	Ia-norm	1	...	...	...
SN 2010gj	2010−07−10	327.7260	−17.7693	0.0370†(c)	0.047	Ia	1	...	...	...
SN 2010gl	2010−07−18	247.9110	59.6239	0.0188	0.013	Ia-norm	2	...	...	...
SN 2010gv	2010−08−09	269.5940	50.7928	...	0.040	Ia	1	...	...	...
SN 2010gz	2010−08−16	23.2128	−12.1893	0.0184	0.021	Ia-norm	1	...	...	...
SN 2010hh	2010−09−01	269.8270	45.8756	0.0190	0.033	Ia-91bg	1	...	...	...
SN 2010hz	2010−09−12	28.4249	29.9346	0.0255	0.047	Ia-norm	1	...	...	...
SN 2010ii	2010−09−30	339.5550	35.4917	0.0269	0.075	Ia-norm	2	...	...	...
SN 2010iw	2010−10−14	131.3130	27.8227	0.0215	0.047	Ia-norm	1	10.4	...	2
SN 2010ju	2010−11−14	85.4833	18.4975	0.0152	0.361	Ia-norm	2	6.1	19.9	1
SN 2010kg	2010−11−29	70.0350	7.3500	0.0166	0.134	Ia-norm	2	−13.0	0.8	2
SN 2011H	2011−01−04	35.7751	43.0423	0.0220	0.073	Ia-norm	1	...	...	...
SN 2011K	2011−01−13	71.3766	−7.3480	0.0145†(d)	0.088	Ia-norm	1	9.1	...	2
SN 2011U	2011−01−28	63.3914	27.5435	0.0134	0.593	Ia-norm	1	...	...	...
SN 2011ao	2011−03−03	178.4630	33.3628	0.0107	0.017	Ia-norm	3	−8.7	37.6	2
SN 2011ay	2011−03−18	105.6420	50.5903	0.0210	0.072	Iax	9	...	...	...
SN 2011by	2011−04−26	178.9400	55.3261	0.0028	0.012	Ia-norm	11	−11.1	310.3	1
SN 2011dm	2011−06−15	329.1730	73.2969	0.0049	0.519	Ia-norm	1	...	...	...
SN 2011dn	2011−06−21	299.6480	2.6045	0.0253	0.151	Ia-pec	1	...	...	...
SN 2011fg	2011−08−20	350.8360	16.7948	0.0450†(d)	0.023	Ia-norm	2	...	...	...
SN 2011fe	2011−08−24	210.7740	54.2737	0.0008	0.008	Ia-norm	17	−17.2	378.5	1
SN 2011fk	2011−08−29	13.6753	36.7643	0.0201	0.048	Ia	1	...	...	...
SN 2011fs	2011−09−15	334.3310	35.5806	0.0209	0.101	Ia-99aa	3	−2.6	25.8	1
SN 2011gy	2011−10−22	52.3971	40.8676	0.0169†(d)	0.166	Ia-norm	1	...	...	...
SN 2011hb	2011−10−24	351.9810	8.7794	0.0289†(d)	0.051	Ia-norm	1	...	...	...
SN 2011iv	2011−12−02	54.7140	−35.5922	0.0065	0.010	Ia-norm	2	...	...	...
SN 2011jh	2011−12−22	191.8100	−10.0631	0.0078	0.032	Ia-norm	3	...	...	...
SN 2011jr	2011−12−25	106.6660	23.8936	0.0226	0.052	Ia-norm	2	...	...	...
SN 2011jn	2011−12−26	194.3120	−17.4001	0.0475†(d)	0.059	Ia-norm	1	...	...	...
SN 2011jt	2011−12−31	223.3460	2.9620	0.0278†(d)	0.039	Ia-norm	2	...	...	...
SN 2012B	2012−01−08	57.8938	37.0785	0.0173†(d)	0.271	Ia-norm	1	...	...	...
SN 2012E	2012−01−14	38.3450	9.5849	0.0203	0.063	Ia-norm	1	−4.3	...	1
SN 2012Z	2012−01−29	50.5223	−15.3877	0.0071	0.034	Iax	4	−7.6	35.1	1
SN 2012c1	2012−03−27	166.3340	−1.8681	0.0908	0.047	Ia-csm	2	...	...	...
SN 2012cg	2012−05−17	186.8030	9.4203	0.0015	0.018	Ia-norm	10	−16.4	46.5	1
SN 2012cu	2012−06−14	193.3720	2.1608	0.0035	0.023	Ia-norm	3	...	...	...
SN 2012de	2012−06−25	333.7720	10.3035	...	0.062	Ia-norm	1	...	...	...
SN 2012dn	2012−07−08	305.9010	−28.2787	0.0102†(d)	0.052	Ia-norm	2	−14.6	−9.6	1
SN 2012dv	2012−07−18	327.1260	−12.8392	0.0700	0.037	Ia-norm	1	...	...	...
SN 2012ea	2012−08−08	266.2930	18.1408	0.0102	0.055	Ia	2	−6.8	29.8	1
PTF 12ild	2012−09−06	338.2420	−0.2152	0.1723	0.051	Ia-norm	1	...	...	...
PTF 12irf	2012−09−15	30.5316	0.1838	0.1921	0.020	Ia	1	...	...	...
LSQ 12fhe	2012−10−02	323.0390	−5.7260	0.0275	0.062	Ia*	1	...	...	...
SN 2012fr	2012−10−27	53.4000	−36.1271	0.0055	0.018	Ia-norm	9	−6.1	92.1	7
SN 2012gl	2012−10−29	153.2100	12.6824	0.0094	0.036	Ia-norm	1	...	...	...

Table 3.6 continued

SN Name	Discovery Date (UT)	R.A. α(2000)	Decl. δ(2000)	$z_{\rm helio}$[a]	$E(B-V)_{\rm MW}$[b] (mag)	SNID[c] (sub)type	# of Spectra	First[d] Epoch	Last[d] Epoch	$\rm MJD^{e}_{max}$ Reference
SN 2012gx	2012−11−18	9.5073	−13.8610	0.0140†(d)	0.019	Ia-norm	1	...	...	...
SN 2012ht	2012−12−18	163.3450	16.7764	0.0036	0.025	Ia-norm	13	1.9	128.2	8
SN 2012ij	2012−12−29	175.0660	17.4562	0.0110†(d)	0.023	Ia-91bg	4	...	...	...
SN 2013E	2013−01−04	150.0230	−34.2337	0.0094	0.084	Ia-norm	5	...	...	...
SN 2013Q	2013−01−25	356.7830	29.4865	0.0172	0.085	Ia-norm	2	...	...	...
SN 2013S	2013−01−25	53.8762	38.2832	0.0186†(d)	0.305	Ia-99aa	1	...	...	...
SN 2013gq	2013−03−25	124.4730	23.4696	0.0139	0.049	Ia-norm	4	1.1	16.7	1
SN 2013ct	2013−05−10	18.2288	0.9794	0.0038	0.024	Ia	1	...	...	...
SN 2013dj	2013−06−10	251.5080	6.4665	0.0253	0.063	Ia-91T	1	...	...	...
SN 2013dh	2013−06−12	232.5050	12.9869	0.0134	0.033	Ia	4	−5.7	19.1	1
SN 2013di	2013−06−12	339.1140	21.6151	0.0238	0.040	Ia-norm	2	...	...	...
SN 2013dy	2013−07−10	334.5730	40.5693	0.0039	0.132	Ia-norm	14	−11.7	422.2	1
SN 2013gh	2013−08−08	330.5910	−18.9168	0.0088	0.025	Ia*	3	−11.8	392.2	1
SN 2013fa	2013−08−25	310.9730	12.5144	0.0155	0.086	Ia-norm	1	2.0	...	1
SN 2013fw	2013−10−21	318.4370	13.5759	0.0170	0.067	Ia*	1	347.3	...	1
SN 2013gs	2013−11−29	142.7870	46.3848	0.0169	0.017	Ia-norm	1	...	...	...
SN 2013gy	2013−12−06	55.5703	−4.7218	0.0140	0.050	Ia-norm	3	5.6	271.8	1
PSN J03055989+0432382	2013−12−21	46.4995	4.5439	...	0.146	Ia-norm	1	...	...	...
SN 2013hs	2013−12−25	29.7237	5.5904	0.0194	0.036	Ia-norm	1	...	...	...
SN 2014J	2014−01−21	148.9260	69.6739	0.0007	0.136	Ia-norm	10	33.9	291.6	1
SN 2014ag	2014−03−11	247.6690	44.5096	0.0317	0.011	Ia	1	...	...	...
SN 2014ao	2014−04−17	128.6390	−2.5434	0.0141	0.031	Ia-norm	1	10.3	...	1
ASASSN 14ar	2014−04−24	137.4240	37.6018	0.0230	0.017	Ia-norm	1	...	...	...
SN 2014ck	2014−06−29	341.4120	73.1619	0.0050†(d)	0.394	Iax	2	...	...	...
SN 2014da	2014−08−07	7.3130	2.8660	0.0141†(d)	0.025	Ia-91bg	1	...	...	...
ASASSN 14gh	2014−08−28	258.7890	41.8109	0.0044†(d)	0.023	Ia-norm	1	...	...	...
SN 2014dg	2014−09−11	57.0824	70.1318	0.0040†(d)	0.628	Ia-norm	11	...	...	...
SN 2014dl	2014−09−25	247.4420	8.6418	0.0330	0.054	Ia-91T	1	...	...	...
SN 2014dm	2014−09−27	62.0297	−8.8270	0.0330†(d)	0.041	Ia-norm	1	...	...	...
SN 2014dt	2014−10−29	185.4900	4.4718	0.0052	0.019	Iax	13	...	...	...
PSN J03034759+0024146	2014−11−17	45.9483	0.4041	0.0430	0.073	Ia-norm	1	...	...	...
iPTF 14jfw	2014−11−23	137.5080	52.3157	...	0.011	Ia-norm	1	...	...	...
ASASSN 14lp	2014−12−09	191.2880	0.4590	0.0052	0.014	Ia-norm	15	−0.8	175.1	9
Gaia 15aba	2015−02−06	240.8760	52.2607	0.0460†(d)	0.015	Ia-norm	1	...	...	...
Gaia 15abu	2015−02−09	256.2090	41.0179	0.0750†(d)	0.024	Ia-norm	1	...	...	...
SNHunt 276	2015−02−10	177.4950	21.3172	0.0261	0.025	Ia-91bg	1	...	...	...
SN 2015H	2015−02−10	163.6760	−21.0705	0.0125	0.047	Iax	1	...	...	...
Gaia 15aby	2015−02−11	214.8040	10.7169	0.0790†(d)	0.026	Ia-norm	1	...	...	...
PSN J13471211−2422171	2015−02−12	206.8000	−24.3714	0.0190	0.064	Ia-norm	1	...	...	...
ASASSN 15db	2015−02−15	236.7450	17.8840	0.0113	0.029	Ia-norm	1	...	...	...
SNHunt 281	2015−03−16	226.3670	1.6350	0.0041	0.045	Ia-norm	3	−5.3	20.5	10
ASASSN 15fr	2015−03−24	140.0850	−7.6408	0.0334†(d)	0.033	Ia-norm	1	...	...	...
ASASSN 15hy	2015−04−25	302.5100	0.7392	0.0250†(d)	0.105	Ia-norm	12	−13.4	152.2	3
ASASSN 15jm	2015−05−19	260.2880	25.5821	...	0.056	Ia-csm	1	...	...	...
iPTF 15awr	2015−05−25	225.3300	16.7800	...	0.036	Ia-norm	1	...	...	...
ASASSN 15kx	2015−06−10	334.0490	37.4739	0.0182	0.141	Ia-norm	3	31.3	121.3	3
ASASSN 15lo	2015−06−19	343.3910	19.7084	...	0.056	Ia-norm	1	...	...	...
ASASSN 15lu	2015−06−20	200.3040	40.2658	0.0350	0.014	Ia-norm	1	−2.2	...	3
ASASSN 15mc	2015−07−05	42.2482	3.1696	0.0138	0.052	Ia-norm	3	...	...	...
SN 2015N	2015−07−06	325.8200	43.5799	0.0149	0.456	Ia-norm	11	−5.3	82.2	1
ASASSN 15mi	2015−07−06	210.8160	41.6040	0.0344†(d)	0.018	Ia-99aa	1	2.0	...	3
ASASSN 15mg	2015−07−09	233.0950	41.8499	0.0428†(d)	0.028	Ia-norm	8	−0.7	83.3	3
ASASSN 15mp	2015−07−17	14.6886	−14.0699	0.0370†(d)	0.020	Ia-99aa	1	...	...	...
SN 2015ac	2015−07−28	349.1810	33.9966	0.0168	0.062	Ia	1	...	...	...
ASASSN 15ns	2015−08−06	250.1170	39.3202	0.0307	0.011	Ia	1	...	...	...
ASASSN 15og	2015−08−13	50.2810	−31.3127	0.0681†(d)	0.011	Ia-csm	7	...	...	...
PS 15cut	2015−09−10	358.1550	14.5526	0.0266	0.036	Ia-norm	1	...	...	...
PSN J02524671+4656470	2015−09−12	43.1946	46.9464	0.0281	0.170	Ia-norm	1	...	...	...
ASASSN 15pr	2015−09−13	346.6650	−12.5729	0.0331†(d)	0.029	Ia-norm	1	31.2	...	3
ASASSN 15qc	2015−10−01	9.8249	3.9500	0.0176	0.022	Ia-norm	1	...	...	...
MOT J041227.87+342902.0	2015−10−06	63.1161	34.4839	0.0214	0.312	Ia-norm	1	...	...	...
PS 15cku	2015−10−16	21.0939	3.5876	0.0230†(d)	0.023	Ia-norm	1	−3.8	...	3
ASASSN 15rm	2015−10−19	94.0160	−16.8249	0.0208	0.147	Ia-norm	1	...	...	...
ASASSN 15rw	2015−10−24	33.9923	12.2374	0.0189†(d)	0.118	Ia-norm	1	15.6	...	3
ASASSN 15sf	2015−10−30	2.8650	−6.4273	0.0270†(d)	0.026	Ia-norm	2	3.9	10.6	3
PS 16ud	2015−11−01	166.7820	−5.3789	0.0373	0.063	Ia-norm	1	...	...	...
ASASSN 15so	2015−11−08	168.5460	48.3187	0.0067	0.013	Ia-norm	2	−7.7	27.0	3
PSN J09100885+5003396	2015−11−08	137.5370	50.0610	0.0343	0.017	Ia-norm	7	...	...	...
PS 15cwx	2015−11−17	78.6992	7.0504	0.0460†(d)	0.149	Ia-99aa	1	−3.0	...	3

Table 3.6 continued

SN Name	Discovery Date (UT)	R.A. α(2000)	Decl. δ(2000)	$z_{\rm helio}$[a]	$E(B-V)_{\rm MW}$[b] (mag)	SNID[c] (sub)type	# of Spectra	First[d] Epoch	Last[d] Epoch	$\rm MJD_{max}$[e] Reference
SN 2015bd	2015−12−07	170.9410	−1.1059	0.0187	0.046	Ia-norm	5	...	...	...
PSN J12265018+1615496	2015−12−07	186.7090	16.2638	0.0455†(d)	0.021	Ia-norm	1	...	...	...
ASASSN 15ub	2015−12−14	166.8040	65.0995	0.0320†(d)	0.014	Ia-norm	2	...	...	...
SN 2016F	2016−01−04	24.8835	33.8267	0.0161†(d)	0.042	Ia	1	22.3	...	3
SN 2016zc	2016−01−28	211.4880	43.8839	0.0337†(d)	0.006	Ia-norm	1	...	...	...
SN 2016aqt	2016−02−28	206.4610	26.7965	...	0.015	Ia-norm	3	...	...	3
SN 2016blh	2016−03−31	212.4190	0.6567	0.0238†(t)	0.032	Ia-norm	1	1.4	...	3
SN 2016bln	2016−04−04	203.6900	13.8540	0.0233	0.025	Ia-norm	3	−4.0	24.2	3
SN 2016bsa	2016−04−22	331.1480	42.3257	0.0143	0.273	Ia-norm	1	...	...	...
SN 2016ccj	2016−05−03	257.6000	26.3966	0.0418†(d)	0.029	Ia-norm	1	110.5	...	3
SN 2016cmn	2016−05−20	277.5100	39.9655	0.0183	0.053	Ia-norm	1	...	...	...
SN 2016coj	2016−05−28	182.0280	65.1773	0.0045	0.016	Ia-norm	20	−11.4	147.1	1
SN 2016flv	2016−08−27	341.3750	−7.3353	0.0530†(t)	0.035	Ia-norm	2	...	...	...
SN 2016hvl	2016−11−04	101.0090	12.3966	0.0130†(t)	0.377	Ia	2	16.6	104.5	1
SN 2016ije	2016−11−22	29.6264	12.9244	...	0.045	Ia-91bg	1	...	...	...
SN 2017cfd	2017−03−16	130.2050	73.4875	0.0119	0.019	Ia-norm	4	3.9	61.1	1
SN 2017drh	2017−05−03	263.1090	7.0632	0.0056	0.106	Ia-norm	7	2.5	101.9	1
SN 2017dws	2017−05−03	235.0590	11.3449	0.0818†(t)	0.035	Ia-norm	1	7.7	...	1
SN 2017dwp	2017−05−04	187.9320	36.2097	0.0334	0.010	Ia*	3	...	...	...
SN 2017erp	2017−06−13	227.3120	−11.3342	0.0063	0.093	Ia-norm	16	−9.6	75.8	1
SN 2017fgc	2017−07−11	20.0602	3.4028	0.0081	0.029	Ia-norm	11	−3.3	99.8	1
SN 2017glx	2017−09−03	295.9180	56.1101	0.0114	0.107	Ia-norm	4	2.0	41.5	1
SN 2017hbi	2017−10−02	38.1315	35.4836	...	0.061	Ia-norm	5	...	...	1
SN 2017hou	2017−10−24	62.2589	−1.1601	0.0167	0.108	Ia-norm	3	...	...	...
SN 2017hpa	2017−10−25	69.9615	7.0652	0.0156	0.154	Ia-norm	5	...	...	...
SN 2017igr	2017−11−18	64.6815	26.9314	0.0250	0.571	Ia	1	...	...	...
SN 2017iji	2017−11−20	183.1130	29.1493	0.0135	0.018	Ia-norm	3	...	...	...
SN 2017iws	2017−12−12	130.6730	13.9678	0.0910†(w)	0.027	Ia-norm	1	...	...	...
SN 2017ixg	2017−12−14	350.1270	24.7776	0.0277†(w)	0.076	Ia-norm	2	...	...	...
SN 2018gl	2018−01−13	149.5260	10.3594	0.0180	0.033	Ia-norm	1	...	...	...
SN 2018gv	2018−01−15	121.3940	−11.4379	0.0053	0.050	Ia-norm	1	8.7	...	1
SN 2018pc	2018−02−03	142.2300	49.2381	0.0090	0.012	Ia-norm	1	...	...	...
SN 2018pv	2018−02−03	178.2320	36.9866	0.0031	0.018	Ia	1	...	...	...
SN 2018oh	2018−02−04	136.6650	19.3383	0.0110	0.039	Ia-norm	1	...	...	...
SN 2018aae	2018−02−06	185.3920	55.5743	0.0290†(d)	0.010	Ia-norm	1	...	...	...
SN 2018aoz	2018−04−02	177.7580	−28.7441	0.0058	0.072	Ia-norm	1	37.7	...	1
SN 2018bsn	2018−05−14	224.3700	5.8425	0.0590	0.031	Ia-norm	1	...	...	...
SN 2018cni	2018−06−13	225.3450	−10.1805	0.0320†(t)	0.087	Iax	1	...	...	...
SN 2018eqq	2018−08−03	46.7298	41.5091	0.0160†(t)	0.127	Ia	1	...	...	...
SN 2018feb	2018−08−16	257.5470	21.6490	0.0148†(t)	0.052	Ia-norm	6	...	...	...
SN 2018hfp	2018−10−07	314.9490	−16.6369	0.0291	0.063	Ia-norm	3	...	...	...
SN 2018hfr	2018−10−10	142.7300	−4.5712	0.0226	0.024	Ia-91T	3	...	...	...
SN 2018hhn	2018−10−13	343.1340	11.6741	0.0288	0.061	Ia-norm	3	...	...	...
SN 2018htt	2018−10−31	46.5121	−15.6116	0.0087†(t)	0.032	Ia-norm	1	...	...	...
SN 2018hzg	2018−11−06	175.5980	10.2644	0.0216	0.049	Ia	1	...	...	...
SN 2018jaz	2018−11−20	204.8340	34.6888	0.0231†(t)	0.009	Ia	1	...	...	...

[a]Host-galaxy heliocentric redshifts are from NED unless marked with a "†" symbol, in which case they are collected using the Open Supernova Catalog (Guillochon et al. 2017) from the following sources: (c) the supernova catalog of Lennarz et al. (2012b), (p) the spectroscopic host-galaxy observations of PTF SNe Ia described by Pan et al. (2014), (t) the TNS, (w) the Weizmann Interactive Supernova Data Repository Yaron and Gal-Yam (WISeREP 2012), or (d) the appropriate discovery or classification announcement (e.g., CBET or IAUC).

[b]Extinction is calculated at the SN position using the dust maps of Schlegel et al. (1998) subject to the recalibration of Schlafly and Finkbeiner (2011).

[c]SN classifications are derived from our SNID classification scheme, as described in Section 3.3. Based on the arguments made by Foley et al. (2013a), we have relabeled all SNe Ia with a "Ia-02cx" subtype as "Iax".

[d]First and last observation epochs are in rest-frame days relative to the time of B-band maximum brightness, and are computed using information from the table.

[e]References for the light-curve-determined MJD corresponding to B-band maximum brightness are as follows: (1) S19, (2) Friedman et al. (2015) and references therein, (3) Foley et al. (2018), (4) Krisciunas et al. (2017), (5) Maguire et al. (2014), (6) Khan et al. (2011), (7) Zhang et al. (2014), (8) Yamanaka et al. (2014), (9) Shappee et al. (2016), and (10) Srivastav et al. (2017).

Chapter 4

deepSIP: Linking Type Ia Supernova Spectra to Photometric Quantities with Deep Learning

A version of this chapter was originally published in *The Monthly Notices of the Royal Astronomical Society* (Stahl et al. 2020a).

Chapter Abstract

We present `deepSIP` (deep learning of Supernova Ia Parameters), a software package for measuring the phase and — for the first time using deep learning — the light-curve shape of a Type Ia supernova (SN Ia) from an optical spectrum. At its core, `deepSIP` consists of three convolutional neural networks trained on a substantial fraction of all publicly-available low-redshift SN Ia optical spectra, onto which we have carefully coupled photometrically-derived quantities. We describe the accumulation of our spectroscopic and photometric datasets, the cuts taken to ensure quality, and our standardised technique for fitting light curves. These considerations yield a compilation of 2754 spectra with photometrically characterised phases and light-curve shapes. Though such a sample is significant in the SN community, it is small by deep-learning standards where networks routinely have millions or even billions of free parameters. We therefore introduce a data-augmentation strategy that meaningfully increases the size of the subset we allocate for training while prioritising model robustness and telescope agnosticism. We demonstrate the effectiveness of our models by deploying them on a sample unseen during training and hyperparameter selection, finding that Model I identifies spectra that have a phase between -10 and 18 d and light-curve shape, parameterised by Δm_{15}, between 0.85 and 1.55 mag with an accuracy of 94.6%. For those spectra that do fall within the aforementioned region in phase–Δm_{15} space, Model II predicts phases with a root-mean-square error (RMSE) of 1.00 d and Model III predicts Δm_{15} values with an RMSE of 0.068 mag.

4.1 Introduction

The optical spectra of Type Ia supernovae (SNe Ia) are rich with information (for a review, see, e.g., Filippenko 1997). In addition to probing ejecta dynamics and chemical composition, spectral features have been found to encode the phase of a SN Ia in its temporal evolution (e.g., Riess et al. 1997c; Foley et al. 2005b; Howell et al. 2005; Blondin and Tonry 2007; Muthukrishna et al. 2019b), and to a somewhat less quantitatively formalised extent, its peak luminosity (Nugent et al. 1995; Arsenijevic et al. 2008; Bailey et al. 2009; Blondin et al. 2011; Silverman et al. 2012c; Zheng et al. 2018b; Siebert et al. 2019). The ability to extract the former (henceforth, the "phase") and the latter (or something that correlates with it via a width-luminosity relation, such as Δm_{15} or Δ; Phillips 1993; Riess et al. 1996, respectively) from optical spectra is of particular significance because both are conventionally derived from photometry. As the requisite light curves must consist of numerous individual observations conducted over at least several weeks, the ability to measure the aforementioned quantities from perhaps just a single observation (i.e., a spectrum) is of great value when allocating limited observing resources to optimise for specific science goals.

The SuperNova IDentification code (`SNID`; Blondin and Tonry 2007) has become the *de facto*[1] tool for classifying the type and phase of a SN from spectra, though alternatives do exist (e.g., `Superfit`; Howell et al. 2005). To determine the phase of a SN Ia, such conventional approaches compare[2] an input spectrum to a large database of spectra with known phases and then perform an aggregation of the phases from the best-matching templates. This approach has the advantage of being easy to understand ("SN X is most similar to SN Y at Z days relative to maximum brightness"), but it has the disadvantage of being inherently slow — prediction time scales linearly with the number of template spectra in the database.

Machine learning (ML; see Ivezić et al. 2014, for an overview of use cases in astronomy) provides an interesting and fundamentally different approach to these tasks. In particular, phase and light-curve-shape determination can both be treated within the "supervised learning" paradigm, where a robust mapping between inputs and outputs is derived from a training set of input-output pairs. Subject to passing user-defined efficacy criteria when applied to a distinct testing set, the derived map can then be deployed to characterise new, unseen data. This approach leads to predictions that are fast (i.e., based on features themselves instead of comparisons against a large database) and therefore scalable. Accordingly, supervised ML has become increasingly prevalent in astronomical research campaigns (e.g., Bloom et al. 2012b; Masci et al. 2014; Goldstein et al. 2015; Wright et al. 2015; Miller et al. 2017; Kim and Brunner 2017; Zhang and Bloom 2020).

Indeed, ML has proven to be a viable approach to photometric SN classification (e.g., Richards et al. 2012; Möller et al. 2016; Lochner et al. 2016; Charnock and Moss 2017; Narayan et al. 2018; Muthukrishna et al. 2019a), but only several studies thus far have applied such techniques to SN spectra. Sasdelli et al. (2016) use *unsupervised* ML techniques

[1] As assessed from its prevalence in spectroscopic classifications issued by the Central Bureau of Electronic Telegrams (CBET) and in International Astronomical Union Circulars (IAUCs).

[2] `SNID` uses cross-correlation (Tonry and Davis 1979) for comparison while `Superfit` uses χ^2 minimisation.

to explore the spectroscopic diversity of SNe Ia, and find that much of the spectral variability, including that of the peculiar SN 1991bg-like (Filippenko et al. 1992a; Leibundgut et al. 1993) and SN 2002cx-like (now known as the distinct "SN Iax" class; Filippenko 2003; Li et al. 2003; Foley et al. 2013b) objects, can be parameterised by a carefully constructed five-dimensional space. As a much faster alternative to the aforementioned template-matching options (i.e., `SNID`, `Superfit`), Muthukrishna et al. (2019b) have used a deep convolutional neural network (CNN; see, e.g., LeCun et al. 2015) to develop `DASH`, a software package that classifies the type, phase, redshift, and host galaxy (but *not* light-curve shape) of a supernova from optical spectra.

Motivated by this and the well-documented ability of CNNs to extract representative low-dimensional features from input signals, we formulate our approach as a set of three models, each of which utilises a similar CNN architecture to (Model I) determine if an input spectrum belongs to a SN Ia within a specific domain in a space defined by phase and light-curve shape, (Model II) calculate the phase if it is within the domain, and (Model III) calculate a measure of the light-curve shape (Δm_{15}; Burns et al. 2011) if the same criterion is met. Although Model II shares a common objective and architectural elements with `DASH` (i.e., phase determination via a CNN architecture), we optimise specifically for SNe Ia that fall within certain thresholds, treat the problem as one of *regression* (not classification), and utilise dropout variational inference as a method by which to model uncertainties (Gal and Ghahramani 2015; Leung and Bovy 2019). Moreover, our development of a CNN to predict the light-curve shape of a SN Ia from its spectrum is novel.

We use the following sections to present the development of the aforementioned models. Section 6.2 details the accumulation of our dataset, including how we process and prepare spectra for ingestion by our models. We outline our model architecture and discuss training and hyperparameter selection procedures in Section 4.3, and we provide model-specific results in Section 6.4. Concluding remarks are then given in Section 6.5.

4.2 Data

4.2.1 Spectra

We source the spectra used herein from the three largest low-redshift SN Ia spectral datasets currently in existence: the Berkeley SuperNova Ia Program (BSNIP; Silverman et al. 2012a; Stahl et al. 2020b, henceforth S12 and S20, respectively) sample with a total of 1935 spectra covering the period from 1989 through 2018 (see S12 for 1989–2008 and S20 for 2009–2018), the Harvard-Smithsonian Center for Astrophysics (CfA) sample with a total of 2603 spectra from observations spanning 1993–2008 (Blondin et al. 2012), and the Carnegie Supernova Program (CSP) sample with 630 spectra observed in the range 2004–2009 (Folatelli et al. 2013). From this initial compilation of 5168 spectra, we perform two modest "usability" cuts that reduce our sample to 4941 (these cuts, in addition to those that are introduced below, are outlined in Figure 6.1). First, we drop the small fraction without a redshift listed in their

associated publication, thereby yielding 5110 spectra, and second, we remove a further 169 that lack full coverage[3] of the Si II λ6355 feature that is ubiquitous in near-maximum-light SN Ia spectra.

In addition to the high quality and sheer size of these datasets, the BSNIP and CfA sets were specifically selected for their complementarity — whereas the observing strategy employed by the BSNIP is generally to prioritise the total number of SNe observed instead of the number of spectra *per* SN, the CfA dataset covers fewer SNe but with higher cadence. This is clearly seen in the distribution of the number of spectra per SN in the top panel of Figure 4.2: the BSNIP sample spans many more SNe with several observations than does the CfA (or CSP) sample, but beyond ~ 6 spectra per object, the CfA sample wins out. Together, then, these datasets offer comprehensive coverage of the spectral diversity of SNe Ia at both the individual and population levels.

We show the distribution of blue (red) wavelength limits for the spectra in our compilation in the lower panel of Figure 4.2. The superior red-wavelength coverage of the Kast double spectrograph on the 3 m Shane telescope at Lick Observatory (responsible for $\sim 79\%$ of the BSNIP sample; Miller and Stone 1993) to that of the FAST spectrograph on the 1.5 m Tillinghast telescope at Whipple Observatory (responsible for $\sim 94\%$ of the CfA sample; Fabricant et al. 1998) is evident. The Lick spectra as well as most from CSP have good relative spectrophotometry owing to the slit being placed at the parallactic angle (Filippenko 1982), but the continuum shapes of the FAST spectra may be inaccurate in some cases since the slit could not be rotated to arbitrary parallactic angles. Because any heterogeneities in the inputs to our models should reflect only physically significant information, we formulate our data preprocessing and augmentation procedures (see Sections 4.2.3.2 & 4.2.3.3, respectively) to obscure as much source-specific information and contamination (e.g., wavelength limits, inaccurate continuum shapes) as possible.

4.2.2 Light curves

As the purpose of this study is to identify and therefore derive, through supervised learning, certain photometrically-derived properties encoded in SN Ia spectra, the aforementioned spectral compilation must be coupled to photometric observations (i.e., light curves), thereby allowing for the desired properties to be measured. To this end, we collect the requisite information from data releases by the same groups responsible for our compilation of spectra (Ganeshalingam et al. 2010; Stahl et al. 2019; Riess et al. 1999; Jha et al. 2006; Hicken et al. 2009a; Krisciunas et al. 2017, henceforth G10 and S19 for the Berkeley sample, CfA1-3 for the CfA sample, and CSP3 for the CSP sample, respectively), as well as publish several new light curves (see Section 4.6). We use the $E(B-V)$ model implemented within the `SNooPy` package (Burns et al. 2011, see Section 4.7 for additional details) to fit the aforementioned light curves (except for those from S19 and CSP3, who have published fits using the same

[3]We consider a SN Ia spectrum to have full coverage of the Si II λ6355 feature if it has a minimum wavelength of less than 5750 Å and a maximum in excess of 6600 Å. These values represent the minimum and maximum extremes of the domains S20 use to search for the feature's blue and red endpoints, respectively.

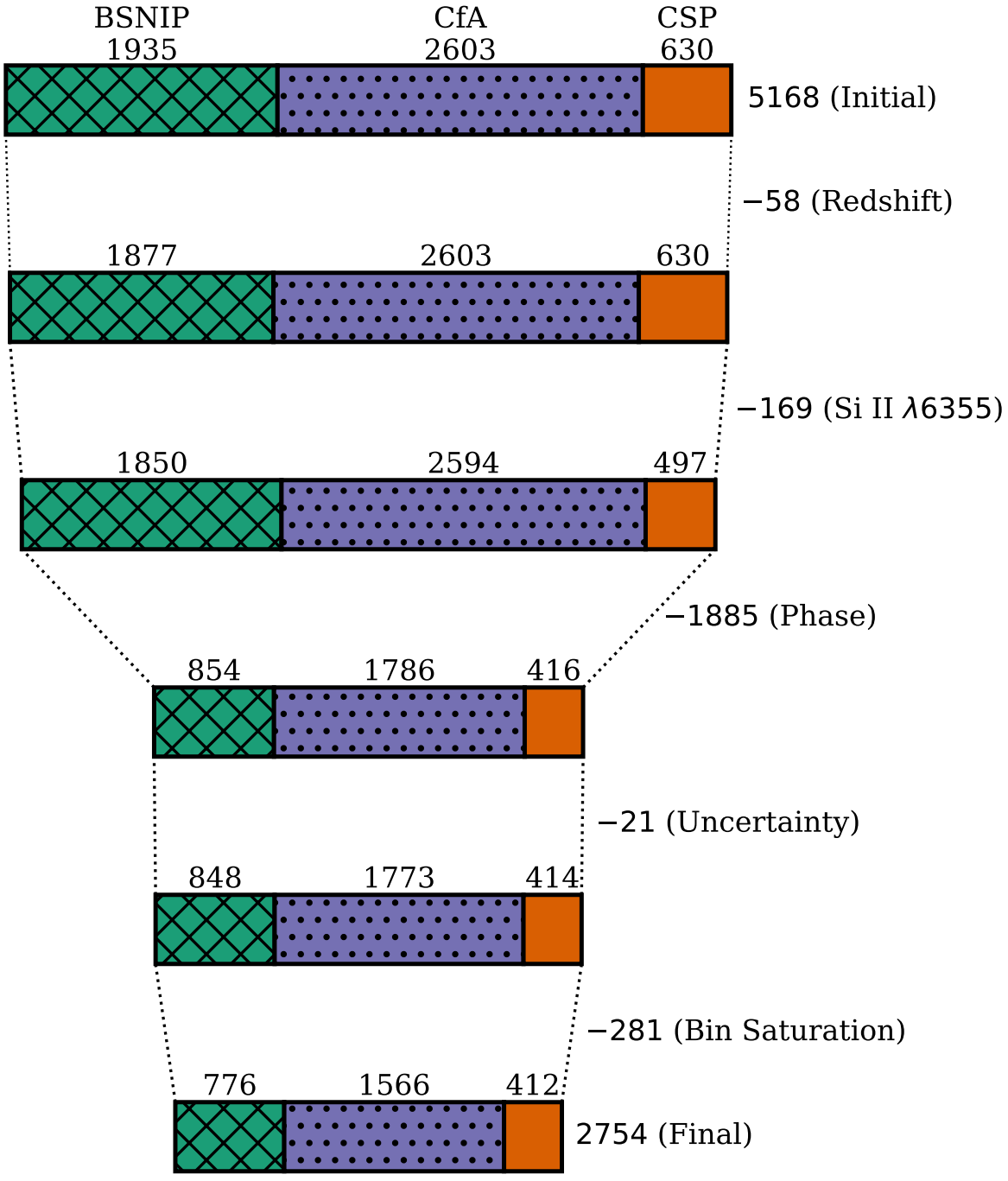

Figure 4.1: Full accounting of all cuts made in distilling our initial set of 5168 spectra down to the 2754 in our final compilation (1113 of which are within the "domain" defined in Section 4.2.3). We delineate the source of each spectrum in the top row. By a wide margin, the lack of suitable photometric observations is responsible for the most severe cut (indicated with "Phase").

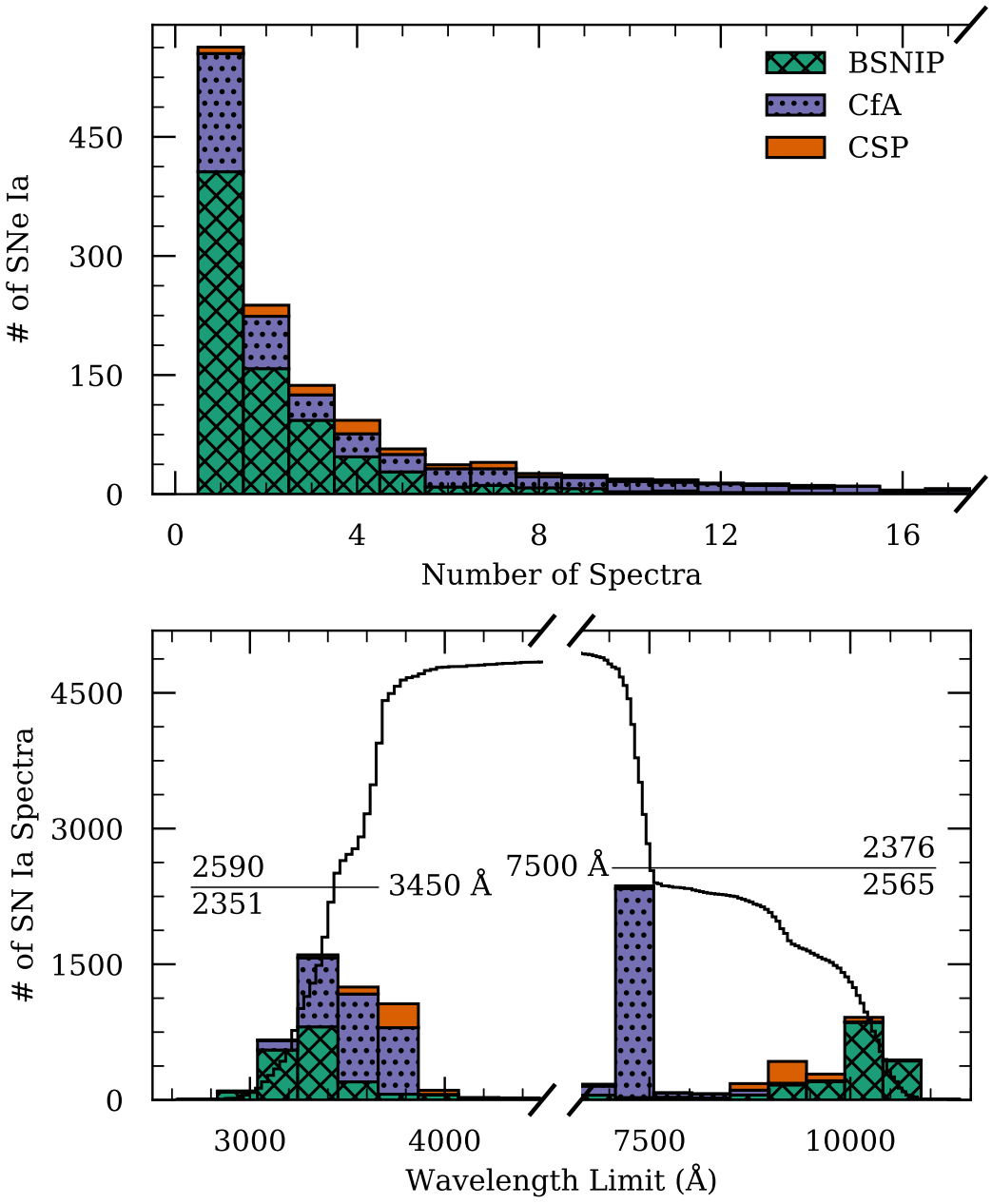

Figure 4.2: Stacked distributions of dataset parameters for our spectral compilation, distinguished by source. The top panel shows the number of spectroscopic observations per object (the tail extends to higher numbers of spectra, but is truncated for clarity) and the bottom panel displays the blue and red wavelength limits of the spectra. Overlaid on the bottom panel is the cumulative (inverse-cumulative) distribution of blue (red) wavelength limits, and the intersecting horizontal lines reflect the bounds defined in Section 4.2.3.2. The number of spectra above and below each intersecting line are also labeled.

procedure along with their photometry), allowing us to measure the time of maximum B-band brightness (and hence the phase[4]) and the decline-rate parameter[5], Δm_{15}.

4.2.3 Final Compilation

All told, 3056 spectra are linked to light curves with successful `SNooPy` fits, but as shown in Figure 6.1, we remove 21 spectra having a phase uncertainty in excess of 1 day (d) and/or a Δm_{15} uncertainty exceeding 0.1 mag, thus yielding 3035 spectra. We visualise this compilation within the photometric parameter space of interest (namely, Δm_{15} and phase) in Figure 4.3. Unsurprisingly, the densest coverage — by a wide margin — occurs for $\Delta m_{15} \approx 1.1$ mag (reflecting that of a prototypical SN Ia), but particularly impressive is the coverage within the region defined by $-10 \lesssim \text{phase} \lesssim 18$ d and $0.85 \lesssim \Delta m_{15} \lesssim 1.55$ mag (albeit a bit sparse for the more rapidly declining objects within this region).

Motivated by this coverage, we impose the aforementioned region as a "domain" on our models in the following way: Model I is tasked with classifying whether an input spectrum lies within its boundaries, while Model II and Model III determine the phase and Δm_{15} (respectively) for spectra within this restricted domain. To mitigate the imbalance caused by the dominance of samples with $\Delta m_{15} \approx 1.1$ mag, we enforce a "saturation point" of 40 samples for each in-domain bin in Figure 4.3. According to this policy, overly dense bins are brought into compliance by removing spectra with the largest Δm_{15} uncertainties until only 40 remain. A total of 281 spectra are removed by this action, leaving 2754 examples (1113 of which are in-domain and thus relevant to Models II & III) in what will henceforth be referred to as our final compilation (see the bottom row of Figure 6.1). Though this runs contrary to the common dogma that *more data is always better*, we have found our choice to be empirically superior in this specific application.

A cursory inspection of Figure 4.3 reveals that our coverage does not drop off significantly at larger phase and Δm_{15} values than those which terminate our selected domain. It is therefore tempting to consider expanding the domain until such a drop is achieved (so as to make predictions over a wider swath of parameter space), but we choose not to do so for a myriad of reasons, the bulk of which are conveyed in the sequences of variance spectra presented in Figure 4.4. If we assume that the spectral energy distribution (SED) of a SN Ia is predominantly[6] determined by its phase and light-curve shape, then considering sequences of

[4]The phase of a spectrum is the time interval between when it is observed and when its SN reaches maximum B-band brightness, as derived in Section 4.7 and listed in Table 4.2, divided by a factor of $(1+z)$ to correct for time dilation. The adopted redshift was listed in the original publication for that spectrum.

[5]Our selected implementation of the SN Ia width-luminosity relation uses a *generalised* light-curve shape parameter, Δm_{15}, which is similar to — but distinct from — the more popular $\Delta m_{15}(B)$ used in the Phillips relation (i.e., the decline in magnitudes of a SN Ia over the first 15 d of its post-maximum B-band evolution). Indeed, the two may deviate randomly and systematically (see Section 3.4.2 of Burns et al. 2011).

[6]We emphasise that "predominantly" does not mean "exclusively" — other factors such as Galactic and host-galaxy extinction have an effect on an *observed* SN Ia SED; our assumption is merely that those factors are of secondary significance to phase and light-curve shape, especially for spectra that have already been pre-processed in accordance with Section 4.2.3.2.

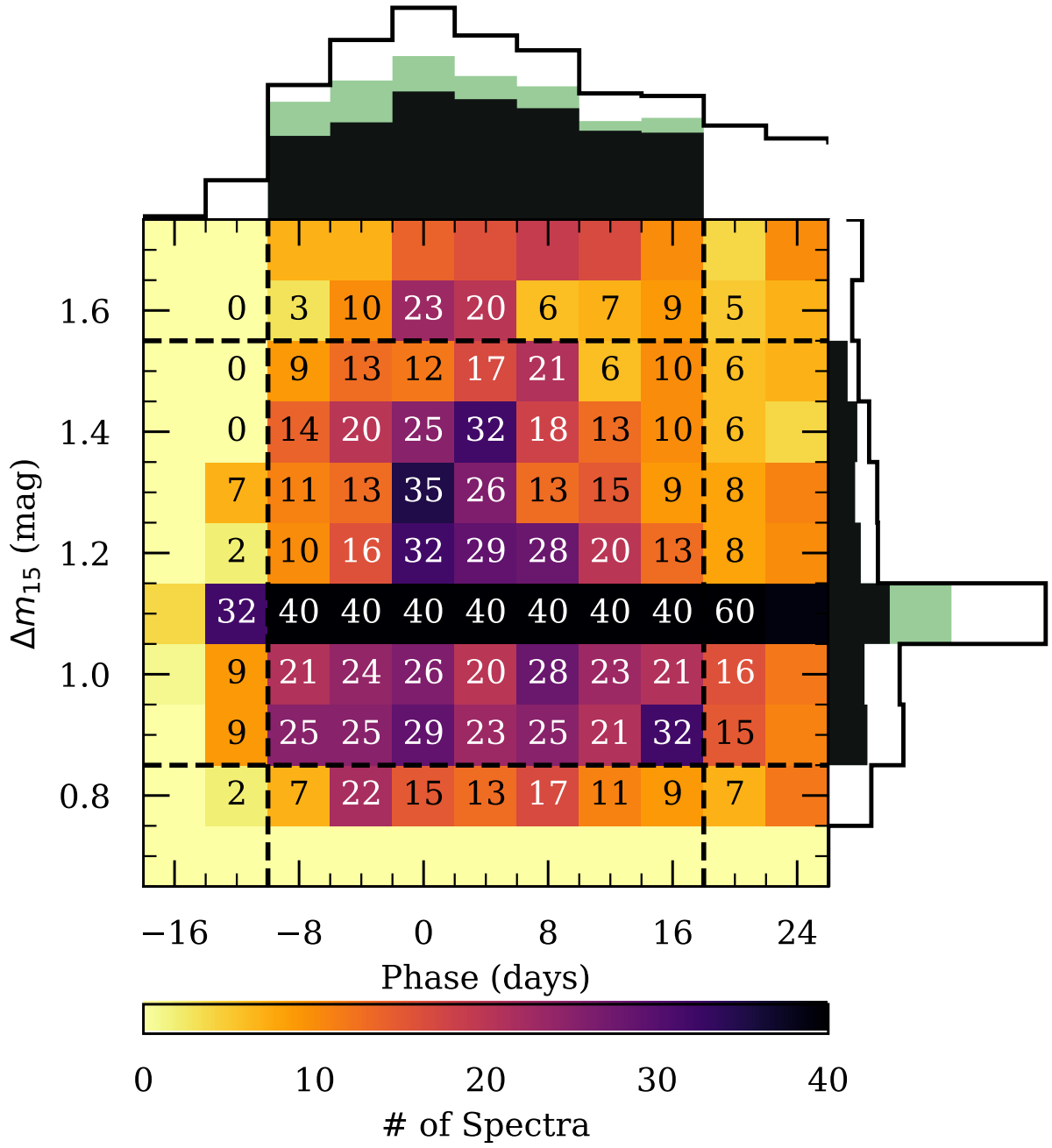

Figure 4.3: Distribution of Δm_{15} and phase for the spectra in our compilation, with axes truncated to focus on the domain of interest. The empty-black one-dimensional projections reflect the full set of 3035 spectra, the green components consider only those 1394 spectra that are within the domain of interest, and the filled-black components show the same once spectra are removed to enforce the saturation criteria of 40 examples per bin (leaving 1113 in-domain spectra). The number of spectra falling within each in-domain bin and their immediate neighbors is labeled.

variance spectra — whereby one of the aforementioned parameters is discretised into narrow bins and the variations within those bins are studied — allows us to infer which regions in SN Ia spectra vary the most at a given point in the sequence. If our assumption that the SED is largely a function of these two parameters holds, then such regions of large variation encode the most discriminating information about the nondiscretised parameter.

With this interpretation established, we note that for spectra with phases between -10 d and 18 d, the variance spectra in the left column of Figure 4.4 show notably similar structure for Δm_{15} bins ranging from 0.90 mag to 1.50 mag. We interpret this as an indication that, at least within this range of Δm_{15} values, phases between -10 d and 18 d are encoded by a common — or "slowly" evolving — set of features. A consequence of this is that a fairly simple convolutional neural network should be able to learn these features without much difficulty (we discuss our network architecture, including the way in which Figure 4.4 motives it, in more detail in Section 4.3.1), and although a sophisticated network may well be able to learn "when" to weight certain features more heavily — in addition to the features themselves — we are content with the range of Δm_{15} values afforded by our selected domain. Indeed, our coverage drops off sharply for lower Δm_{15} and the more rapidly declining SNe Ia in our dataset (i.e., those with $\Delta m_{15} \gtrsim 1.6$ mag) are likely to be SN 1991bg-like objects which do not follow the Phillips relation (or its derivatives).

The aforementioned arguments do not perfectly carry over when we consider the phase-binned variance spectra for those SNe Ia in our sample having $0.85 \leq \Delta m_{15} < 1.55$ mag. Before maximum light, the blue wing of the Ca II H&K feature exhibits the most variability and thus offers the best discrimination of Δm_{15}, but beyond peak, this variability fades and the dominant variation is observed in the blue wing of the Si II λ6355 feature. At phases $\gtrsim 10$ d, this too begins to fade and variability is strongest at intermediate wavelengths, typically those in the vicinity of the S II "W" feature. It is beyond the scope of this study to speculate about — or offer an explanation of — the physical mechanism(s) that give rise to these observations, but we note that Nugent et al. (1995) identified these features in particular as a probe of SN Ia luminosity, with the cause ascribed to temperature differences (and thus, to the total amount of ^{56}Ni produced) between explosions. We do not pursue earlier phases owing to a paucity of data (indeed, Figure 4.3 reveals that doing so would result in several empty bins), and while our compilation may well support an extension to later phases, we do not undertake such an addition here because Model III would have to become very robust to evolving features.

4.2.3.1 Training, Validation, and Testing Sets

In developing a neural network (or any supervised ML model), one typically divides the available data into three distinct subsets: a "training" set used to derive the decision path between features and outputs, a "validation" set to assess model performance during training and tune externally assigned hyperparameters, and finally, a completely separate "testing" set, which is used to probe the efficacy of the final model against unseen data, and *not* used for either the optimisation of the network or the assignment of hyperparameters. In light of

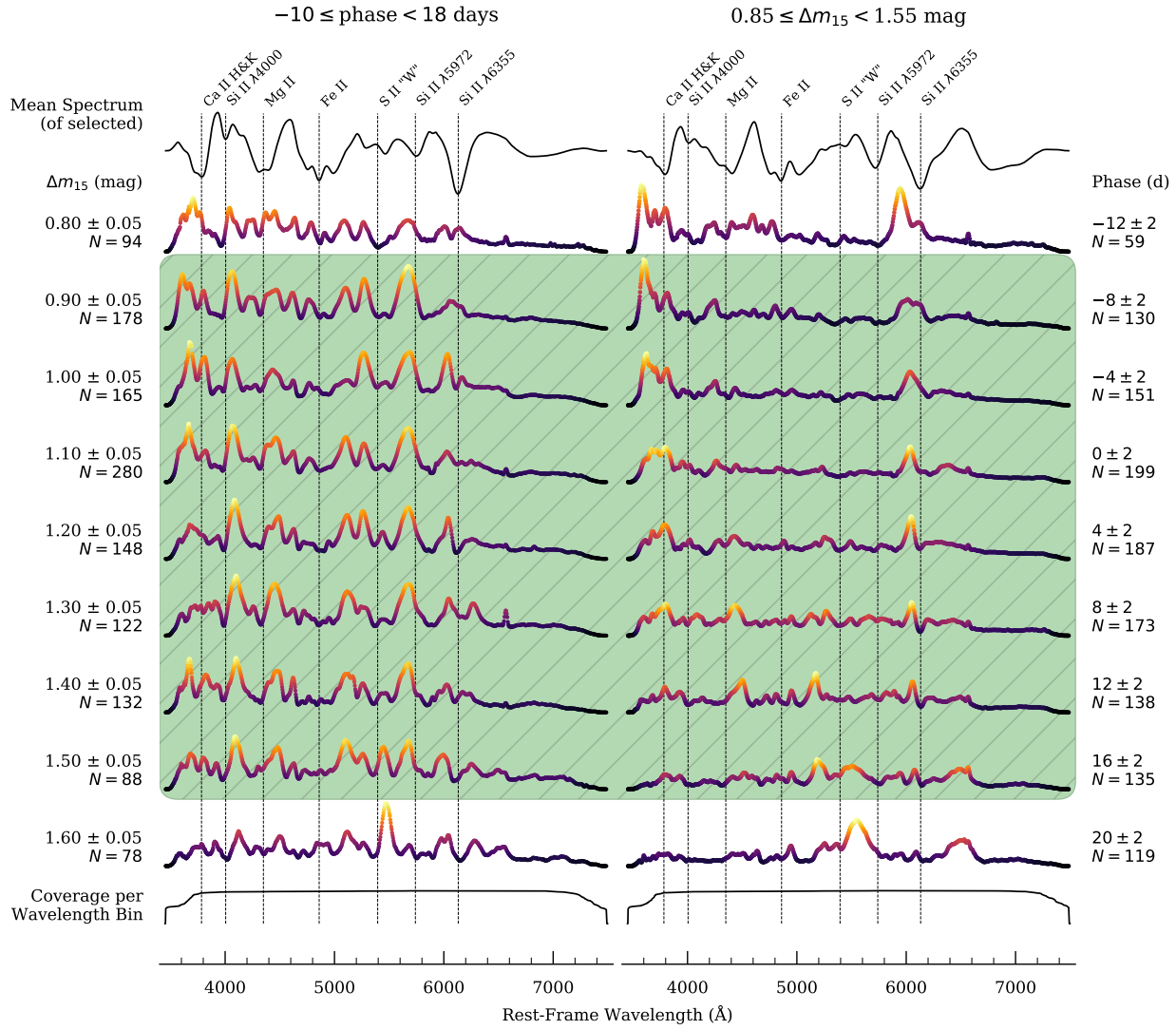

Figure 4.4: Sequences of variance spectra progressing through equally spaced Δm_{15} (left column) and phase (right column) bins. Each column begins with the selection criteria for the spectra in it and the mean spectrum of all those that are selected. Prominent spectral features are indicated. After advancing through the indicated variance sequence, the column terminates with the coverage per wavelength bin of the selected spectra. The same vertical scaling is applied to all variance spectra, but the colour map is normalised to each and is used to emphasise regions of significant variation. Our selected domain of interest is covered by the green region with diagonal hatching. All spectra used in generating the sequences have been preprocessed according to the specifications of Section 4.2.3.2. The narrow spike that appears redward of the Si II λ6355 line in some variance spectra is due to nebular Hα emission from the host galaxy.

the small absolute size of our compilation (by modern ML standards), we intentionally set the validation and testing splits (10% each) to be smaller than conventional allocations so as to keep our training set as large as possible.

We take a nuanced approach to ensure that our proportionally smaller validation and testing sets provide a realistic representation of our final compilation. Specifically, we sample according to a pseudostratified scheme for the 1113 in-domain spectra in our compilation, whereby we select random subsets of the appropriate size from each bin in Figure 4.3. In this way, the Model II & III training, validation, and testing sets have approximately the same binwise distribution. We impose a floor so that even bins with fewer than 10 total instances have at least one sample for each of the validation and testing sets. As a result, the actual validation and testing ratios are elevated slightly higher than the targeted 10%. The Model I sets are generated by randomly sampling all out-of-domain spectra at the prescribed ratios and then adding them to the pseudostratified in-domain sets. This ensures that all spectra in the Model II/III sets are just subsets of the corresponding Model I sets. Therefore, we can holistically assess `deepSIP` via the Model I testing set without fear of Model II or III inadvertently being asked to characterise spectra that occur in their training or validation sets.

4.2.3.2 Preprocessing

Our models should be sensitive only to the physical characteristics encoded in the spectra they are trained on, not to any peculiarities relating to how the spectra were collected or reduced. Furthermore, it is imperative that each spectrum is processed in a carefully controlled and systematic way to avoid inadvertent biases. We therefore perform the following preprocessing steps to homogenise input spectra prior to ingestion by our models.

1. Each spectrum is de-redshifted — that is, the redshift is removed. This step is skipped for augmented spectra (see Section 4.2.3.3) which are already in (or near) the rest frame.

2. Each spectrum is smoothed using a Savitzky-Golay filter (Savitzky and Golay 1964) with a window equivalent to 100 Å, though the window is varied for augmented spectra.

3. The pseudocontinuum is modeled by again smoothing the spectrum, but with a much wider window of 3000 Å (unless this exceeds the range of the spectrum, in which case we use a dynamically determined value corresponding to $\sim 70\%$ of the available wavelength range). We then subtract it from the spectrum.

4. The spectrum is binned onto a log-wavelength scale consisting of 1024 points between 3450 Å and 7500 Å. As shown in Figure 4.2, these endpoints are such that $\sim 50\%$ of our global compilation (i.e., including those *without* phase information) have additional spectral information either below 3450 Å or above 7500 Å that is disregarded. This painful step of throwing away potentially useful information is necessary to avoid

inducing significant biases between our data sources. If a spectrum does not have signal all the way to the blue or red ends of this range, we set it to zero in the missing end(s). In addition to ensuring that all spectra are represented by vectors of the same length, this transformation has the useful consequence that redshifting corresponds to a linear translation (see Section 4.2.3.3 for more details).

5. We scale the signal so that it has a range of unity and then translate it such that it has a mean of zero.

6. The first and last 5% of the signal in the spectrum is tapered using a Cosine Bell (i.e., a Hanning window) so that it smoothly goes to zero at the ends.

7. Finally, we add 0.5 to the signal so that it is positive everywhere. Henceforth, we refer to this quantity as "scaled flux."

We show an example of the intermediate stages and final result derived from our preprocessing procedure in Figure 4.5.

4.2.3.3 Augmentation

Though we have taken care to assemble a significant fraction of *all* publicly available low-redshift SN Ia optical spectra currently in existence, our final compilation is still rather small by modern standards in deep learning (especially for the domain-restricted subset that is relevant for Models II and III). For this reason, we formulate a data-augmentation strategy (i.e., a method for extending our training set beyond its limited size while preserving its characteristics; e.g., Dieleman et al. 2015; Cabrera-Vives et al. 2017; Martínez-Palomera et al. 2018; Boone 2019) that generates a training set of substantially increased size. To accomplish this, we randomly sample data from the Model I (II/III) training set, with replacement, until we have a collection whose size, when combined with the non-augmented training set, equals 5000 examples (a $\sim$ 4-to-1 ratio of augmented to original training samples for the Model II/III set). After obtaining samples according to this prescription, we transform each sampled spectrum using the following operations.

1. **Redshifting:** As noted in Section 4.2.3.2, we remove the redshift from all spectra that are fed into our models. However, we expect our models to be robust to small redshift errors that propagate into the rest-wavelength transformation. To this end, we perturb the rest wavelength array of each sampled spectrum by a multiplicative factor of $(1 + \delta z)$, where δz is drawn from a uniform distribution, $\delta z \sim \mathcal{U}(-0.004, 0.004)$, motivated by the mean uncertainty in the `SNID`-derived redshifts reported by S20 for their dataset. Coupled with log-binning (which converts redshifting/de-redshifting into a linear offset; see Section 4.2.3.2), this allows us to reinforce and exploit the invariance to small translations that CNN architectures exhibit (LeCun et al. 2015).

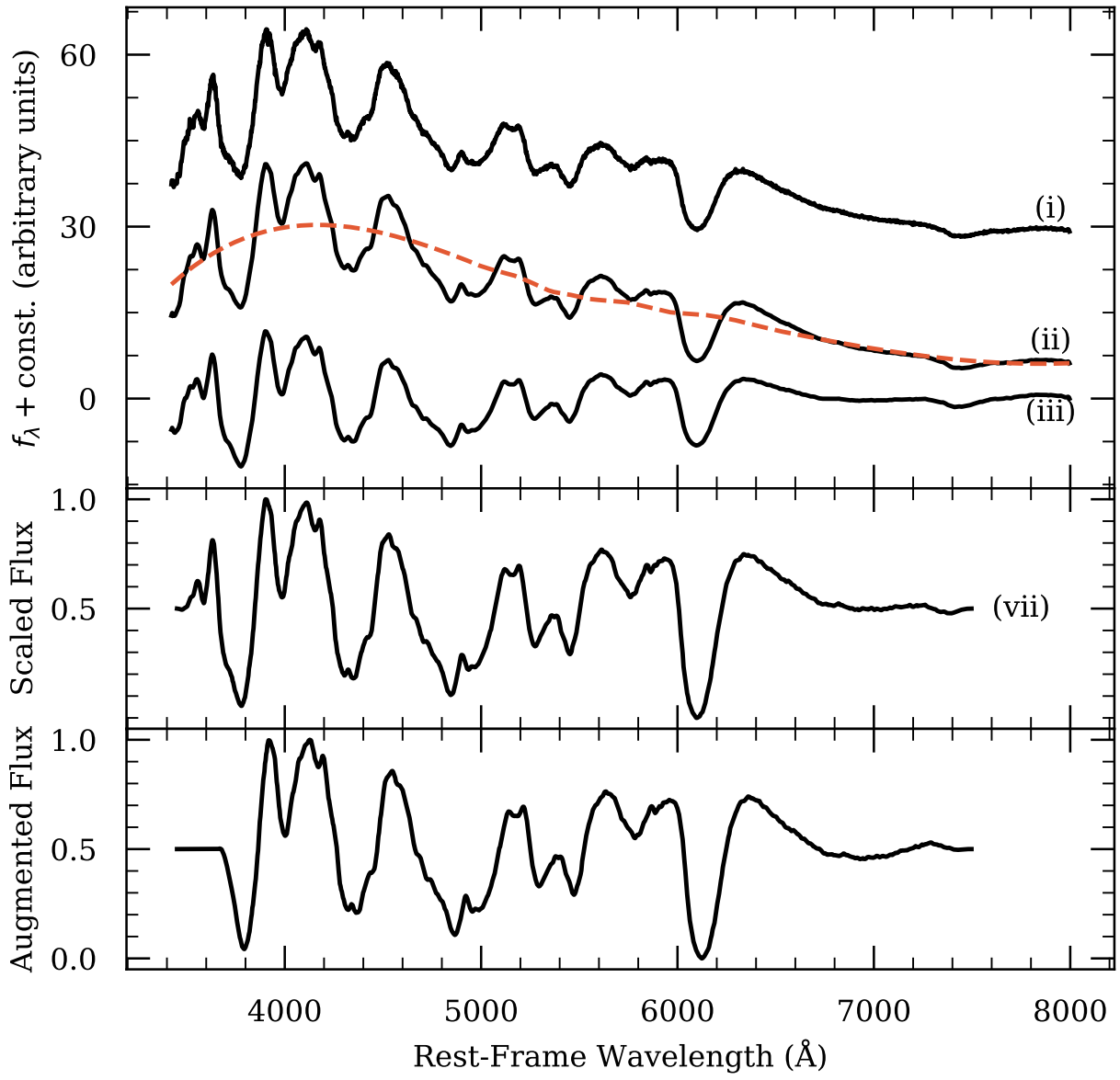

Figure 4.5: Snapshots showing various stages of our preprocessing routine as applied to a spectrum of SN 2016coj at +1.3 d. The numerals indicate the last preprocessing step to have been performed on the plotted spectrum, and the dashed orange line illustrates the fitted (and subsequently removed) pseudocontinuum. The bottom panel shows an example of the spectrum after data augmentation steps have been applied.

2. **Noise:** To encourage our models to be robust to variations in the signal-to-noise ratios of input spectra, we vary the degree of smoothing applied to each sampled spectrum during our preprocessing procedures (see Section 4.5). We do this by randomly selecting the smoothing window, $w \sim \mathcal{U}(50, 150)\,\text{Å}$, with these bounds chosen to be roughly consistent with the range of wavelength-space extents of the high-variance regions identified in Figure 4.4.

3. **Trimming:** We expect our models to be insensitive to any information about the observing apparatus and configuration that might be encoded in a spectrum. For example, the median phase of the BSNIP-collected spectra in our compilation is $\sim 18\,\text{d}$, while for the CfA-collected spectra it is $\sim 9\,\text{d}$, but our models should *not* form a decision path that preferentially associates spectra having extensive red-wavelength coverage (namely, the BSNIP spectra) with later phases — this correlation is purely a consequence of exogenous biases in our compilation. Therefore, in addition to the preprocessing steps outlined in Section 4.2.3.2, we remove a random proportion, f, from the blue and red ends of each sampled spectrum, where $f \sim \mathcal{U}(0, 0.1)$, with the upper bound chosen so as to maintain full coverage of the characteristic Si II λ6355 feature that we require for spectra in our compilation to possess.

We show an example of the results of the aforementioned augmentation procedures in the bottom panel of Figure 4.5.

4.3 Models

As noted, we have constructed three models to ultimately determine the phase and light-curve shape parameter, Δm_{15}, of a SN Ia from an optical spectrum. The first model determines if the input is from a SN Ia with a phase of $-10 \leq \text{phase} < 18\,\text{d}$ that has a light-curve-shape parameter of $0.85 \leq \Delta m_{15} < 1.55\,\text{mag}$. The second model determines the phase, and the third, Δm_{15}, both only within the domain for which Model I discerns. We formulate the first model as a binary classification problem — either a spectrum belongs to a SN Ia subject to the aforementioned photometric restrictions, or it does not. The remaining models can be construed as a regression problem, where a continuous quantity (e.g., phase or Δm_{15}) is to be predicted. Despite their differing applications, each model uses a similar neural network architecture, and much of the work flow of training and evaluating them is common. We therefore devote the following subsections to discussing the underlying architecture employed in our models and the common aspects of our work flow. We present model-specific results in Section 6.4.

4.3.1 Architecture

At the heart of our models is a deep (i.e., multilayer) CNN, but whereas the prototypical use-case is two-dimensional (2D) — deep 2D CNNs have a storied history in image classification

(e.g., LeCun et al. 1990, 1998; Szegedy et al. 2014) and even Muthukrishna et al. (2019b) resorted to tiling 1D SN spectra into 2D "images" to formulate their problem as one of image identification — we follow the inherent dimensionality of our data by using a 1D implementation (for a summary of 1D CNNs, see Kiranyaz et al. 2019). In addition to being more conceptually compatible with our application, our use of a 1D CNN gives us much more control over the degree to which nonlocal features are aggregated though pooling operations.

We present a schematic of our neural architecture, which utilises a total of four convolutional layers to extract representative features from input spectra, in Figure 4.6. We apply the Rectified Linear Unit (ReLU, Nair and Hinton 2010) activation function to the output of each convolutional and fully connected layer. Following each convolutional layer we apply max pooling to reduce computational complexity and remove irrelevant features. Finally, we conclude each "block" (i.e., convolution + ReLU + max pool + dropout) in our network with a dropout layer to assist in the prevention of overfitting (Srivastava et al. 2014). Each convolutional and fully connected layer has its weights initialised with zero-centred Gaussian noise and its bias to a small, positive value. All of our models are implemented using `PyTorch` 1.0 (Paszke et al. 2019), and we make our trained models and framework available as `deepSIP`[7], an open-source Python package (see Section 4.8 for guidelines on basic usage).

Our selected architecture is largely motivated by insights gleaned from the sequences of variance spectra presented in Figure 4.4. As noted earlier, the Δm_{15}-binned sequence shows more or less the same structure over our selected range of values. This homogeneity supports the use of a simple feed-forward network in the case of Model II, but the depth of the network (i.e., how many convolutional layers are used) and the progression in the number of filters computed per layer are motivated by the *heterogeneity* in features as they progress through the sequence. For example, the blue wing of the Si II λ6355 feature shows variation throughout the sequence, but the exact "shape" of that variation as a function of wavelength varies. For this reason, we use multiple convolutional layers and increase the number of convolutional kernels per layer in all but the last so that our networks have the capacity to make decisions based on many complex, highly-specialised features that are computed from a smaller number of basic features supplied by the earlier layers. The situation is mostly the same for Model III, but the relevant variance spectra (i.e., those in the right column of Figure 4.4) exhibit fewer common features and more extreme evolution in their shapes as the sequence progresses through phase bins. Motivated by this, we did carry out experiments with several architectures capable of predicting the phase in tandem with Δm_{15}, but none performed substantively better than our set of simple, independent networks. We do expect, however, that in addition to requiring much more high-quality training data, a specialised architecture would be crucial in expanding the output domain of Models II and III. Indeed, extending the sequences of Figure 4.4 out to larger phase and Δm_{15} values reveals significant feature evolution. A network capable of providing feedback between phase and Δm_{15} predictions would allow for this evolution to be properly modeled.

The aforementioned dropout layers — each of which randomly drops elements from their

[7] `https://github.com/benstahl92/deepSIP`

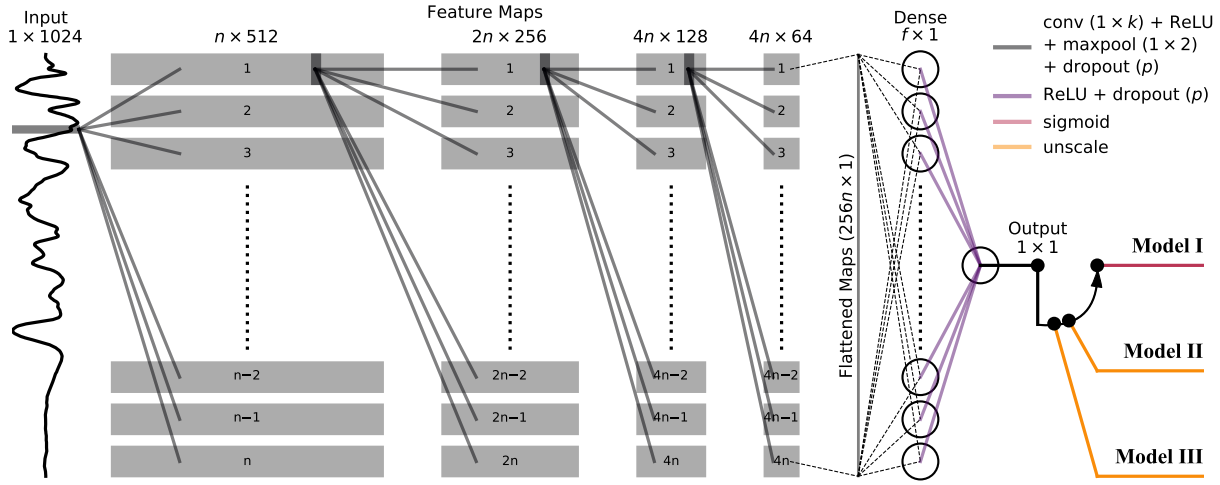

Figure 4.6: Schematic of the common neural network architecture used by each of the three fully independent networks that constitute Models I–III (which collectively comprise `deepSIP`). A set of n feature maps is computed from the preprocessed input spectrum and down-sampled using max pooling (the resulting maps are indicated by grey boxes). This operation is then recursively applied to the down-sampled feature maps a total of three additional times, with the number of feature maps doubling for all but the last set. The final set of down-sampled feature maps is then flattened into a vector of length $256n$ and fed through a fully connected layer consisting of f neurons before reaching the output neuron. Then, depending on the model, a final operation is performed to transform the raw output of the network into the appropriate context ("probabilities" in the case of Model I or dimensional phase or Δm_{15} values for Models II and III, respectively). The convolution kernel, k, number of feature maps generated by the first convolutional layer, n, and the number of neurons in the fully-connected layer, f, are all hyperparameters whose preferred value depends on the specific model. A dropout layer with dropout probability p follows each weight layer aside from the output neuron.

input with Bernoulli-distributed probability, p, and (in our implementation) rescales outputs by a factor of $1/(1-p)$ during training — serve a secondary purpose in our networks. Namely, this purpose is to make the networks probabilistic (Gal and Ghahramani 2015): each forward pass *with dropout enabled in training mode* produces a different prediction, and thus, it is straightforward to quantitatively describe not only a point estimate (the prediction of a model) but also, an estimate of its uncertainty. To do so when generating predictions, we make N stochastic (i.e., with dropout turned on) forward passes[8] for a given input and assign the mean and standard deviation of the resulting collection of predictions as the final model prediction and an estimate of its uncertainty.

4.3.2 Training

To train each of our models, we supply the appropriate training set in small batches and utilise an adaptive gradient descent algorithm (ADAM; Kingma and Ba 2014) to minimise the appropriate objective function by updating the weights and biases in each layer of the network. For Model I we employ the binary cross-entropy loss as our objective function, while for Models II and III we use the mean squared error (MSE) loss. We also scale training outputs that are continuous (i.e., phase and Δm_{15}) such that they range from 0 to 1 using a transformation of the form $\mathbf{y}' = (\mathbf{y} - y_{\min})/(y_{\max} - y_{\min})$, where $(y_{\min}, y_{\max})$ represent the domain boundary (as shown in Figure 4.3) along the output's dimension. Subsequent predictions by these models are then unscaled using the inverse of this transformation. Model I predictions are transformed into "probabilities" using the sigmoid function.

We train each of our models for a total of 75 epochs, with the learning rate set to step down by a multiplicative factor of 0.1 after thresholds of 45, 60, and 70 epochs are reached. In testing, we found these choices to yield stable convergences without requiring excessive training time. At the culmination of each epoch we compute success metrics against the relevant validation set, thereby affording a specific measure of model-performance evolution in terms of the metrics we care most about (e.g., in dimensional, unscaled units for Models II and III). For Model I, we primarily use the area under the curve (AUC) of the Receiver Operating Characteristic (ROC) curve[9], whereas for Models II and III, we primarily use the root-mean-square error (RMSE). We emphasise that although these are the primary metrics, we consider secondary indicators as well (see Sections 4.4.1 & 4.4.2 for Models I and II/III, respectively).

[8] We use a fiducial value of $N = 75$ when evaluating on the validation sets to select preferred *training* hyperparameters (see Section 4.3.3), but then treat it is a parameter to be further optimised prior to production-scale use (see Section 4.4.2.1).

[9] An ROC curve shows the true-positive rate (ordinate) versus the false-positive rate (see Figure 4.7). The most optimal AUC score is 1, corresponding to a false-positive rate of 0 and a true positive rate of 1.

4.3.3 Hyperparameter Selection

There are several external parameters (i.e., not determined through backpropagation; henceforth referred to as "hyperparameters") that must be selected specifically for each of our models. Some are architectural (e.g., k, the size of each convolutional kernel; n, the number of distinct feature maps computed by the first convolutional layer; f, the number of neurons in the fully-connected layer; and p, the dropout probability used for training; see Figure 4.6), and some have to do with our training algorithm (e.g., training batch size, learning rate, and weight decay). The optimal choice of such parameters is not known *a priori* and is application dependent (e.g., we find that Model II performs best when k is less than the value that maximises Model III performance; see Table 4.1). We note that the dropout probability used during training *need not* be the same as that used when generating predictions. We therefore consider them separately as follows: the dropout probability for training is chosen as part of our hyperparameter selection process and the dropout probability used for generating predictions is separately chosen in tandem with N (see Section 4.4.2.1).

Thus, for each of Models I, II, & III, we perform a randomised search whereby we select preferred hyperparameter values by training and validating the models on many combinations of hyperparameters that are randomly drawn from a grid. A total of 12 hr of compute time on a single of NVIDIA Tesla K80 GPU was allocated, per model, for these searches. We increase efficiency by automatically stopping training after 20 epochs when a performance threshold is not achieved on the validation set, and as a result, we are able to explore a significant portion of the selected hyperparameter space. Table 4.1 details the full hyperparameter grid, and summarises the final set for each model. We discuss our selection criteria for determining these final, preferred sets in Sections 4.4.1 & 4.4.2 for Models I and II/III, respectively.

4.4 Results

4.4.1 Model I: Domain Classification

4.4.1.1 Preferred Hyperparameters

Our first model is designed to determine if an input spectrum belongs to a SN Ia having $-10 \leq \text{phase} < 18\,\text{d}$ and $0.85 \leq \Delta m_{15} < 1.55\,\text{mag}$. If a spectrum satisfies these criteria, it is said to be *in* the domain of interest; otherwise it is *out*. In this way, Model I serves as a precursor to Models II and III: the subsequent predictions for spectra that it classifies as being outside the domain of interest should be carefully scrutinised, if not disregarded altogether. From our Model I hyperparameter search (as discussed in Section 4.3.3 and summarised in Table 4.1), we find that the highest achieved validation ROC AUC score is 0.992 (see Figure 4.7), and on the basis of this score, we select the hyperparameters that yield it as the final, preferred set. These hyperparameters produce a network with a relatively modest number ($\sim$ 75k) of trainable parameters. Though we currently do not consider uncertainty estimates for Model I, we still use the full machinery of our probabilistic architecture with

Table 4.1: Hyperparameter Grid.

Hyperparameter	Values[a]
convolution kernel[b] (k)	$5, 15, 25^{\mathrm{I,II}}, 35^{\mathrm{III}}$
filters in first convolution (n)	$8^{\mathrm{I,II,III}}, 16, 32$
fully connected neurons (f)	$16^{\mathrm{I,II}}, 32, 64, 128^{\mathrm{III}}$
training dropout probability (p)	$0.01^{\mathrm{I,II,III}}, 0.05, 0.1$
batch size[c]	$2, 4, 8, 16^{\mathrm{I,II}}, 32^{\mathrm{III}}$
learning rate	$0.0005^{\mathrm{II,III}}, 0.001^{\mathrm{I}}$
weight decay	$0.00001^{\mathrm{III}}, 0.0001^{\mathrm{I,II}}$

[a]Superscripts mark the preferred hyperparameter of the denoted model.
[b]Though small (e.g., 3×3) kernels are typical in 2D scenarios, significantly larger kernels have proven optimal in some 1D applications to astrophysical signals (e.g., quasar spectra, Parks et al. 2018).
[c]Masters and Luschi (2018) have suggested that batch sizes between 2 and 32 yield the best performance.

settings aligned to those of Models II and III (i.e., $N = 30$ and $p = 0.02$; see Section 4.4.2.1) for consistency and to make possible straightforward extensibility in the future.

4.4.1.2 Decision Threshold

With the information afforded by Figure 4.7, we are also able to tune the decision threshold of our model (i.e., the minimum "probability" of being *in* to be classified as such). While many opt to use a default threshold of 50% without further consideration, the optimal choice depends on striking an application-specific balance between the extent to which false positives can be tolerated and true positives can be missed. Taking a holistic view and recalling the aforementioned role of Model I in the overall output of `deepSIP`, it becomes obvious that the quality of Model II and III predictions should be given the utmost priority. The optimal decision threshold in our case is therefore the one that yields the best Model II and III performance on spectra that Model I classifies as in-domain (which will be a mixture of true positives and false positives). This criterion is much more important than the overall classification accuracy[10] given the "blurry" nature of the domain boundary — individual spectra can *and do* fall so close to it that the particular side they end up on is determined by statistical variations.

[10]The accuracy score is the fraction of all predicted labels that are correct.

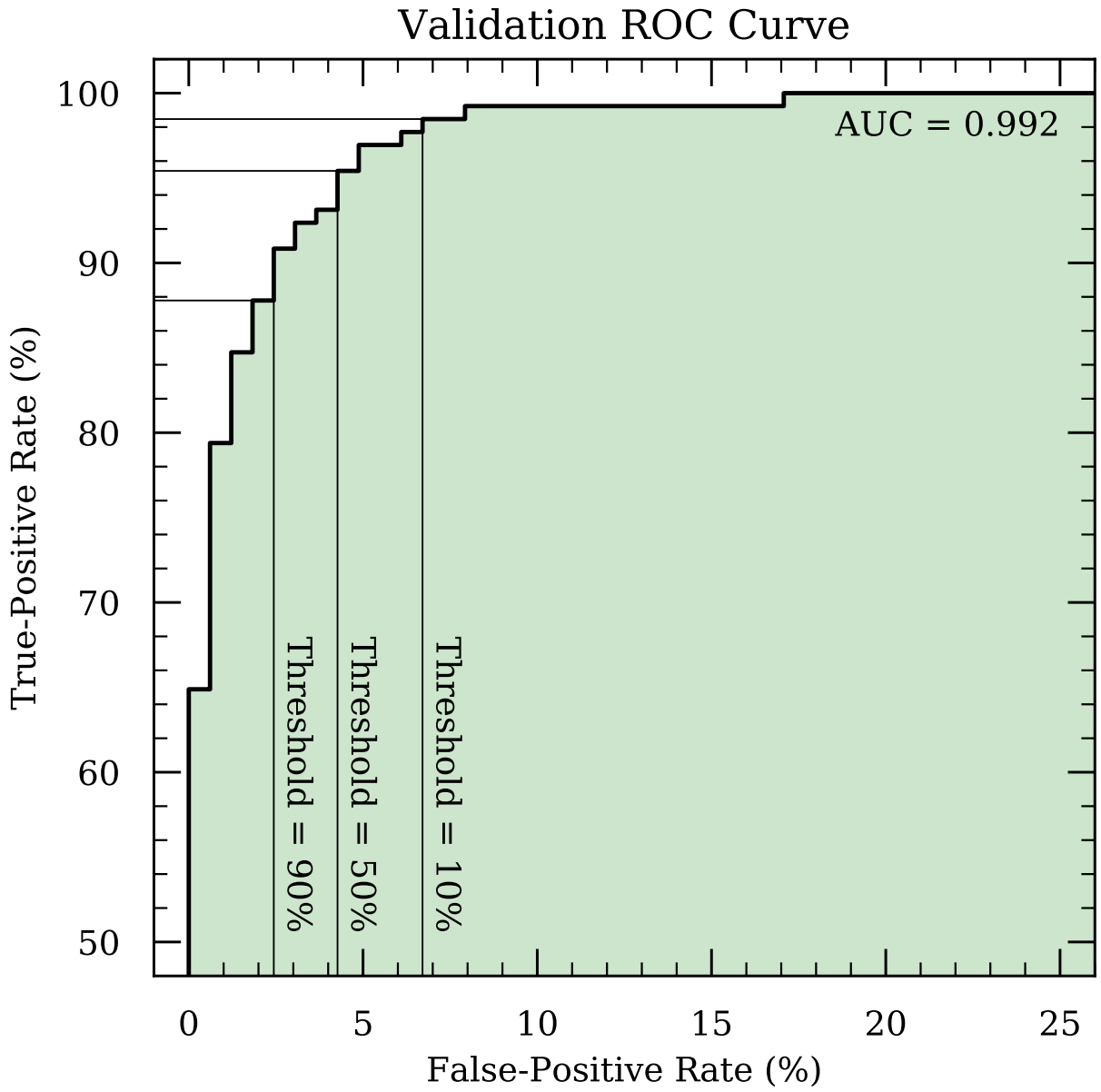

Figure 4.7: ROC curve for Model I deployed on its validation set. The locations that correspond to various decision thresholds are indicated.

To identify the optimal threshold, then, we use the Model I validation[11] set to study, as a function of decision threshold, Model II/III RMSE scores segmented, based on the classifications of Model I, into false negatives (FN), false positives (FP), true positives (TP), and all positives (P = FP + TP). We find that the Model II scores belonging to FN and FP both follow a trend of decrease with rising decision threshold, and that those for FN are generally larger by a modest (~ 0.5 d) amount. The corresponding FN scores for Model III also follow a decreasing trend (with rising threshold) but are significantly lower than those for the FP, which remain roughly constant at ~ 0.2 mag until a dip forms between $\sim$ 90–95%. While one could argue that the FP scores for Model II are acceptable over a wide range of thresholds ($\sim$ 2–2.5 d for thresholds of $\sim$ 5–80%, and lower thereafter), the aforementioned Model III scores over a similar range are prohibitive. We simply cannot tolerate any significant contamination by FP with such high RMSE scores. This constrains the range of acceptable decision thresholds to just $\sim$ 90–95%, even at the expense of more FN with reasonable Model II/III performance.

As the P scores are fairly flat between these bounds, we err to the low side (thereby minimising the number of incorrect classifications) and set our Model I decision threshold to 90%. This yields 13 FN (with RMSE scores of 1.91 d and 0.080 mag from Models II and III, respectively) and 122 P (with scores of 1.05 d and 0.068 mag, respectively) of which 4 are FP (with scores of 1.39 d and 0.160 mag, respectively) from the 295 spectra (including 160 true negatives) in our validation set. Though this results in an accuracy score (94.2%) that is slightly suboptimal to the peak value of 95.9% achieved at a different threshold, it is still vastly in excess of the baseline score yielded by picking the most popular class every time (55.6%) and it gives us confidence that the positives Model I passes on to Models II and III are sufficiently "pure."

4.4.1.3 Performance on Testing Set

With the decision threshold determined, we now make predictions on the testing set (which, as outlined in Section 4.2.3.1, has *not* been used to optimise the network or hyperparameters) and assess the efficacy of Model I by comparing predicted labels to true labels. We find a similarly high ROC AUC of 0.989 and note that Model I achieves a TP rate of 90.8% at a FP rate of 2.4% for our selected threshold of 90%. From the 295 spectra in the testing set, Model I delivers 160 true negatives, 12 FN, 4 FP, and 119 TP, collectively yielding an accuracy score of 94.6% (as compared to the 55.6% baseline score obtained by picking the most popular class every time). Of those marked as in-domain (i.e., P), Models II and III yield RMSE scores of 1.06 d and 0.072 mag, respectively, while the TP subset performs even better at 1.00 d and 0.064 mag. These measures give us a high level of satisfaction with Model I, and we therefore consider it complete.

[11] As discussed in Section 4.2.3.1, our careful preparation of the Model I validation and testing sets ensures that they are supersets of the corresponding sets for Models II and III. Because of this, we can make predictions with the latter models on the former sets without concern for contamination.

4.4.2 Models II & III: Photometric Quantity Estimation

4.4.2.1 Preferred Hyperparameters

Models II and III are intended to determine the rest-frame phase and Δm_{15}, respectively, of a SN Ia from its spectrum, assuming that it is within the phase and light-curve shape bounds that Model I identifies (i.e., the spectrum is *in* the relevant domain). As previously stated, our primary metric for regression tasks is the RMSE, but we consider two secondary indicators when selecting the final hyperparameter values: (i) the slope of a linear fit to predictions as a function of ground truth values, and (ii) the maximum absolute difference between predictions and labels (henceforth MR, for maximum residual). The first diagnoses the directionality of prediction errors — systematic overestimates for low values and underestimates for high values are conveyed in a fitted slope of less than unity (and vice versa, though our models only bias in the aforementioned direction; see Section 4.4.2.5), and the second gives an indication of how homogeneous the absolute residuals are (when compared with the corresponding RMSE score). It is not sufficient for a set of hyperparameters to yield a competitive RMSE score; they must yield competitive scores across each of these three metrics.

We therefore identify the preferred hyperparameters for Models II and III using a tiered approach to our search results. First, we filter to select only those results that have a slope above and an MR below a fiducial value when evaluated against the relevant validation set. Then, from the resulting subset, we select the entry with the lowest RMSE score. In this way, the final, preferred Model II hyperparameters are chosen for yielding an RMSE of 1.15 d, a slope of 0.96, and an MR of 4.32 d and the Model III hyperparameters on the basis of yielding scores of 0.065 mag, 0.823, and 0.206 mag, respectively. The final networks have $\sim$ 75k and $\sim$ 320k trainable parameters, respectively. Although it is beyond the scope of this study to make any definitive or in-depth statements about the significance of the final hyperparameters, it is interesting to note the differences between those that yield the best observed performance in Models II and III. For example, we find that Model III performs best with a larger convolution kernel, k, than does Model II (35 for Model III versus 25 for Model II); this may indicate that features encoding phase information are generally narrower than those which encode Δm_{15}. At the same time, Model II requires fewer neurons in the fully connected layer than does Model III. This is consistent with our general intuition that phases are more "simply" codified in spectral features than Δm_{15} (or other luminosity indicators), which may be best parameterised by ratios of nonlocal features (as suggested by Nugent et al. 1995).

As a final refinement to the parameters that govern Models II and III, we study the effect of varying the number of stochastic forward passes (N) and dropout probability (p) when the models are used to generate predictions. To do so, we use Models II and III to generate predictions from the relevant validation set over a grid of (N, p) values and then tabulate the RMSE and mean estimated uncertainty at each point. The results (visualised in Figure 4.8) are generally consistent with our expectations: mean predicted uncertainties steadily grow

with p as do RMSE values, albeit at a much less significant rate. For Model III, both metrics show minimal dependence on N, but for Model II there are "bands" of improved RMSE performance at $N = 30$–80, 140–160, and beyond 180 (though they only outperform their surroundings by $\lesssim 0.2$ d). While our primary concern is optimising model performance (i.e., achieving low RMSE scores and "reasonable" uncertainty estimates), it is desirable from a compute-time perspective to use the lowest N value possible. We therefore select $(N, p) = (30, 0.02)$ for all `deepSIP` predictions. As Figure 4.8 clearly shows, this yields the desired low N (for fast prediction times) without compromising the quality of model predictions.

4.4.2.2 Performance on Testing Set

Having selected the final hyperparameters for each model, we make predictions on the relevant testing sets. As shown in Figure 4.9, we find strong agreement when we compare predictions to ground truth labels, achieving RMSE, slope, and MR scores of 1.00 d, 0.97, and 3.22 d; and 0.068 mag, 0.809, and 0.228 mag, respectively. For the 131 samples in each testing set, the median phase (Δm_{15}) residual is -0.19 d (0.001 mag); also, 94 (94) are within one standard deviation of the median, 122 (123) are within two, and 130 (129) are within three.

In Section 4.4.2.6, we investigate the quality of the uncertainty estimates produced by our models, which serve as a systematic error probe by quantifying the dispersion between N realisations drawn (for each input spectrum) from the underlying distribution that *is* each of our models. Here we do the opposite in an attempt to quantify statistical error: we remove the stochasticity from our models (by disabling dropout) and assess prediction robustness when they are fed perturbed inputs. We generate such inputs using our data-augmentation strategy (see Section 4.2.3.3) to bootstrap our Model II and III testing sets up to 5000 instances, each of which is slightly perturbed in redshift, noise, and signal length. The results, which we assess by means of the RMSE, are highly satisfactory: Model II yields 1.05 d and Model III delivers 0.080 mag, both broadly consistent with the corresponding measures reported above. One could potentially use a variation of this strategy to generate a unique statistical uncertainty estimate for each input spectrum and include that with each prediction, but we defer that task to future study and development.

4.4.2.3 Comparison with `SNID`-derived Phases

To contextualise the level of performance of Model II with regard to phase predictions, we attempt to characterise the spectra in the testing set using a series of `SNID` runs that adhere to the specifications[12] laid out by S20. When we do so, we find that `deepSIP` performs

[12]The `SNID` procedure is minimally intrusive, but intended to increase reliability by determining the type, subtype, redshift, and phase from a SN Ia spectrum in consecutive runs which progressively refine the set of templates used for comparison.

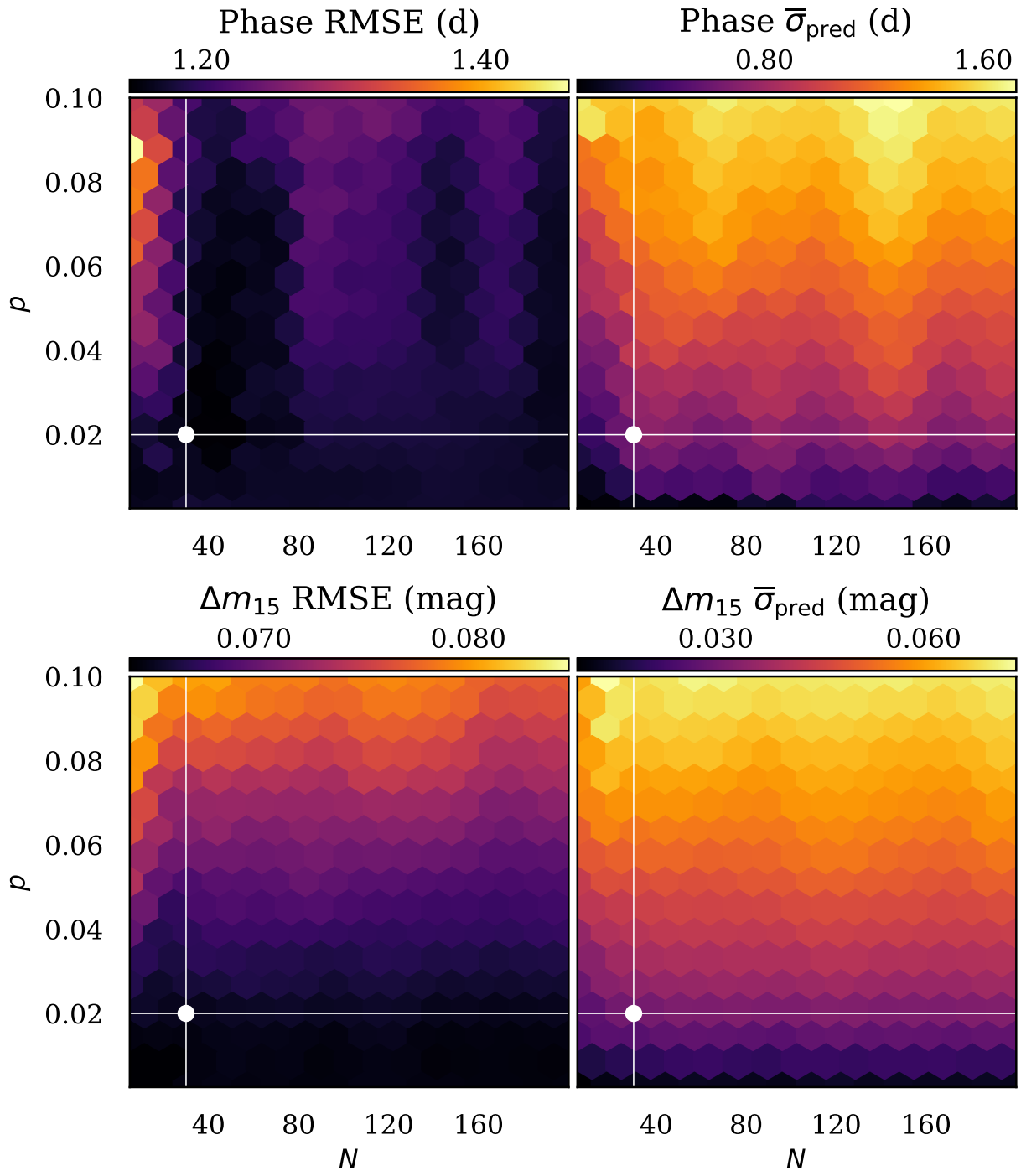

Figure 4.8: Validation RMSE and mean predicted uncertainty values for Models II and III over a grid of N and p values. A separate colour bar is provided for each panel, and the selected (N, p) set is indicated.

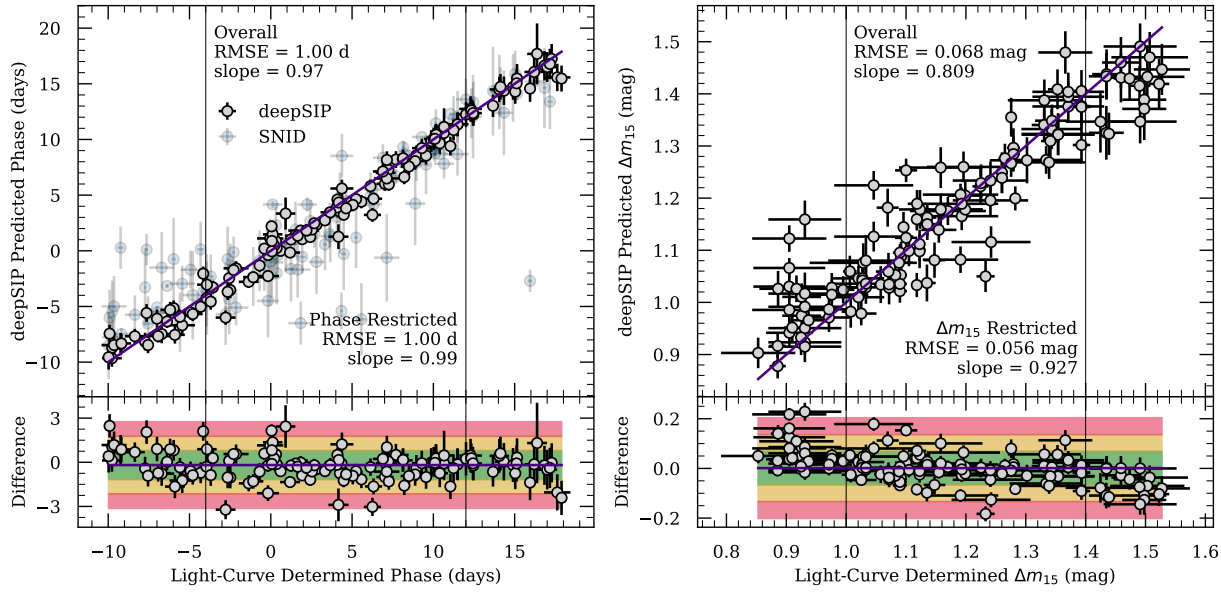

Figure 4.9: Phase (left panel) and Δm_{15} (right panel) determined by `deepSIP` versus ground truth values from the respective Model II and III testing sets, with residuals in the lower panels. The indigo line in each upper plot shows the one-to-one correspondence for ground truth values, while in the lower plots, it indicates the median residual. The green, yellow, and red regions indicate the $1\sigma, 2\sigma$, and 3σ bounds about the median residual, respectively. We mark the relevant RSME and slope, both globally and for a restricted subset (see Section 4.4.2.5) in each panel. `SNID`-based phase predictions are presented as an overlay to the upper-left panel, but they are omitted from the residuals for clarity.

significantly better than `SNID` in virtually every way. Whereas the `SNID`-based scheme (consisting of a total of four runs per spectrum, all of which are controlled and read using a `Python` script and hence subject to small `Python` overheads) takes ~ 7 min to process all 131 testing samples on a server with a modern CPU, our Model II (which entails a total of 30 stochastic forward passes per spectrum) takes under 1 s on a single NVIDIA Tesla K80 GPU to characterise preprocessed spectra (< 1 min on a modern, four-core CPU), with < 1 s for preprocessing. Moreover, the `SNID` approach fails to derive a phase in 18/131 instances while `deepSIP` is successful in making a prediction in all cases. Perhaps most significantly, the RMSE between those instances where `SNID` successfully predicts a phase and the true phases is 3.48 d, a factor of ~ 3.5 times worse (in RMSE; ~ 12 times worse in MSE) than that for our `deepSIP`-derived results. The `SNID` results are also much more afflicted by a bias to overestimate the earliest phases (a tendency that has been observed and discussed by S20 and others); the mean residual (predicted minus true) at phases from -10 d to -5 d is $+3.30$ d for `SNID`-derived results, but just $+0.31$ d for those from `deepSIP`. This bias is

also exhibited in the aforementioned fitted-slope metric, with `SNID` yielding a value of 0.80 compared to 0.97 for Model II.

4.4.2.4 Δm_{15} Consistency

Unfortunately, we are unable to perform an analogous `SNID`-based comparison for Δm_{15} values, but we can exploit a unique feature that the Δm_{15} labels possess to perform a separate test on the validity of Model III. Unlike phases which are are unique to individual spectra, Δm_{15} values are unique to individual SNe Ia. As a result, it is not uncommon for multiple spectra in the training, validation, or testing sets to map to the same Δm_{15} value. We can test how well Model III deals with this degeneracy by looking at the scatter (parameterised by the standard deviation) in Δm_{15} predictions in the testing set, grouped by distinct Δm_{15} label (and therefore, by distinct object).

When we do so, we find encouraging results which we summarise with the following observations: (i) as compared to the global scatter in predicted Δm_{15} values (0.161 mag), the median scatter in predicted values *per* distinct Δm_{15} label is just 0.018 mag; (ii) the observed distribution is positively skewed so that the majority of the scatter is near zero (e.g., the 25th percentile is 0.007 mag while the 75th percentile is 0.045 mag); and (iii) of the two examples with scatter > 0.07 mag, both are at or near the extremes of the predicted Δm_{15} values (i.e., where the model's predictions are typically the most uncertain and the training data are sparsest).

4.4.2.5 Biases

Though mitigated by our selection criteria (namely, our choice to enforce a 40 spectrum-per-bin saturation policy), Model II and (especially) Model III do exhibit some bias toward the more central values in their prediction ranges. This is unfortunate, but expected given the nonuniformity of our training data (e.g., see Figures 4.3 & 4.10). We emphasise that despite this bias, the *residual* distributions are approximately symmetric. Still, it is useful to quantify the extent of this bias, and we choose to do so by means of the previously mentioned slope of a linear fit to the results presented in Figure 4.9.

In doing so, we find a slope of 0.97 for phases and 0.809 for Δm_{15} values, confirming our suspicion that the bias is present (and more pronounced in Model III). However, if we select a more restrictive subset to exclude the biased ends (taken to be the equivalent of 1.5 bins from Figure 4.3; i.e., 6 d and 0.15 mag from each end), the fitted slopes improve to 0.99 and 0.927, respectively. The Model III RMSE value improves as well, dropping to 0.056 mag. Users of `deepSIP` may therefore choose to give more weight to results within these restricted ranges. Such improvements reinforce our belief that more performance could be extracted from our models with a larger and more balanced training set.

4.4.2.6 Estimated Uncertainties

The aforementioned metrics are quite satisfactory, but we must also verify the quality of the uncertainty estimates produced by our models. A basic measure of this is afforded by comparing RMSE to *weighted* RMSE values (henceforth, wRMSE), defined by

$$\text{wRMSE} = \sqrt{\frac{\sum_{i=1}^{N}(\hat{y}_i - y_i)^2 \hat{\sigma}_i^{-2}}{\sum_{i=1}^{N} \hat{\sigma}_i^{-2}}}, \tag{4.1}$$

where $\mathbf{y}$ are ground truth labels, and $(\hat{\mathbf{y}}, \hat{\sigma})$ are the corresponding predicted labels and estimated uncertainties (i.e., the mean and standard deviation of the stochastic samples generated as described in Section 4.3.1). A situation where wRMSE $>$ RMSE would reflect poorly on the uncertainty estimates because it would imply, in aggregate, an inverse correlation between them and residuals (i.e., model predictions are generally *more* wrong where the model is *more* certain); conversely, a situation where wRMSE $<$ RMSE is an affirmation (but not conclusive determination) of the quality of our uncertainty estimates because it suggests that model predictions are generally *more* correct where the model is *more* certain. In our case, the results are favorable (albeit at only a modest level): Model II yields a wRMSE score of 0.92 d while Model III yields 0.065 mag.

To further probe the quality of our estimated uncertainties, one might be tempted to study the relationship between estimated and true uncertainties (i.e., those derived from light-curve fits). This, however, would not be appropriate because the true uncertainties were not accounted for by our loss function during model training (nor anywhere else aside from selection cuts). Instead, we can ask a more appropriate question of our estimated uncertainties: *how do they behave relative to the data our models were trained on?* The answer, depicted in Figure 4.10, is encouraging. We see that our estimated uncertainties for both models are generally smallest in the region where training data are most abundant, and that the uncertainties grow steadily as the training data become more scarce. This captures the general behaviour we desire, though the uncertainties may be modestly underestimated (given the lower panels in Figure 4.9, but we defer an extensive study of this to future work). Thus, on the basis of this desired behaviour and all prior points elucidated above, we consider Models II and III ready for deployment.

4.5 Conclusion

In this paper we present and characterise the performance of `deepSIP`, an open-source software package that encapsulates a set of three CNNs that collectively map optical SN Ia spectra to their corresponding phases and light-curve shapes (parameterised by Δm_{15}). The treatment of these tasks with supervised learning — and the specific use of a CNN architecture — is a natural choice in many regards. This choice is rewarded with highly satisfactory performance.

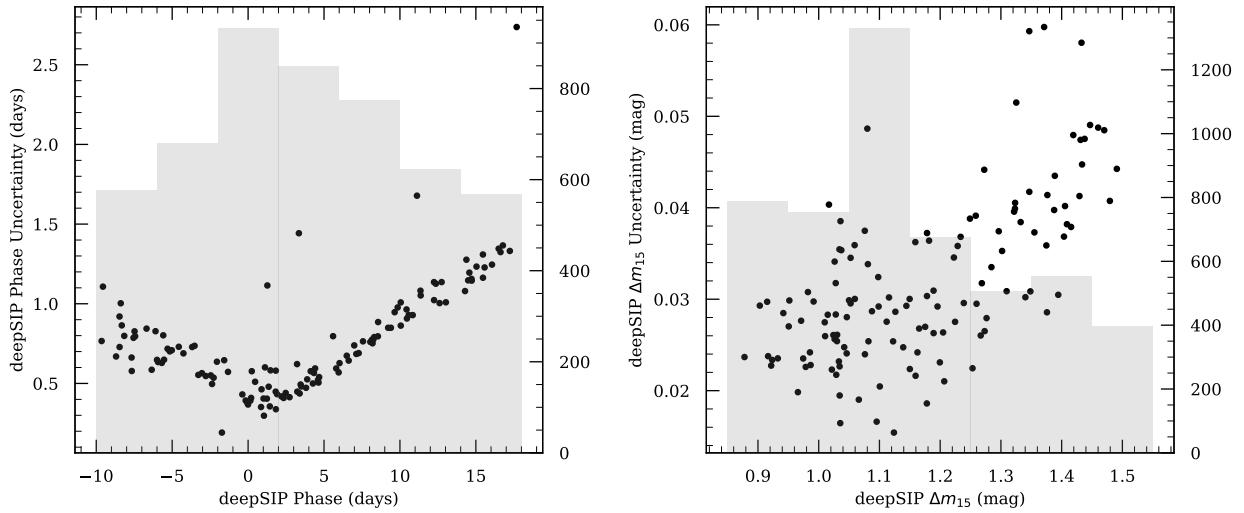

Figure 4.10: `deepSIP`-determined phase (left panel) and Δm_{15} (right panel) uncertainties versus predicted values from the respective Model II and III testing sets. The grey distributions behind each convey the relevant training data (including those from the augmented training set).

To train, validate, and test our models, we compile a significant collection of low-redshift SN Ia spectra by drawing from public data releases from the CfA, CSP, and our own BSNIP. These spectra form, after preprocessing, the inputs of the input-output pairs that our models learn to map. To assemble the corresponding outputs (i.e., phases and light-curve shapes), we draw from the photometric data releases of the same research campaigns, supplementing with five SNe Ia for which we publish light curves that have recently become available in our own archives. We fit all light curves (except for those from S19 and CSP3 who performed the same fits) using the `SNooPy` $E(B-V)$ model, ensuring systematic consistency between all phase and Δm_{15} values used herein. After all cuts are accounted for, our final compilation consists of 2754 spectra with photometrically-derived phase and Δm_{15} values, and of these, 1113 are within the phase and Δm_{15} constrained domain of interest for Models II and III.

Because we draw spectra from multiple sources, we take great care to both understand and mitigate systematic differences between sources so that our models form decision paths exclusively from physically significant features encoded in the spectra. Our mitigation strategy manifests chiefly in our preprocessing procedure which, among other things, discards any spectral information below 3450 Å or above 7500 Å. Though painful, this prevents our models from being affected by the presence or absence of signal at more extreme wavelengths — a distinction which on the red end almost perfectly segments CfA, CSP, and BSNIP spectra. We also let our desire for telescope agnosticism guide the data augmentation strategy that we employ to increase our modest sample size. In addition to a redshift perturbation, we vary the extent to which augmented spectra are smoothed and randomly drop signal from

the ends. The latter two actions serve to blur out the signature imparted by the specific equipment used to collect a given spectrum.

We describe the common neural network architecture which underlies each of our models and whose organisation and layout is largely motivated by our consideration of sequences of variance spectra. Under the assumption that spectral variations in SNe Ia are *mostly* a result of phase and light-curve shape (i.e., luminosity, via a width-luminosity relation), such sequences inform us about which regions in spectra most strongly encode a given target. Our observation of a relatively consistent set of features in such sequences has informed our adoption of a rather simple feed-forward network. To estimate uncertainties alongside point values for our targets, we use a probabilistic model provided by dropout variational inference. We employ a randomised grid search to determine the preferred set of hyperparameters for each of Models I–III, and upon doing so, set out to assess their performance.

To do so, we deploy each model against a distinct (i.e., unused during training and hyperparameter selection) testing set. In the case of Model I (a binary classifier of "in/out" with regard to a domain defined by $-10 \leq \text{phase} < 18\,\text{d}$ and $0.85 \leq \Delta m_{15} < 1.55\,\text{mag}$), we achieve an accuracy score of 94.6% and ROC AUC of 0.989. At a false-positive rate of 2.4%, Model I has an in-domain detection rate of 90.8%. With Model II (a continuous predictor of phases from $-10\,\text{d}$ to $18\,\text{d}$), we achieve an RMSE (wRMSE) of $1.00\,\text{d}$ ($0.92\,\text{d}$), a marked improvement over `SNID`-derived predictions on the same spectra. Finally, for Model III (a continuous predictor of Δm_{15} values from $0.85\,\text{mag}$ to $1.55\,\text{mag}$), we achieve an RMSE (wRMSE) of $0.068\,\text{mag}$ ($0.065\,\text{mag}$). These final, trained models are publicly available through `deepSIP` which provides an easy-to-use API for deploying them to characterise new SN Ia spectra. We strongly encourage public use of `deepSIP` for this purpose.

Looking to the future, we expect that the performance of `deepSIP` could be significantly improved as more spectra with corresponding light curves become available. Indeed, the dominant factor in our selection of the phase–Δm_{15} domain inside of which Models II and III offer predictions is the paucity of data available with more extreme light-curve shapes. As such data become more prevalent, the networks which underly `deepSIP` can easily be retrained and if necessary, modified to accommodate feedback between predicted phase and Δm_{15} values that may be necessary given the substantial feature evolution observed beyond the domain boundary. We welcome community involvement on these fronts (accumulating more data and designing more sophisticated network architectures), and intend to continue active, transparent development on our publicly hosted `GitHub` repository.

4.6 Supplementary Light Curves

In the time since the photometric dataset presented by S19 was published, we have continued to obtain host-galaxy template images for the unpublished SNe Ia in our archives. With these new observations, we are able to process five additional SNe Ia (SN 2007S, SN 2008hv, SN 2010kg, SN 2017hpa, and SN 2018oh.) of utility to this work. We therefore present their *BVRI* light curves (some also have unfiltered observations, which we refer to as *Clear*). All

processing steps are identical to those described by S19, so we provide only a brief summary of the methodology before delivering results.

All images were collected using either the 0.76 m Katzman Automatic Imaging Telescope (KAIT; Li et al. 2000; Filippenko et al. 2001) or the 1 m Nickel telescope, both of which are located at Lick Observatory where the seeing averages $\sim 2''$. After removing bias and dark current, flat-field correcting, and deriving an astrometric solution, we pass images to our automated photometry pipeline[13] (`LOSSPhotPypeline`; see S19), which handles all aspects of the remaining processing.

With host-galaxy template images obtained on dark nights using the Nickel telescope, the pipeline removes contaminating flux due to a SN's host galaxy and then performs point-spread function (PSF) photometry using procedures from the IDL Astronomy User's Library[14] to measure the SN's flux relative to selected standard stars in the same field. The resulting instrumental magnitudes are calibrated with at least two (but often more) of the selected standard stars from the Pan-STARRS1 Survey (PS1; Chambers and Pan-STARRS Team 2018). To do this, PS1 magnitudes are transformed to the Landolt (1992) system using the prescription given by Tonry et al. (2012), and then into the appropriate natural-system magnitudes using coupled equations of the form

$$b = B + C_B(B - V) + \text{constant}, \tag{4.2}$$
$$v = V + C_V(B - V) + \text{constant}, \tag{4.3}$$
$$r = R + C_R(V - R) + \text{constant, and} \tag{4.4}$$
$$i = I + C_I(V - I) + \text{constant}, \tag{4.5}$$

where natural (Landolt) system magnitudes are expressed in lower (upper)-case letters and C_X is the linear colour term corresponding to filter X (given in S19's Table 1). Temporally close (< 0.4 d) observations in the *same* passband are averaged together and then those in *distinct* passbands are grouped by their midpoint epoch to form natural-system light curves. Finally, the aforementioned equations are inverted to yield standardised light curves on the Landolt system. The uncertainties on each magnitude in our light curves are ultimately derived from three sources: "statistical" (e.g., Poisson variations in observed brightness, scatter in sky values, uncertainty in sky brightness), "calibration" (e.g., derived colour terms, uncertainty in PS1 magnitudes), and "simulation" (as described by S19).

We present the final Landolt-system light curves derived from the aforementioned processing steps in Figure 4.11. The final light curves are publicly available through our U.C. Berkeley SuperNova DataBase[15] (SNDB; S12; Shivvers et al. 2016) and in the Supplementary Materials included with the corresponding journal article. We describe our method for (and results from) fitting these light curves (and the others in our compilation) using `SNooPy` in the following section.

[13] `https://github.com/benstahl92/LOSSPhotPypeline`
[14] `https://idlastro.gsfc.nasa.gov/homepage.html`
[15] `http://heracles.astro.berkeley.edu/sndb/`

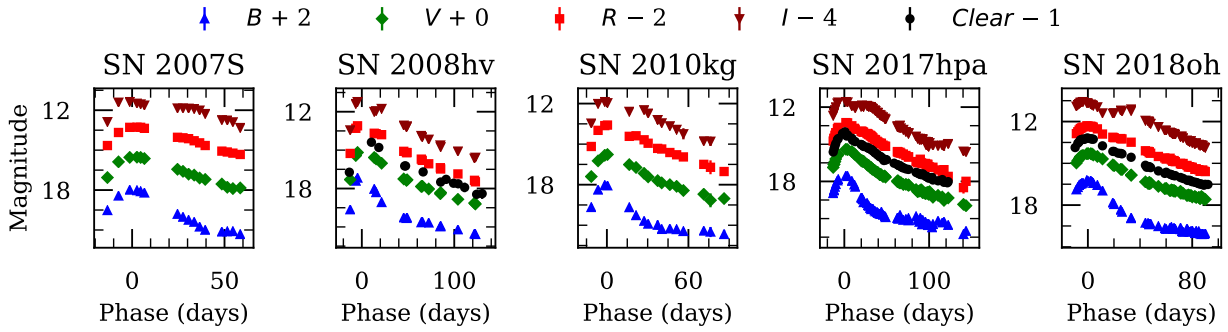

Figure 4.11: Observed light curves for the previously unpublished SNe Ia in our archives. In most cases the error bars are smaller than the points themselves. All dates have been shifted relative to the time of maximum B-band brightness. The light curves are available in tabular form through our SNDB and are also accessible via the online supplementary materials in the corresponding journal article.

4.7 Light-Curve Fitting

We use the $E(B-V)$ model as implemented by the `SNooPy` package to simultaneously fit the $BVRI$ (or subset thereof) light curves in our photometry compilation. The model assumes a peak B-band magnitude and $B-X$ colours parameterised by the decline rate, and the results from fitting are the time of maximum B-band light ($t_{\max}$), decline-rate parameter[16] (Δm_{15}), host-galaxy reddening, and distance modulus. We use the fitting results obtained by S19 and CSP for their datasets, and employ the strategy of the former to fit the remaining SNe Ia in our photometry compilation (i.e., those from G10 and CfA1-3). We give the resulting values of $t_{\max}$ and Δm_{15} for all SNe which pass a visual inspection for fit quality in Table 4.2, and defer a more thorough explanation of the fitting process to S19 (and their listed references).

[16]Though already stated, we emphasise again that Δm_{15} may deviate from $\Delta m_{15}(B)$, as discussed by Burns et al. (2011) and subsequently verified by S19.

Table 4.2: SNooPy Fitted Parameters.

SN	Source[a]	t_{max} (MJD)	Δm_{15} (mag)	SN	Source[a]	t_{max} (MJD)	Δm_{15} (mag)	SN	Source[a]	t_{max} (MJD)	Δm_{15} (mag)
1993ac	CfA1	49269.34 ± 0.70	1.098 ± 0.040	2001bg	G10	52039.95 ± 0.24	1.155 ± 0.029	2004dt	G10	53240.19 ± 0.18	1.136 ± 0.022
1993ae	CfA1	49289.15 ± 0.19	1.480 ± 0.022	2001br	G10	52051.78 ± 0.16	1.435 ± 0.024	2004fu	CfA3	53325.28 ± 0.48	1.170 ± 0.063
1994M	CfA1	49474.56 ± 0.29	1.331 ± 0.021	2001cj	G10	52064.98 ± 0.11	0.903 ± 0.013	2004fz	G10	53333.53 ± 0.10	1.473 ± 0.027
1994Q	CfA1	49495.35 ± 0.40	1.093 ± 0.020	2001ck	G10	52072.10 ± 0.12	1.079 ± 0.017	2005bc	G10	53469.96 ± 0.12	1.646 ± 0.028
1994S	CfA1	49517.90 ± 0.36	1.021 ± 0.038	2001cp	G10	52087.82 ± 0.08	0.884 ± 0.009	2005bo	G10	53478.10 ± 0.16	1.270 ± 0.008
1994ae	CfA1	49685.19 ± 0.10	1.058 ± 0.011	2001da	G10	52107.02 ± 0.19	1.149 ± 0.021	2005cf	G10	53533.85 ± 0.08	1.123 ± 0.008
1995D	CfA1	49767.78 ± 0.16	0.886 ± 0.012	2001dl	G10	52130.58 ± 0.12	1.022 ± 0.023	2005de	G10	53598.65 ± 0.10	1.216 ± 0.012
1995E	CfA1	49774.49 ± 0.22	1.069 ± 0.018	2001eh	G10	52168.42 ± 0.16	0.837 ± 0.006	2005eu	G10	53659.81 ± 0.12	1.099 ± 0.018
1995ac	CfA1	49992.44 ± 0.30	0.941 ± 0.036	2001en	G10	52192.43 ± 0.10	1.282 ± 0.005	2005hf	CfA3	53660.68 ± 0.95	1.449 ± 0.053
1995ak	CfA1	50022.22 ± 0.50	1.278 ± 0.018	2001ep	G10	52199.65 ± 0.17	1.133 ± 0.023	2005ls	CfA3	53714.40 ± 0.31	0.930 ± 0.033
1995al	CfA1	50028.26 ± 0.19	0.910 ± 0.014	2001ex	G10	52204.27 ± 0.28	1.813 ± 0.029	2005lz	CfA3	53735.82 ± 0.39	1.276 ± 0.031
1995bd	CfA1	50086.33 ± 0.15	0.937 ± 0.030	2001fe	CfA3	52229.01 ± 0.30	0.956 ± 0.019	2005mc	CfA3	53733.83 ± 0.22	1.733 ± 0.026
1996C	CfA1	50127.77 ± 0.33	0.965 ± 0.019	2002G	G10	52297.43 ± 0.43	1.145 ± 0.050	2005ms	CfA3	53744.16 ± 0.10	1.079 ± 0.018
1996X	CfA1	50190.73 ± 0.13	1.225 ± 0.009	2002aw	G10	52324.57 ± 0.25	1.123 ± 0.017	2005mz	CfA3	53745.01 ± 0.13	1.864 ± 0.003
1996ai	CfA1	50256.52 ± 0.38	1.112 ± 0.036	2002bf	G10	52335.09 ± 0.00	1.093 ± 0.032	2006X	G10	53786.01 ± 0.55	0.971 ± 0.038
1996bk	CfA1	50369.07 ± 0.55	1.758 ± 0.010	2002bo	G10	52356.29 ± 0.12	1.105 ± 0.014	2006ac	G10	53779.74 ± 0.51	1.199 ± 0.029
1996bl	CfA1	50376.23 ± 0.19	1.100 ± 0.019	2002bz	CfA3	52368.19 ± 0.53	1.366 ± 0.045	2006al	CfA3	53789.06 ± 0.35	1.569 ± 0.044
1996bo	CfA1	50386.51 ± 0.38	1.156 ± 0.036	2002cd	G10	52384.39 ± 0.23	1.101 ± 0.024	2006az	CfA3	53826.76 ± 0.13	1.354 ± 0.027
1996bv	CfA1	50403.42 ± 0.39	0.930 ± 0.023	2002cf	G10	52384.39 ± 0.10	1.823 ± 0.001	2006bb	CfA3	53815.83 ± 0.48	1.615 ± 0.018
1997bp	CfA2	50550.08 ± 0.43	1.114 ± 0.049	2002cr	G10	52409.07 ± 0.09	1.260 ± 0.007	2006bt	G10	53857.71 ± 0.23	1.091 ± 0.036
1997bq	CfA2	50558.43 ± 0.31	1.136 ± 0.031	2002cs	G10	52410.26 ± 0.17	1.097 ± 0.020	2006cc	CfA3	53874.13 ± 0.13	1.044 ± 0.030
1997br	CfA2	50559.90 ± 0.27	1.122 ± 0.027	2002cu	G10	52416.12 ± 0.10	1.461 ± 0.022	2006cp	G10	53896.91 ± 0.31	1.130 ± 0.054
1997cw	CfA2	50627.98 ± 0.44	0.811 ± 0.020	2002de	G10	52432.99 ± 0.16	1.071 ± 0.021	2006dm	G10	53928.20 ± 0.09	1.523 ± 0.017
1997do	CfA2	50766.18 ± 0.23	1.088 ± 0.023	2002dj	G10	52450.79 ± 0.35	1.149 ± 0.046	2006ef	G10	53968.14 ± 0.22	1.273 ± 0.012
1997dt	CfA2	50786.77 ± 0.23	1.341 ± 0.054	2002dl	G10	52451.92 ± 0.09	1.759 ± 0.007	2006ej	G10	53975.67 ± 0.17	1.498 ± 0.037
1998ab	CfA2	50914.39 ± 0.19	1.103 ± 0.021	2002do	G10	52441.42 ± 0.47	1.718 ± 0.010	2006em	G10	53976.32 ± 0.24	1.823 ± 0.001
1998bp	CfA2	50936.36 ± 0.18	1.800 ± 0.012	2002dp	G10	52450.38 ± 0.11	1.214 ± 0.008	2006en	G10	53970.97 ± 0.34	0.974 ± 0.021
1998de	G10	51025.70 ± 0.12	1.821 ± 0.001	2002eb	G10	52494.31 ± 0.08	1.067 ± 0.012	2006gr	G10	54012.41 ± 0.13	1.084 ± 0.017
1998dh	G10	51029.00 ± 0.12	1.118 ± 0.015	2002ef	G10	52489.88 ± 0.17	1.144 ± 0.019	2006hb	G10	54000.62 ± 0.29	1.693 ± 0.011
1998dk	CfA2	51057.17 ± 0.29	1.135 ± 0.015	2002el	G10	52507.93 ± 0.07	1.367 ± 0.020	2006le	G10	54047.74 ± 0.16	1.082 ± 0.018
1998dm	G10	51060.25 ± 0.12	1.008 ± 0.015	2002er	G10	52524.49 ± 0.16	1.140 ± 0.018	2006lf	G10	54045.03 ± 0.17	1.459 ± 0.032
1998ec	G10	51088.65 ± 0.93	1.146 ± 0.072	2002eu	G10	52520.22 ± 0.24	1.731 ± 0.010	2006mo	CfA3	54048.02 ± 0.35	1.653 ± 0.047
1998ef	G10	51113.19 ± 0.10	1.280 ± 0.007	2002fb	G10	52529.02 ± 0.09	1.824 ± 0.000	2006mp	CfA3	54053.92 ± 0.12	0.995 ± 0.019
1998eg	G10	51110.13 ± 0.70	1.117 ± 0.047	2002fk	G10	52547.13 ± 0.10	1.027 ± 0.010	2006oa	CfA3	54066.52 ± 0.19	0.953 ± 0.054
1998es	G10	51142.61 ± 0.07	0.925 ± 0.010	2002ha	G10	52580.77 ± 0.04	1.362 ± 0.008	2006qo	CfA3	54082.94 ± 0.15	1.054 ± 0.014
1999aa	G10	51231.89 ± 0.13	0.886 ± 0.014	2002he	G10	52585.40 ± 0.06	1.439 ± 0.011	2006sr	CfA3	54092.38 ± 0.14	1.279 ± 0.011
1999ac	G10	51249.98 ± 0.19	1.104 ± 0.022	2002hu	CfA3	52592.12 ± 0.13	1.089 ± 0.015	2006td	CfA3	54099.32 ± 0.14	1.422 ± 0.020
1999by	G10	51307.95 ± 0.10	1.824 ± 0.000	2002hw	CfA3	52595.63 ± 0.12	1.552 ± 0.027	2006te	CfA3	54096.89 ± 0.40	1.130 ± 0.021
1999cc	CfA2	51315.33 ± 0.18	1.344 ± 0.028	2002jg	G10	52609.62 ± 0.07	1.417 ± 0.019	2007O	G10	54122.77 ± 0.40	1.139 ± 0.041
1999cl	G10	51340.88 ± 0.22	1.144 ± 0.026	2002jy	CfA3	52634.02 ± 0.37	0.881 ± 0.026	2007S	this	54144.73 ± 0.24	0.836 ± 0.005
1999cp	G10	51362.61 ± 0.12	1.032 ± 0.021	2002kf	CfA3	52638.27 ± 0.43	1.236 ± 0.016	2007al	CfA3	54169.59 ± 0.25	1.857 ± 0.016
1999da	G10	51369.79 ± 0.09	1.823 ± 0.001	2003W	G10	52679.65 ± 0.23	1.130 ± 0.029	2007ap	CfA3	54168.31 ± 0.15	1.490 ± 0.018
1999dg	G10	51392.64 ± 0.32	1.509 ± 0.049	2003Y	G10	52676.54 ± 0.12	1.822 ± 0.001	2007au	G10	54183.75 ± 0.17	1.754 ± 0.017

Table 4.2 continued

SN	Source[a]	$t_{\max}$ (MJD)	Δm_{15} (mag)	SN	Source[a]	$t_{\max}$ (MJD)	Δm_{15} (mag)	SN	Source[a]	$t_{\max}$ (MJD)	Δm_{15} (mag)
1999dk	G10	51414.72 ± 0.13	1.103 ± 0.014	2003cg	G10	52729.24 ± 0.14	1.136 ± 0.015	2007bj	G10	54199.92 ± 0.70	0.905 ± 0.039
1999dq	G10	51435.95 ± 0.10	1.090 ± 0.012	2003ch	CfA3	52725.42 ± 0.35	1.274 ± 0.019	2007bz	CfA3	54213.68 ± 0.50	0.888 ± 0.051
1999ej	G10	51482.78 ± 0.06	1.565 ± 0.010	2003cq	G10	52737.64 ± 0.33	1.170 ± 0.023	2007ci	G10	54246.24 ± 0.18	1.732 ± 0.015
1999ek	CfA2	51481.16 ± 0.39	1.164 ± 0.016	2003du	G10	52765.71 ± 0.11	1.055 ± 0.007	2007co	G10	54264.07 ± 0.13	1.108 ± 0.020
1999gd	CfA2	51518.85 ± 0.53	1.168 ± 0.025	2003fa	G10	52806.74 ± 0.08	1.072 ± 0.009	2007cq	G10	54280.01 ± 0.16	1.148 ± 0.018
1999gh	CfA2	51513.29 ± 0.37	1.737 ± 0.008	2003gn	G10	52852.44 ± 0.09	1.399 ± 0.028	2007fr	G10	54301.70 ± 0.16	1.755 ± 0.013
1999gp	G10	51549.68 ± 0.12	1.076 ± 0.014	2003gs	G10	52847.65 ± 0.25	1.820 ± 0.001	2007qe	G10	54429.37 ± 0.24	1.128 ± 0.029
2000ce	CfA2	51666.53 ± 0.46	1.015 ± 0.034	2003gt	G10	52861.61 ± 0.06	1.095 ± 0.008	2007sr	G10	54447.66 ± 0.33	1.085 ± 0.015
2000cf	CfA2	51671.86 ± 0.29	1.144 ± 0.022	2003he	G10	52875.89 ± 0.11	0.956 ± 0.016	2008C	G10	54463.84 ± 0.53	1.100 ± 0.019
2000cn	G10	51706.76 ± 0.08	1.713 ± 0.008	2003hv	G10	52890.04 ± 0.09	1.554 ± 0.008	2008L	G10	54493.79 ± 0.14	1.545 ± 0.023
2000cp	G10	51719.52 ± 0.68	1.158 ± 0.070	2003ic	CfA3	52906.73 ± 0.71	1.425 ± 0.058	2008Q	G10	54504.62 ± 0.23	1.029 ± 0.090
2000cu	G10	51743.78 ± 0.10	1.502 ± 0.017	2003it	CfA3	52934.97 ± 0.21	1.435 ± 0.029	2008Z	G10	54514.74 ± 0.21	1.020 ± 0.043
2000cw	G10	51747.89 ± 0.17	1.153 ± 0.022	2003iv	CfA3	52933.94 ± 0.20	1.527 ± 0.047	2008af	CfA3	54503.68 ± 0.73	1.532 ± 0.041
2000cx	G10	51752.60 ± 0.15	1.265 ± 0.011	2003kf	G10	52980.13 ± 0.22	1.025 ± 0.025	2008ar	G10	54534.35 ± 0.17	1.113 ± 0.023
2000dk	G10	51811.79 ± 0.05	1.712 ± 0.005	2004E	G10	53014.95 ± 0.43	1.121 ± 0.023	2008dr	G10	54649.53 ± 0.22	1.463 ± 0.035
2000dm	G10	51815.25 ± 0.11	1.535 ± 0.017	2004S	G10	53039.57 ± 0.26	1.115 ± 0.013	2008ec	G10	54673.78 ± 0.09	1.341 ± 0.016
2000dn	G10	51824.52 ± 0.15	1.107 ± 0.023	2004as	G10	53084.66 ± 0.18	1.133 ± 0.037	2008ei	G10	54670.78 ± 0.75	1.142 ± 0.058
2000dr	G10	51833.97 ± 0.00	1.753 ± 0.007	2004at	G10	53091.65 ± 0.07	1.092 ± 0.009	2008hv	this	54817.01 ± 0.08	1.276 ± 0.007
2000fa	G10	51891.78 ± 0.12	0.974 ± 0.012	2004bd	G10	53096.93 ± 0.39	1.736 ± 0.007	2010kg	this	55543.89 ± 0.19	1.269 ± 0.014
2001E	G10	51926.16 ± 0.41	1.021 ± 0.058	2004bg	G10	53108.35 ± 0.22	1.024 ± 0.018	2017hpa	this	58066.66 ± 0.05	1.101 ± 0.005
2001V	G10	51971.43 ± 0.30	0.849 ± 0.013	2004bk	G10	53111.45 ± 0.46	0.892 ± 0.019	2018oh	this	58163.16 ± 0.07	1.064 ± 0.008
2001ah	G10	52005.19 ± 0.21	0.921 ± 0.036	2004br	G10	53147.60 ± 0.23	0.880 ± 0.022	SNF20071021-000	G10	54406.73 ± 0.18	1.180 ± 0.017
2001az	CfA3	52031.82 ± 0.59	1.016 ± 0.043	2004bv	G10	53160.48 ± 0.10	1.083 ± 0.010	SNF20080514-002	G10	54611.84 ± 0.13	1.393 ± 0.015
2001bf	G10	52044.66 ± 0.00	0.921 ± 0.025	2004bw	G10	53162.66 ± 0.11	1.323 ± 0.012	SNF20080909-030	G10	54730.08 ± 0.62	0.926 ± 0.032

Note: only fitted parameters used in our final compilation are presented. See CSP3 and S19 for the corresponding fits for their datasets.
[a]Sources of light curves used for fitting. Those marked by "this" refer to those that we publish here (see Section 4.6).

4.8 Usage

In tandem with this paper, we provide a well-documented[17] and easy-to-use `Python` package called `deepSIP`. The final, trained models presented herein are shipped with the code base, and hence, it is ready for deployment on new spectra. To use `deepSIP` for this purpose, one must prepare `spectra` as a `pandas` DataFrame with three mandatory columns: `SN, filename, z` for the for name(s) of the SN(e) Ia, their filenames, and their redshifts (it is assumed that the spectra need to be de-redshifted), respectively. Generating predictions is then accomplished as follows:

```
from deepSIP import deepSIP
ds = deepSIP()
predictions = ds.predict(spectra, status=True)
```

All necessary spectral preprocessing steps are performed automatically prior to generating predictions. No arguments are necessary to instantiate `deepSIP` under normal use cases (though one may give the keyword argument `drop_rate` to change the dropout probability). When generating predictions from `spectra`, three keyword arguments can — but need not be — invoked: (i) `threshold` sets the decision threshold for Model I (0.9 by default), (ii) `mcnum` sets the number of stochastic forward passes (30 by default), and (iii) `status` can be used to enable status bars. The returned `predictions` are provided as a `pandas` DataFrame with five columns: `Domain, prob_Domain, Phase, e_Phase, dm15, e_dm15`, corresponding to the respective predictions of Models I–III. Each row in `predictions` corresponds to the spectrum from the same row in `spectra`.

[17] `https://deepsip.readthedocs.io`

Chapter 5

The Snapshot Distance Method: Estimating the Distance to a Type Ia Supernova from Minimal Observations

A version of this chapter has been accepted for publication in *The Monthly Notices of the Royal Astronomical Society* (Stahl et al. 2021b).

Chapter Abstract

We present the snapshot distance method (SDM), a modern incarnation of a proposed technique for estimating the distance to a Type Ia supernova (SN Ia) from minimal observations. Our method, which has become possible owing to recent work in the application of deep learning to SN Ia spectra (we use the `deepSIP` package), allows us to estimate the distance to an SN Ia from a single optical spectrum and epoch of 2+ passband photometry — one night's worth of observations (though contemporaneity is not a requirement). Using a compilation of well-observed SNe Ia, we generate snapshot distances across a wide range of spectral and photometric phases, light-curve shapes, photometric passband combinations, and spectrum signal-to-noise ratios. By comparing these estimates to the corresponding distances derived from fitting all available photometry for each object, we demonstrate that our method is robust to the relative temporal sampling of the provided spectroscopic and photometric information, and to a broad range of light-curve shapes that lie within the domain of standard width-luminosity relations. Indeed, the median residual (and asymmetric scatter) between SDM distances derived from two-passband photometry and conventional light-curve-derived distances that utilise all available photometry is $0.013^{+0.154}_{-0.143}$ mag. Moreover, we find that the time of maximum brightness and light-curve shape (both of which are spectroscopically derived in our method) are only minimally responsible for the observed scatter. In a companion paper, we apply the SDM to a large number of sparsely observed SNe Ia as part of a cosmological study.

5.1 Introduction

Type Ia supernovae (SNe Ia) result from the thermonuclear runaway explosions of carbon/oxygen white dwarfs in binary star systems (e.g., Hoyle and Fowler 1960; Colgate and McKee 1969; Nomoto et al. 1984) in which the stellar companion may (e.g., Webbink 1984; Iben and Tutukov 1984) or may not (e.g., Whelan and Iben 1973) be another white dwarf. Despite our incomplete understanding of SN Ia progenitor systems and explosion mechanisms (see Jha et al. 2019, for a recent review), it remains an empirical fact that SNe Ia (or at least, a subset thereof) follow photometric (e.g., Phillips 1993; Riess et al. 1996; Jha et al. 2007) and spectroscopic (e.g., Nugent et al. 1995) sequences with regard to peak luminosity. This fact, in conjunction with their extraordinary luminosities, makes SNe Ia immensely valuable as cosmological distance indicators. Indeed, exploitation of the aforementioned photometric sequence, whereby the width of an SN Ia light curve is used to standardise its peak luminosity (hence the "width-luminosity relation" moniker), along with photometrically-derived corrections for reddening due to host-galaxy dust, led to the discovery of the accelerating expansion of the Universe (Riess et al. 1998; Perlmutter et al. 1999).

As the photometric samples of nearby (redshift $z \lesssim 0.1$; Riess et al. 1999; Jha et al. 2006; Hicken et al. 2009a; Ganeshalingam et al. 2010; Contreras et al. 2010; Stritzinger et al. 2011; Krisciunas et al. 2017; Foley et al. 2018; Stahl et al. 2019) and distant ($z \gtrsim 0.1$; e.g., Miknaitis et al. 2007; Frieman et al. 2008; Narayan et al. 2016) SNe Ia have grown, parameterisations of the SN Ia width-luminosity relation (WLR) have become increasingly robust (e.g., Guy et al. 2007; Burns et al. 2011). Together, these have aided in placing increasingly stringent constraints on the composition (Wood-Vasey et al. 2007; Kessler et al. 2009; Conley et al. 2011; Sullivan et al. 2011; Suzuki et al. 2012; Ganeshalingam et al. 2013; Betoule et al. 2014; Scolnic et al. 2018) and present expansion rate (Riess et al. 2016, 2019) of the Universe.

At the same time, the spectroscopic sample of SNe Ia has grown considerably (e.g., Silverman et al. 2012a; Blondin et al. 2012; Folatelli et al. 2013; Stahl et al. 2020b). Consequently, there has been forward progress in identifying spectroscopic parameters to potentially improve the precision of SN Ia distance measurements (e.g., Bailey et al. 2009; Wang et al. 2009; Blondin et al. 2011; Silverman et al. 2012c; Fakhouri et al. 2015; Zheng et al. 2018b; Siebert et al. 2019; Léget et al. 2020). Relatedly, recent work has demonstrated that Δm_{15}, a measure of light-curve shape — and hence, of peak luminosity via the SN Ia WLR — can be recovered from a single optical spectrum with a high degree of precision through the use of convolutional neural networks (using, e.g., the `deepSIP`[1] package; Stahl et al. 2020a, S20 hereafter). Moreover, owing to the data-augmentation strategy employed in the training of its models, `deepSIP` is robust to the signal-to-noise ratios (SNRs) of spectra it processes (we defer the reader to S20 for more details). In addition to Δm_{15}, `deepSIP` can also, again from a single optical spectrum, predict the the time elapsed since maximum light — i.e., the phase — of an SN Ia in the rest frame, from which the time of maximum brightness, $t_{\max}$, can be calculated. Together, these two quantities (Δm_{15} and $t_{\max}$) amount to half of those

[1] `https://github.com/benstahl92/deepSIP`

that are conventionally derived from a light-curve-fitting analysis, with other two being (i) a measure of the extinction produced by dust in the SN's host galaxy and (ii) the distance to the SN (see, e.g., Jha et al. 2007; Burns et al. 2011, for WLR implementations that function in this way).

As a result, a single SN Ia spectrum — via `deepSIP` — can powerfully constrain the family of light curves that could *possibly* correspond to that object. This motivates us to revisit the notion of a "snapshot" distance (Riess et al. 1998, hereafter R98): the idea that a single night's worth of SN Ia observations — an optical spectrum and one epoch of multiband photometry — is sufficient to estimate the distance to an SN Ia. Although photometric classification schemes are now available (e.g., Richards et al. 2012; Muthukrishna et al. 2019a), the results are not yet — and may never be — competitive with spectra. Hence, spectra are still the preferred method for classifying SNe (see, e.g., Filippenko 1997; Gal-Yam 2017, for reviews of SN classification), and as a result, a viable method of snapshot distances could render some cosmologically-motivated follow-up photometry unnecessary, thereby conserving valuable and limited observing resources.

In this paper, we present the snapshot distance method (SDM), a modern version of the initial concept established by R98. We describe the method itself in Section 6.3 before undertaking a rigorous and comprehensive study of its efficacy in Section 5.3. We conclude with a discussion of possible variations of the SDM and anticipated uses in Section 5.4.

5.2 The Snapshot Distance Method

As demonstrated by S20, the phase and light-curve shape of an SN Ia can be inferred (with an expected precision of $\sim 1.0\,\mathrm{d}$ and $\sim 0.07\,\mathrm{mag}$, respectively; see S20 for additional details) from an optical spectrum using `deepSIP`. This information, in conjunction with an apparent magnitude and an estimate of the extinction produced by host-galaxy dust (which can be derived from a single epoch of multiband photometry), is sufficient to estimate the distance to an SN Ia. Figure 5.1 provides a schematic representation of the procedure, which is also described comprehensively below.

While R98 treat this and the associated uncertainty estimation analytically within the multicolour light-curve shape (MLCS) formalism of Riess et al. (1996), we use the spectroscopically recovered parameters (and their uncertainties) as priors in a Markov Chain Monte Carlo (MCMC) fit of the $E(B-V)$ model from the `SNooPy` light-curve fitter to the available photometry (see Burns et al. 2011, for details on `SNooPy` and its capabilities). This has the advantage of allowing for the best estimates of the time of maximum brightness and light-curve shape — which are derived solely from an optical spectrum — to be updated in light of additional evidence: the multiband photometry. The resulting distance estimate is therefore derived from parameters that extract maximal utility from the available data.

Our algorithm for estimating the distance to an SN Ia from an optical spectrum and an epoch of multiband photometry that can, but need not, be contemporaneous, is as follows.

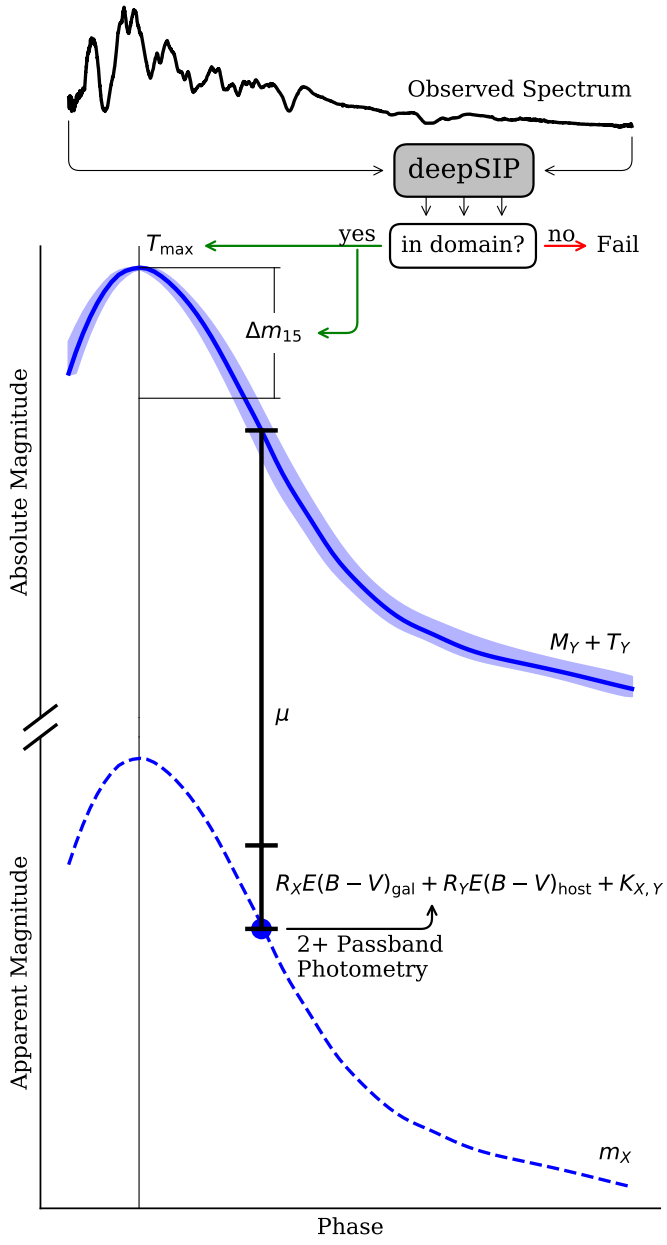

Figure 5.1: Schematic representation of the SDM applied to observations of SN 2017erp (Stahl et al. 2019, 2020b). Using `deepSIP`, the phase and light-curve shape (each with uncertainties) are extracted from an optical spectrum. These parameters alone are sufficient to derive the intrinsic luminosity evolution, $M_Y + T_Y$, in rest-frame passband Y (see Equation 5.1 for details). By comparing an observed magnitude, m_X, in the corresponding observer-frame passband (blue circle) to this evolution sampled at the epoch of the observed magnitude, the distance modulus can be readily derived after computing K-corrections and accounting for Galactic and host-galaxy reddening using a second observed magnitude in a distinct passband.

1. Using `deepSIP`'s Model I — a binary classifier — we determine if the spectrum belongs to an SN Ia with a phase and light-curve shape[2] satisfying the conditions $-10 \leq$ phase $< 18\,\mathrm{d}$ and $0.85 \leq \Delta m_{15} < 1.55\,\mathrm{mag}$, corresponding to the bounds within which `deepSIP` can reliably make continuous predictions with its other models. If the spectrum is classified as being within this "domain" in phase$-\Delta m_{15}$ space, we measure its phase and light-curve shape using Models II and III from `deepSIP`. The time of maximum brightness, $t_{\max}$, is then computed as the difference between the time at which the spectrum was observed minus the reconstructed phase, multiplied by a factor of $1 + z$ to express the time interval in the *observer* frame. As shown in Equation 5.1 and Figure 5.1, these two parameters are sufficient to reconstruct the intrinsic luminosity evolution of an SN Ia through the use of a WLR. In the work described herein, we use the `SNooPy` $E(B-V)$ model (Burns et al. 2011), but others could conceivably be used if `deepSIP` were retrained to predict the required light-curve-shape parameter.

2. We then perform an initial, nonlinear least-squares fit — holding $t_{\max}$ and Δm_{15} fixed at their `deepSIP`-determined values — to the available photometry using the $E(B-V)$ model, which takes the mathematical form

$$\begin{aligned} m_X(t - t_{\max}) = M_Y(\Delta m_{15}) + T_Y\left(t_{\mathrm{rel}}, \Delta m_{15}\right) + \mu + \\ R_X E(B-V)_{\mathrm{gal}} + R_Y E(B-V)_{\mathrm{host}} + K_{X,Y} \end{aligned} \tag{5.1}$$

   where X (Y) refers to the observed (rest-frame) passband, m is the observed magnitude, $t_{\mathrm{rel}} = (t' - t_{\max})/(1+z)$ is the rest-frame phase, M is the rest-frame absolute magnitude of the SN, T is a light-curve template[3] generated from the prescription of Prieto et al. (2006), μ is the distance modulus, $E(B-V)_{\mathrm{gal}}$ and $E(B-V)_{\mathrm{host}}$ are the reddening due to the Galactic foreground and host galaxy (respectively), R is the total-to-selective absorption, and $K_{X,Y}$ is the K-correction (Oke and Sandage 1968; Hamuy et al. 1993; Kim et al. 1996). In effect, this reduces the number of parameters fit from four $[\mu, E(B-V)_{\mathrm{host}}, t_{\max}, \Delta m_{15}]$ to two [μ and $E(B-V)_{\mathrm{host}}$], because the other two (i.e., $t_{\max}$ and Δm_{15}) are constrained directly by `deepSIP`. We show $K_{X,Y}$ — which is computed by warping the appropriate SED template from Hsiao et al. (2007) such that performing synthetic photometry on it yields colours that match those from the observed photometry — without its redshift, temporal, and extinction dependences for clarity. Thus, $K_{X,Y}$ depends *mostly* on the supplied photometric information, but the spectroscopically derived value for $t_{\max}$ factors into the calculation of t_{rel} as shown above. Note that in the low-redshift limit (within which we primarily work herein), X and Y are very nearly the same passband and the K-corrections are small.

[2] We note that Δm_{15} is a *generalised* light-curve-shape parameter, distinct from the traditional $\Delta m_{15}(B)$. The two may deviate randomly and systematically (see Section 3.4.2 in Burns et al. 2011).

[3] $M_Y(\Delta m_{15}) + T_Y\left(t_{\mathrm{rel}}, \Delta m_{15}\right)$ gives the absolute magnitude of an SN Ia having the specified light-curve shape in passband Y at the given phase.

3. The results from this initial fit serve as the starting point for the MCMC chains in the final fit, during which we fit for the full four parameters of the $E(B-V)$ model. In doing so, we employ Gaussian priors for $t_{\max}$ and Δm_{15} with means (standard deviations) set to the predictions (predicted uncertainties) derived from `deepSIP`'s Models II and III, respectively. All other facets of the model — e.g., priors for the other fitted parameters and values for static paremeters — are left at `SNooPy` defaults (see Burns et al. 2011, for more details). We adopt the distance modulus resulting from this final fit as our best estimate of the SN's distance.

5.3 Validating the Snapshot Distance Method

As argued in Section 6.3, it is possible — in principle — to estimate the distance to an SN Ia from a single epoch of multiband photometry and an optical spectrum. However, before such estimates can be made with any confidence, the SDM must be subjected to a rigorous assessment to quantify its effectiveness and reliability. We endeavor to administer such a "stress test" by constructing snapshot distances from a masked collection of (photometrically) well-monitored objects having at least one available optical spectrum. In the following subsections we describe this collection of photometric and spectroscopic observations, the details of our validation exercise, and quantitative statements that our results substantiate.

5.3.1 Data

In developing `deepSIP`, S20 assembled a significant compilation of low-redshift SN Ia optical spectra from the data releases of the Berkeley SuperNova Ia Program (BSNIP; Silverman et al. 2012a; Stahl et al. 2020b), the Harvard-Smithsonian Center for Astrophysics (CfA; Blondin et al. 2012), and the Carnegie Supernova Program (CSP; Folatelli et al. 2013) that they then coupled to photometrically derived quantities (i.e., $t_{\max}$ and Δm_{15}) obtained by either (i) refitting the SN Ia light curves published by the same groups (Ganeshalingam et al. 2010; Riess et al. 1999; Jha et al. 2006; Hicken et al. 2009a, the first for the initial Berkeley sample and the last three for the CfA sample), or (ii) taking the (identically derived) fitted parameters as directly published (Krisciunas et al. 2017; Stahl et al. 2019, the former for the CSP sample and the latter for the latest Berkeley sample).

Altogether, this sample is nearly ideal for our purposes — it consists of optical SN Ia spectra spanning a wide range of phases and light-curve shapes, both of which are ultimately determined from fits to well-sampled light curves — but we must impose two cuts on the full sample (i.e., the "in-domain" sample from S20 satisfying $-10 \leq \text{phase} < 18\,\text{d}$ and $0.85 \leq \Delta m_{15} < 1.55\,\text{mag}$; we defer the reader to S20 for more details) in order to proceed. First, we drop all spectra that were used to train[4] `deepSIP`. This ensures that `deepSIP`-based phase and Δm_{15} predictions used in constructing snapshot distances during validation are

[4]S20 allocated $\sim 80\%$ of their compilation for training, leaving the remainder (which we use in this work) for validation and testing.

not unrealistically accurate. Second, we drop all spectra corresponding to SNe Ia whose photometrically-derived parameters (e.g., Δm_{15}) were derived from the $uBVgriYJH$ observations published by Krisciunas et al. (2017) because, for simplicity, we prefer to use a consistent photometric system and set of passbands (i.e., standard $BVRI$) in the analysis described herein. Moreover, this second cut mitigates the potential for performance indicators that are favourably biased due to the fact that `SNooPy` was developed for use with CSP (and more generally, natural system) photometry — by removing these, our analysis proceeds with *only* Landolt-system data, thereby ensuring uniformity in the inputs to `SNooPy`. In the end, this leaves us with 190 spectra of 97 distinct SNe Ia, which are collectively covered by 2450 epochs of multipassband photometry.

5.3.2 Validation Strategy

With the aforementioned dataset, we are able to test the SDM at scale. We do so by generating snapshot distances — whereby we provide one epoch of photometry and one optical spectrum corresponding to the same SN Ia and generate a distance estimate according to the algorithm detailed in Section 6.3 — exhaustively across our dataset. Our strategy is organised as follows. For each spectrum in our dataset, we generate a distinct distance estimate by providing the `deepSIP`-inferred $t_{\max}$ and Δm_{15} values from the spectrum and every possible combination of a single photometric epoch in at least two passbands from the available photometry of the relevant SN Ia. Thus, for the typical $BVRI$ coverage available in the photometric component of our dataset, there are 11 unique passband combinations[5] and hence as many distinct distance estimates *per* single epoch of photometry. Altogether, then, a total of 34,721 distinct distance estimates are attempted after we remove those photometric epochs that have rest-frame phases outside the range spanned by -10 and 70 d (i.e., the full temporal extent of the light-curve templates used in fitting), as determined relative to the `deepSIP`-inferred $t_{\max}$.

5.3.3 Results

Of the 34,721 attempted distance estimates, only 238 fail during the preliminary least-squares fitting and a further 101 fail during the final MCMC fit. In contrast, when we repeat the exercise but do not provide the spectroscopically derived parameters (i.e., we attempt to fit only the sparse photometry), over 24,000 failures occur. This is, of course, expected because `SNooPy` (and indeed, all light-curve-fitting methods) is not intended to be used with a single epoch of photometry. Though the SDM failures represent only a small proportion of all attempts, it is important to understand their origin. Our investigations reveal that the dominant mechanism in these failure modes is the phase of the supplied photometric epoch. Aggregating over the 339 total failures, the median photometric phase is ~ 65 d, but just

[5]The 11 possible combinations for selecting 2+ passbands from $BVRI$ are BV, BR, BI, VR, VI, RI, BVR, BVI, BRI, VRI, and $BVRI$.

$\sim 15\,\mathrm{d}$ for those with successful fits. We reiterate that we impose an upper limit of 70 d with respect to photometric phases that we even attempt to fit, so the fact that the median failure has a photometric phase so near to the upper bound illuminates how skewed the distribution of failures is toward late phases. More concretely, it is negligible up to $\sim 30\,\mathrm{d}$, slowly grows from there until $\sim 60\,\mathrm{d}$, and then blows up beyond. This follows our expectation — SN Ia photometric evolution progresses more slowly at later phases, and thus, it is reassuring to find that when our method breaks down, it coincides with this late-time behaviour.

Before we delve into the quantitative efficacy measures discussed in the following paragraphs, it is important that we establish clear criteria for evaluation. We will henceforth consider the parameters derived from an $E(B-V)$ model fit to all available photometry for a given well-sampled object in our data compilation to comprise a set of "reference" values (hereafter, `SNooPy` reference values). The goal of the SDM is therefore to reproduce the reference values of our selected light-curve fitter (i.e., `SNooPy`) using a severely limited amount of data, and although we have assumed a specific light-curve fitter in our current implementation, our algorithm is sufficiently general to transcend it — the basic requirement would be to retrain `deepSIP` to predict the specific light-curve-shape parameter of relevance. In this spirit, we focus our subsequent study on our current SDM implementation's ability to reconstruct the `SNooPy` reference values described above, quantified in most cases by distance-modulus residuals,

$$\mu^{\mathrm{resid}} \equiv \mu^{\mathrm{SDM}} - \mu^{\mathrm{ref}}, \tag{5.2}$$

where μ^{SDM} is the distance modulus produced by the SDM for the data subset under consideration and μ^{ref} is that produced by a standard light-curve fitter (e.g., `SNooPy` in this case) without the use of spectral information, but with the object's full light curve.

The top-level result (see Figure 5.2) is encouraging: the median residual across all validation snapshot distances is just $0.008^{+0.138}_{-0.124}\,\mathrm{mag}$ (16th and 84th percentile differences are reported for scatter in this fashion here and throughout), and as we shall see in the following subsections, an even higher level of performance is realised when we restrict to the more information-rich maskings of our data. By way of comparison, the corresponding result for our "control" exercise (where we omit spectroscopically-derived quantities) is $-0.034^{+0.290}_{-0.288}\,\mathrm{mag}$.

Despite the notation used above and throughout (which we employ for compactness), we emphasise that the reported scatter values *should not* be confused with uncertainty estimates — indeed, they are in no way derived from μ^{SDM} error bars. To provide such an uncertainty estimate on a single metric (e.g., μ^{resid}) that describes our full set of residuals would be difficult, given the correlations induced by the repetition of spectra and photometry in our validation exercise. Instead, we perform another test where we pick three characteristic points in the photometric evolution of each distinct SN Ia in our sample: (i) "Earliest," corresponding to the first available photometric epoch for a given object; (ii) "Nearest to Max," for the photometric epoch closest to t_{max}; and (iii) "Latest," giving the last available photometric epoch. Iterating through each of the 11 distinct passband combinations available

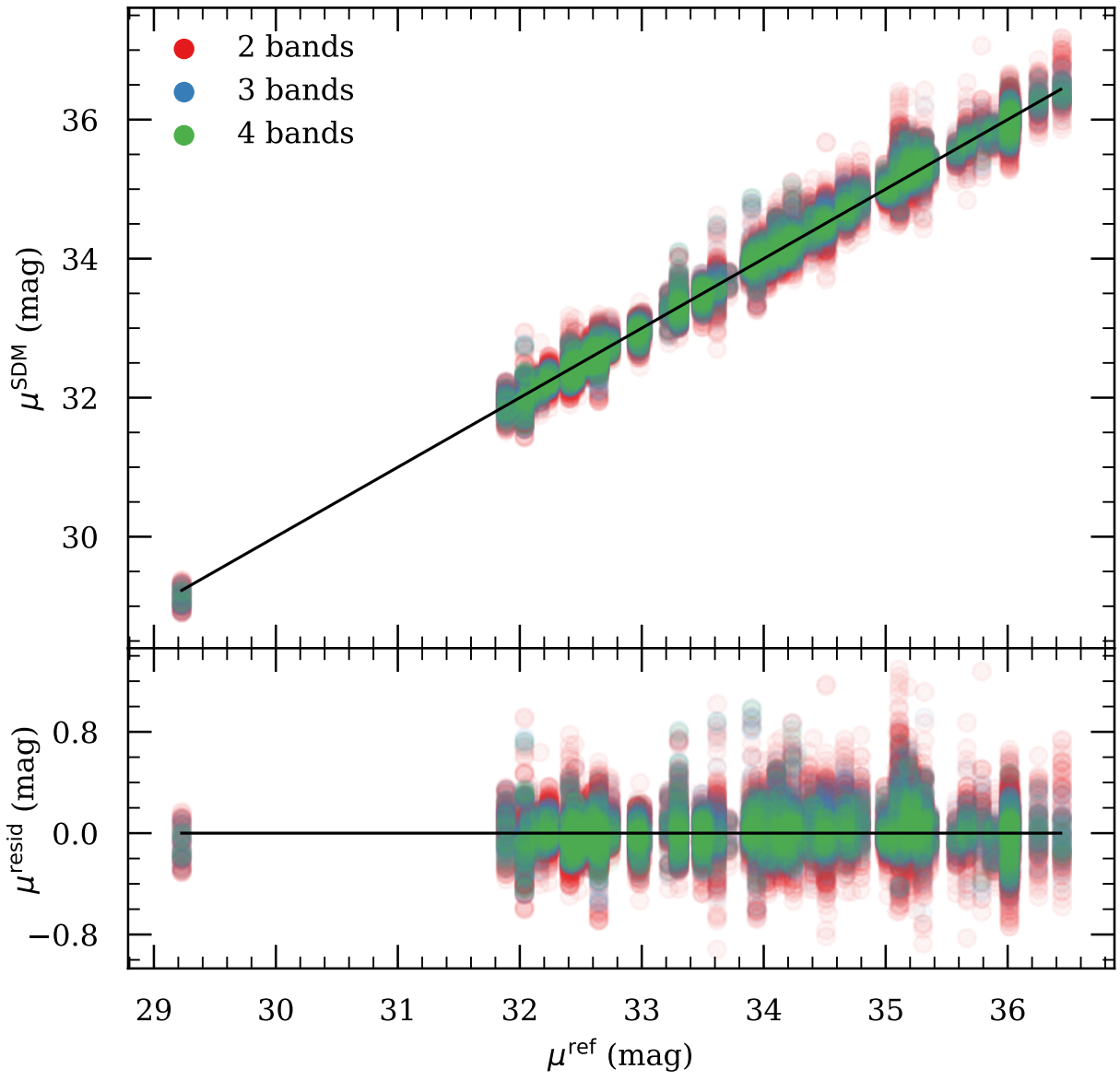

Figure 5.2: Comparison of SDM-derived distance moduli to their `SNooPy` reference values, with residuals in the bottom panel. Colours distinguish the number of passbands used for the single photometric epoch in the SDM fit.

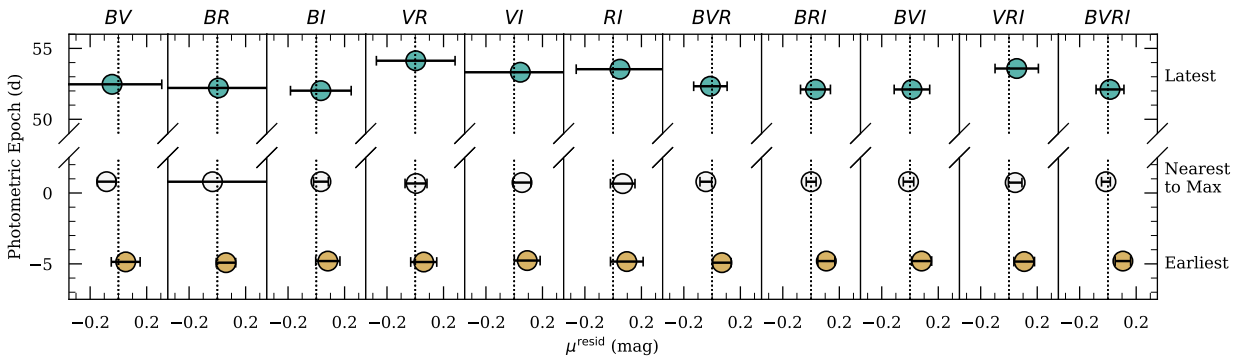

Figure 5.3: Mean residuals with propagated uncertainties in a grid determined by passband combination and representative photometric epoch. Each point uses a single value for each SN Ia in our compilation to derive the mean and its propagated uncertainty from SDM-distance error bars, thus avoiding data repetition and the correlations it can induce.

for our compilation, we select — for each distinct SN Ia in our sample — the single μ^{resid} value (and its error bar) corresponding to each of these photometric-evolution points, from which we compute the mean and its propagated uncertainty for each. In cases where multiple spectra are available for a given object, we use only the one closest to t_{max}.

These values, shown in Figure 5.3, represent aggregations over nonrepeated data, thus affording a proper uncertainty diagnostic that is free from artifacts introduced by correlation. Across the 33 distinct mean residual values (11 passband combinations $\times$ 3 characteristic photometric-evolution points), 25 are consistent (i.e., within their 1σ error bars) with zero. Aggregating over the selected photometric evolution points, we find that, given their generally large uncertainty values (median uncertainty: 0.21 mag) 11/11 "Latest" residuals are consistent with zero, while 9/11 "Nearest to Max" values (having a median uncertainty of 0.05 mag) are, and just 5/11 "Earliest" values (with a median uncertainty of 0.07 mag) are. Moreover, all are consistent with zero at the 2σ level. These results are satisfactory and consistent with our expectations: maximum performance is achieved when the photometric data are near maximum light, but the performance degradation at earlier or later times is not so significant as to mitigate the utility of the SDM.

5.3.3.1 Parameter Dependence

To search for biases in the snapshot distances generated by our validation exercise, we study distance-modulus residuals, μ^{resid}, as a function of temporal indicators, luminosity indicators inferred from `deepSIP` predictions, and spectrum SNRs, each segmented by the number of passbands included in the photometric epoch. The results, conveyed in Figure 5.4, are highly encouraging. We find that the distance-modulus residuals are consistent with zero and show no obvious correlation with `deepSIP`-predicted phase, rest-frame photometric epoch, rest-

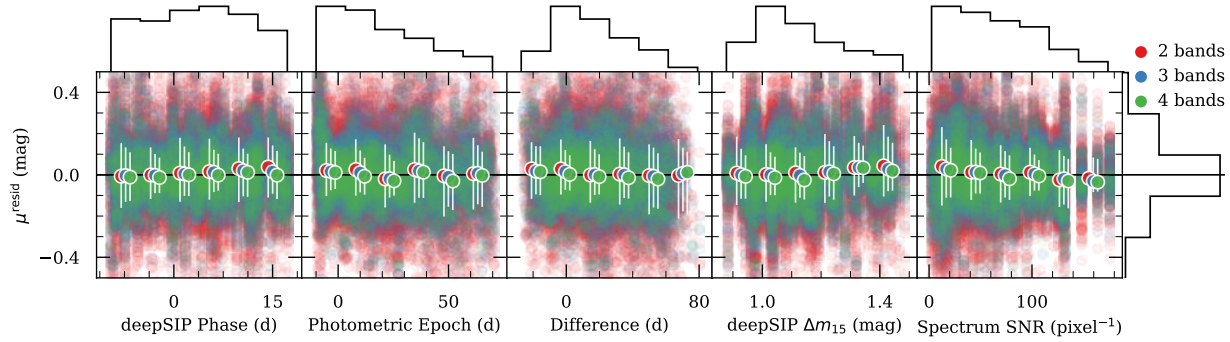

Figure 5.4: Distance-modulus residuals (SDM minus `SNooPy` reference) as a function of (from left to right) `deepSIP`-predicted phase, rest-frame photometric epoch relative to maximum, rest-frame difference between phase of photometric epoch and phase of spectrum, `deepSIP`-predicted Δm_{15} value, and spectrum SNR (the average pixel size of spectra in our compilation is 1.7 Å). The distributions of each quantity are projected outside the axes. Data points are colour-coded according to the same scheme as in Figure 5.2, and the white error bars signify the median residual (and its 16th and 84th percentile differences) for each fixed-width bin in the upper projections. The error bars — which are indicative of scatter, not propagated uncertainty — are slightly horizontally offset as a visual aid to see the number of passbands used in computing them, again denoted by colour.

frame difference between the phase of the photometric epoch and that of the spectrum, `deepSIP`-predicted Δm_{15}, or spectrum SNR. Moreover, we find that both the median absolute residual and scatter decrease as we permit more passbands to be included in the SDM fit (see Table 5.1 for a summary of all results, segmented by passband combination).

As evidenced in Table 5.1, the median residual for each of the 11 distinct passband combinations overlap within their scatter (and are all consistent with zero), but interestingly, the residuals for SDM fits using the BR passband combination perform markedly better than all other two-passband fits (having a median $\sim$ 3–8 times closer to zero), and better than all three-passband fits as well (except for BVI). The scatter for BR fits is competitive with that for $BVRI$ (and *much* tighter than all other two-passband combinations except BI), but the latter outperforms the median residual of the former by a factor of ~ 3. Though the origin of the relatively high quality of BR (and to a lesser extent, BI) SDM fits remains somewhat unclear, the fact remains that, at least for our data compilation, distances can be estimated to a very satisfactory degree of certainty using just one optical spectrum and two contemporaneous photometric points in distinct passbands (and the relative quality increases as more passbands are added). Moreover, given the relative scale of all scatter values reported in Table 5.1 relative to their corresponding median residual values, the discussion in this paragraph is, perhaps, nearing the limit of being overly detailed. We emphasise the main takeaway: that all median residual values are consistent with zero, given the scale of the

Table 5.1: Validation Results.

Bands	$\mathrm{med}(\mu^{\mathrm{resid}})$ (mag)	Bands	$\mathrm{med}(\mu^{\mathrm{resid}})$ (mag)	Bands	$\mathrm{med}(\mu^{\mathrm{resid}})$ (mag)
BI	$0.031^{+0.126}_{-0.120}$	BRI	$0.010^{+0.109}_{-0.092}$	$BVRI$	$-0.003^{+0.107}_{-0.097}$
BR	$-0.009^{+0.107}_{-0.098}$	BVI	$-0.008^{+0.109}_{-0.105}$		
BV	$-0.075^{+0.143}_{-0.156}$	BVR	$-0.024^{+0.107}_{-0.098}$		
RI	$0.053^{+0.177}_{-0.182}$	VRI	$0.056^{+0.127}_{-0.115}$		
VI	$0.049^{+0.145}_{-0.142}$				
VR	$0.053^{+0.149}_{-0.158}$				
2	$0.012^{+0.156}_{-0.143}$	3	$0.007^{+0.120}_{-0.107}$	4	$-0.003^{+0.107}_{-0.097}$

Note: The last row shows the results segmented by the number of passbands, instead of the specific combination. Following the convention of this paper, the median values are reported with 16th and 84th percentile differences to show the scale of the scatter.

observed scatter.

5.3.3.2 Fit Quality

Next, we investigate the quality of SDM fits by computing the residuals between realised model parameters in such fits and the corresponding `SNooPy` reference values for a given SN Ia. We present the one- and two-dimensional distributions of these residuals in Figure 5.5, and we note that they are best grouped into two categories: those determined largely by `deepSIP` from spectra (e.g., t_{max} and Δm_{15}) and those derived via the MCMC fit [e.g., μ and $E(B-V)_{\mathrm{host}}$].

The former (i.e., t_{max} and Δm_{15} residuals) are mostly — but not exclusively, as we shall shortly discuss — a measure of the quality of `deepSIP` predictions. From the one-dimensional distributions in Figure 5.5, we can see that `deepSIP`-predicted Δm_{15} values in aggregate fall within ~ 0.005 mag of the corresponding values from a fit to all photometry, and `deepSIP`-inferred t_{max} values to within ~ 0.05 d. Perhaps unsurprisingly, these metrics (derived from the final MCMC fit described in Section 6.3) represent a modest improvement over what is obtained by doing the preliminary least-squares fit. More significantly, the fact that we perform an MCMC fit is why the aforementioned metrics are not a perfect measure of the quality of `deepSIP` predictions — we allow our estimates for t_{max} and Δm_{15}, initially derived from an optical spectrum via `deepSIP`, to be updated in light of additional evidence: the photometric data. The fact that this procedure leads to superior agreement is a very promising result indeed; `deepSIP` predictions provide an excellent starting point for t_{max} and Δm_{15}, but both are generally even better fit when photometric information is taken into account. Moreover, it is precisely because of this that the "clumpiness" in the $t_{\mathrm{max}}^{\mathrm{resid}} - \Delta m_{15}^{\mathrm{resid}}$ distribution in Figure 5.5 gets modestly blurred out. This inherent

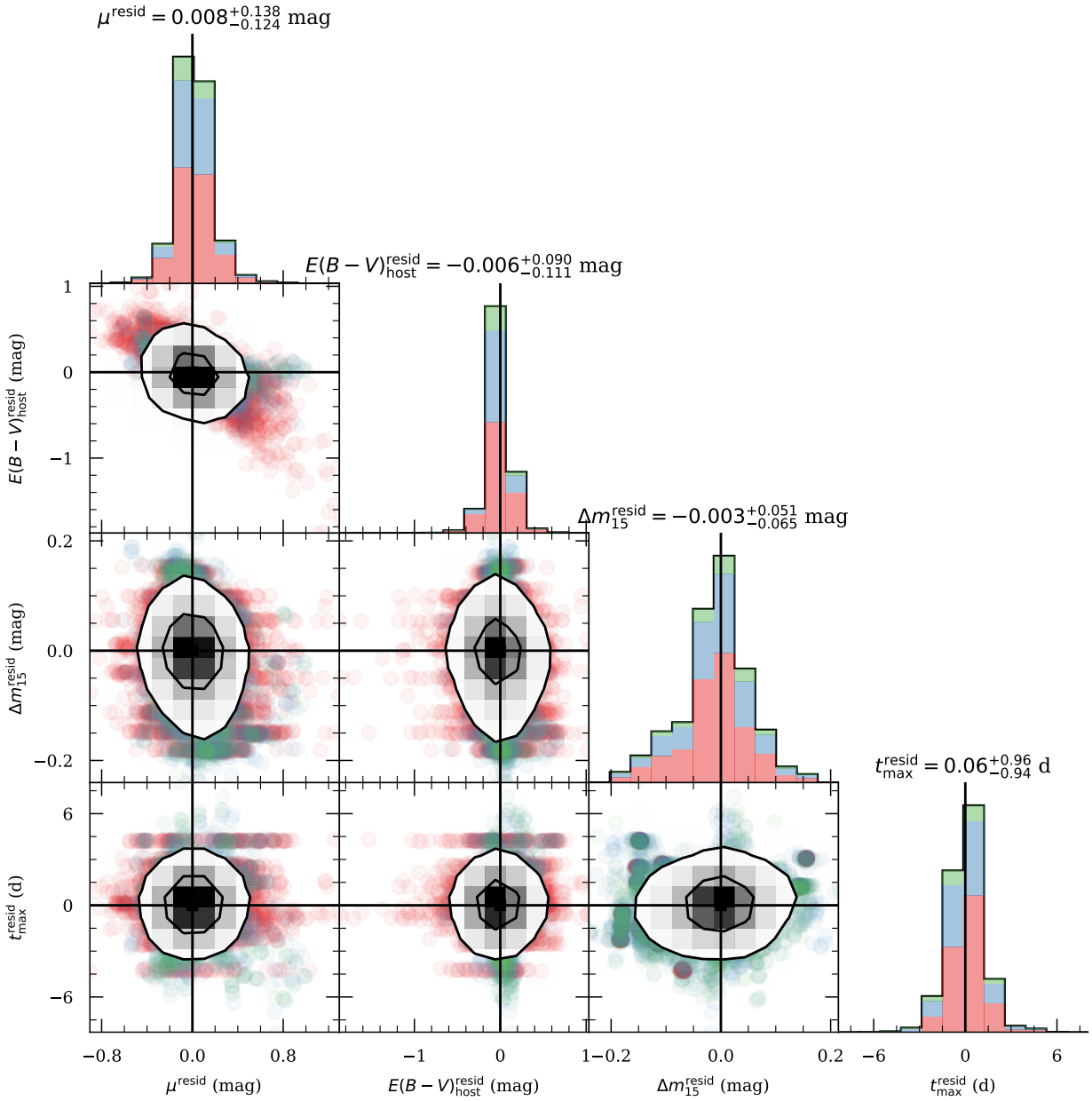

Figure 5.5: One- and two-dimensional projections of $E(B-V)$ model parameter residuals between SDM fits and `SNooPy` reference values (made with the `corner` package; Foreman-Mackey 2016). Data points and stacked histograms are colour-coded according to the same scheme as in Figure 5.2, and smoothed 1σ and 2σ contours are given in black. For each set of residuals, the median value and 16th and 84th percentile differences are labeled (the latter as an indicator of scatter, not propagated uncertainty), and vertical and horizontal lines are used to locate the expected zero-residual location.

"clumpiness" is expected owing to the fact that $t_{\rm max}$ and Δm_{15} are properties of a specific SN Ia, not a specific spectrum: many distinct points corresponding to different spectra, photometric epochs, and passband combinations should map to exactly the same point in the $t_{\rm max}^{\rm resid} - \Delta m_{15}^{\rm resid}$ distribution. We also note that the scatters in residuals (~ 0.06 mag for Δm_{15} and ~ 1 d for $t_{\rm max}$) are broadly consistent with the findings of S20 when they studied the quality of `deepSIP` predictions.

Moving now to the latter set of residuals [i.e., μ and $E(B-V)_{\rm host}$], we first remark on the quality of the fits: in aggregate, μ is recovered to $\lesssim 0.01$ mag with a scatter of ~ 0.13 mag while $E(B-V)_{\rm host}$ is recovered even more closely and tightly. As our focus in this work is on *distances*, we limit the following discussion to μ except for where $E(B-V)_{\rm host}$ has an impact. Looking at the left-most bottom two panels in Figure 5.5, we are encouraged to see nearly negligible dependence of the μ residuals on those for $t_{\rm max}$ or Δm_{15}. Indeed, the colour scale implies that the number of passbands used in the SDM fit has a much bigger impact on the quality of μ predictions, with 2-band fits (signified by red dots) visibly protruding from the horizontal edges of the 2σ contours, thereby broadening the distribution of distance-modulus residuals. The full, 4-band $BVRI$ fits (green dots), when visible, only "bleed" out from the top and bottom of the contours, thus maintaining the narrow subdistribution that is seen in the one-dimensional $\mu^{\rm resid}$ distribution at the top of Figure 5.5. There is some evidence for an inverse correlation between μ residuals and those for $E(B-V)_{\rm host}$, but this is unsurprising given the form of Equation 5.1: since the sum of $\mu + E(B-V)_{\rm host}$ is in part responsible for the observed magnitude, an overestimate by one can be compensated by an underestimate of the other. Regardless, the effect of this degeneracy is most pronounced for the 2-band fits which, as shown in Table 5.1, underperform the 3-band and 4-band fits in most regards.

5.4 Discussion

5.4.1 Summary

As we have shown in Section 6.3, it is possible to generate robust "snapshot" distance estimates to SNe Ia from a very limited observing expenditure — one optical spectrum and one epoch of multipassband photometry per object are sufficient. The optical spectrum, via `deepSIP`, delivers the *intrinsic* photometric evolution (parameterised in our case by $t_{\rm max}$ and Δm_{15}), and the epoch of photometry provides a sampling of this evolution, but in the *observer* frame. The discrepancy between the former and the latter is due *mostly* to the inverse-square law of light (i.e., because of the distance to the object), and the remainder can be appropriately modeled and accounted for using the colour information provided by the photometry.

To test the efficacy of our method, we assemble a compilation of SN Ia spectra with corresponding well-observed light curves from a larger set that was uniformly prepared by S20. Using this compilation, we generate $> 30,000$ snapshot distances by providing every possible combination of one spectrum and one epoch of 2+ passband photometry that fall

within minimally restrictive temporal bounds. We then compare these validation snapshot distances to the corresponding distances obtained from a light-curve fit to all available photometry (taken reference values), and use the residuals as an overall probe of our method's ability to reproduce the latter, `SNooPy` reference values.

To this end, our method performs very well, with a median residual between *all* snapshot distance moduli and their `SNooPy` reference counterparts of just $0.008^{+0.138}_{-0.124}$ mag. Performance roughly at this level is maintained over a wide range of rest-frame spectral (-10–18 d) and photometric (-10–70 d) phases, as well as Δm_{15} values (0.85–1.5 mag) and spectrum SNRs. Indeed, our investigations reveal that a much stronger determinant of performance is the number of passbands available in the single epoch of photometry — in aggregate, the median absolute residual and scatter decrease as we supply more contemporaneous photometric points in distinct passbands, reaching a level of $-0.003^{+0.107}_{-0.097}$ mag (a scatter in distance of just $\sim 5\%$ relative to the "true" values) when each epoch includes information in $BVRI$. This trend follows our intuition that SDM fits should be better constrained and hence of higher quality as more data are provided. Interestingly, however, one 2-passband combination (BR) and three 3-passband combinations (BRI, BVI, and BVR) have a similarly small degree of scatter, but none produces a median residual quite as close to zero.

5.4.2 Variations of the Snapshot Distance Method

Returning to the aforementioned trend (of increasing quality as more data are provided), we can investigate the extent to which adding data along the temporal dimension — as opposed to the wavelength dimension, which is accomplished by adding more contemporaneous passbands — reduces scatter. Such supplementation of temporal data can be accomplished either by providing additional spectra or additional epochs of multiband photometry, and the results can help us to identify which component of our method has the largest leverage in reducing the observed scatter in $\mu^{\rm resid}$. We therefore study both as follows.

5.4.2.1 Additional Spectra

The former is straightforward to implement. We simply repeat the validation exercise described in Section 5.3.2, except that instead of iterating over all spectra, we step through the 50 SNe Ia having at least two spectra in our compilation and set $t_{\rm max}$ and Δm_{15} for each object as the mean of the `deepSIP`-inferred values from all of the available spectra. Uncertainties are derived through error propagation.

The top-level result is $\mu^{\rm resid} = 0.013^{+0.129}_{-0.111}$ mag, consistent with the corresponding metric from our original validation exercise, albeit with slightly reduced scatter. A similar trend is realised when we look at the BR ($\mu^{\rm resid} = -0.008^{+0.090}_{-0.084}$ mag) and $BVRI$ ($\mu^{\rm resid} = 0.002^{+0.085}_{-0.071}$ mag) subsets. We find a "sweet spot" of ~ 3 spectra per object where the scatter is further reduced, and although one might expect a continuing trend of reduction as more spectra are provided, we do not see this in our *low-number-statistics* data for > 4 spectra per object. In any case (and independent of the number of spectra provided), the improved

metrics noted above only modestly outperform the results of our original validation exercise — spectra appear *not* to be the origin of most of the observed scatter. We take this to be an indication of the quality of `deepSIP` predictions: one spectrum, truly, is sufficient to robustly estimate $t_{\rm max}$ and Δm_{15}.

5.4.2.2 Additional Photometry

Testing the latter — i.e., incorporating additional epochs of photometry — is much more computationally expensive. With $(2,450\,\text{total epochs})/(97\,\text{SNe Ia}) \approx 25$ epochs of multiband photometry per object, on average, the task of handling all possible combinations of two epochs grows by a factor of 12 relative to the one-epoch case, and by a factor of 92 for the three-epoch case. As our primary validation exercise already takes $\sim 26\,\text{hr}$ to run on a modern 20-core server, it is hard to justify an even larger expenditure for this investigation, and even if we did, an exhaustive search over all possible combinations is simply intractable; e.g., there are $> 5 \times 10^6$ ways to select a sample of 12 from 25. We therefore perform another validation exercise, but instead of selecting all possible combinations, NCn, where N is the number of photometric epochs available for a given SN Ia and $1 \leq n < N$ is the subset size (this is the very expensive part), we select subsets using a simple "dilution" factor, ϕ. Specifically, we perform an identical exercise to that described in Section 5.3.2, except that instead of masking all but one epoch, we mask all but every ϕth epoch for $\phi = 2, 3, \cdots, 12$ (the special case of $\phi = 1$ corresponds to a fit to all available photometry, which we refer to as "`SNooPy` reference" throughout).

Unsurprisingly, the best results are found with $\phi = 2$ (corresponding to the densest temporal sampling, yielding $\mu^{\rm resid} = 0.011^{+0.075}_{-0.071}\,\text{mag}$), and particularly for the subset provided with simultaneous[6] $BVRI$ information in each epoch ($\mu^{\rm resid} = 0.005^{+0.021}_{-0.027}\,\text{mag}$). In the case of $\phi = 12$ (i.e., ~ 2 photometric epochs per SN Ia, on average) the corresponding metrics grow (in scatter) to $0.010^{+0.101}_{-0.097}\,\text{mag}$ and $0.003^{+0.067}_{-0.079}\,\text{mag}$, respectively. In comparing against "control" exercises (where we do not provide spectroscopically-derived quantities), we find comparable levels of performance up to $\phi = 4$ and then a growing trend of SDM outperforming the control with increasing ϕ (i.e., as the photometric coverage becomes more sparse). This suggests that above a certain threshold of photometric coverage, the SDM is consistent with, but not necessarily superior to, a conventional light-curve fit, but below this threshold, it offers significantly improved prediction power (as is our expectation).

As a result of this, we can identify two "levers" that wield significant influence over the scatter in $\mu^{\rm resid}$: (i) the number of simultaneous passbands provided per epoch (i.e., the wavelength-space extent of the SN Ia spectral energy distribution sampled at a specific instant; as we have concluded above, more is better), and (ii) the number of distinct multiband epochs of photometry available for the fit (i.e., the temporal-space extent of the SN Ia spectral energy distribution evolution, with sampling provided by the photometric observations; more is better). Neither appears to be decisively stronger than the other; e.g., the size of

[6] We consider photometric points within $\pm 0.001\,\text{d}$ of one another to be simultaneous.

the scatter reduction in taking $\phi = 12 \rightarrow 2$ in the global set is roughly the same as that harnessed in holding fixed $\phi = 12$ and going from the global set to the $BVRI$ subset. This suggests that sparser temporal coverage can be compensated for by providing more extensive wavelength coverage (i.e., supplying more passbands per epoch). Though it is beyond the scope of this study, it would be interesting to examine how well these conclusions are rederived by a more extensive (and necessarily, expensive) validation exercise that makes fewer simplifying assumptions than we have invoked here.

5.4.3 Applications and Future Work

There are, of course, many further variations that one could explore with regard to our method (e.g., the photometric contemporaneity requirement could be relaxed). Nevertheless, the studies presented herein demonstrate that the distance to an SN Ia can be robustly estimated from just one night's worth of observations, and that when more data are available, the estimates improve in quality until reaching a level of consistency with conventional light-curve fits. Thus, in the coming era of wide-field, large-scale surveys, our snapshot distance method will ensure maximal scientific utility from the hundreds of thousands of SNe Ia that will be discovered, but which may not be sufficiently well monitored to derive reliable distances by conventional means. Moreover, our method holds the prospect of "unlocking" a significant number of otherwise unusable observations that currently exist. As a case study, we present (in a companion paper) our use of the SDM to estimate the distances to > 100 sparsely observed SNe Ia which, when combined with a literature sample, deliver cutting-edge constraints on the cosmological parameter combination, $f\sigma_8$ (Stahl et al. 2021a).

Chapter 6

Peculiar-velocity Cosmology with Types Ia and II Supernovae

A version of this chapter has been submitted for publication in *The Monthly Notices of the Royal Astronomical Society* (Stahl et al. 2021a).

Chapter Abstract

We present the Democratic Samples of Supernovae (DSS), a compilation of 775 low-redshift Type Ia and II supernovae (SNe Ia & II), of which 137 SN Ia distances are derived via the newly developed snapshot distance method. Using the objects in the DSS as tracers of the peculiar-velocity field, we compare against the corresponding reconstruction from the 2M++ galaxy redshift survey. Our analysis — which takes special care to properly weight each DSS subcatalogue and cross-calibrate the relative distance scales between them — results in a measurement of the cosmological parameter combination $f\sigma_8 = 0.390^{+0.022}_{-0.022}$ as well as an external bulk flow velocity of $195^{+22}_{-23}\,\mathrm{km\,s^{-1}}$ in the direction $(\ell, b) = (292^{+7}_{-7}, -6^{+5}_{-4})\,\mathrm{deg}$, which originates from beyond the 2M++ reconstruction. Similarly, we find a bulk flow of $245^{+32}_{-31}\,\mathrm{km\,s^{-1}}$ toward $(\ell, b) = (294^{+7}_{-7}, 3^{+6}_{-5})\,\mathrm{deg}$ on a scale of $\sim 30\,h^{-1}\,\mathrm{Mpc}$ if we ignore the reconstructed peculiar-velocity field altogether. Our constraint on $f\sigma_8$ — the tightest derived from SNe to date (considering only statistical error bars), and the only one to utilise SNe II — is broadly consistent with other results from the literature. We intend for our data accumulation and treatment techniques to become the prototype for future studies that will exploit the unprecedented data volume from upcoming wide-field surveys.

6.1 Introduction

In observational cosmology, Type Ia supernovae (SNe Ia) — titanic explosions of white dwarfs in multistar systems (e.g., Hoyle and Fowler 1960; Colgate and McKee 1969; Nomoto et al. 1984) — are highly prized for their standardiseability via the so-called "width-luminosity relationship"[1] (WLR; e.g., Phillips 1993; Riess et al. 1996; Jha et al. 2007; Guy et al. 2007; Burns et al. 2011), which imbues them with the property of being precise extragalactic distance indicators. Exploiting this property with statistical samples of SNe Ia has borne considerable fruit, including the discovery of the accelerating expansion of the Universe (Riess et al. 1998; Perlmutter et al. 1999), as well as the identification of a tension between local and distant measurements of the Hubble constant (as reviewed by Riess 2019). More recently, SNe II — colossal explosions of massive, evolved, hydrogen-envelope-bearing stars via core collapse (see, e.g., Smartt 2015, for a review) — have been used for such purposes (e.g., de Jaeger et al. 2020a,b) owing to their standardiseability via the standard candle method (SCM; Hamuy and Pinto 2002).

In both sets of aforementioned cosmological analyses, recession velocities (i.e., redshifts) are compared to luminosity distances (i.e., distance moduli) to constrain the relevant cosmological parameters (see, e.g., Jha et al. 2019, and references therein). There exists, however, a distinct set of cosmologically important parameters that can be probed not by the relationship between the aforementioned observables, but instead by the residuals that remain between them after removing a fiducial cosmological model (e.g., Peebles 1993; Huterer and Shafer 2018; Scolnic et al. 2019). Discounting unmodeled diversity in the underlying populations of SNe Ia and SNe II (which is still considerable in the latter), a significant contributor to these residuals comes from peculiar velocities — i.e., deviations from the Hubble flow that are gravitationally induced by inhomogeneities. In turn, this makes SNe Ia (and now, for the first time thanks to the SCM, SNe II) an excellent probe of peculiar velocities (e.g., Miller and Branch 1992; Riess et al. 1997a; Weyant et al. 2011; Tully et al. 2016), as well as quantities derivable from them such as bulk flows in the nearby Universe (which can shed light on the structures driving the flows of galaxies; e.g., Riess et al. 1995; Colin et al. 2011; Dai et al. 2011; Feindt et al. 2013; Mathews et al. 2016) and the cosmological parameter combination $f\sigma_8$ (e.g., Turnbull et al. 2012; Howlett et al. 2017; Huterer et al. 2017; Boruah et al. 2020).

Though our analysis touches on each of these facets, our primary focus is on $f\sigma_8$, which can be decomposed as the dimensionless growth rate, $f = \frac{d\ln D}{d\ln a}$ (where D is the growth function of linear perturbations and a is the scale factor; see Peebles 1993), times the matter overdensity root-mean-squared fluctuations in a sphere of radius $8\,h^{-1}$ Mpc, σ_8. The link back to peculiar velocities is provided by linear perturbation theory (Peebles 1993) via

$$\mathbf{v}(\mathbf{r}) = \frac{H_0 f}{4\pi} \int d^3\mathbf{r}' \delta(\mathbf{r}') \frac{\mathbf{r}' - \mathbf{r}}{|\mathbf{r}' - \mathbf{r}|^3}, \tag{6.1}$$

[1]Here, "width" is with regard to an optical light curve, thus capturing the characteristic luminosity evolution timescale.

where $\delta = \rho/\overline{\rho} - 1$ is the overdensity field. Through $f \approx \Omega_m^\gamma$ (where, e.g., $\gamma = 0.55$ for general relativity and a simple function of the dark energy equation of state in general; see Linder and Cahn 2007), a constraint on $f\sigma_8$ can serve as a test of gravity (e.g., Said et al. 2020). As Linder (2013) show in their Figure 2, $f\sigma_8$ is most influenced by γ at low redshifts. Thus, the use of SNe II in our analysis (in addition to a large sample of SNe Ia as described below) yields a tertiary benefit beyond (i) increasing statistical weight via a larger sample, and (ii) laying the foundation for future such analyses, of (iii) lowering the aggregate redshift of our full sample.

Still, as noted, the bulk of our sample is intentionally composed of SNe Ia: they (with typical distance uncertainties of $\lesssim 10\%$ after standardisation via a WLR) offer more constraining power per unit object than do SNe II (with distance uncertainties of 10–15% after applying the SCM; de Jaeger et al. 2020a) and galaxies (with distance uncertainties of $\sim 25\%$ after applying scaling relationships; e.g., Said et al. 2020). An unfortunate requirement, however, of applying a standard WLR-based standardisation to SN Ia observations is that the requisite photometry must be sufficiently well sampled to reconstruct the "width" of the light curve. Consequently, there exists a significant set of SN Ia observations that have not been used in cosmological analyses (SNe Ia are routinely cut for having too few epochs of photometry; e.g., Betoule et al. 2014; Foley et al. 2018).

With the advent of `deepSIP` (Stahl et al. 2020a), this requirement and the waste it incurs can be mitigated *if* an optical spectrum is available — by using a sophisticated convolutional neural network trained on a significant fraction of all relevant SN Ia observations, `deepSIP` is able to map the spectrum of an SN Ia to its corresponding light-curve shape with impressive precision. In turn, this has enabled the snapshot distance method (SDM; Stahl et al. 2021b), which allows SN Ia distances to be estimated with as little as one spectrum and two photometric points in different passbands. For the first time ever, we use the SDM to "resurrect" a significant sample of SNe Ia which would otherwise have to be discarded in cosmological studies, and we include this sample in our analysis.

The remainder of this paper is organised as follows. First, we describe our accumulation of a sizeable dataset (Sec. 6.2) consisting of SNe Ia and SNe II, and then provide a comprehensive description of our analysis methodology (Sec. 6.3). We present our results in Section 6.4 and then offer conclusions in Section 6.5. Throughout we assume a flat ΛCDM cosmology with $\Omega_m = 0.3$ and $h = \mathrm{H}_0/(100\,\mathrm{km\,s^{-1}})$, where H_0 is the local Hubble constant.

6.2 Data

6.2.1 Type Ia Supernovae

6.2.1.1 Amended Second Amendment SN Ia Compilation

As a starting point we turn to the — until now — largest ever peculiar-velocity catalogue derived from nearby SNe Ia: the Second Amendment (A2) compilation of 465 SN Ia distances (Boruah et al. 2020). A2 draws SNe Ia from the third Carnegie Supernova Program

(CSP) data release (Krisciunas et al. 2017), the Lick Observatory Supernova Search (LOSS) cosmology sample (Ganeshalingam et al. 2013), the first Foundation Supernova Survey data release (Foley et al. 2018), and the First Amendment (A1) compilation (Turnbull et al. 2012), which is itself an aggregation of SNe Ia from the first CSP data release (Folatelli et al. 2010) and the "Constitution" set (Hicken et al. 2009b), atop which the "Amendments" are made.

Though nicely organised and homogenised in many regards, the A2 compilation remains fundamentally heterogeneous. For example, the A1 and CSP DR3 subcatalogs consist of distance moduli (derived using *different* light-curve fitters), while the Foundation and LOSS subcatalogs provide only SALT2 (Guy et al. 2007) light-curve parameters[2], from which distances are derived using the Tripp (1998) formula,

$$\mu = m_B - M + \alpha x_1 - \beta_{\rm SN} c, \tag{6.2}$$

where we have added the "SN" subscript to β to avoid any confusion with $\beta = f/b$ used elsewhere in our analysis. Our analysis method (see Sec. 6.3) is therefore carefully formulated to account for these and other differences between subcatalogs, ensuring (among other things) a consistent relative distance scale and proper weighting.

For the analysis described herein we use an *amended* version of A2 (hereafter A2.1), derived by removing[3] all duplicates of individual SNe Ia from A2. Though scientifically important in the sense that it prevents any particular peculiar-velocity signal from having an artificially high weight in our fit, this removes just 13/465 distances. As a result, prior and future analyses that use the full A2 set (instead of the 452 in A2.1) should only suffer from a minimal (perhaps imperceptible) bias due to duplication.

6.2.1.2 Lick Observatory Supernova Search Sample

In the time since the publication of the first LOSS data release (Ganeshalingam et al. 2010) — the source for many of the low-redshift objects used in the LOSS cosmology sample — the LOSS team has continued to perform multiband photometric and spectroscopic follow-up observations of newly discovered SNe Ia (Stahl et al. 2019, 2020b,a). We draw from these new data to construct LOSS2.0: a set of 45 distinct (from A2.1) SNe Ia that pass minimal cuts for utility and reliability. In contrast to the SALT2 parameters of LOSS1.0 (from A2.1), LOSS2.0 is a catalog of distance moduli taken directly from the `SNooPy` (Burns et al. 2011) fits that were published in accompaniment to the light curves from which they were derived, and then uniformly shifted to be consistent with our fiducial distance scale. The corresponding redshifts are all firmly established from SN host galaxies and in the CMB frame, except that those objects known to be within a group of galaxies have their redshifts updated to that of their host group. This is consistent with the preparation of A2 (and hence

[2]The parameters derived from fitting the SALT2 model to a multipassband temporal series of SN Ia fluxes (i.e., a multiband light curve) are m_B, the observed B-band magnitude at maximum light; x_1, the light-curve stretch parameter; and c, the colour parameter.

[3]In cases of duplicated SNe Ia, we choose which set of data to keep by using the following order of preference (highest first): CSP DR3, CSP DR1 (in A1), LOSS, Constitution (in A1).

A2.1; Boruah et al. 2020), and helps to mitigate the noise induced by the velocity dispersion between member galaxies.

6.2.1.3 Snapshot Distances Sample

The amalgamation described above (A2.1 + LOSS2.0) is, perhaps, the largest ever compilation of low-redshift SN Ia distances ever assembled, utilising the collective observations of many campaigns over the last 30+ years. With conventional methods (i.e., applying a WLR to well-sampled SN Ia light curves), one would find that this set already accounts for the majority of data that are publicly available. However, this set *can* be further expanded by employing the SDM, which removes the requirement that light curves be well sampled in exchange for providing an optical spectrum. We therefore devote this section to describing the accumulation of a significant sample of SDM-derived distances for sparsely observed SNe Ia.

To do so, we turn to the Open Supernova Catalog[4] (OSC; Guillochon et al. 2017) which, as of the date of our original query, contained a total of 64,715 transients with 14,140 classified as some form of SN Ia. From this subset, we impose three additional cuts to derive our initial candidate pool for the SDM: (i) we keep only those 6359 that have redshift $z < 0.07$ as required by our analysis method (see Sec. 6.3), (ii) of these, we keep those 3951 that have at least one spectrum, and (iii) we keep those 2900 objects that, in addition to the above, have at least two epochs of photometry. We emphasise that these cuts yield only an *initial* sample of candidates that satisfy the most basic prerequisites of our analysis.

Following a sequence of judiciously chosen cuts to ensure quality, consistency, and compatibility (see Appendix 6.6 and Figure 6.1), we perform the SDM and as a check, a naïve fit to the light curves using no `deepSIP`-derived information. The top-line results are consistent with our high expectations for the power of the SDM: out of the 223 objects considered, the SDM succeeds in deriving a distance in 197 cases while the standard fit succeeds in only 175 (owing mostly to data sparsity). Moreover, we find a high degree of consistency between SDM distances and their conventionally derived counterparts when both methods are successful — a Kolmorgorov-Smirnoff test produces a p-value of 0.993, and the distances have a median residual of just 0.001 mag.

Still, there are several instances where the difference between an individual SDM distance and its corresponding conventional estimate do differ significantly. This is not unexpected, given the highly underconstrained nature of the conventional fits in the presence of sparse data; however, to be cautious, we visually inspect the fits for all SNe whose distance estimates (SDM and conventional) differ by more than the lesser of their corresponding error bars. Of the 34 SNe for which this is the case, we manually assign the distance used in our analysis to be from the SDM in 19 cases, from the conventional fit in one case, and for the remainder, to be selected using our default strategy of using the distance with a smaller uncertainty. All told, this distills our OSC sample into 199 SNe, 150 of which have distances derived using the SDM (the remainder are derived via the conventional method).

[4] `https://sne.space`

	SNe	Spec.	Phot.
initial	2900	8974*	136589*
overlap	2507	4759*	69733*
MJD < 47892	2481	4623	67771
Si II λ6355	2469	4330	67393
resolution	1781	3624	60140
passbands	1476	3227	44516
uncertainties	1187	2879	40123
< 2 passbands	747	2359	34682
literature	670	1976	21743
< 2 passbands	625	1915	21391
redshift	480	1752	20267
deepSIP	243	631	12941
Phase	232	620	11063
< 2 passbands	223	610	11034
fit failure	199	585	10942
quality cuts	180	524	10083

Figure 6.1: Full accounting of the cuts that take the initial sample of Open-Supernova-Catalog-obtained SN Ia candidates for snapshot distances to the final sample of robust, high-confidence distances. The colour map shows the size of each cut (per column) as a percentage of the number initially retrieved. Numbers marked with an asterisk (*) are omitted from the calculations because they are self-reported by the Open Supernova Catalog. Boxes are used to denote the data level (e.g., SNe, spectra, photometry) to which a given cut is applied. Repeated cuts are intentional and explained in Appendix 6.6.

After uniformly shifting all distances to our fiducial distance scale, we impose minimal reliability cuts that reduce the sample to 193 objects, and we cut a further 13 objects for having distance moduli that differ by more than 1 mag from the cosmologically-expected value at their redshifts. In our sample, this preferentially removes fainter-than-expected objects — an encouraging result in light of the fact that our selection criteria do not include a spectroscopic classification step to explicitly identify and remove contaminating transient events (such as core-collapse SNe) that may be spuriously present. This results in a final sample of 180 distances (137 of which are derived from the SDM).

6.2.2 Type II Supernovae

With the addition of the OSC sample, our low-redshift SN Ia distance compilation provides *comprehensive* coverage of all publicly available objects that satisfy basic suitability criteria (note that these criteria are now agnostic to how well sampled an individual object's light curve is, thanks to the SDM). Without proprietary datasets, one would be unable to meaningfully increase the sample size at the present time. With this limitation in mind and a persisting desire to grow the sample larger while simultaneously building a foundation for further work, we turn to another class of standardiseable SNe.

In contrast to SNe Ia (which are standardised via a WLR), SNe II can be standardised using the SCM (Hamuy and Pinto 2002; de Jaeger et al. 2017), which exploits the empirical fact that intrinsically brighter SNe II have higher expansion velocities (as probed by the Hβ spectral feature velocity, $v_{\mathrm{H}\beta}$) and are bluer in colour (c). As such, one can write (similar to Eq. 6.2)

$$\mu = m - M + \alpha \log_{10}\left(\frac{v_{\mathrm{H}\beta}}{\overline{v}_{\mathrm{H}\beta}}\right) - \beta_{\mathrm{SN}}(c - \overline{c}), \tag{6.3}$$

where m is the apparent magnitude in a given passband at 43 d after the explosion and the overbars are used to denote averaged quantities. As in Equation 6.2, the absolute magnitude (M) and slopes (α and β_{SN}) are nuisance parameters to be derived jointly with the scientifically important parameters in our analysis (see Sec. 6.3 for more details).

We therefore compile a sample of 98 low-redshift SNe II — the first ever to be used in a peculiar-velocity analysis — from the following surveys: CSP-I (Hamuy et al. 2006), LOSS (de Jaeger et al. 2019), the Sloan Digital Sky Survey-II SN Survey (SDSS-II; Frieman et al. 2008; D'Andrea et al. 2010), and the Dark Energy Survey Supernova Program (DES-SN; Bernstein et al. 2012; de Jaeger et al. 2020a). More information about our SN II compilation is provided by de Jaeger et al. (2020b). Consistent with the other samples used herein, we use group redshifts for any SNe II known to be in a group of galaxies.

6.2.3 Final Compilation: The Democratic Samples of SNe

Aggregating over all sources listed above (A2.1 + LOSS2.0 + OSC + SNe II), we arrive at a catalog of 775 SN-based distances. As it is built atop the "Constitution" set and its "first"

and "second" amendments, we dub this catalog the "Democratic Samples of Supernovae" (DSS). The DSS represents a $\sim 70\%$ increase over the number of unique objects in A2 (i.e, the number of SNe Ia in A2.1), which was, until now, the largest such catalog used to study bulk flows in the nearby Universe. Moreover, our sample is the first *ever* to use SNe II for this purpose. In addition to opening an entirely new avenue with which to study peculiar velocities, our SN II subcatalog benefits our analysis by lowering the aggregate redshift (as is clearly visible in Fig. 6.2) and characteristic depth,

$$d_* = \frac{\sum_i r_i/\sigma_i^2}{\sum_i 1/\sigma_i^2}, \tag{6.4}$$

of our full sample (e.g., $d_*^{\mathrm{A2.1}} = 39\,h^{-1}\,\mathrm{Mpc}$, $d_*^{\mathrm{SNe\,II}} = 10\,h^{-1}\,\mathrm{Mpc}$, and $d_*^{\mathrm{DSS}} = 28\,h^{-1}\,\mathrm{Mpc}$). As noted in Section 6.1, our analysis has the most discriminating power between gravitational models at low redshifts.

A secondary benefit of including the SN II subcatalog in our analysis is the added Southern-hemisphere coverage that it yields (see Fig. 6.3, though our SN Ia sample also fares much better than prior samples in this regard). With upcoming wide-field surveys, we expect sky coverage to become even better in short order, and especially for studies that use SNe Ia (both well and sparsely observed) and SNe II as we do here.

6.2.4 Reconstructed Density and Velocity Fields

As will be shortly understood, our analysis methodology requires *observed* peculiar velocities (e.g., our DSS catalog) and knowledge of the overdensity field (δ) which, in light of Equation 6.1, dictates the peculiar-velocity field for a given set of cosmological parameters. There are, however, two problems that prevent the direct application of Equation 6.1 in our (and indeed, every) case:

1. δ is not observable. The density contrast as traced by galaxies (δ_g) is, however, and we assume the two are related by $\delta_g = b\delta$, where b is the linear bias factor.

2. δ_g cannot be measured for all space. Instead, we assume it is measured only up to some maximum distance, R_{max}, by (for example) an all-sky redshift survey.

Invoking the above and defining $\beta \equiv f/b$, we modify Equation 6.1 to

$$\mathbf{v}(\mathbf{r}) = \frac{H_0\beta}{4\pi}\int_0^{R_{\mathrm{max}}} d^3\mathbf{r}'\delta_g(\mathbf{r}')\frac{\mathbf{r}'-\mathbf{r}}{|\mathbf{r}'-\mathbf{r}|^3} + \mathbf{V}_{\mathrm{ext}}, \tag{6.5}$$

where the first term is the peculiar-velocity field generated by structure within the volume covered by the redshift survey, and the second term ($\mathbf{V}_{\mathrm{ext}}$) is a coherent, residual bulk flow driven by structure *outside* the covered volume. Together, then, these terms constitute a *reconstructed* peculiar field that can be compared with direct measurements (as we do here)

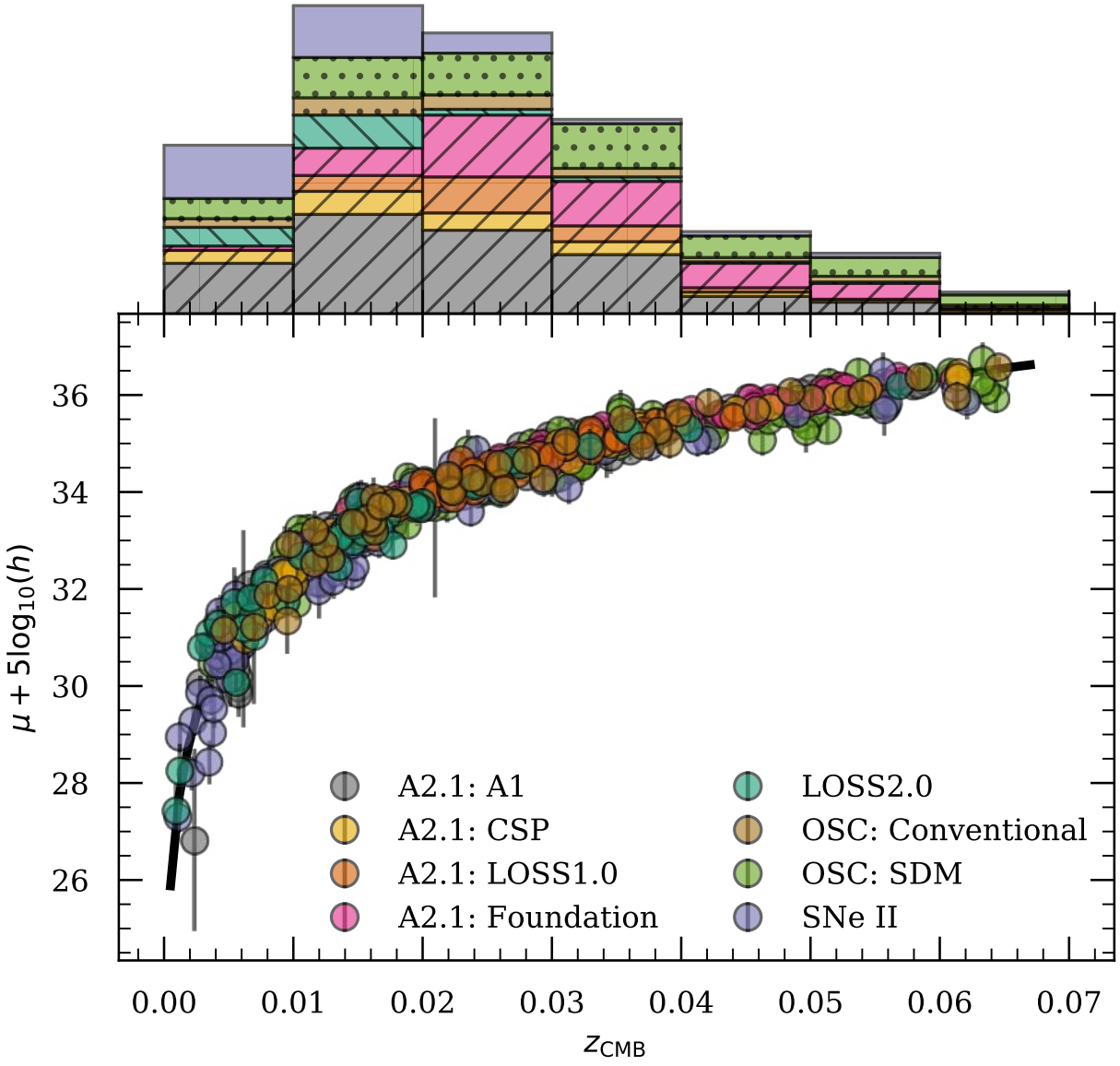

Figure 6.2: Hubble diagram with redshift distribution projected above for our DSS sample, with subcatalogs distinguished by colour. Distance moduli and error bars (which include subcatalog-specific instrinsic scatter) are derived following the prescription of Section 6.3.

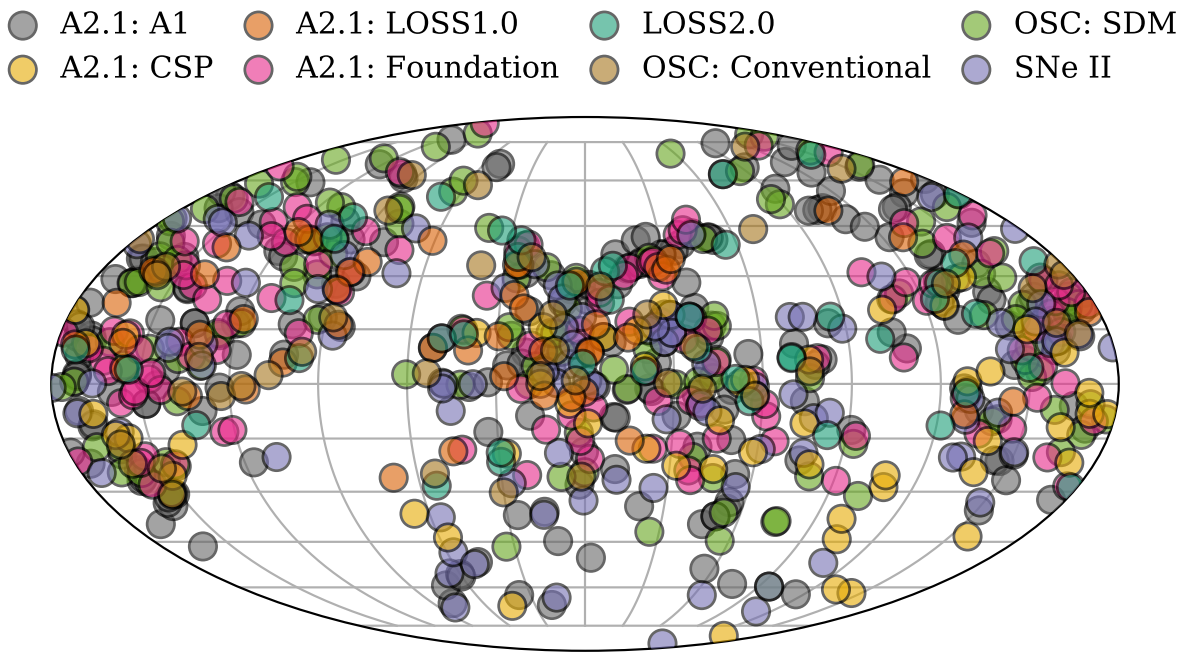

Figure 6.3: Mollweide projection of the on-the-sky distribution of our sample (in equatorial coordinates), with subcatalogs distinguished by colour. Unlike some prior studies, our Southern-hemisphere coverage is substantial.

to constrain β and $\mathbf{V}_{\rm ext}$. This method has been validated with N-body simulations and semi-analytic galaxy formation models; bias in the resulting values of $f\sigma_8$ (as derived from β) are found to be $\lesssim 5\%$ (Hollinger and Hudson 2021). We note that all uncertainties reported herein are statistical only.

As a matter of implementation, we derive δ and $\mathbf{v}$ (both as a function of position) by interpolating over the reconstructions[5] produced by Carrick et al. (2015) up to $R_{\rm max} = 200\,h^{-1}\,$Mpc using the 2M++ galaxy redshift catalog (Lavaux and Hudson 2011). For $\mathbf{v}$, we remove the coherent bulk flow, $\mathbf{V}_{\rm ext} = (89, -131, 17)\,{\rm km\,s^{-1}}$ in galactic Cartesian coordinates, and normalise over $\beta = 0.43$, included in their published velocity field, because our aim is to refit those quantities here. Hereafter, $\mathbf{v}$ will refer to the peculiar-velocity reconstruction with this modification.

6.3 Method

The fundamental aim of this study is to compare the reconstructed peculiar-velocity field (see Sec. 6.2.4) to the tracers which comprise our DSS catalog, and in doing so, to fit for β

[5]The reconstructions are available at `https://cosmicflows.iap.fr`.

and $\mathbf{V}_{\rm ext}$. The former allows us to constrain the degenerate cosmological parameter combination $f\sigma_8$ (see Sec. 6.4), while the latter may result from, and thus constrain, properties of large-scale structures that exist beyond the volume of our selected peculiar velocity field reconstruction. We devote the remainder of this section to describing our method for fitting these quantities, which we denote collectively as the *flow model*, as well as a number of subcatalog-specific nuisance parameters that homogenise the objects in our global catalog.

6.3.1 The Forward Likelihood Method

We use an updated implementation of the *forward likelihood method* (Pike and Hudson 2005) used by Boruah et al. (2020). In this method, the flow model $(\beta, \mathbf{V}_{\rm ext})$ and (mostly subcatalog-specific) nuisance parameters $(\mathbf{\Theta})$ are coupled to the observable parameters of an SN $(\mathbf{x}_i)$ through the conditional probability $\mathcal{P}(\beta, \mathbf{V}_{\rm ext}, \mathbf{\Theta}|\mathbf{x}_i)$, which, given Bayes' theorem, can be expressed as

$$\mathcal{P}(\beta, \mathbf{V}_{\rm ext}, \mathbf{\Theta}|\mathbf{x}_i) \propto \mathcal{P}(\mathbf{x}_i|\beta, \mathbf{V}_{\rm ext}, \mathbf{\Theta})\mathcal{P}(\beta, \mathbf{V}_{\rm ext}, \mathbf{\Theta}). \tag{6.6}$$

An advantage of this method is that it mitigates inhomogeneous Malmquist bias, which arises when line-of-sight inhomogeneities are ignored (Strauss and Willick 1995) and can cause the inferred value of β to be biased high (e.g., Carrick et al. 2015). This is accomplished by accounting for inhomogeneities along the line of sight via the radial distribution

$$\mathcal{P}(\mathbf{r}|\mathbf{\Theta}) = \frac{1}{\mathcal{N}(\mathbf{\Theta})} r^2 \exp\left\{-\frac{\left[\mu(r) - \mu(\mathbf{\Theta})\right]^2}{2\sigma_\mu^2(\mathbf{\Theta})}\right\}\left[1 + \delta_g(\mathbf{r})\right], \tag{6.7}$$

where $\mathbf{r}$ is a vector whose length (r) denotes a comoving distance and whose direction corresponds to a point on the celestial sphere, $\mathcal{N}(\mathbf{\Theta})$ is a nuisance-parameter-dependent normalisation factor, δ_g is the overdensity in the galaxy field, and σ_μ — the quadrature-sum of the (fitted, subcatalog-specific) intrinsic scatter and the propagated distance uncertainty — is explicitly shown as a function of $\mathbf{\Theta}$ for clarity. This is then marginalised over to derive the likelihood

$$\mathcal{P}(\mathbf{x}_i|\beta, \mathbf{V}_{\rm ext}, \mathbf{\Theta}) = \int_0^{R_{\rm max}} dr \mathcal{P}(\mathbf{x}_i|\mathbf{r}, \beta, \mathbf{V}_{\rm ext}, \mathbf{\Theta})\mathcal{P}(\mathbf{r}|\mathbf{\Theta}), \tag{6.8}$$

where $R_{\rm max}$ corresponds to the extent of our reconstructed density and peculiar velocity fields, and

$$\mathcal{P}(\mathbf{x}_i|\mathbf{r}, \beta, \mathbf{V}_{\rm ext}, \mathbf{\Theta}) = \frac{1}{\sqrt{2\pi\sigma_v^2}} \exp\left\{-\frac{\left[cz_{\rm obs} - cz_{\rm pred}(\mathbf{r}, \beta, \mathbf{V}_{\rm ext})\right]^2}{2\sigma_v^2}\right\}. \tag{6.9}$$

In our analysis, we treat σ_v as a global nuisance parameter (i.e., a component of $\mathbf{\Theta}$) to be fit simultaneously with the other parameters of our model (in contrast to other studies that

fix σ_v to (for example) $200\,\mathrm{km\,s^{-1}}$ or $150\,\mathrm{km\,s^{-1}}$; Pike and Hudson 2005; Boruah et al. 2020, respectively), take z_{obs} as a mandatory component of $\mathbf{x}_i$ (prepared as discussed in Sec. 6.2), and compute the predicted redshift (shown above with its explicit parameter dependence) according to (Davis and Scrimgeour 2014)

$$1 + z_{\mathrm{pred}} = [1 + \tilde{z}(r)] \left\{ 1 + \frac{1}{c} \left[\beta \mathbf{v}(\mathbf{r}) + \mathbf{V}_{\mathrm{ext}} \right] \cdot \hat{\mathbf{r}} \right\}, \tag{6.10}$$

where $\mathbf{v}$ is the reconstructed peculiar velocity and $\tilde{z}$ is the cosmological redshift, approximated to second order (Peebles 1993) as

$$\tilde{z} = \frac{1}{1 + q_0} \left[1 - \sqrt{1 - \frac{2H_0 r}{c}(1 + q_0)} \right], \tag{6.11}$$

which makes it clear that $\tilde{z}$ is solely a function of the assumed cosmological model and a precise, redshift-independent SN distance (parameterised here by the comoving distance, r). For the deceleration parameter, we use $q_0 = \Omega_m/2 - \Omega_\Lambda$ for a flat ΛCDM Universe.

6.3.2 Observable Parameters, Nuisance Parameters, and Priors

Thus far, we have maintained a level of abstraction from the data-specific details of our method, but in order to continue our development, we must now delve into them. Namely, we have referred to the observable parameters of a given SN only as $\mathbf{x}_i$ and nuisance parameters (with the exception of σ_v) as $\mathbf{\Theta}$. Moreover, we have not yet addressed the prior probability term in Equation 6.6, $\mathcal{P}(\beta, \mathbf{V}_{\mathrm{ext}}, \mathbf{\Theta})$. There are three specific cases to describe, but first we delineate those attributes that are generically present, regardless of the case.

As was stated in Section 6.3.1, z_{obs} is a mandatory component of all $\mathbf{x}_i$. This is also true for object coordinates (right ascension and declination), from which $\hat{\mathbf{r}}$ (i.e., the direction of $\mathbf{r}$) is computed. The remaining components of a given $\mathbf{x}_i$ — which are responsible for providing a redshift-independent distance — depend on the type of subcatalog to which it belongs. We delve into this, along with nuisance parameters and priors, in the following paragraphs.

6.3.2.1 "Simple Distance" Subcatalogs

"Simple distance" subcatalogs are those which directly include distance moduli (e.g., A1, CSP, LOSS2.0, OSC). These distance moduli (and their corresponding error bars) are converted into comoving distances (with propagated error bars), which then become the final components of the vector of observables for a given SN, $\mathbf{x}_i$.

For such catalogs there are two nuisance parameters, $\mathbf{\Theta} = (\eta, \sigma_{\mathrm{int}})$, that are jointly fit with the flow model. The first, η[6], rescales the reported distance as $r \to \eta r$, ensuring a globally consistent relative distance scale across multiple subcatalogs. The second, σ_{int}, is the usual

[6]Our η plays the same role as the $\tilde{h}$ used by Boruah et al. (2020).

(fitted) intrinsic scatter employed in SN analyses to account for unmodeled behaviour that is not captured in the standardisation technique. In our analysis, $\sigma_{\rm int}$ serves a secondary purpose of controlling the weight of a given subcatalogue in the global fit (because each catalogue has its own fitted $\sigma_{\rm int}$).

For η, we impose a simple, positive-only prior and for $\sigma^2_{\rm int}$ we use a log-normal prior with a peak corresponding to $\sigma_{\rm int} = 0.15\,$mag. The latter enforces the requirement that $\sigma_{\rm int}$ be positive while simultaneously being flexible enough to accommodate the range of values expected for both conventionally- and SDM-standardised SNe Ia.

6.3.2.2 SN Ia Tripp Distance Subcatalogues

For the remaining SN Ia subcatalogues in the DSS (e.g., LOSS, Foundation), we add the fitted SALT2 parameters (m_B, x_1, c) and their uncertainties as the final components of the vector of observable quantities for a given SN, $\mathbf{x}_i$. Distance moduli are then derived via Equation 6.2 with the requisite nuisance parameters being jointly fit with the flow model and drawn from $\mathbf{\Theta} = (M, \alpha, \beta_{\rm SN}, \sigma_{\rm int})$. Using concepts from differential calculus, we express the propagated distance modulus error (including the intrinsic scatter term) as

$$\sigma^2_\mu = \sigma^2_{m_B} + (\alpha\sigma_{x_1})^2 + (\beta_{\rm SN}\sigma_c)^2 + \sigma^2_{\rm int}. \tag{6.12}$$

Finally, we convert the distance moduli (and their corresponding error bars) into comoving distances (with propagated error bars). From a practical point of view, the peak *absolute* magnitude, M, serves a role analogous to η, in the sense that its value brings the relative distance scale of the subcatalogue for which it is fit into agreement with the global scale used in our analysis.

We place only very simple and nonrestrictive priors on M, α, and $\beta_{\rm SN}$, requiring $M < 0$ and $\alpha, \beta_{\rm SN} > 0$. For $\sigma_{\rm int}$ we impose the same log-normal prior as for simple distance subcatalogues.

6.3.2.3 SN II Subcatalogue

Parallel to our treatment of SN Ia Tripp Distance Subcatalogues, we add the parameters (and their uncertainties) required by Equation 6.3 (i.e., $m, v_{\rm H\beta}, c$) for deriving SN II distance moduli as the final components of the vector of observable quantities for a given object, $\mathbf{x}_i$. Propagating all uncertainties and including the intrinsic scatter term, the distance modulus error can be expressed (in light of Eq. 6.3) as

$$\sigma^2_\mu = \sigma^2_m + \left(\frac{\alpha\sigma_{v_{\rm H\beta}}}{\ln(10)v_{\rm H\beta}}\right)^2 + (\beta_{\rm SN}\sigma_c)^2 + \sigma^2_{\rm int}. \tag{6.13}$$

As a result, the nuisance parameters for our SN II Tripp Distance Subcatalogue are $\mathbf{\Theta} = (M, \alpha, \beta_{\rm SN}, \sigma_{\rm int})$, consistent with the previous case. We therefore impose the same priors, except that the peak of the $\sigma_{\rm int}$ prior is shifted to $0.27\,$mag, consistent with the result found by de Jaeger et al. (2020b).

6.3.3 Implementation

Given the definitions above and the dataset described in Section 6.2, we are now able to implement our model and derive the best-fitting flow model (and nuisance parameters). Formally, these optimal values are, in light of Equation 6.6, the ones that given our entire DSS catalogue, $\{\mathbf{x}\}$, maximise the joint posterior (assuming statistical independence),

$$\mathcal{P}(\beta, \mathbf{V}_{\rm ext}, \mathbf{\Theta}|\{\mathbf{x}\}) \propto \mathcal{P}(\beta, \mathbf{V}_{\rm ext}, \mathbf{\Theta}) \prod_i \mathcal{P}(\mathbf{x}_i|\beta, \mathbf{V}_{\rm ext}, \mathbf{\Theta}). \tag{6.14}$$

In practice, it is more convenient to work with the logarithm of this which we define up to a multiplicative constant as $\mathcal{L}$, so that (using logarithm algebra)

$$\mathcal{L} = \ln \mathcal{P}(\beta, \mathbf{V}_{\rm ext}, \mathbf{\Theta}) + \sum_i \ln \mathcal{P}(\mathbf{x}_i|\beta, \mathbf{V}_{\rm ext}, \mathbf{\Theta}). \tag{6.15}$$

The flow model and nuisance parameters are thus inferred by sampling (using the `emcee` package; Foreman-Mackey et al. 2013) assuming uniform priors on $\beta > 0$ and $\mathbf{V}_{\rm ext}$, and a reasonably broad ($\sigma = 15\,{\rm km\,s^{-1}}$) Gaussian prior on σ_v centred at $150\,{\rm km\,s^{-1}}$ (the static value used by other studies; e.g., Carrick et al. 2015; Boruah et al. 2020). In this Markov Chain Monte Carlo (MCMC) simulation, we find that 256 walkers and 2000 steps (after removing 500 for "burn in") yields robust convergences of all parameters. We describe the results in the following section.

6.4 Results

As discussed in Section 6.3, our method of analysis results in best-fit sets of parameters that broadly belong to two categories: (i) subcatalogue-specific nuisance parameters, and (ii) the flow model, which itself bears cosmological significance. Prior to discussing the latter and its implications, we investigate the former as derived from our DSS catalogue, and through this validation exercise, we strengthen the weight of all subsequent conclusions.

6.4.1 Nuisance Parameters

The most straightforward of all the subcatalogue-specific nuisance parameters to compare is the intrinsic scatter term, $\sigma_{\rm int}$, because it is present in each set. We perform such a comparison by visualising the posterior distribution for each subcatalogue's $\sigma_{\rm int}$ term (as derived from our MCMC analysis) in Figure 6.4. As expected, we find that our SN II subcatalogue exhibits the largest scatter at $0.30^{+0.03}_{-0.03}\,{\rm mag}$ (median value with 16th and 84th percentile differences; reported here and throughout), consistent[7] with the corresponding determination made with a superset of the subcatalogue in a different application ($0.27^{+0.04}_{-0.04}\,{\rm mag}$; de Jaeger et al. 2020b).

[7]Here and henceforth, we consider two measurements to be consistent if the lesser plus its upper uncertainty bound exceeds the greater minus its lower uncertainty bound.

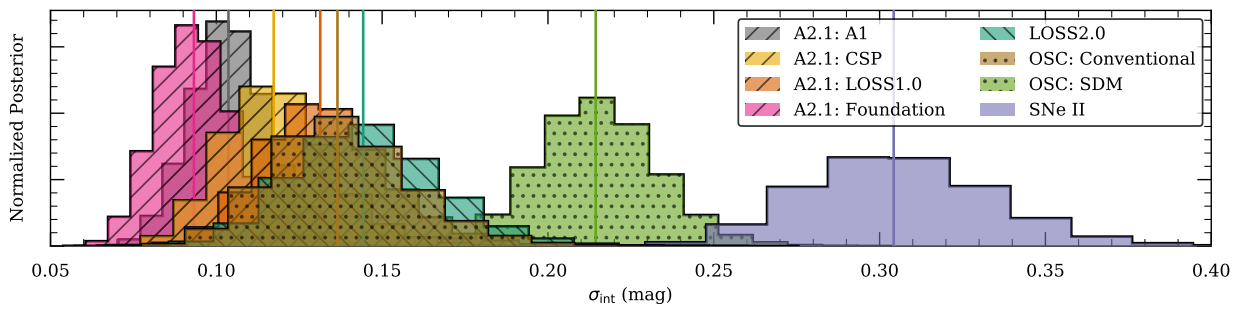

Figure 6.4: Posterior distributions for each subcatalogue's $\sigma_{\rm int}$ term. Each is normalised to unit area and as a result, distributions with lower peaks are necessarily broader. The distinct populations are visually apparent: (in order of increasing $\sigma_{\rm int}$) those subcatalogues with WLR-determined SN Ia distances, SDM-derived SN Ia distances, and SCM-derived SN II distances. Colour-coded vertical lines are used to denote the median of each posterior.

Turning to those SN Ia subcatalogues with distances derived via conventional WLRs (i.e., all but our SDM subcatalogue), we note that all have $\sigma_{\rm int}$ posteriors that peak within the vicinity of ~ 0.1 mag, consitent with recent analyses that have used related datasets (e.g., Foley et al. 2018; Burns et al. 2018; Boruah et al. 2020). Finally, we note that our subcatalogue of SDM-derived SN Ia distances has a $\sigma_{\rm int}$ posterior that falls nicely within a SN Ia – SN II continuum, peaking at $0.21^{+0.02}_{-0.02}$ mag. This represents a further ~ 0.16 mag in (quadrature-added) scatter relative to the conventional WLR OSC catalogue and lies within the range found by Stahl et al. (2021b) when validating the SDM.

To compare other nuisance parameters across distinct subcatalogues is less straightforward given the differences in parameters for different subcatalogue types (e.g., η for "Simple Distance" subcatalogues, and $M, \alpha, \beta_{\rm SN}$ for SN Ia and SN II Tripp Distance subcatalogues). Still, we find sensible results which we summarise by way of the following comments.

1. The parameters of our SN Ia Tripp Distance subcatalogues are all consistent (within the uncertainties) with the corresponding values found by Boruah et al. (2020).

2. Our SN II Distance subcatalogue's α and $\beta_{\rm SN}$ values agree (within the uncertainties, albeit just barely for the former) with those found by de Jaeger et al. (2020b), but M does not. However, as Figure 3 from de Jaeger et al. (2020b) reveals a strong positive correlation between H_0 and M, a weaker (but clearly present) negative correlation with α, and negligible correlation with $\beta_{\rm SN}$, our lack of consistency with M is not a concern; rather, it is an expected consequence of our use of a different relative distance scale.

3. Our fitted values of η for the three Simple Distance subcatalogues that have distances derived via the same light-curve fitter (i.e., LOSS2.0 and both OSC subcatalogues) are consistent with one another, given their uncertainties.

Table 6.1: Flow model parameters derived from the DSS and subsets of it.

Sample	N	$f\sigma_8^{\rm lin}$	$V_{\rm ext}$ (km s^{-1})	l (deg)	b (deg)
SNe Ia (WLR)	540	$0.393^{+0.024}_{-0.024}$	193^{+25}_{-25}	289^{+8}_{-8}	-1^{+6}_{-6}
SNe Ia (SDM)	137	$0.450^{+0.057}_{-0.055}$	254^{+67}_{-63}	285^{+18}_{-19}	-2^{+11}_{-11}
SNe Ia (all)	677	$0.400^{+0.023}_{-0.023}$	200^{+24}_{-23}	289^{+7}_{-7}	-2^{+5}_{-5}
SNe II	98	$0.388^{+0.061}_{-0.063}$	184^{+62}_{-59}	319^{+29}_{-29}	-21^{+16}_{-17}
DSS	775	$0.390^{+0.022}_{-0.022}$	195^{+22}_{-23}	292^{+7}_{-7}	-6^{+5}_{-4}

The only global nuisance parameter in our analysis is σ_v, for which we find $\sigma_v = 128^{+10}_{-9}$ km s^{-1} — lower than 150 km s^{-1}, but not significantly so given the scale of the prior placed on it. Regardless, the flow-model results are not particularly sensitive to the exact value owing to a degree of degeneracy between σ_v and $\sigma_{\rm int}$ (i.e., increasing the former tends to lead to decreases in the latter).

6.4.2 Residual Bulk-Flow Velocity

Deferring a discussion of β until the following section, we turn our focus to $\mathbf{V}_{\rm ext}$, the residual, coherent bulk-flow velocity arising from the gravitational interaction between the objects in our DSS set and large-scale structure existing beyond the volume encompassed by our reconstruction. Our result, that $V_{\rm ext} = 195^{+22}_{-23}$ km s^{-1} in the direction $(\ell, b) = (292^{+7}_{-7}, -6^{+5}_{-4})$ deg, is listed in Table 6.1 along with the corresponding values for various subsets of our full DSS sample.

Our result is mostly in agreement with Boruah et al. (2020), who find[8] $V_{\rm ext} = 177^{+24}_{-26}$ km s^{-1} toward $(\ell, b) = (289^{+9}_{-8}, 9^{+9}_{-9})$ deg for the A2 compilation and similar (albeit more tightly constrained values) when they jointly fit A2 with a large sample of galaxy-derived peculiar velocities. Discrepancies between our result and theirs may stem from our use of a different dataset (both in the sense of using A2.1 instead of A2, and in the sense of including additional subcatalogues), slightly different priors (that we believe to be more valid for the domain of application), or our incorporation of SALT2-parameter uncertainties in Equations 6.12 and 6.13. We note that our result is also consistent with (but again higher in magnitude than) that found by Carrick et al. (2015). Our hope is that larger, homeogeneous samples of SNe Ia and SNe II may bring further convergence in the coming years.

[8]In the original journal publication, Boruah et al. (2020) quoted a significantly lower $V_{\rm ext}$ for the A2 sample, but this was the result of a systematic redshift error. A revision is underway with the journal that reflects the value we report herein.

6.4.2.1 Bulk-Flow Velocity

Distinct from the residual bulk-flow velocity, $\mathbf{V}_{\rm ext}$, discussed herein, many studies measure a "bulk flow" from their peculiar-velocity catalogues. The difference between the two is that the former is intended to be due *solely* to structure beyond the 2M++ reconstruction, while the latter (which we refer to as $\mathbf{V}_{\rm bulk}$ for clarity) makes no such distinction. In order to facilitate a comparison between our work and the aforementioned studies, we derive an analogous bulk-flow measurement by repeating the procedures of Section 6.3 except with the constraint that $\beta = 0$ enforced.

In effect, this "turns off" the peculiar-velocity reconstruction (as evidenced in Eqs. 6.5 & 6.10), and with it being no longer able to contribute in the comparison to the observed peculiar velocities, all that remains is $\mathbf{V}_{\rm ext} \rightarrow \mathbf{V}_{\rm bulk}$. Following this approach, we find $V_{\rm bulk} = 245^{+32}_{-31}\,{\rm km\,s^{-1}}$ in the direction $(\ell, b) = (294^{+7}_{-7}, 3^{+6}_{-5})\,{\rm deg}$.

In comparing to other bulk-flow measurements (see Fig. 6.5), we caution that a variety of methods exist — each with their own advantages and drawbacks (see, e.g., Turnbull et al. 2012, for a discussion of two such methods; ours is of the *maximum-likelihood estimate* variety). Moreover (and independent of the method), each peculiar-velocity catalogue will have its own characteristic depth (e.g., ours is $\sim 30\,h^{-1}\,{\rm Mpc}$), and comparisons should only be made at comparable depths. Keeping these caveats in mind, we are contented to find consistency between our result and those of other SN-based studies, as well is with the ΛCDM expectation. Though we show only bulk-flow magnitudes in Figure 6.5, we find reasonable directional consistency as well.

6.4.3 Constraint on $f\sigma_8$

Our result, $\beta = 0.418^{+0.020}_{-0.020}$, is best interpreted after transforming according to $f\sigma_8 = (f/b)(b\sigma_8) = \beta\sigma_8^g$. Here $\sigma_8^g = 0.99 \pm 0.04$ is the root-mean-squared fluctuation in the galaxy field as determined by Carrick et al. (2015). We perform this operation directly on the β posterior samples from our MCMC chains, resulting in $f\sigma_8 = 0.413^{+0.026}_{-0.026}$. We must, however, note that the value of σ_8 appearing in this equation is the measured, nonlinear value of the root-mean-square density fluctuation in an $8\,h^{-1}$ Mpc sphere at $z \approx 0$. As a result, it cannot be directly compared with other measurements in the literature which refer to the linear value of this quantity (hereafter, $\sigma_8^{\rm lin}$) extrapolated to $z = 0$. Thus, we need to linearise our result prior to comparing it with constraints derived at high redshifts. To do so, we adopt the prescription outlined in Equation 3.13 of Juszkiewicz et al. (2010),

$$\left(\sigma_8^{\rm lin}\right)^2 = \frac{\sqrt{1 + 0.864\sigma_8^2} - 1}{0.432}, \tag{6.16}$$

which requires that we explicitly assume a value of Ω_m (we use 0.3, as stated in Sec. 6.1) to break the degeneracy in $f\sigma_8$ to constrain σ_8 directly. We do this via $f \approx \Omega_m^{0.55}$, which, as introduced in Section 6.1, is valid for ΛCDM cosmology, resulting in $\sigma_8 = 0.801^{+0.050}_{-0.050}$. After linearising according to Equation 6.16, this gives $\sigma_8^{\rm lin} = 0.756^{+0.043}_{-0.043}$. Similar results

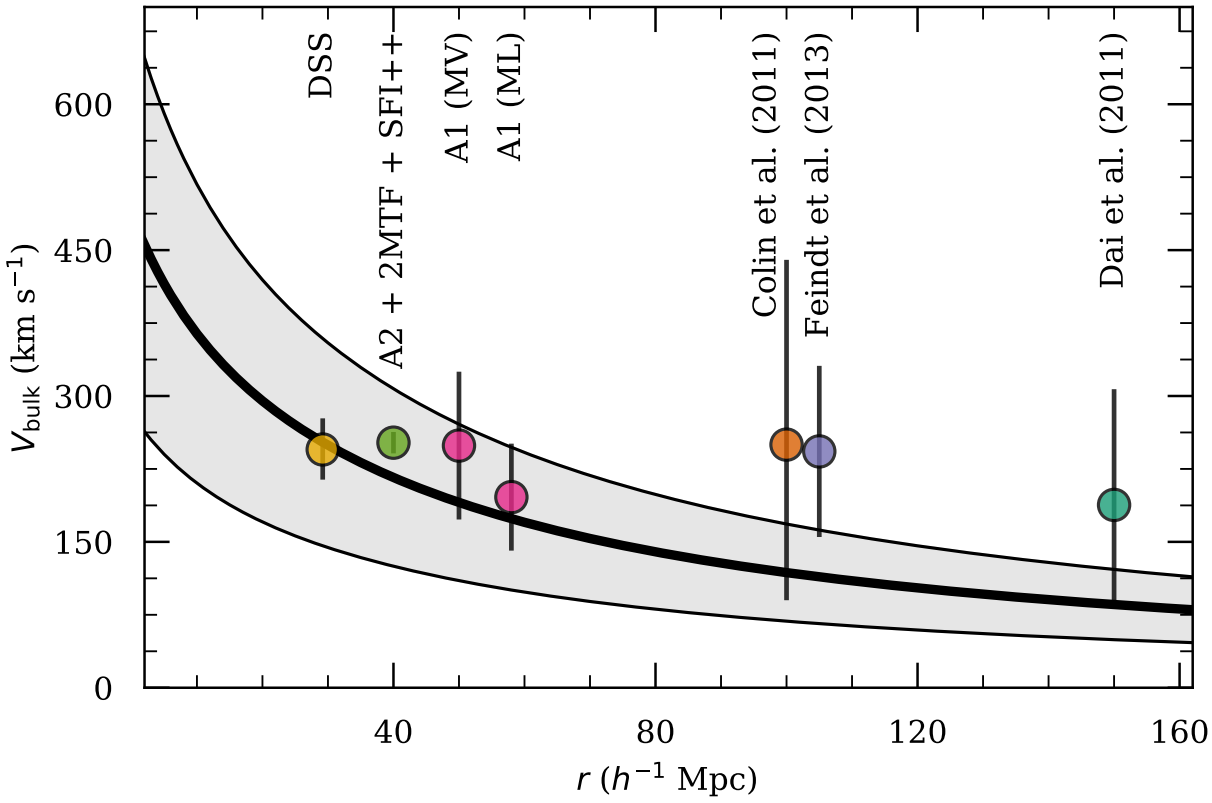

Figure 6.5: Our result for the bulk-flow amplitude (left-most point) compared with other SN-based results and the ΛCDM prediction (shown as the black line with 68% confidence region). The two comparison values from the A1 compilation are derived via the *minimum-variance* and *maximum-likelihood* methods, respectively (see Turnbull et al. 2012, for more details). Where results are quoted over a redshift shell instead of at a characteristic distance (e.g., Dai et al. 2011; Feindt et al. 2013), we convert the more distant end of the shell to the distance used in our comparison.

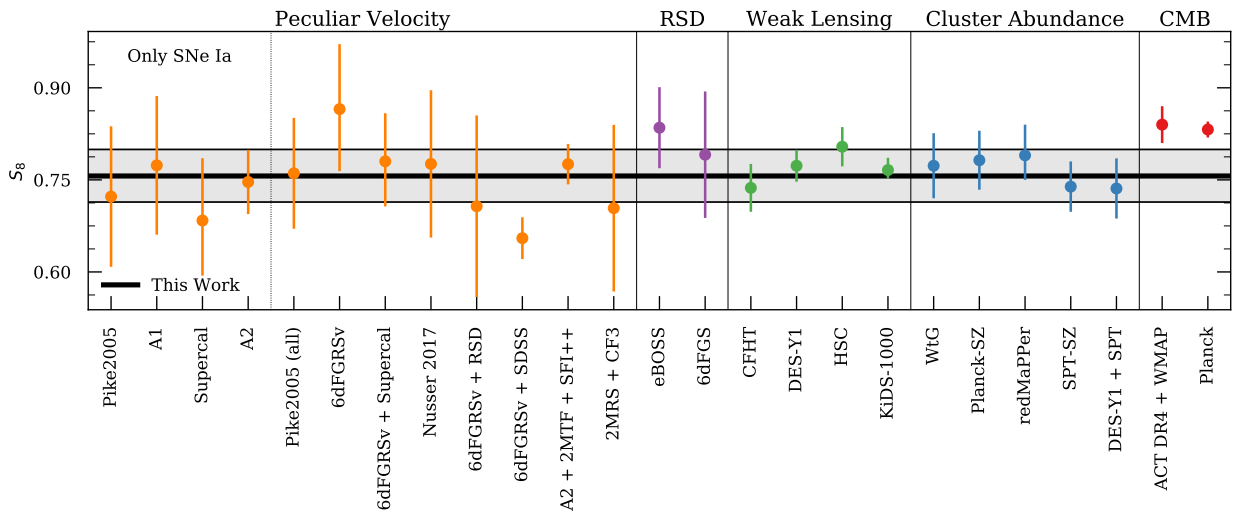

Figure 6.6: Our result for S_8 (horizontal line) compared with results from the literature derived via multiple means (as delineated at the top of each distinct section). All names and values used in the RSD, Weak Lensing, Cluster Abundance (except DES-Y1 + SPT), and CMB (except ACT DR4 + WMAP) sections are as listed in Table 7 of Boruah et al. (2020), as are Nusser2017, 6dFGRSv + RSD, and 6dFGRSv + SDSS of the Peculiar Velocity section. All others are as discussed herein. References are as follows (in order of first appearance from left to right): Pike and Hudson (Pike2005; 2005), Turnbull et al. (A1; 2012), Huterer et al. (Supercal and/or 6dFGRSv; 2017), Boruah et al. (A2; 2020), Nusser (Nusser2017; 2017), Adams and Blake (6dFGRSv + RSD; 2020), Said et al. (6dFGRSv + SDSS; 2020), Lilow and Nusser (2MRS + CF3; 2021), eBOSS Collaboration et al. (eBOSS; 2020), Beutler et al. (6dFGS; 2012), Heymans et al. (CFHT; 2013), Abbott et al. (DES-Y1; 2018), Hamana et al. (HSC; 2020), Heymans et al. (KiDS-1000; 2020), Mantz et al. (WtG; 2015), Planck Collaboration et al. (Planck-SZ; 2016), Costanzi et al. (redMaPPer; 2019), Bocquet et al. (SPT-SZ; 2019), Costanzi et al. (DES-Y1 + SPT; 2021), Aiola et al. (ACT DR4 + WMAP; 2020), and Planck Collaboration et al. (Planck; 2020).

are obtained using the Mead et al. (2021) nonlinear modifications to the power spectrum (without baryonic feedback) to calculate σ_8 and $\sigma_8^{\rm lin}$. Hence, we find $f\sigma_8^{\rm lin} = 0.390^{+0.022}_{-0.022}$, representing the tightest SN-based constraint on the quantity to date. As with $\mathbf{V}_{\rm ext}$, we summarise our DSS-derived result as well as those derived from subsets of it in Table 6.1.

Our result is consistent with both the A2-only and A2 + galaxy constraints derived by Boruah et al. (2020), albeit closer to the latter. We find this encouraging — it would seem that our larger sample of SNe (including SDM-treated SNe Ia and SNe II) is on the path to converging with comprehensive, large-scale studies utilising thousands of galaxies. Indeed, we find this to be the case after comparing to a vast array of studies that utilise multiple methods (see Fig. 6.6).

Instead of $f\sigma_8$, however, we use a related quantity for this comparison: $S_8 \equiv \sigma_8(\Omega_m/0.3)^{0.5} \approx f\sigma_8^{\rm lin}/(0.3^{0.55})$, where the equivalency denotes the definition and the approximation denotes its mapping from our results. In doing so, we can easily compare our result to those derived through a variety of observations including the cosmic microwave background (CMB), cluster abundances, weak gravitational lensing, redshift-space distortions (RSDs), and of course peculiar velocities (as we have used in this work). In all but the last category (i.e., peculiar velocities) and the cases of DES-Y1 + SPT and ACT DR4 + WMAP (which we take directly from the publications; Costanzi et al. 2021; Aiola et al. 2020, respectively), we obtain S_8 values directly from Table 7 of Boruah et al. (2020), who have already taken the requisite steps to convert and homogenise the values reported by the original studies. This remains true for the peculiar-velocity category as well, excepting the following.

1. Pike2005: Pike and Hudson (2005) report $\sigma_8(\Omega_m/0.3)^{0.6} = 0.86 \pm 0.15$ for their SN Ia-only sample and $\sigma_8(\Omega_m/0.3)^{0.6} = 0.91 \pm 0.12$ for their full compilation (including SNe Ia and galaxies). We convert both to S_8 by means of a multiplicative factor of $(\Omega_m/0.3)^{-0.1}$ and the linearisation procedure described above, prior to including them in Figure 6.6.

2. A1: Turnbull et al. (2012) derive $f\sigma_8 = 0.424 \pm 0.069$ from their A1 SN Ia sample. We convert this to S_8 identically to our own result after linearisation.

3. Supercal and/or 6dFGRSv: Huterer et al. (2017) produce three constraints on $f\sigma_8$: $0.370^{+0.060}_{-0.053}$ for the "Supercal" sample of SNe Ia (Scolnic et al. 2015), $0.481^{+0.067}_{-0.064}$ for a large set of fundamental-plane distances from the 6dF galaxy survey (Springob et al. 2014), and $0.428^{+0.048}_{-0.045}$ for both samples combined. Our conversion of each to S_8 is identical to our treatment of A1 and our own result.

4. A2: Although Boruah et al. (2020) provide S_8 for their full compilation (which we refer to in Fig. 6.6 as A2 + 2MTF + SFI++), they do not provide the conversion for just the A2 sample. Thus, we convert the relevant value in order to include it in Figure 6.6.

5. 2MRS + CF3: By comparing constrained realisations of the peculiar-velocity field from the Two-Micron All-Sky Redshift Survey (2MRS; Huchra et al. 2012; Macri et al. 2019) with observed peculiar velocities from the Cosmicflows-3 catalogue (CF3; Tully et al. 2016), Lilow and Nusser (2021) derive $f\sigma_8^{\rm lin} = 0.363 \pm 0.070$. We convert this to S_8 identically to our own result.

As Figure 6.6 shows, our result is highly consistent with those of other peculiar-velocity-based studies, along with those derived across multiple other methods (except for CMB-based measurements, which we discuss below). Indeed, even the most egregious disagreement (6dFGRSv + SDSS; Said et al. 2020) amounts to $< 1.9\sigma$ — comfortably below the threshold for statistical significance — and only two more out of a total of 25 exceed the 1σ discrepancy level, though we emphasise that the samples used in the comparison are not all mutually independent. Moreover, our result — derived with < 800 SNe — is more tightly constrained

(based on its statistical-only error bars) than all but two other peculiar-velocity-based constraints, both of which use many thousands of galaxy distances (and in one case, the A2 SN Ia sample as well). Thus, in the coming era of wide-field, relatively high-cadence surveys, the prospect for SNe (i.e., well-sampled SNe Ia standardised with a WLR, and now SNe II as well as sparsely observed SNe Ia standardised with the SDM) to produce the best low-redshift constraint on $f\sigma_8$ is particularly bright.

6.4.3.1 Aside: The S_8 Tension

As an interesting aside, we note that the single most tightly constrained value in our comparison (i.e., *Planck*; Planck Collaboration et al. 2020) is one of the two remaining values at $> 1\sigma$ tension with our result (and the other, ACT DR4 + WMAP, is also CMB-based). Given our result's consistency with those it is compared against, this means that the CMB results are in modest tension with *most* other comparison values. In fact, the second most tightly constrained (i.e., KiDS-1000; Heymans et al. 2020) value we consider — which is in full agreement (i.e., 0.2σ difference) with our result — differs from the *Planck* value at the $\sim 3\sigma$ level. Moreover, if we pull out the *Planck* result and compare it with the inverse-variance-weighted mean of all other values (including ours), the tension reaches 4.1σ and remains $\gtrsim 3\sigma$ when we compare it to the same aggregation applied separately to the Peculiar Velocity (4.5σ), Weak Lensing (3.3σ), and Cluster Abundance (2.8σ) categories.

Though these levels are overestimated in some cases (e.g., there is overlap in the datasets used to derive some of the comparison values, and there is no guarantee that the comparison values we have used are a truly comprehensive sample), we would be remiss not to note the parallels to the current H_0 tension (e.g., Riess 2019) — once again, we have a cosmological parameter whose value as measured with low-redshift data is in significant disagreement with the value inferred from CMB measurements. The difference here is that, discounting the 6dFGRSv + SDSS result (which appears to be an outlier in the Peculiar Velocity category), it is only the *aggregation* of multiple measurements (with the marginal exception of KiDS-1000; see Di Valentino et al. 2020, for more discussion on this "S_8 tension") that is in tension, and thus we *do not* escalate our findings in this area beyond simply noting them here. As with other parts of our analysis, we are optimistic that larger, homogeneous samples of SNe Ia and II studied using our methodology will be able to shed more light on this issue.

6.5 Conclusion

In this paper, we painstakingly assemble the largest-ever SN-based peculiar-velocity catalogue: the Democratic Samples of Supernovae, consisting of 775 objects. In addition to its sheer size, the DSS is novel for (i) its "resurrection" of otherwise unusable SN Ia observations (owing to data sparsity) via the snapshot distance method, and (ii) its inclusion of SNe II, which have not until now been used in such a way. Our SDM-enabled subcatalogue of 137 objects represents the final distillation of a candidate pool that started at $\sim 2,500$

objects; with future improvements to the SDM and the tools that enable it, the efficiency may well increase significantly. On this and both other fronts (SNe II and conventional SN Ia distances), significantly larger samples than our DSS should rapidly become feasible with the prevalence of wide-field surveys in the coming years that will discover hundreds of thousands of SNe. Our intent is for the work described herein to become the prototype for future studies that leverage such upcoming datasets.

To draw inferences from our DSS catalogue, we update and utilise a forward-likelihood framework that has been used in related works for the last $\sim 15\,\mathrm{yr}$. In this approach, a parameter ($\beta = f/b$) related to $f\sigma_8$ and the magnitude and direction of a coherent, external bulk flow are jointly fit with subcatalogue-specific nuisance parameters that serve to cross-calibrate between distinct subcatalogues. After performing basic validity checks on the fitted nuisance parameter values (all of which are satisfactory), we report top-level results of $f\sigma_8^{\mathrm{lin}} = 0.390^{+0.022}_{-0.022}$ and $V_{\mathrm{ext}} = 195^{+22}_{-23}\,\mathrm{km\,s^{-1}}$ in the direction $(\ell, b) = (292^{+7}_{-7}, -6^{+5}_{-4})\,\mathrm{deg}$ — the tightest SN-based constraints (considering statistical error bars only) ever produced on each. Moreover, we find a bulk flow (ignoring any influence from the peculiar-velocity reconstruction) of $V_{\mathrm{bulk}} = 245^{+32}_{-31}\,\mathrm{km\,s^{-1}}$ toward $(\ell, b) = (294^{+7}_{-7}, 3^{+6}_{-5})\,\mathrm{deg}$ on a scale of $\sim 30\,h^{-1}\,\mathrm{Mpc}$.

By converting $f\sigma_8$ to S_8, we demonstrate that our result is consistent with that of many other studies leveraging multiple methodologies. Indeed, none deviate from ours at a level that warrants statistical significance, though we do find the *Planck* value (Planck Collaboration et al. 2020) — which differs from our result by 1.7σ — to be significantly different from aggregations of our value with other comparisons. Our result for $\mathbf{V}_{\mathrm{ext}}$ is consistent in direction with prior studies (e.g., Boruah et al. 2020), but falls at the high end of magnitudes in the same studies (though still consistent with the central values). We discuss this briefly, but ultimately conclude that a larger, more homogeneous SN sample will be instrumental in clarifying the matter. Consistent with what is stated above, we believe that such samples will become available in the near future, offering an answer to this question while perhaps opening others. Indeed, the future of SN Ia and II cosmology, particularly in the era of wide-field surveys, holds much promise.

6.6 Snapshot Distance Sample Selection

Beyond the cuts employed in selecting our initial SDM candidate pool (see Sec. 6.2.1.3), many more are required to ensure sufficient quality and homogeneity, and thus we carefully document the sequence of cuts leading to our final sample below (the cuts are also summarised in Fig. 6.1). Given the sheer size of our initial sample (2900 SNe with $>$ 8900 spectra and $>$ 136,000 photometric points), we judiciously select the order so that algorithmic cuts are always applied before those that require human attention.

Overlap: Our first cut is to remove the nearly 400 SNe in our sample that also occur in A2.1 + LOSS2.0. The fact that almost all SNe from the latter are present in the

former is expected, and those that are not usually fail the requirement that at least one optical spectrum be available on the OSC. After imposing this cut, 2507 SNe remain with $\sim$ 4700 spectra and $\sim$ 70,000 photometric points. It is encouraging that the percentages of spectra and photometric points removed are both larger than the corresponding percentage of SNe — those SNe that are removed are, on the average, much better sampled than those that remain, rendering support to our assertion that our A2.1 + LOSS2.0 amalgamation accounts for the majority of publicly-available SN Ia observations.

Recency: To ensure that the data used herein were collected with relatively modern techniques and equipment (e.g., CCDs), we drop spectra and photometric points that were observed prior to 1990 (formally, we required that the MJD of all observations is $\geq$ 47892). Since the vast majority of human-studied SNe have been discovered in recent years, this removes only a very modest number of objects, spectra, and photometric points.

Spectral Coverage and Resolution: As `deepSIP` forms a central component of the SDM, we must cut spectra that are not suitable for it. Specifically, this means that we must drop spectra that do not have full coverage[9] of the Si II λ6355 feature, along with those having insufficient resolution. Though the former removes $\sim$ 300 spectra, only 13 SNe are removed as a result. The latter is much more impactful, however, removing $\sim$ 700 spectra (mostly from the SED Machine; Blagorodnova et al. 2018) and nearly as many SNe. In fact, this amounts to the most severe cut on SNe and the second most severe cut on spectra (after the "overlap" cut). With future improvements to `deepSIP` it may be possible to revisit and lessen the extremity of this cut, but this will have to wait until those improvements can be realised.

Irrelevant Photometric Passbands: After the cuts described above, the 60,140 photometric points that remain are in one of 62 different passbands, some of which are irrelevant to our analysis and must therefore be removed. By far, the primary factor in rendering observations in a given passband "irrelevant" is if that band is too broad. For example, 4923 *Gaia* G-band (Jordi et al. 2010), 2104 Pan-STARRS w-band (Chambers and Pan-STARRS Team 2018), 612 ATLAS c-band or o-band (Tonry et al. 2018), and many other wide-band observations are removed, along with a further 5061 unfiltered photometric points. A second factor in determining the relevance of a passband is the wavelengths of light that it passes. As our SDM uses a WLR implementation that is trained at optical and near-infrared wavelengths, we must discard passbands that lie outside this domain, thereby removing some *Swift* observations (Brown et al. 2014) amongst others. All told, 15,624 photometric points are removed, and those that remain are homogenised down to 21 distinct passbands.

[9]Following S20, we define "full coverage" as having a minimum wavelength of less than 5750 Å and a maximum that exceeds 6600 Å.

Photometric Uncertainties: Of the remaining 44,516 photometric points, 10,429 do not include a symmetric uncertainty in the reported magnitude. We are able to "fix" 6120 of these by taking the larger of their (asymmetric) lower and upper magnitude uncertainty estimates, but 4393 remain which have no identifiable quantitative uncertainty indicator. We take the conservative approach of removing these data, leaving us with just under 1200 SNe covered by $\sim$ 2900 spectra and $\sim$ 40,000 photometric points.

2+ **Distinct Passbands:** As the SDM requires, at a minimum, two photometric points in *different* passbands (and a spectrum), we remove SNe that fail this requirement. This reduces the sample to 747 SNe with $\sim$ 2400 spectra and $\sim$ 35,000 photometric points.

Literature Search for Photometric Systems: While we have taken care above to homogenise the passbands in our sample (in the sense of resolving the differing names given to identical filters), we must also understand the photometric systems to which they belong. To do so, we visit the primary source provided by the OSC for each remaining point in our photometry sample (amounting to 248 sources) and attempt to determine the photometric system. We find that 26 SNe (covered by 5719 photometric points) are either not an SN Ia or are not an SN Ia subclass that can be handled by our WLR. These are dropped, as are an additional 7220 photometric points whose photometric system is either not clear or not supported by our light-curve fitter (consistent with LOSS2.0 distances, we use the "EBV_model" in `SNooPy`; Burns et al. 2011). This leaves 21,743 photometric points remaining (covering 670 SNe) in 16 distinct photometric systems, with the plurality being the standard Landolt system (Landolt 1983, 1992), followed by the CSP natural system (Contreras et al. 2010), and then by the *Swift* photometric system (Brown et al. 2014). To maximise the amount of data we can use, we have registered the photometric systems of the Zwicky Transient Facility (Bellm et al. 2019) and LOSS 1.0 (Ganeshalingam et al. 2010) into our light-curve fitter.

2+ **Distinct Passbands:** As the cut described above modifies the photometric coverage for some objects in our sample, we must repeat the 2+ passband cut. Though this repetition is, perhaps, aesthetically unappealing, it represents a significant savings of human time compared to the option of performing it only once at this stage (we would have needed to review many additional sources in the literature-search stage). Upon repeating this cut, we are left with 625 SNe covered by $\sim$ 1900 spectra and $\sim$ 21,000 photometric points.

Redshifts: As the purpose of this paper is to study the peculiar velocity field, precise redshifts are of paramount importance (Davis and Scrimgeour 2014). We therefore devote significant effort to obtaining high-quality host-galaxy redshifts for the SNe in our sample using the following strategy. First, we query NED[10] for the (heliocentric)

[10]The NASA/IPAC Extragalactic Database (NED) is operated by the Jet Propulsion Laboratory, California Institute of Technology, under contract with the National Aeronautics and Space Administration.

redshift of the host galaxy of each SN in our sample. For those that fail (either due to the host galaxy not having a listed redshift, or the host galaxy not being provided by the OSC), we perform a careful literature search, accepting only host-galaxy-derived (and not SN-feature-derived) redshifts. This reduces our sample to 480 objects with reliable, high-quality redshifts. We convert each (heliocentric) redshift to the CMB frame and then (consistent with A2.1 + LOSS2.0), for those objects known to be in a cluster of galaxies, we update the redshift to that of the cluster.

deepSIP: At this stage, we deploy `deepSIP` on the spectra that remain in our sample to derive the phase and light-curve shape measurements required by the SDM. Of the 1752 spectra processed by `deepSIP`, 631 are categorised as "in-domain" — a requirement of the SDM — leaving us 243 SNe with which to proceed with our analysis. For those SNe having multiple spectra, we assign their time of maximum brightness and light-curve shape as the average of the relevant `deepSIP`-reconstructed quantities. As with other cuts that stem from `deepSIP`, the severity of this cut can likely be reduced in the future as the model is improved.

Photometric Phase: Using the `deepSIP`-inferred times of maximum light, we compute the rest-frame phase of every photometric point in our dataset, and remove any that are earlier than -10 d or later than 70 d, corresponding to the temporal domain over which `SNooPy` models light curves. This reduces our sample only modestly, leaving 11,063 photometric points covering 232 SNe.

2+ **Distinct Passbands:** As the cut described above modifies the photometric coverage for some objects in our sample, we must again repeat the 2+ passband cut. This reduces our sample by a further nine objects, leaving 223 SNe covered by 610 spectra and 11,034 photometric points.

Those objects that remain at this point are then processed in accordance with the description in Section 6.2.1.3.

Chapter 7

Conclusion

This thesis is best decomposed into three parts, each of which enables the next: Chapters 2 & 3 deliver novel, large-scale photometric and spectroscopic SN Ia datasets, respectively. These data are then combined with a meticulously homogenized literature sample to develop `deepSIP` (Chapter 4), which, in turn, breathes life into the snapshot distance method (SDM; Chapter 5). Finally, in Chapter 6, I use the SDM to "resurrect" a significant sample of otherwise discarded SN Ia observations, which, when combined with a large literature sample of SNe Ia and SNe II, provide the tightest-ever SN-based constraints on the degenerate cosmological parameter combination $f\sigma_8$. In the following paragraphs, I briefly summarize key findings from each chapter.

In Chapter 2, I present light curves (in the $BVRI$, and in some cases unfiltered, passbands) of 93 SNe Ia collected by the Lick Observatory Supernova Search (LOSS) between 2005 and 2018. The median SN Ia in the sample is covered by 16 photometric epochs at a cadence of 5.4 days, has a redshift of 0.0192, and is first observed at ~ -4.6 days relative to maximum light. I describe the methods by which the SNe are discovered, observed, and processed, with particular emphasis placed on documenting the functionality of `LOSSPhotPypeline`[1], the automatic photometry pipeline I developed to handle the large volume of data. I demonstrate that `LOSSPhotPypeline` produces results that are consistent with LOSS's old, manual processing methods. All of the constituent data are openly available[2] to the astronomical community, as are the parameters derived from a light-curve-fitting analysis.

In complement with the photometry presented in Chapter 2, I provide, in Chapter 3, 637 low-redshift SN Ia optical spectra collected over a similar time period. After employing an automated classification scheme[3], I find that 626 spectra unambiguously belong to 242 distinct SNe Ia. At the SN level, the median object is first observed 1.1 days after maximum light and has a redshift of 0.0208; at the single-spectrum-level, the median signal-to-noise ratio is $31.8\,\mathrm{pixel}^{-1}$. I proceed with an analysis of prominent spectral features in the avail-

[1] `https://github.com/benstahl92/LOSSPhotPypeline`

[2] `http://heracles.astro.berkeley.edu/sndb/info#DownloadDatasets(BSNIP,LOSS,deepSIP)`

[3] `https://github.com/benstahl92/pySNID`

able early-time and late-time spectra, in which velocities and pseudo-equivalent widths are measured. These measurements, the code base[4] developed and utilized to make them, and the spectra that underly them are publicly available and will prove useful to the community.

When combined with prior data releases, Chapters 2 & 3 push the Berkeley SN Ia dataset to nearly 2000 optical spectra and more than 250 multiband light curves. Accumulated over the last $\sim$ 20 years, these data have been judiciously handled to ensure consistency across all observing and processing stages, and as such, offer a tantalizing dataset with which astronomers can study SNe Ia. In particular, I utilize these data (along with a comprehensive literature sample) in Chapter 4 to explore the extent to which the parameters derived via a light-curve-fitting analysis can be recovered from an optical spectrum (without any information from the light curve). The result is `deepSIP`[5], a software package capable of measuring the phase and light-curve shape (both with impressive precision) of an SN Ia from a single optical spectrum. "Under the hood," `deepSIP` is comprised of three convolutional neural networks that are trained on a significant fraction of all publicly-available low-redshift SN Ia data, including in an augmented format to promote model robustness and telescope agnosticism. `deepSIP` is open source and readily available to the astronomical community.

I demonstrate in Chapter 5 that `deepSIP` provides exactly what one needs to derive an SN Ia distance estimate from as little as one epoch of two-passband photometry (and the optical spectrum required by `deepSIP`, which need not be contemporaneous with the photometry) using the snapshot distance method (SDM). After subjecting the SDM to a suite of "stress tests," I find that the method is robust across a wide range of "normal" light-curve shapes, and to the relative temporal sampling of the photometry and spectroscopy that it utilizes. Moreover, the precision of the method follows an intuitive trend, performing better when more photometric information is provided (either in the form of more passbands per epoch, or in the form of more epochs). Notably, more spectra do not appear to wield much influence — a testament to the quality of `deepSIP` predictions.

In addition to the promise that the SDM holds in the near future when large, wide-field surveys will discover many hundreds of thousands of SNe that they will not be able to monitor at high cadence, I utilize it in Chapter 6 to turn *trash to treasure* by deriving distance estimates to 137 sparsely observed SNe Ia that have been repeatedly omitted from cosmological analyses owing to their data sparsity. By combining these objects with a large sample of SNe Ia and SNe II, I utilize a sophisticated Bayesian framework to infer the cosmological parameter combination $f\sigma_8$ and the parameters that describe a coherent, bulk motion in the local Universe, while taking care to enforce a consistent relative distance scale between disparate subcatalogs, each weighted according to the precision of the objects of which they consist. The constraints I present are the tightest ever derived from SNe, but perhaps more importantly, the contents of Chapter 6 represent a prototype that can be readily deployed as the aforementioned, massive SN datasets become available in the coming years.

[4] `https://github.com/benstahl92/respext`

[5] `https://github.com/benstahl92/deepSIP`

Indeed, the future of supernova cosmology is quite *bright*. From the foundational datasets of Chapters 2 & 3, to the suite of extensible (but immediately practical) tools of Chapters 4 & 5, to the cosmological constraints and framework they enable in Chapter 6, this dissertation represents my own small contributions to this future. Onward!

Bibliography

T. M. C. Abbott, F. B. Abdalla, A. Alarcon, J. Aleksić, S. Allam, S. Allen, A. Amara, J. Annis, J. Asorey, S. Avila, D. Bacon, E. Balbinot, M. Banerji, N. Banik, W. Barkhouse, M. Baumer, E. Baxter, K. Bechtol, M. R. Becker, A. Benoit-Lévy, B. A. Benson, G. M. Bernstein, E. Bertin, J. Blazek, S. L. Bridle, D. Brooks, D. Brout, E. Buckley-Geer, D. L. Burke, M. T. Busha, A. Campos, D. Capozzi, A. Carnero Rosell, M. Carrasco Kind, J. Carretero, F. J. Castander, R. Cawthon, C. Chang, N. Chen, M. Childress, A. Choi, C. Conselice, R. Crittenden, M. Crocce, C. E. Cunha, C. B. D'Andrea, L. N. da Costa, R. Das, T. M. Davis, C. Davis, J. De Vicente, D. L. DePoy, J. DeRose, S. Desai, H. T. Diehl, J. P. Dietrich, S. Dodelson, P. Doel, A. Drlica-Wagner, T. F. Eifler, A. E. Elliott, F. Elsner, J. Elvin-Poole, J. Estrada, A. E. Evrard, Y. Fang, E. Fernandez, A. Ferté, D. A. Finley, B. Flaugher, P. Fosalba, O. Friedrich, J. Frieman, J. García-Bellido, M. Garcia-Fernandez, M. Gatti, E. Gaztanaga, D. W. Gerdes, T. Giannantonio, M. S. S. Gill, K. Glazebrook, D. A. Goldstein, D. Gruen, R. A. Gruendl, J. Gschwend, G. Gutierrez, S. Hamilton, W. G. Hartley, S. R. Hinton, K. Honscheid, B. Hoyle, D. Huterer, B. Jain, D. J. James, M. Jarvis, T. Jeltema, M. D. Johnson, M. W. G. Johnson, T. Kacprzak, S. Kent, A. G. Kim, A. King, D. Kirk, N. Kokron, A. Kovacs, E. Krause, C. Krawiec, A. Kremin, K. Kuehn, S. Kuhlmann, N. Kuropatkin, F. Lacasa, O. Lahav, T. S. Li, A. R. Liddle, C. Lidman, M. Lima, H. Lin, N. MacCrann, M. A. G. Maia, M. Makler, M. Manera, M. March, J. L. Marshall, P. Martini, R. G. McMahon, P. Melchior, F. Menanteau, R. Miquel, V. Miranda, D. Mudd, J. Muir, A. Möller, E. Neilsen, R. C. Nichol, B. Nord, P. Nugent, R. L. C. Ogando, A. Palmese, J. Peacock, H. V. Peiris, J. Peoples, W. J. Percival, D. Petravick, A. A. Plazas, A. Porredon, J. Prat, A. Pujol, M. M. Rau, A. Refregier, P. M. Ricker, N. Roe, R. P. Rollins, A. K. Romer, A. Roodman, R. Rosenfeld, A. J. Ross, E. Rozo, E. S. Rykoff, M. Sako, A. I. Salvador, S. Samuroff, C. Sánchez, E. Sanchez, B. Santiago, V. Scarpine, R. Schindler, D. Scolnic, L. F. Secco, S. Serrano, I. Sevilla-Noarbe, E. Sheldon, R. C. Smith, M. Smith, J. Smith, M. Soares-Santos, F. Sobreira, E. Suchyta, G. Tarle, D. Thomas, M. A. Troxel, D. L. Tucker, B. E. Tucker, S. A. Uddin, T. N. Varga, P. Vielzeuf, V. Vikram, A. K. Vivas, A. R. Walker, M. Wang, R. H. Wechsler, J. Weller, W. Wester, R. C. Wolf, B. Yanny, F. Yuan, A. Zenteno, B. Zhang, Y. Zhang, J. Zuntz, and Dark Energy Survey Collaboration. Dark Energy Survey year 1 results: Cosmological constraints from galaxy clustering and weak lensing. *Phys. Rev. D*, 98(4):043526, Aug. 2018. doi: 10.1103/PhysRevD.98.043526.

C. Adams and C. Blake. Joint growth-rate measurements from redshift-space distortions and peculiar velocities in the 6dF Galaxy Survey. *MNRAS*, 494(3):3275–3293, May 2020. doi: 10.1093/mnras/staa845.

S. Aiola, E. Calabrese, L. Maurin, S. Naess, B. L. Schmitt, M. H. Abitbol, G. E. Addison, P. A. R. Ade, D. Alonso, M. Amiri, S. Amodeo, E. Angile, J. E. Austermann, T. Baildon, N. Battaglia, J. A. Beall, R. Bean, D. T. Becker, J. R. Bond, S. M. Bruno, V. Calafut, L. E. Campusano, F. Carrero, G. E. Chesmore, H.-m. Cho, S. K. Choi, S. E. Clark, N. F. Cothard, D. Crichton, K. T. Crowley, O. Darwish, R. Datta, E. V. Denison, M. J. Devlin, C. J. Duell, S. M. Duff, A. J. Duivenvoorden, J. Dunkley, R. Dünner, T. Essinger-Hileman, M. Fankhanel, S. Ferraro, A. E. Fox, B. Fuzia, P. A. Gallardo, V. Gluscevic, J. E. Golec, E. Grace, M. Gralla, Y. Guan, K. Hall, M. Halpern, D. Han, P. Hargrave, M. Hasselfield, J. M. Helton, S. Henderson, B. Hensley, J. C. Hill, G. C. Hilton, M. Hilton, A. D. Hincks, R. Hložek, S.-P. P. Ho, J. Hubmayr, K. M. Huffenberger, J. P. Hughes, L. Infante, K. Irwin, R. Jackson, J. Klein, K. Knowles, B. Koopman, A. Kosowsky, V. Lakey, D. Li, Y. Li, Z. Li, M. Lokken, T. Louis, M. Lungu, A. MacInnis, M. Madhavacheril, F. Maldonado, M. Mallaby-Kay, D. Marsden, J. McMahon, F. Menanteau, K. Moodley, T. Morton, T. Namikawa, F. Nati, L. Newburgh, J. P. Nibarger, A. Nicola, M. D. Niemack, M. R. Nolta, J. Orlowski-Sherer, L. A. Page, C. G. Pappas, B. Partridge, P. Phakathi, G. Pisano, H. Prince, R. Puddu, F. J. Qu, J. Rivera, N. Robertson, F. Rojas, M. Salatino, E. Schaan, A. Schillaci, N. Sehgal, B. D. Sherwin, C. Sierra, J. Sievers, C. Sifon, P. Sikhosana, S. Simon, D. N. Spergel, S. T. Staggs, J. Stevens, E. Storer, D. D. Sunder, E. R. Switzer, B. Thorne, R. Thornton, H. Trac, J. Treu, C. Tucker, L. R. Vale, A. Van Engelen, J. Van Lanen, E. M. Vavagiakis, K. Wagoner, Y. Wang, J. T. Ward, E. J. Wollack, Z. Xu, F. Zago, and N. Zhu. The Atacama Cosmology Telescope: DR4 maps and cosmological parameters. *J. Cosmology Astropart. Phys.*, 2020(12):047, Dec. 2020. doi: 10.1088/1475-7516/2020/12/047.

S. Alam, F. D. Albareti, C. Allende Prieto, F. Anders, S. F. Anderson, T. Anderton, B. H. Andrews, E. Armengaud, É. Aubourg, S. Bailey, and et al. The Eleventh and Twelfth Data Releases of the Sloan Digital Sky Survey: Final Data from SDSS-III. *ApJS*, 219:12, July 2015. doi: 10.1088/0067-0049/219/1/12.

C. Alard. Image subtraction with non-constant kernel solutions. *arXiv e-prints*, art. astro-ph/9903111, Mar. 1999.

C. Alard and R. H. Lupton. A Method for Optimal Image Subtraction. *ApJ*, 503(1):325–331, Aug. 1998. doi: 10.1086/305984.

V. Arsenijevic, S. Fabbro, A. M. Mourão, and A. J. Rica da Silva. Diversity of supernovae Ia determined using equivalent widths of Si II 4000. *A&A*, 492(2):535–544, Dec 2008. doi: 10.1051/0004-6361:200810675.

P. Astier, J. Guy, N. Regnault, R. Pain, E. Aubourg, D. Balam, S. Basa, R. G. Carlberg, S. Fabbro, D. Fouchez, I. M. Hook, D. A. Howell, H. Lafoux, J. D. Neill, N. Palanque-Delabrouille, K. Perrett, C. J. Pritchet, J. Rich, M. Sullivan, R. Taillet, G. Aldering, P. Antilogus, V. Arsenijevic, C. Balland, S. Baumont, J. Bronder, H. Courtois, R. S. Ellis, M. Filiol, A. C. Gonçalves, A. Goobar, D. Guide, D. Hardin, V. Lusset, C. Lidman, R. McMahon, M. Mouchet, A. Mourao, S. Perlmutter, P. Ripoche, C. Tao, and N. Walton. The Supernova Legacy Survey: measurement of Ω_M, Ω and w from the first year data set. *A&A*, 447:31–48, Feb. 2006. doi: 10.1051/0004-6361:20054185.

W. Baade and F. Zwicky. Remarks on Super-Novae and Cosmic Rays. *Physical Review*, 46 (1):76–77, July 1934. doi: 10.1103/PhysRev.46.76.2.

S. Bailey, G. Aldering, P. Antilogus, C. Aragon, C. Baltay, S. Bongard, C. Buton, M. Childress, N. Chotard, Y. Copin, E. Gangler, S. Loken, P. Nugent, R. Pain, E. Pecontal, R. Pereira, S. Perlmutter, D. Rabinowitz, G. Rigaudier, K. Runge, R. Scalzo, G. Smadja, H. Swift, C. Tao, R. C. Thomas, C. Wu, and Nearby Supernova Factory. Using spectral flux ratios to standardize SN Ia luminosities. *A&A*, 500:L17–L20, June 2009. doi: 10.1051/0004-6361/200911973.

E. C. Bellm, S. R. Kulkarni, M. J. Graham, R. Dekany, R. M. Smith, R. Riddle, F. J. Masci, G. Helou, T. A. Prince, S. M. Adams, C. Barbarino, T. Barlow, J. Bauer, R. Beck, J. Belicki, R. Biswas, N. Blagorodnova, D. Bodewits, B. Bolin, V. Brinnel, T. Brooke, B. Bue, M. Bulla, R. Burruss, S. B. Cenko, C.-K. Chang, A. Connolly, M. Coughlin, J. Cromer, V. Cunningham, K. De, A. Delacroix, V. Desai, D. A. Duev, G. Eadie, T. L. Farnham, M. Feeney, U. Feindt, D. Flynn, A. Franckowiak, S. Frederick, C. Fremling, A. Gal-Yam, S. Gezari, M. Giomi, D. A. Goldstein, V. Z. Golkhou, A. Goobar, S. Groom, E. Hacopians, D. Hale, J. Henning, A. Y. Q. Ho, D. Hover, J. Howell, T. Hung, D. Huppenkothen, D. Imel, W.-H. Ip, Ž. Ivezić, E. Jackson, L. Jones, M. Juric, M. M. Kasliwal, S. Kaspi, S. Kaye, M. S. P. Kelley, M. Kowalski, E. Kramer, T. Kupfer, W. Landry, R. R. Laher, C.-D. Lee, H. W. Lin, Z.-Y. Lin, R. Lunnan, M. Giomi, A. Mahabal, P. Mao, A. A. Miller, S. Monkewitz, P. Murphy, C.-C. Ngeow, J. Nordin, P. Nugent, E. Ofek, M. T. Patterson, B. Penprase, M. Porter, L. Rauch, U. Rebbapragada, D. Reiley, M. Rigault, H. Rodriguez, J. van Roestel, B. Rusholme, J. van Santen, S. Schulze, D. L. Shupe, L. P. Singer, M. T. Soumagnac, R. Stein, J. Surace, J. Sollerman, P. Szkody, F. Taddia, S. Terek, A. Van Sistine, S. van Velzen, W. T. Vestrand, R. Walters, C. Ward, Q.-Z. Ye, P.-C. Yu, L. Yan, and J. Zolkower. The Zwicky Transient Facility: System Overview, Performance, and First Results. *PASP*, 131(995):018002, Jan. 2019. doi: 10.1088/1538-3873/aaecbe.

S. Benetti, E. Cappellaro, P. A. Mazzali, M. Turatto, G. Altavilla, F. Bufano, N. Elias-Rosa, R. Kotak, G. Pignata, M. Salvo, and V. Stanishev. The Diversity of Type Ia Supernovae: Evidence for Systematics? *The Astrophysical Journal*, 623(2):1011–1016, Apr 2005. doi: 10.1086/428608.

J. P. Bernstein, R. Kessler, S. Kuhlmann, et al. Supernova Simulations and Strategies for the Dark Energy Survey. *ApJ*, 753:152, July 2012. doi: 10.1088/0004-637X/753/2/152.

M. S. Bessell. UBVRI passbands. *PASP*, 102:1181–1199, Oct. 1990. doi: 10.1086/132749.

M. Betoule, R. Kessler, J. Guy, J. Mosher, D. Hardin, R. Biswas, P. Astier, P. El-Hage, M. Konig, S. Kuhlmann, J. Marriner, R. Pain, N. Regnault, C. Balland, B. A. Bassett, P. J. Brown, H. Campbell, R. G. Carlberg, F. Cellier-Holzem, D. Cinabro, A. Conley, C. B. D'Andrea, D. L. DePoy, M. Doi, R. S. Ellis, S. Fabbro, A. V. Filippenko, R. J. Foley, J. A. Frieman, D. Fouchez, L. Galbany, A. Goobar, R. R. Gupta, G. J. Hill, R. Hlozek, C. J. Hogan, I. M. Hook, D. A. Howell, S. W. Jha, L. Le Guillou, G. Leloudas, C. Lidman, J. L. Marshall, A. Möller, A. M. Mourão, J. Neveu, R. Nichol, M. D. Olmstead, N. Palanque-Delabrouille, S. Perlmutter, J. L. Prieto, C. J. Pritchet, M. Richmond, A. G. Riess, V. Ruhlmann-Kleider, M. Sako, K. Schahmaneche, D. P. Schneider, M. Smith, J. Sollerman, M. Sullivan, N. A. Walton, and C. J. Wheeler. Improved cosmological constraints from a joint analysis of the SDSS-II and SNLS supernova samples. *Astronomy and Astrophysics*, 568:A22, Aug 2014. doi: 10.1051/0004-6361/201423413.

F. Beutler, C. Blake, M. Colless, D. H. Jones, L. Staveley-Smith, G. B. Poole, L. Campbell, Q. Parker, W. Saunders, and F. Watson. The 6dF Galaxy Survey: z$\approx$ 0 measurements of the growth rate and σ_8. *MNRAS*, 423(4):3430–3444, July 2012. doi: 10.1111/j.1365-2966.2012.21136.x.

N. Blagorodnova, J. D. Neill, R. Walters, S. R. Kulkarni, C. Fremling, S. Ben-Ami, R. G. Dekany, J. R. Fucik, N. Konidaris, R. Nash, C.-C. Ngeow, E. O. Ofek, D. O' Sullivan, R. Quimby, A. Ritter, and K. E. Vyhmeister. The SED Machine: A Robotic Spectrograph for Fast Transient Classification. *PASP*, 130(985):035003, Mar. 2018. doi: 10.1088/1538-3873/aaa53f.

S. Blondin and J. L. Tonry. Determining the type, redshift, and age of a supernova spectrum. *AJ*, 666(2):1024, 2007. URL `http://stacks.iop.org/0004-637X/666/i=2/a=1024`.

S. Blondin, K. S. Mandel, and R. P. Kirshner. Do spectra improve distance measurements of Type Ia supernovae? *A&A*, 526:A81, Feb. 2011. doi: 10.1051/0004-6361/201015792.

S. Blondin, T. Matheson, R. P. Kirshner, K. S. Mand el, P. Berlind, M. Calkins, P. Challis, P. M. Garnavich, S. W. Jha, M. Modjaz, A. G. Riess, and B. P. Schmidt. The Spectroscopic Diversity of Type Ia Supernovae. *The Astronomical Journal*, 143(5):126, May 2012. doi: 10.1088/0004-6256/143/5/126.

J. S. Bloom, D. Kasen, K. J. Shen, P. E. Nugent, N. R. Butler, M. L. Graham, D. A. Howell, U. Kolb, S. Holmes, C. A. Haswell, V. Burwitz, J. Rodriguez, and M. Sullivan. A Compact Degenerate Primary-star Progenitor of SN 2011fe. *ApJ*, 744(2):L17, Jan. 2012a. doi: 10.1088/2041-8205/744/2/L17.

J. S. Bloom, J. W. Richards, P. E. Nugent, R. M. Quimby, M. M. Kasliwal, D. L. Starr, D. Poznanski, E. O. Ofek, S. B. Cenko, N. R. Butler, S. R. Kulkarni, A. Gal-Yam, and N. Law. Automating Discovery and Classification of Transients and Variable Stars in the Synoptic Survey Era. *PASP*, 124(921):1175, Nov 2012b. doi: 10.1086/668468.

S. Bocquet, J. P. Dietrich, T. Schrabback, L. E. Bleem, M. Klein, S. W. Allen, D. E. Applegate, M. L. N. Ashby, M. Bautz, M. Bayliss, B. A. Benson, M. Brodwin, E. Bulbul, R. E. A. Canning, R. Capasso, J. E. Carlstrom, C. L. Chang, I. Chiu, H. M. Cho, A. Clocchiatti, T. M. Crawford, A. T. Crites, T. de Haan, S. Desai, M. A. Dobbs, R. J. Foley, W. R. Forman, G. P. Garmire, E. M. George, M. D. Gladders, A. H. Gonzalez, S. Grandis, N. Gupta, N. W. Halverson, J. Hlavacek-Larrondo, H. Hoekstra, G. P. Holder, W. L. Holzapfel, Z. Hou, J. D. Hrubes, N. Huang, C. Jones, G. Khullar, L. Knox, R. Kraft, A. T. Lee, A. von der Linden, D. Luong-Van, A. Mantz, D. P. Marrone, M. McDonald, J. J. McMahon, S. S. Meyer, L. M. Mocanu, J. J. Mohr, R. G. Morris, S. Padin, S. Patil, C. Pryke, D. Rapetti, C. L. Reichardt, A. Rest, J. E. Ruhl, B. R. Saliwanchik, A. Saro, J. T. Sayre, K. K. Schaffer, E. Shirokoff, B. Stalder, S. A. Stanford, Z. Staniszewski, A. A. Stark, K. T. Story, V. Strazzullo, C. W. Stubbs, K. Vanderlinde, J. D. Vieira, A. Vikhlinin, R. Williamson, and A. Zenteno. Cluster Cosmology Constraints from the 2500 deg^2 SPT-SZ Survey: Inclusion of Weak Gravitational Lensing Data from Magellan and the Hubble Space Telescope. *ApJ*, 878(1):55, June 2019. doi: 10.3847/1538-4357/ab1f10.

K. Boone. Avocado: Photometric Classification of Astronomical Transients with Gaussian Process Augmentation. *AJ*, 158(6):257, Dec. 2019. doi: 10.3847/1538-3881/ab5182.

S. S. Boruah, M. J. Hudson, and G. Lavaux. Cosmic flows in the nearby Universe: new peculiar velocities from SNe and cosmological constraints. *MNRAS*, 498(2):2703–2718, Aug. 2020. doi: 10.1093/mnras/staa2485.

D. Branch, L. C. Dang, N. Hall, W. Ketchum, M. Melakayil, J. Parrent, M. A. Troxel, D. Casebeer, D. J. Jeffery, and E. Baron. Comparative Direct Analysis of Type Ia Supernova Spectra. II. Maximum Light. *Publications of the Astronomical Society of the Pacific*, 118(842):560–571, Apr 2006. doi: 10.1086/502778.

P. J. Brown, A. A. Breeveld, S. Holland, P. Kuin, and T. Pritchard. SOUSA: the Swift Optical/Ultraviolet Supernova Archive. *Ap&SS*, 354(1):89–96, Nov. 2014. doi: 10.1007/s10509-014-2059-8.

C. R. Burns, M. Stritzinger, M. M. Phillips, S. Kattner, S. E. Persson, B. F. Madore, W. L. Freedman, L. Boldt, A. Campillay, and C. Contreras. The Carnegie Supernova Project: Light-curve Fitting with SNooPy. *AJ*, 141(1):19, Jan 2011. doi: 10.1088/0004-6256/141/1/19.

C. R. Burns, E. Parent, M. M. Phillips, M. Stritzinger, K. Krisciunas, N. B. Suntzeff, E. Y. Hsiao, C. Contreras, J. Anais, L. Boldt, L. Busta, A. Campillay, S. Castellón, G. Folatelli,

W. L. Freedman, C. González, M. Hamuy, P. Heoflich, W. Krzeminski, B. F. Madore, N. Morrell, S. E. Persson, M. Roth, F. Salgado, J. Serón, and S. Torres. The Carnegie Supernova Project: Absolute Calibration and the Hubble Constant. *ApJ*, 869(1):56, Dec. 2018. doi: 10.3847/1538-4357/aae51c.

G. Cabrera-Vives, I. Reyes, F. Förster, P. A. Estévez, and J.-C. Maureira. Deep-HiTS: Rotation Invariant Convolutional Neural Network for Transient Detection. *ApJ*, 836(1): 97, Feb. 2017. doi: 10.3847/1538-4357/836/1/97.

J. A. Cardelli, G. C. Clayton, and J. S. Mathis. The relationship between infrared, optical, and ultraviolet extinction. *ApJ*, 345:245–256, Oct. 1989. doi: 10.1086/167900.

J. Carrick, S. J. Turnbull, G. Lavaux, and M. J. Hudson. Cosmological parameters from the comparison of peculiar velocities with predictions from the 2M++ density field. *MNRAS*, 450(1):317–332, June 2015. doi: 10.1093/mnras/stv547.

K. Chambers and Pan-STARRS Team. The Pan-STARRS1 Surveys. In *American Astronomical Society Meeting Abstracts #231*, volume 231 of *American Astronomical Society Meeting Abstracts*, page 102.01, Jan 2018.

T. Charnock and A. Moss. Deep Recurrent Neural Networks for Supernovae Classification. *ApJ*, 837(2):L28, Mar 2017. doi: 10.3847/2041-8213/aa603d.

M. J. Childress, R. A. Scalzo, S. A. Sim, B. E. Tucker, F. Yuan, B. P. Schmidt, S. B. Cenko, J. M. Silverman, C. Contreras, E. Y. Hsiao, M. Phillips, N. Morrell, S. W. Jha, C. McCully, A. V. Filippenko, J. P. Anderson, S. Benetti, F. Bufano, T. de Jaeger, F. Forster, A. Gal-Yam, L. Le Guillou, K. Maguire, J. Maund, P. A. Mazzali, G. Pignata, S. Smartt, J. Spyromilio, M. Sullivan, F. Taddia, S. Valenti, D. D. R. Bayliss, M. Bessell, G. A. Blanc, D. J. Carson, K. I. Clubb, C. de Burgh-Day, T. D. Desjardins, J. J. Fang, O. D. Fox, E. L. Gates, I. T. Ho, S. Keller, P. L. Kelly, C. Lidman, N. S. Loaring, J. R. Mould, M. Owers, S. Ozbilgen, L. Pei, T. Pickering, M. B. Pracy, J. A. Rich, B. E. Schaefer, N. Scott, M. Stritzinger, F. P. A. Vogt, and G. Zhou. Spectroscopic Observations of SN 2012fr: A Luminous, Normal Type Ia Supernova with Early High-velocity Features and a Late Velocity Plateau. *The Astrophysical Journal*, 770(1):29, Jun 2013. doi: 10.1088/0004-637X/770/1/29.

M. J. Childress, A. V. Filippenko, M. Ganeshalingam, and B. P. Schmidt. High-velocity features in Type Ia supernova spectra. *MNRAS*, 437(1):338–350, Jan 2014. doi: 10.1093/mnras/stt1892.

S. A. Colgate and C. McKee. Early Supernova Luminosity. *ApJ*, 157:623, Aug. 1969. doi: 10.1086/150102.

S. A. Colgate and R. H. White. The Hydrodynamic Behavior of Supernovae Explosions. *ApJ*, 143:626, Mar. 1966. doi: 10.1086/148549.

J. Colin, R. Mohayaee, S. Sarkar, and A. Shafieloo. Probing the anisotropic local Universe and beyond with SNe Ia data. *MNRAS*, 414(1):264–271, June 2011. doi: 10.1111/j.1365-2966.2011.18402.x.

A. Conley, J. Guy, M. Sullivan, N. Regnault, P. Astier, C. Balland, S. Basa, R. G. Carlberg, D. Fouchez, D. Hardin, I. M. Hook, D. A. Howell, R. Pain, N. Palanque-Delabrouille, K. M. Perrett, C. J. Pritchet, J. Rich, V. Ruhlmann-Kleider, D. Balam, S. Baumont, R. S. Ellis, S. Fabbro, H. K. Fakhouri, N. Fourmanoit, S. González-Gaitán, M. L. Graham, M. J. Hudson, E. Hsiao, T. Kronborg, C. Lidman, A. M. Mourao, J. D. Neill, S. Perlmutter, P. Ripoche, N. Suzuki, and E. S. Walker. Supernova Constraints and Systematic Uncertainties from the First Three Years of the Supernova Legacy Survey. *ApJS*, 192(1):1, Jan. 2011. doi: 10.1088/0067-0049/192/1/1.

C. Contreras, M. Hamuy, M. M. Phillips, G. Folatelli, N. B. Suntzeff, S. E. Persson, M. Stritzinger, L. Boldt, S. González, W. Krzeminski, N. Morrell, M. Roth, F. Salgado, M. J. Maureira, C. R. Burns, W. L. Freedman, B. F. Madore, D. Murphy, P. Wyatt, W. Li, and A. V. Filippenko. The Carnegie Supernova Project: First Photometry Data Release of Low-Redshift Type Ia Supernovae. *AJ*, 139(2):519–539, Feb. 2010. doi: 10.1088/0004-6256/139/2/519.

M. Costanzi, E. Rozo, M. Simet, Y. Zhang, A. E. Evrard, A. Mantz, E. S. Rykoff, T. Jeltema, D. Gruen, S. Allen, T. McClintock, A. K. Romer, A. von der Linden, A. Farahi, J. DeRose, T. N. Varga, J. Weller, P. Giles, D. L. Hollowood, S. Bhargava, A. Bermeo-Hernandez, X. Chen, T. M. C. Abbott, F. B. Abdalla, S. Avila, K. Bechtol, D. Brooks, E. Buckley-Geer, D. L. Burke, A. C. Rosell, M. C. Kind, J. Carretero, M. Crocce, C. E. Cunha, L. N. da Costa, C. Davis, J. De Vicente, H. T. Diehl, J. P. Dietrich, P. Doel, T. F. Eifler, J. Estrada, B. Flaugher, P. Fosalba, J. Frieman, J. García-Bellido, E. Gaztanaga, D. W. Gerdes, T. Giannantonio, R. A. Gruendl, J. Gschwend, G. Gutierrez, W. G. Hartley, K. Honscheid, B. Hoyle, D. J. James, E. Krause, K. Kuehn, N. Kuropatkin, M. Lima, H. Lin, M. A. G. Maia, M. March, J. L. Marshall, P. Martini, F. Menanteau, C. J. Miller, R. Miquel, J. J. Mohr, R. L. C. Ogando, A. A. Plazas, A. Roodman, E. Sanchez, V. Scarpine, R. Schindler, M. Schubnell, S. Serrano, I. Sevilla-Noarbe, E. Sheldon, M. Smith, M. Soares-Santos, F. Sobreira, E. Suchyta, M. E. C. Swanson, G. Tarle, D. Thomas, and R. H. Wechsler. Methods for cluster cosmology and application to the SDSS in preparation for DES Year 1 release. *MNRAS*, 488(4):4779–4800, Oct. 2019. doi: 10.1093/mnras/stz1949.

M. Costanzi, A. Saro, S. Bocquet, T. M. C. Abbott, M. Aguena, S. Allam, A. Amara, J. Annis, S. Avila, D. Bacon, B. A. Benson, S. Bhargava, D. Brooks, E. Buckley-Geer, D. L. Burke, A. Carnero Rosell, M. Carrasco Kind, J. Carretero, A. Choi, L. N. da Costa, M. E. S. Pereira, J. De Vicente, S. Desai, H. T. Diehl, J. P. Dietrich, P. Doel, T. F. Eifler, S. Everett, I. Ferrero, A. Ferté, B. Flaugher, P. Fosalba, J. Frieman, J. García-Bellido, E. Gaztanaga, D. W. Gerdes, T. Giannantonio, P. Giles, S. Grandis, D. Gruen, R. A. Gruendl, N. Gupta, G. Gutierrez, W. G. Hartley, S. R. Hinton, D. L. Hollowood,

K. Honscheid, D. J. James, T. Jeltema, E. Krause, K. Kuehn, N. Kuropatkin, O. Lahav, M. Lima, N. MacCrann, M. A. G. Maia, J. L. Marshall, F. Menanteau, R. Miquel, J. J. Mohr, R. Morgan, J. Myles, R. L. C. Ogando, A. Palmese, F. Paz-Chinchón, A. A. Plazas, D. Rapetti, C. L. Reichardt, A. K. Romer, A. Roodman, F. Ruppin, L. Salvati, S. Samuroff, E. Sanchez, V. Scarpine, S. Serrano, I. Sevilla-Noarbe, P. Singh, M. Smith, M. Soares-Santos, A. A. Stark, E. Suchyta, M. E. C. Swanson, G. Tarle, D. Thomas, C. To, D. L. Tucker, T. N. Varga, R. H. Wechsler, Z. Zhang, DES, and SPT Collaborations. Cosmological constraints from DES Y1 cluster abundances and SPT multiwavelength data. *Phys. Rev. D*, 103(4):043522, Feb. 2021. doi: 10.1103/PhysRevD.103.043522.

D.-C. Dai, W. H. Kinney, and D. Stojkovic. Measuring the cosmological bulk flow using the peculiar velocities of supernovae. *J. Cosmology Astropart. Phys.*, 2011(4):015, Apr. 2011. doi: 10.1088/1475-7516/2011/04/015.

C. B. D'Andrea, M. Sako, B. Dilday, et al. Type II-P Supernovae from the SDSS-II Supernova Survey and the Standardized Candle Method. *ApJ*, 708:661–674, Jan. 2010. doi: 10.1088/0004-637X/708/1/661.

T. M. Davis and M. I. Scrimgeour. Deriving accurate peculiar velocities (even at high redshift). *MNRAS*, 442(2):1117–1122, Aug. 2014. doi: 10.1093/mnras/stu920.

T. de Jaeger, L. Galbany, A. V. Filippenko, S. González-Gaitán, N. Yasuda, K. Maeda, M. Tanaka, T. Morokuma, T. J. Moriya, N. Tominaga, K. Nomoto, Y. Komiyama, J. P. Anderson, T. G. Brink, R. G. Carlberg, G. Folatelli, M. Hamuy, G. Pignata, and W. Zheng. SN 2016jhj at redshift 0.34: extending the Type II supernova Hubble diagram using the standard candle method. *MNRAS*, 472(4):4233–4243, Dec. 2017. doi: 10.1093/mnras/stx2300.

T. de Jaeger, W. Zheng, B. E. Stahl, A. V. Filippenko, T. G. Brink, A. Bigley, K. Blanchard, P. K. Blanchard, J. Bradley, S. K. Cargill, C. Casper, S. B. Cenko, S. Channa, B. Y. Choi, K. I. Clubb, B. E. Cobb, D. Cohen, M. de Kouchkovsky, M. Ellison, E. Falcon, O. D. Fox, K. Fuller, M. Ganeshalingam, C. Gould, M. L. Graham, G. Halevi, K. T. Hayakawa, J. Hestenes, M. P. Hyland, B. Jeffers, N. Joubert, M. T. Kandrashoff, P. L. Kelly, H. Kim, M. Kim, S. Kumar, E. J. Leonard, G. Z. Li, T. B. Lowe, P. Lu, M. Mason, K. J. McAllister, J. C. Mauerhan, M. Modjaz, J. Molloy, D. A. Perley, K. Pina, D. Poznanski, T. W. Ross, I. Shivvers, J. M. Silverman, C. Soler, S. Stegman, S. Taylor, K. Tang, A. Wilkins, X. Wang, X. Wang, H. Yuk, S. Yunus, and K. D. Zhang. The Berkeley sample of Type II supernovae: BVRI light curves and spectroscopy of 55 SNe II. *MNRAS*, 490(2):2799–2821, Dec 2019. doi: 10.1093/mnras/stz2714.

T. de Jaeger, L. Galbany, S. González-Gaitán, R. Kessler, A. V. Filippenko, F. Förster, M. Hamuy, P. J. Brown, T. M. Davis, C. P. Gutiérrez, C. Inserra, G. F. Lewis, A. Möller, D. Scolnic, M. Smith, D. Brout, D. Carollo, R. J. Foley, K. Glazebrook, S. R. Hinton, E. Macaulay, B. Nichol, M. Sako, N. E. Sommer, B. E. Tucker, T. M. C. Abbott,

M. Aguena, S. Allam, J. Annis, S. Avila, E. Bertin, S. Bhargava, D. Brooks, D. L. Burke, A. Carnero Rosell, M. Carrasco Kind, J. Carretero, M. Costanzi, M. Crocce, L. N. da Costa, J. De Vicente, S. Desai, H. T. Diehl, P. Doel, A. Drlica-Wagner, T. F. Eifler, J. Estrada, S. Everett, B. Flaugher, P. Fosalba, J. Frieman, J. García-Bellido, E. Gaztanaga, D. Gruen, R. A. Gruendl, J. Gschwend, G. Gutierrez, W. G. Hartley, D. L. Hollowood, K. Honscheid, D. J. James, K. Kuehn, N. Kuropatkin, T. S. Li, M. Lima, M. A. G. Maia, F. Menanteau, R. Miquel, A. Palmese, F. Paz-Chinchón, A. A. Plazas, A. K. Romer, A. Roodman, E. Sanchez, V. Scarpine, M. Schubnell, S. Serrano, I. Sevilla-Noarbe, M. Soares-Santos, E. Suchyta, M. E. C. Swanson, G. Tarle, D. Thomas, D. L. Tucker, T. N. Varga, A. R. Walker, J. Weller, R. Wilkinson, and DES Collaboration. Studying Type II supernovae as cosmological standard candles using the Dark Energy Survey. *MNRAS*, 495(4):4860–4892, May 2020a. doi: 10.1093/mnras/staa1402.

T. de Jaeger, B. E. Stahl, W. Zheng, A. V. Filippenko, A. G. Riess, and L. Galbany. A measurement of the Hubble constant from Type II supernovae. *MNRAS*, 496(3):3402–3411, Aug. 2020b. doi: 10.1093/mnras/staa1801.

S. Dhawan, S. W. Jha, and B. Leibundgut. Measuring the Hubble constant with Type Ia supernovae as near-infrared standard candles. *Astronomy and Astrophysics*, 609:A72, Jan 2018. doi: 10.1051/0004-6361/201731501.

E. Di Valentino, L. A. Anchordoqui, O. Akarsu, Y. Ali-Haimoud, L. Amendola, N. Arendse, M. Asgari, M. Ballardini, S. Basilakos, E. Battistelli, M. Benetti, S. Birrer, F. R. Bouchet, M. Bruni, E. Calabrese, D. Camarena, S. Capozziello, A. Chen, J. Chluba, A. Chudaykin, E. Ó. Colgáin, F.-Y. Cyr-Racine, P. de Bernardis, J. de Cruz Pérez, J. Delabrouille, J. Dunkley, C. Escamilla-Rivera, A. Ferté, F. Finelli, W. Freedman, N. Frusciante, E. Giusarma, A. Gómez-Valent, W. Handley, I. Harrison, L. Hart, A. Heavens, H. Hildebrandt, D. Holz, D. Huterer, M. M. Ivanov, S. Joudaki, M. Kamionkowski, T. Karwal, L. Knox, S. Kumar, L. Lamagna, J. Lesgourgues, M. Lucca, V. Marra, S. Masi, S. Matarrese, A. Mazumdar, A. Melchiorri, O. Mena, L. Mersini-Houghton, V. Miranda, C. Moreno-Pulido, D. F. Mota, J. Muir, A. Mukherjee, F. Niedermann, A. Notari, R. C. Nunes, F. Pace, A. Paliathanasis, A. Palmese, S. Pan, D. Paoletti, V. Pettorino, F. Piacentini, V. Poulin, M. Raveri, A. G. Riess, V. Salzano, E. N. Saridakis, A. A. Sen, A. Shafieloo, A. J. Shajib, J. Silk, A. Silvestri, M. S. Sloth, T. L. Smith, J. Solà, C. van de Bruck, L. Verde, L. Visinelli, B. D. Wandelt, D. Wang, J.-M. Wang, A. K. Yadav, and W. Yang. Cosmology Intertwined III: $f\sigma_8$ and S_8. *arXiv e-prints*, art. arXiv:2008.11285, Aug. 2020.

S. Dieleman, K. W. Willett, and J. Dambre. Rotation-invariant convolutional neural networks for galaxy morphology prediction. *MNRAS*, 450(2):1441–1459, June 2015. doi: 10.1093/mnras/stv632.

S. Dong, B. Katz, D. Kushnir, and J. L. Prieto. Type Ia supernovae with bimodal explosions are common - possible smoking gun for direct collisions of white dwarfs. *MNRAS*, 454: L61–L65, Nov. 2015. doi: 10.1093/mnrasl/slv129.

eBOSS Collaboration, S. Alam, M. Aubert, S. Avila, C. Balland, J. E. Bautista, M. A. Bershady, D. Bizyaev, M. R. Blanton, A. S. Bolton, J. Bovy, J. Brinkmann, J. R. Brownstein, E. Burtin, S. Chabanier, M. J. Chapman, P. D. Choi, C.-H. Chuang, J. Comparat, A. Cuceu, K. S. Dawson, A. de la Macorra, S. de la Torre, A. de Mattia, V. de Sainte Agathe, H. du Mas des Bourboux, S. Escoffier, T. Etourneau, J. Farr, A. Font-Ribera, P. M. Frinchaboy, S. Fromenteau, H. Gil-Marín, A. X. Gonzalez-Morales, V. Gonzalez-Perez, K. Grabowski, J. Guy, A. J. Hawken, J. Hou, H. Kong, M. Klaene, J.-P. Kneib, J.-M. Le Goff, S. Lin, D. Long, B. W. Lyke, M.-C. Cousinou, P. Martini, K. Masters, F. G. Mohammad, J. Moon, E.-M. Mueller, A. Munõz-Gutieŕrez, A. D. Myers, S. Nadathur, R. Neveux, J. A. Newman, P. Noterdaeme, A. Oravetz, D. Oravetz, N. Palanque-Delabrouille, K. Pan, I. Parker, James, R. Paviot, W. J. Percival, I. Pérez-Ràfols, P. Petitjean, M. M. Pieri, A. Prakash, A. Raichoor, C. Ravoux, M. Rezaie, J. Rich, A. J. Ross, G. Rossi, R. Ruggeri, V. Ruhlmann-Kleider, A. G. Sańchez, F. J. Sańchez, J. R. Sańchez-Gallego, C. Sayres, D. P. Schneider, H.-J. Seo, A. Shafieloo, A. Slosar, A. Smith, J. Stermer, A. Tamone, J. L. Tinker, R. Tojeiro, M. Vargas-Magaña, A. Variu, Y. Wang, B. A. Weaver, A.-M. Weijmans, C. Yeche, P. Zarrouk, C. Zhao, G.-B. Zhao, and Z. Zheng. The Completed SDSS-IV extended Baryon Oscillation Spectroscopic Survey: Cosmological Implications from two Decades of Spectroscopic Surveys at the Apache Point observatory. *arXiv e-prints*, art. arXiv:2007.08991, July 2020.

D. Fabricant, P. Cheimets, N. Caldwell, and J. Geary. The FAST Spectrograph for the Tillinghast Telescope. *PASP*, 110(743):79–85, Jan. 1998. doi: 10.1086/316111.

H. K. Fakhouri, K. Boone, G. Aldering, P. Antilogus, C. Aragon, S. Bailey, C. Baltay, K. Barbary, D. Baugh, S. Bongard, C. Buton, J. Chen, M. Childress, N. Chotard, Y. Copin, P. Fagrelius, U. Feindt, M. Fleury, D. Fouchez, E. Gangler, B. Hayden, A. G. Kim, M. Kowalski, P. F. Leget, S. Lombardo, J. Nordin, R. Pain, E. Pecontal, R. Pereira, S. Perlmutter, D. Rabinowitz, J. Ren, M. Rigault, D. Rubin, K. Runge, C. Saunders, R. Scalzo, G. Smadja, C. Sofiatti, M. Strovink, N. Suzuki, C. Tao, R. C. Thomas, B. A. Weaver, and T. Nearby Supernova Factory. Improving Cosmological Distance Measurements Using Twin Type Ia Supernovae. *ApJ*, 815(1):58, Dec 2015. doi: 10.1088/0004-637X/815/1/58.

U. Feindt, M. Kerschhaggl, M. Kowalski, G. Aldering, P. Antilogus, C. Aragon, S. Bailey, C. Baltay, S. Bongard, C. Buton, A. Canto, F. Cellier-Holzem, M. Childress, N. Chotard, Y. Copin, H. K. Fakhouri, E. Gangler, J. Guy, A. Kim, P. Nugent, J. Nordin, K. Paech, R. Pain, E. Pecontal, R. Pereira, S. Perlmutter, D. Rabinowitz, M. Rigault, K. Runge, C. Saunders, R. Scalzo, G. Smadja, C. Tao, R. C. Thomas, B. A. Weaver, and C. Wu. Measuring cosmic bulk flows with Type Ia supernovae from the Nearby Supernova Factory. *A&A*, 560:A90, Dec. 2013. doi: 10.1051/0004-6361/201321880.

A. V. Filippenko. The importance of atmospheric differential refraction in spectrophotometry. *PASP*, 94:715–721, Aug. 1982. doi: 10.1086/131052.

A. V. Filippenko. Optical spectra of supernovae. *ARA&A*, 35(1):309–355, 1997. doi: 10.1146/annurev.astro.35.1.309. URL `https://doi.org/10.1146/annurev.astro.35.1.309`.

A. V. Filippenko. Optical spectra and light curves of supernovae. In W. Hillebrandt and B. Leibundgut, editors, *From Twilight to Highlight: The Physics of Supernovae*, pages 171–182, Berlin, Heidelberg, 2003. Springer Berlin Heidelberg. ISBN 978-3-540-36427-6.

A. V. Filippenko, M. W. Richmond, D. Branch, M. Gaskell, W. Herbst, C. H. Ford, R. R. Treffers, T. Matheson, L. C. Ho, A. Dey, W. L. W. Sargent, T. A. Small, and W. J. M. van Breugel. The Subluminous, Spectroscopically Peculiar Type 1a Supernova 1991bg in the Elliptical Galaxy NGC 4374. *AJ*, 104:1543, Oct 1992a. doi: 10.1086/116339.

A. V. Filippenko, M. W. Richmond, T. Matheson, J. C. Shields, E. M. Burbidge, R. D. Cohen, M. Dickinson, M. A. Malkan, B. Nelson, J. Pietz, D. Schlegel, P. Schmeer, H. Spinrad, C. C. Steidel, H. D. Tran, and W. Wren. The Peculiar Type IA SN 1991T: Detonation of a White Dwarf? *ApJ*, 384:L15, Jan 1992b. doi: 10.1086/186252.

A. V. Filippenko, W. D. Li, R. R. Treffers, and M. Modjaz. The Lick Observatory Supernova Search with the Katzman Automatic Imaging Telescope. In B. Paczynski, W.-P. Chen, and C. Lemme, editors, *IAU Colloq. 183: Small Telescope Astronomy on Global Scales*, volume 246 of *Astronomical Society of the Pacific Conference Series*, page 121, 2001.

G. Folatelli. Spectral homogeneity of type Ia supernovae. *New Astronomy Reviews*, 48(7-8): 623–628, May 2004. doi: 10.1016/j.newar.2003.12.039.

G. Folatelli, M. M. Phillips, C. R. Burns, C. Contreras, M. Hamuy, W. L. Freedman, S. E. Persson, M. Stritzinger, N. B. Suntzeff, K. Krisciunas, L. Boldt, S. González, W. Krzeminski, N. Morrell, M. Roth, F. Salgado, B. F. Madore, D. Murphy, P. Wyatt, W. Li, A. V. Filippenko, and N. Miller. The Carnegie Supernova Project: Analysis of the First Sample of Low-Redshift Type-Ia Supernovae. *AJ*, 139(1):120–144, Jan. 2010. doi: 10.1088/0004-6256/139/1/120.

G. Folatelli, N. Morrell, M. M. Phillips, E. Hsiao, A. Campillay, C. Contreras, S. Castellón, M. Hamuy, W. Krzeminski, M. Roth, M. Stritzinger, C. R. Burns, W. L. Freedman, B. F. Madore, D. Murphy, S. E. Persson, J. L. Prieto, N. B. Suntzeff, K. Krisciunas, J. P. Anderson, F. Förster, J. Maza, G. Pignata, P. A. Rojas, L. Boldt, F. Salgado, P. Wyatt, F. Olivares E., A. Gal-Yam, and M. Sako. Spectroscopy of Type Ia Supernovae by the Carnegie Supernova Project. *ApJ*, 773(1):53, Aug 2013. doi: 10.1088/0004-637X/773/1/53.

R. J. Foley and D. Kasen. Measuring Ejecta Velocity Improves Type Ia Supernova Distances. *ApJ*, 729:55, Mar. 2011. doi: 10.1088/0004-637X/729/1/55.

R. J. Foley, A. V. Filippenko, D. C. Leonard, A. G. Riess, P. Nugent, and S. Perlmutter. A Definitive Measurement of Time Dilation in the Spectral Evolution of the Moderate-Redshift Type Ia Supernova 1997ex. *ApJ*, 626(1):L11–L14, Jun 2005a. doi: 10.1086/431241.

R. J. Foley, A. V. Filippenko, D. C. Leonard, A. G. Riess, P. Nugent, and S. Perlmutter. A Definitive Measurement of Time Dilation in the Spectral Evolution of the Moderate-Redshift Type Ia Supernova 1997ex. *ApJ*, 626(1):L11–L14, Jun 2005b. doi: 10.1086/431241.

R. J. Foley, P. Challis, T. Groner, J. M. Silverman, S. B. Cenko, A. V. Filippenko, and W. Li. Supernovae 2009eq, 2009er, 2009es, 2009et, and 2009eu. *Central Bureau Electronic Telegrams*, 1817:2, May 2009.

R. J. Foley, P. J. Challis, A. V. Filippenko, M. Ganeshalingam, W. Landsman, W. Li, G. H. Marion, J. M. Silverman, R. L. Beaton, V. N. Bennert, S. B. Cenko, M. Childress, P. Guhathakurta, L. Jiang, J. S. Kalirai, R. P. Kirshner, A. Stockton, E. J. Tollerud, J. Vinkó, J. C. Wheeler, and J. H. Woo. Very Early Ultraviolet and Optical Observations of the Type Ia Supernova 2009ig. *The Astrophysical Journal*, 744(1):38, Jan 2012. doi: 10.1088/0004-637X/744/1/38.

R. J. Foley, P. J. Challis, R. Chornock, M. Ganeshalingam, W. Li, G. H. Marion, N. I. Morrell, G. Pignata, M. D. Stritzinger, J. M. Silverman, X. Wang, J. P. Anderson, A. V. Filippenko, W. L. Freedman, M. Hamuy, S. W. Jha, R. P. Kirshner, C. McCully, S. E. Persson, M. M. Phillips, D. E. Reichart, and A. M. Soderberg. Type Iax Supernovae: A New Class of Stellar Explosion. *The Astrophysical Journal*, 767(1):57, Apr 2013a. doi: 10.1088/0004-637X/767/1/57.

R. J. Foley, P. J. Challis, R. Chornock, M. Ganeshalingam, W. Li, G. H. Marion, N. I. Morrell, G. Pignata, M. D. Stritzinger, J. M. Silverman, X. Wang, J. P. Anderson, A. V. Filippenko, W. L. Freedman, M. Hamuy, S. W. Jha, R. P. Kirshner, C. McCully, S. E. Persson, M. M. Phillips, D. E. Reichart, and A. M. Soderberg. Type Iax Supernovae: A New Class of Stellar Explosion. *ApJ*, 767(1):57, Apr. 2013b. doi: 10.1088/0004-637X/767/1/57.

R. J. Foley, O. D. Fox, C. McCully, M. M. Phillips, D. J. Sand, W. Zheng, P. Challis, A. V. Filippenko, G. Folatelli, W. Hillebrandt, E. Y. Hsiao, S. W. Jha, R. P. Kirshner, M. Kromer, G. H. Marion, M. Nelson, R. Pakmor, G. Pignata, F. K. Röpke, I. R. Seitenzahl, J. M. Silverman, M. Skrutskie, and M. D. Stritzinger. Extensive HST ultraviolet spectra and multiwavelength observations of SN 2014J in M82 indicate reddening and circumstellar scattering by typical dust. *MNRAS*, 443(4):2887–2906, Oct. 2014. doi: 10.1093/mnras/stu1378.

R. J. Foley, S. D. Van Dyk, S. W. Jha, K. I. Clubb, A. V. Filippenko, J. C. Mauerhan, A. A. Miller, and N. Smith. On the Progenitor System of the Type Iax Supernova 2014dt in M61. *The Astrophysical Journal*, 798(2):L37, Jan 2015. doi: 10.1088/2041-8205/798/2/L37.

R. J. Foley, S. W. Jha, Y.-C. Pan, W. K. Zheng, L. Bildsten, A. V. Filippenko, and D. Kasen. Late-time spectroscopy of Type Iax Supernovae. *Monthly Notices of the Royal Astronomical Society*, 461(1):433–457, Sep 2016. doi: 10.1093/mnras/stw1320.

R. J. Foley, D. Scolnic, A. Rest, S. W. Jha, Y. C. Pan, A. G. Riess, P. Challis, K. C. Chambers, D. A. Coulter, K. G. Dettman, M. M. Foley, O. D. Fox, M. E. Huber, D. O. Jones, C. D. Kilpatrick, R. P. Kirshner, A. S. B. Schultz, M. R. Siebert, H. A. Flewelling, B. Gibson, E. A. Magnier, J. A. Miller, N. Primak, S. J. Smartt, K. W. Smith, R. J. Wainscoat, C. Waters, and M. Willman. The Foundation Supernova Survey: motivation, design, implementation, and first data release. *MNRAS*, 475(1):193–219, Mar 2018. doi: 10.1093/mnras/stx3136.

D. Foreman-Mackey. corner.py: Scatterplot matrices in python. *The Journal of Open Source Software*, 1(2):24, jun 2016. doi: 10.21105/joss.00024. URL `https://doi.org/10.21105/joss.00024`.

D. Foreman-Mackey, D. W. Hogg, D. Lang, and J. Goodman. emcee: The MCMC Hammer. *PASP*, 125(925):306, Mar. 2013. doi: 10.1086/670067.

A. S. Friedman, W. M. Wood-Vasey, G. H. Marion, P. Challis, K. S. Mandel, J. S. Bloom, M. Modjaz, G. Narayan, M. Hicken, R. J. Foley, C. R. Klein, D. L. Starr, A. Morgan, A. Rest, C. H. Blake, A. A. Miller, E. E. Falco, W. F. Wyatt, J. Mink, M. F. Skrutskie, and R. P. Kirshner. CfAIR2: Near-infrared Light Curves of 94 Type Ia Supernovae. *ApJS*, 220(1):9, Sep 2015. doi: 10.1088/0067-0049/220/1/9.

J. A. Frieman, B. Bassett, A. Becker, C. Choi, D. Cinabro, F. DeJongh, D. L. Depoy, B. Dilday, M. Doi, P. M. Garnavich, C. J. Hogan, J. Holtzman, M. Im, S. Jha, R. Kessler, K. Konishi, H. Lampeitl, J. Marriner, J. L. Marshall, D. McGinnis, G. Miknaitis, R. C. Nichol, J. L. Prieto, A. G. Riess, M. W. Richmond, R. Romani, M. Sako, D. P. Schneider, M. Smith, N. Takanashi, K. Tokita, K. van der Heyden, N. Yasuda, C. Zheng, J. Adelman-McCarthy, J. Annis, R. J. Assef, J. Barentine, R. Bender, R. D. Bland ford, W. N. Boroski, M. Bremer, H. Brewington, C. A. Collins, A. Crotts, J. Dembicky, J. Eastman, A. Edge, E. Edmondson, E. Elson, M. E. Eyler, A. V. Filippenko, R. J. Foley, S. Frank, A. Goobar, T. Gueth, J. E. Gunn, M. Harvanek, U. Hopp, Y. Ihara, Ž. Ivezić, S. Kahn, J. Kaplan, S. Kent, W. Ketzeback, S. J. Kleinman, W. Kollatschny, R. G. Kron, J. Krzesiński, D. Lamenti, G. Leloudas, H. Lin, D. C. Long, J. Lucey, R. H. Lupton, E. Malanushenko, V. Malanushenko, R. J. McMillan, J. Mendez, C. W. Morgan, T. Morokuma, A. Nitta, L. Ostman, K. Pan, C. M. Rockosi, A. K. Romer, P. Ruiz-Lapuente, G. Saurage, K. Schlesinger, S. A. Snedden, J. Sollerman, C. Stoughton, M. Stritzinger, M. Subba Rao, D. Tucker, P. Vaisanen, L. C. Watson, S. Watters, J. C. Wheeler, B. Yanny,

and D. York. The Sloan Digital Sky Survey-II Supernova Survey: Technical Summary. *AJ*, 135(1):338–347, Jan. 2008. doi: 10.1088/0004-6256/135/1/338.

Y. Gal and Z. Ghahramani. Dropout as a Bayesian Approximation: Representing Model Uncertainty in Deep Learning. *arXiv e-prints*, art. arXiv:1506.02142, Jun 2015.

A. Gal-Yam. *Observational and Physical Classification of Supernovae*, page 195. 2017. doi: 10.1007/978-3-319-21846-5_35.

M. Ganeshalingam, W. Li, A. V. Filippenko, C. Anderson, G. Foster, E. L. Gates, C. V. Griffith, B. J. Grigsby, N. Joubert, J. Leja, T. B. Lowe, B. Macomber, T. Pritchard, P. Thrasher, and D. Winslow. Results of the Lick Observatory Supernova Search Follow-up Photometry Program: BVRI Light Curves of 165 Type Ia Supernovae. *ApJS*, 190: 418–448, Oct. 2010. doi: 10.1088/0067-0049/190/2/418.

M. Ganeshalingam, W. Li, and A. V. Filippenko. Constraints on dark energy with the LOSS SN Ia sample. *MNRAS*, 433(3):2240–2258, Aug. 2013. doi: 10.1093/mnras/stt893.

G. Garavini, G. Folatelli, S. Nobili, G. Aldering, R. Amanullah, P. Antilogus, P. Astier, G. Blanc, T. Bronder, and M. S. Burns. Quantitative comparison between type Ia supernova spectra at low and high redshifts: a case study. *A&A*, 470(2):411–424, Aug 2007. doi: 10.1051/0004-6361:20065400.

D. A. Goldstein, C. B. D'Andrea, J. A. Fischer, R. J. Foley, R. R. Gupta, R. Kessler, A. G. Kim, R. C. Nichol, P. E. Nugent, A. Papadopoulos, M. Sako, M. Smith, M. Sullivan, R. C. Thomas, W. Wester, R. C. Wolf, F. B. Abdalla, M. Banerji, A. Benoit-Lévy, E. Bertin, D. Brooks, A. Carnero Rosell, F. J. Castander, L. N. da Costa, R. Covarrubias, D. L. DePoy, S. Desai, H. T. Diehl, P. Doel, T. F. Eifler, A. Fausti Neto, D. A. Finley, B. Flaugher, P. Fosalba, J. Frieman, D. Gerdes, D. Gruen, R. A. Gruendl, D. James, K. Kuehn, N. Kuropatkin, O. Lahav, T. S. Li, M. A. G. Maia, M. Makler, M. March, J. L. Marshall, P. Martini, K. W. Merritt, R. Miquel, B. Nord, R. Ogando, A. A. Plazas, A. K. Romer, A. Roodman, E. Sanchez, V. Scarpine, M. Schubnell, I. Sevilla-Noarbe, R. C. Smith, M. Soares-Santos, F. Sobreira, E. Suchyta, M. E. C. Swanson, G. Tarle, J. Thaler, and A. R. Walker. Automated Transient Identification in the Dark Energy Survey. *AJ*, 150(3):82, Sep 2015. doi: 10.1088/0004-6256/150/3/82.

M. L. Graham, R. J. Foley, W. Zheng, P. L. Kelly, I. Shivvers, J. M. Silverman, A. V. Filippenko, K. I. Clubb, and M. Ganeshalingam. Twins for life? A comparative analysis of the Type Ia supernovae 2011fe and 2011by. *MNRAS*, 446(2):2073–2088, Jan. 2015. doi: 10.1093/mnras/stu2221.

J. Guillochon, J. Parrent, L. Z. Kelley, and R. Margutti. An Open Catalog for Supernova Data. *ApJ*, 835(1):64, Jan 2017. doi: 10.3847/1538-4357/835/1/64.

J. Guy, P. Astier, S. Baumont, D. Hardin, R. Pain, N. Regnault, S. Basa, R. G. Carlberg, A. Conley, S. Fabbro, D. Fouchez, I. M. Hook, D. A. Howell, K. Perrett, C. J. Pritchet, J. Rich, M. Sullivan, P. Antilogus, E. Aubourg, G. Bazin, J. Bronder, M. Filiol, N. Palanque-Delabrouille, P. Ripoche, and V. Ruhlmann-Kleider. SALT2: using distant supernovae to improve the use of type Ia supernovae as distance indicators. *A&A*, 466(1): 11–21, Apr. 2007. doi: 10.1051/0004-6361:20066930.

E. Hadjiyska, D. Rabinowitz, C. Baltay, N. Ellman, R. McKinnon, A. Effron, F. Cellier-Holzem, A. Canto, P. Antilogus, S. Bongard, R. Pain, Y. Copin, E. Gangler, R. Pereira, M. Rigault, G. Smadja, G. Aldering, D. Birchall, M. Childress, H. Fakhouri, A. Kim, J. Nordin, P. Nugent, S. Perlmutter, K. Runge, C. Saunders, N. Suzuki, R. C. Thomas, E. Pecontal, C. Buton, U. Feindt, M. Kerschhaggl, M. Kowalski, S. Benitez, W. Hillebrand t, M. Kromer, M. Sasdelli, A. Sternberg, S. Taubenberger, D. Baugh, J. Chen, N. Chotard, C. W. C. Tao, D. Fouchez, and A. Tilquin. Spectroscopic classification of three supernovae by the Nearby Supernova Factory II. *The Astronomer's Telegram*, 4461:1, Oct 2012.

T. Hamana, M. Shirasaki, S. Miyazaki, C. Hikage, M. Oguri, S. More, R. Armstrong, A. Leauthaud, R. Mandelbaum, H. Miyatake, A. J. Nishizawa, M. Simet, M. Takada, H. Aihara, J. Bosch, Y. Komiyama, R. Lupton, H. Murayama, M. A. Strauss, and M. Tanaka. Cosmological constraints from cosmic shear two-point correlation functions with HSC survey first-year data. *PASJ*, 72(1):16, Feb. 2020. doi: 10.1093/pasj/psz138.

M. Hamuy and P. A. Pinto. Type II Supernovae as Standardized Candles. *ApJ*, 566:L63–L65, Feb. 2002. doi: 10.1086/339676.

M. Hamuy, M. M. Phillips, L. A. Wells, and J. Maza. K-Corrections for Type IA Supernovae. *PASP*, 105:787, Jul 1993. doi: 10.1086/133231.

M. Hamuy, M. M. Phillips, N. B. Suntzeff, R. A. Schommer, J. Maza, A. R. Antezan, M. Wischnjewsky, G. Valladares, C. Muena, L. E. Gonzales, R. Aviles, L. A. Wells, R. C. Smith, M. Navarrete, R. Covarrubias, G. M. Williger, A. R. Walker, A. C. Layden, J. H. Elias, J. A. Baldwin, M. Hernandez, H. Tirado, P. Ugarte, R. Elston, N. Saavedra, F. Barrientos, E. Costa, P. Lira, M. T. Ruiz, C. Anguita, X. Gomez, P. Ortiz, M. della Valle, J. Danziger, J. Storm, Y. C. Kim, C. Bailyn, E. P. Rubenstein, D. Tucker, S. Cersosimo, R. A. Mendez, L. Siciliano, W. Sherry, B. Chaboyer, R. A. Koopmann, D. Geisler, A. Sarajedini, A. Dey, N. Tyson, R. M. Rich, R. Gal, R. Lamontagne, N. Caldwell, P. Guhathakurta, A. C. Phillips, P. Szkody, C. Prosser, L. C. Ho, R. McMahan, G. Baggley, K. P. Cheng, R. Havlen, K. Wakamatsu, K. Janes, M. Malkan, F. Baganoff, P. Seitzer, M. Shara, C. Sturch, J. Hesser, P. Hartigan, J. Hughes, D. Welch, T. B. Williams, H. Ferguson, P. J. Francis, L. French, M. Bolte, J. Roth, S. Odewahn, S. Howell, and W. Krzeminski. BVRI Light Curves for 29 Type IA Supernovae. *AJ*, 112:2408, Dec. 1996. doi: 10.1086/118192.

M. Hamuy, G. Folatelli, N. I. Morrell, et al. The Carnegie Supernova Project: The Low-Redshift Survey. *PASP*, 118:2–20, Jan. 2006. doi: 10.1086/500228.

A. A. Henden, S. Levine, D. Terrell, D. L. Welch, U. Munari, and B. K. Kloppenborg. APASS Data Release 10. In *American Astronomical Society Meeting Abstracts #232*, volume 232 of *American Astronomical Society Meeting Abstracts*, page 223.06, June 2018.

C. Heymans, E. Grocutt, A. Heavens, M. Kilbinger, T. D. Kitching, F. Simpson, J. Benjamin, T. Erben, H. Hildebrandt, H. Hoekstra, Y. Mellier, L. Miller, L. Van Waerbeke, M. L. Brown, J. Coupon, L. Fu, J. Harnois-Déraps, M. J. Hudson, K. Kuijken, B. Rowe, T. Schrabback, E. Semboloni, S. Vafaei, and M. Velander. CFHTLenS tomographic weak lensing cosmological parameter constraints: Mitigating the impact of intrinsic galaxy alignments. *MNRAS*, 432(3):2433–2453, July 2013. doi: 10.1093/mnras/stt601.

C. Heymans, T. Tröster, M. Asgari, C. Blake, H. Hildebrandt, B. Joachimi, K. Kuijken, C.-A. Lin, A. G. Sánchez, J. L. van den Busch, A. H. Wright, A. Amon, M. Bilicki, J. de Jong, M. Crocce, A. Dvornik, T. Erben, M. C. Fortuna, F. Getman, B. Giblin, K. Glazebrook, H. Hoekstra, S. Joudaki, A. Kannawadi, F. Köhlinger, C. Lidman, L. Miller, N. R. Napolitano, D. Parkinson, P. Schneider, H. Shan, E. Valentijn, G. Verdoes Kleijn, and C. Wolf. KiDS-1000 Cosmology: Multi-probe weak gravitational lensing and spectroscopic galaxy clustering constraints. *arXiv e-prints*, art. arXiv:2007.15632, July 2020.

M. Hicken, P. Challis, S. Jha, R. P. Kirshner, T. Matheson, M. Modjaz, A. Rest, W. M. Wood-Vasey, G. Bakos, E. J. Barton, P. Berlind, A. Bragg, C. Briceño, W. R. Brown, N. Caldwell, M. Calkins, R. Cho, L. Ciupik, M. Contreras, K.-C. Dendy, A. Dosaj, N. Durham, K. Eriksen, G. Esquerdo, M. Everett, E. Falco, J. Fernandez, A. Gaba, P. Garnavich, G. Graves, P. Green, T. Groner, C. Hergenrother, M. J. Holman, V. Hradecky, J. Huchra, B. Hutchison, D. Jerius, A. Jordan, R. Kilgard, M. Krauss, K. Luhman, L. Macri, D. Marrone, J. McDowell, D. McIntosh, B. McNamara, T. Megeath, B. Mochejska, D. Munoz, J. Muzerolle, O. Naranjo, G. Narayan, M. Pahre, W. Peters, D. Peterson, K. Rines, B. Ripman, A. Roussanova, R. Schild, A. Sicilia-Aguilar, J. Sokoloski, K. Smalley, A. Smith, T. Spahr, K. Z. Stanek, P. Barmby, S. Blondin, C. W. Stubbs, A. Szentgyorgyi, M. A. P. Torres, A. Vaz, A. Vikhlinin, Z. Wang, M. Westover, D. Woods, and P. Zhao. CfA3: 185 Type Ia Supernova Light Curves from the CfA. *ApJ*, 700(1):331–357, Jul 2009a. doi: 10.1088/0004-637X/700/1/331.

M. Hicken, W. M. Wood-Vasey, S. Blondin, P. Challis, S. Jha, P. L. Kelly, A. Rest, and R. P. Kirshner. Improved Dark Energy Constraints from ˜100 New CfA Supernova Type Ia Light Curves. *ApJ*, 700:1097–1140, Aug. 2009b. doi: 10.1088/0004-637X/700/2/1097.

M. Hicken, P. Challis, R. P. Kirshner, A. Rest, C. E. Cramer, W. M. Wood-Vasey, G. Bakos, P. Berlind, W. R. Brown, N. Caldwell, M. Calkins, T. Currie, K. de Kleer, G. Esquerdo, M. Everett, E. Falco, J. Fernandez, A. S. Friedman, T. Groner, J. Hartman, M. J. Holman, R. Hutchins, S. Keys, D. Kipping, D. Latham, G. H. Marion, G. Narayan, M. Pahre, A. Pal, W. Peters, G. Perumpilly, B. Ripman, B. Sipocz, A. Szentgyorgyi, S. Tang, M. A. P. Torres, A. Vaz, S. Wolk, and A. Zezas. CfA4: Light Curves for 94 Type Ia Supernovae. *ApJS*, 200(2):12, June 2012. doi: 10.1088/0067-0049/200/2/12.

A. M. Hollinger and M. J. Hudson. Assessing the accuracy of cosmological parameters estimated from velocity - density comparisons via simulations. *MNRAS*, 502(3):3723–3732, Apr. 2021. doi: 10.1093/mnras/staa4039.

S. Holmbo, M. D. Stritzinger, B. J. Shappee, M. A. Tucker, W. Zheng, C. Ashall, M. M. Phillips, C. Contreras, A. V. Filippenko, P. Hoeflich, M. Huber, A. L. Piro, X. F. Wang, J. J. Zhang, J. Anais, E. Baron, C. R. Burns, A. Campillay, S. Castellón, C. Corco, E. Y. Hsiao, K. Krisciunas, N. Morrell, M. T. B. Nielsen, S. E. Persson, F. Taddia, L. Tomasella, T. M. Zhang, and X. L. Zhao. Discovery and progenitor constraints on the Type Ia supernova 2013gy. *A&A*, 627:A174, July 2019. doi: 10.1051/0004-6361/201834389.

D. A. Howell. Type Ia supernovae as stellar endpoints and cosmological tools. *Nature Communications*, 2:350, June 2011. doi: 10.1038/ncomms1344.

D. A. Howell, M. Sullivan, K. Perrett, T. J. Bronder, I. M. Hook, P. Astier, E. Aubourg, D. Balam, S. Basa, R. G. Carlberg, S. Fabbro, D. Fouchez, J. Guy, H. Lafoux, J. D. Neill, R. Pain, N. Palanque-Delabrouille, C. J. Pritchet, N. Regnault, J. Rich, R. Taillet, R. Knop, R. G. McMahon, S. Perlmutter, and N. A. Walton. Gemini Spectroscopy of Supernovae from the Supernova Legacy Survey: Improving High-Redshift Supernova Selection and Classification. *ApJ*, 634:1190–1201, Dec. 2005. doi: 10.1086/497119.

C. Howlett, A. S. G. Robotham, C. D. P. Lagos, and A. G. Kim. Measuring the Growth Rate of Structure with Type IA Supernovae from LSST. *ApJ*, 847(2):128, Oct. 2017. doi: 10.3847/1538-4357/aa88c8.

F. Hoyle and W. A. Fowler. Nucleosynthesis in Supernovae. *ApJ*, 132:565, Nov. 1960. doi: 10.1086/146963.

E. Y. Hsiao, A. Conley, D. A. Howell, M. Sullivan, C. J. Pritchet, R. G. Carlberg, P. E. Nugent, and M. M. Phillips. K-Corrections and Spectral Templates of Type Ia Supernovae. *ApJ*, 663(2):1187–1200, July 2007. doi: 10.1086/518232.

J. P. Huchra, L. M. Macri, K. L. Masters, T. H. Jarrett, P. Berlind, M. Calkins, A. C. Crook, R. Cutri, P. Erdoğdu, E. Falco, T. George, C. M. Hutcheson, O. Lahav, J. Mader, J. D. Mink, N. Martimbeau, S. Schneider, M. Skrutskie, S. Tokarz, and M. Westover. The 2MASS Redshift Survey—Description and Data Release. *ApJS*, 199(2):26, Apr. 2012. doi: 10.1088/0067-0049/199/2/26.

D. Huterer and D. L. Shafer. Dark energy two decades after: observables, probes, consistency tests. *Reports on Progress in Physics*, 81(1):016901, Jan. 2018. doi: 10.1088/1361-6633/aa997e.

D. Huterer, D. L. Shafer, D. M. Scolnic, and F. Schmidt. Testing ΛCDM at the lowest redshifts with SN Ia and galaxy velocities. *J. Cosmology Astropart. Phys.*, 2017(5):015, May 2017. doi: 10.1088/1475-7516/2017/05/015.

J. Iben, I. and A. V. Tutukov. Supernovae of type I as end products of the evolution of binaries with components of moderate initial mass. *The Astrophysical Journal Supplement Series*, 54:335–372, Feb 1984. doi: 10.1086/190932.

O. Ilbert, S. Arnouts, H. J. McCracken, M. Bolzonella, E. Bertin, O. Le Fèvre, Y. Mellier, G. Zamorani, R. Pellò, A. Iovino, L. Tresse, V. Le Brun, D. Bottini, B. Garilli, D. Maccagni, J. P. Picat, R. Scaramella, M. Scodeggio, G. Vettolani, A. Zanichelli, C. Adami, S. Bardelli, A. Cappi, S. Charlot, P. Ciliegi, T. Contini, O. Cucciati, S. Foucaud, P. Franzetti, I. Gavignaud, L. Guzzo, B. Marano, C. Marinoni, A. Mazure, B. Meneux, R. Merighi, S. Paltani, A. Pollo, L. Pozzetti, M. Radovich, E. Zucca, M. Bondi, A. Bongiorno, G. Busarello, S. de La Torre, L. Gregorini, F. Lamareille, G. Mathez, P. Merluzzi, V. Ripepi, D. Rizzo, and D. Vergani. Accurate photometric redshifts for the CFHT legacy survey calibrated using the VIMOS VLT deep survey. *A&A*, 457:841–856, Oct. 2006. doi: 10.1051/0004-6361:20065138.

Ž. Ivezić, A. J. Connelly, J. T. Vand erPlas, and A. Gray. *Statistics, Data Mining, and Machine Learning in Astronomy*. 2014.

S. Jha, R. P. Kirshner, P. Challis, P. M. Garnavich, T. Matheson, A. M. Soderberg, G. J. M. Graves, M. Hicken, J. F. Alves, H. G. Arce, Z. Balog, P. Barmby, E. J. Barton, P. Berlind, A. E. Bragg, C. Briceño, W. R. Brown, J. H. Buckley, N. Caldwell, M. L. Calkins, B. J. Carter, K. D. Concannon, R. H. Donnelly, K. A. Eriksen, D. G. Fabricant, E. E. Falco, F. Fiore, M. R. Garcia, M. Gómez, N. A. Grogin, T. Groner, P. J. Groot, J. Haisch, Karl E., L. Hartmann, C. W. Hergenrother, M. J. Holman, J. P. Huchra, R. Jayawardhana, D. Jerius, S. J. Kannappan, D.-W. Kim, J. T. Kleyna, C. S. Kochanek, D. M. Koranyi, M. Krockenberger, C. J. Lada, K. L. Luhman, J. X. Luu, L. M. Macri, J. A. Mader, A. Mahdavi, M. Marengo, B. G. Marsden, B. A. McLeod, B. R. McNamara, S. T. Megeath, D. Moraru, A. E. Mossman, A. A. Muench, J. A. Muñoz, J. Muzerolle, O. Naranjo, K. Nelson-Patel, M. A. Pahre, B. M. Patten, J. Peters, W. Peters, J. C. Raymond, K. Rines, R. E. Schild, G. J. Sobczak, T. B. Spahr, J. R. Stauffer, R. P. Stefanik, A. H. Szentgyorgyi, E. V. Tollestrup, P. Väisänen, A. Vikhlinin, Z. Wang, S. P. Willner, S. J. Wolk, J. M. Zajac, P. Zhao, and K. Z. Stanek. UBVRI Light Curves of 44 Type Ia Supernovae. *AJ*, 131(1):527–554, Jan 2006. doi: 10.1086/497989.

S. Jha, A. G. Riess, and R. P. Kirshner. Improved Distances to Type Ia Supernovae with Multicolor Light-Curve Shapes: MLCS2k2. *ApJ*, 659:122–148, Apr. 2007. doi: 10.1086/512054.

S. W. Jha, K. Maguire, and M. Sullivan. Observational properties of thermonuclear supernovae. *Nature Astronomy*, 3:706–716, Aug. 2019. doi: 10.1038/s41550-019-0858-0.

Z. Jin, X. Gao, R. A. Koff, G. Masi, F. Nocentini, P. Schmeer, N. James, J. Brimacombe, D. A. Howell, D. Sand, S. Valenti, and I. Arcavi. Supernova 2013fw in NGC 7042 = Psn J21134481+1334335. *Central Bureau Electronic Telegrams*, 3681:1, Oct 2013.

D. O. Jones, D. M. Scolnic, A. G. Riess, A. Rest, R. P. Kirshner, E. Berger, R. Kessler, Y. C. Pan, R. J. Foley, R. Chornock, C. A. Ortega, P. J. Challis, W. S. Burgett, K. C. Chambers, P. W. Draper, H. Flewelling, M. E. Huber, N. Kaiser, R. P. Kudritzki, N. Metcalfe, J. Tonry, R. J. Wainscoat, C. Waters, E. E. E. Gall, R. Kotak, M. McCrum, S. J. Smartt, and K. W. Smith. Measuring Dark Energy Properties with Photometrically Classified Pan-STARRS Supernovae. II. Cosmological Parameters. *ApJ*, 857(1):51, Apr 2018. doi: 10.3847/1538-4357/aab6b1.

C. Jordi, M. Gebran, J. M. Carrasco, J. de Bruijne, H. Voss, C. Fabricius, J. Knude, A. Vallenari, R. Kohley, and A. Mora. Gaia broad band photometry. *A&A*, 523:A48, Nov. 2010. doi: 10.1051/0004-6361/201015441.

R. Juszkiewicz, H. A. Feldman, J. N. Fry, and A. H. Jaffe. Weakly nonlinear dynamics and the σ_8 parameter. *J. Cosmology Astropart. Phys.*, 2010(2):021, Feb. 2010. doi: 10.1088/1475-7516/2010/02/021.

D. Kasen and S. E. Woosley. On the Origin of the Type Ia Supernova Width-Luminosity Relation. *ApJ*, 656(2):661–665, Feb. 2007. doi: 10.1086/510375.

B. Katz and S. Dong. The rate of WD-WD head-on collisions may be as high as the SNe Ia rate. *arXiv e-prints*, art. arXiv:1211.4584, Nov. 2012.

D. D. Kelson. Optimal Techniques in Two-dimensional Spectroscopy: Background Subtraction for the 21st Century. *PASP*, 115:688–699, June 2003. doi: 10.1086/375502.

D. D. Kelson, G. D. Illingworth, P. G. van Dokkum, and M. Franx. The Evolution of Early-Type Galaxies in Distant Clusters. II. Internal Kinematics of 55 Galaxies in the z=0.33 Cluster CL 1358+62. *ApJ*, 531:159–183, Mar. 2000. doi: 10.1086/308445.

R. Kessler, A. C. Becker, D. Cinabro, J. Vand erplas, J. A. Frieman, J. Marriner, T. M. Davis, B. Dilday, J. Holtzman, S. W. Jha, H. Lampeitl, M. Sako, M. Smith, C. Zheng, R. C. Nichol, B. Bassett, R. Bender, D. L. Depoy, M. Doi, E. Elson, A. V. Filippenko, R. J. Foley, P. M. Garnavich, U. Hopp, Y. Ihara, W. Ketzeback, W. Kollatschny, K. Konishi, J. L. Marshall, R. J. McMillan, G. Miknaitis, T. Morokuma, E. Mörtsell, K. Pan, J. L. Prieto, M. W. Richmond, A. G. Riess, R. Romani, D. P. Schneider, J. Sollerman, N. Takanashi, K. Tokita, K. van der Heyden, J. C. Wheeler, N. Yasuda, and D. York. First-Year Sloan Digital Sky Survey-II Supernova Results: Hubble Diagram and Cosmological Parameters. *ApJS*, 185(1):32–84, Nov. 2009. doi: 10.1088/0067-0049/185/1/32.

R. Khan, J. L. Prieto, G. Pojmański, K. Z. Stanek, J. F. Beacom, D. M. Szczygiel, B. Pilecki, K. Mogren, J. D. Eastman, P. Martini, and R. Stoll. Pre-discovery and Follow-up Observations of the Nearby SN 2009nr: Implications for Prompt Type Ia Supernovae. *ApJ*, 726 (2):106, Jan 2011. doi: 10.1088/0004-637X/726/2/106.

A. Kim, A. Goobar, and S. Perlmutter. A Generalized K Correction for Type IA Supernovae: Comparing R-band Photometry beyond z=0.2 with B, V, and R-band Nearby Photometry. *PASP*, 108:190, Feb 1996. doi: 10.1086/133709.

E. J. Kim and R. J. Brunner. Star-galaxy classification using deep convolutional neural networks. *MNRAS*, 464(4):4463–4475, Feb 2017. doi: 10.1093/mnras/stw2672.

D. P. Kingma and J. Ba. Adam: A method for stochastic optimization, 2014. URL `http://arxiv.org/abs/1412.6980`. cite arxiv:1412.6980Comment: Published as a conference paper at the 3rd International Conference for Learning Representations, San Diego, 2015.

S. Kiranyaz, O. Avci, O. Abdeljaber, T. Ince, M. Gabbouj, and D. J. Inman. 1d convolutional neural networks and applications: A survey, 2019.

K. Krisciunas, C. Contreras, C. R. Burns, M. M. Phillips, M. D. Stritzinger, N. Morrell, M. Hamuy, J. Anais, L. Boldt, L. Busta, A. Campillay, S. Castellón, G. Folatelli, W. L. Freedman, C. González, E. Y. Hsiao, W. Krzeminski, S. E. Persson, M. Roth, F. Salgado, J. Serón, N. B. Suntzeff, S. Torres, A. V. Filippenko, W. Li, B. F. Madore, D. L. DePoy, J. L. Marshall, J.-P. Rheault, and S. Villanueva. The Carnegie Supernova Project. I. Third Photometry Data Release of Low-redshift Type Ia Supernovae and Other White Dwarf Explosions. *AJ*, 154(5):211, Nov 2017. doi: 10.3847/1538-3881/aa8df0.

D. Kushnir, B. Katz, S. Dong, E. Livne, and R. Fernández. Head-on Collisions of White Dwarfs in Triple Systems Could Explain Type Ia Supernovae. *ApJ*, 778(2):L37, Dec. 2013. doi: 10.1088/2041-8205/778/2/L37.

A. U. Landolt. UBVRI Photometric standard stars around the celestial equator. *AJ*, 88: 439–460, Mar. 1983. doi: 10.1086/113329.

A. U. Landolt. UBVRI Photometric Standard Stars in the Magnitude Range 11.5 < V < 16.0 Around the Celestial Equator. *AJ*, 104:340, Jul 1992. doi: 10.1086/116242.

G. Lavaux and M. J. Hudson. The 2M++ galaxy redshift catalogue. *MNRAS*, 416(4): 2840–2856, Oct. 2011. doi: 10.1111/j.1365-2966.2011.19233.x.

Y. LeCun, B. E. Boser, J. S. Denker, D. Henderson, R. E. Howard, W. E. Hubbard, and L. D. Jackel. Handwritten digit recognition with a back-propagation network. In D. S. Touretzky, editor, *Advances in Neural Information Processing Systems 2*, pages 396–404. Morgan-Kaufmann, 1990.

Y. LeCun, L. Bottou, Y. Bengio, and P. Haffner. Gradient-based learning applied to document recognition. *Proceedings of the IEEE*, 86(11):2278–2324, November 1998.

Y. LeCun, Y. Bengio, and G. Hinton. Deep learning. *Nature*, 521(7553):436–444, May 2015. doi: 10.1038/nature14539.

P. F. Léget, E. Gangler, F. Mondon, G. Aldering, P. Antilogus, C. Aragon, S. Bailey, C. Baltay, K. Barbary, S. Bongard, K. Boone, C. Buton, N. Chotard, Y. Copin, S. Dixon, P. Fagrelius, U. Feindt, D. Fouchez, B. Hayden, W. Hillebrandt, A. Kim, M. Kowalski, D. Kuesters, S. Lombardo, Q. Lin, J. Nordin, R. Pain, E. Pecontal, R. Pereira, S. Perlmutter, K. A. Ponder, M. V. Pruzhinskaya, D. Rabinowitz, M. Rigault, K. Runge, D. Rubin, C. Saunders, L. P. Says, G. Smadja, C. Sofiatti, N. Suzuki, S. Taubenberger, C. Tao, and R. C. Thomas. SUGAR: An improved empirical model of Type Ia supernovae based on spectral features. *A&A*, 636:A46, Apr. 2020. doi: 10.1051/0004-6361/201834954.

B. Leibundgut, R. P. Kirshner, M. M. Phillips, L. A. Wells, N. B. Suntzeff, M. Hamuy, R. A. Schommer, A. R. Walker, L. Gonzalez, P. Ugarte, R. E. Williams, G. Williger, M. Gomez, R. Marzke, B. P. Schmidt, B. Whitney, N. Coldwell, J. Peters, F. H. Chaffee, C. B. Foltz, D. Rehner, L. Siciliano, T. G. Barnes, K. P. Cheng, P. M. N. Hintzen, Y. C. Kim, J. Maza, J. W. Parker, A. C. Porter, P. C. Schmidtke, and G. Sonneborn. SN 1991bg: A Type IA Supernova With a Difference. *AJ*, 105:301, Jan 1993. doi: 10.1086/116427.

D. Lennarz, D. Altmann, and C. Wiebusch. A unified supernova catalogue. *A&A*, 538:A120, Feb. 2012a. doi: 10.1051/0004-6361/201117666.

D. Lennarz, D. Altmann, and C. Wiebusch. A unified supernova catalogue. *A&A*, 538:A120, Feb 2012b. doi: 10.1051/0004-6361/201117666.

H. W. Leung and J. Bovy. Deep learning of multi-element abundances from high-resolution spectroscopic data. *MNRAS*, 483(3):3255–3277, Mar. 2019. doi: 10.1093/mnras/sty3217.

W. Li, A. V. Filippenko, R. Chornock, E. Berger, P. Berlind, M. L. Calkins, P. Challis, C. Fassnacht, S. Jha, R. P. Kirshner, T. Matheson, W. L. W. Sargent, R. A. Simcoe, G. H. Smith, and G. Squires. SN 2002cx: The Most Peculiar Known Type Ia Supernova. *PASP*, 115(806):453–473, Apr 2003. doi: 10.1086/374200.

W. D. Li, A. V. Filippenko, R. R. Treffers, A. Friedman, E. Halderson, R. A. Johnson, J. Y. King, M. Modjaz, M. Papenkova, Y. Sato, and T. Shefler. The Lick Observatory Supernova Search. In S. S. Holt and W. W. Zhang, editors, *American Institute of Physics Conference Series*, volume 522 of *American Institute of Physics Conference Series*, pages 103–106, June 2000. doi: 10.1063/1.1291702.

R. Lilow and A. Nusser. Constrained realizations of 2MRS density and peculiar velocity fields: growth rate and local flow. *arXiv e-prints*, art. arXiv:2102.07291, Feb. 2021.

E. V. Linder. Testing dark matter clustering with redshift space distortions. *J. Cosmology Astropart. Phys.*, 2013(4):031, Apr. 2013. doi: 10.1088/1475-7516/2013/04/031.

E. V. Linder and R. N. Cahn. Parameterized beyond-Einstein growth. *Astroparticle Physics*, 28(4-5):481–488, Dec. 2007. doi: 10.1016/j.astropartphys.2007.09.003.

M. Lochner, J. D. McEwen, H. V. Peiris, O. Lahav, and M. K. Winter. Photometric Supernova Classification with Machine Learning. *ApJS*, 225(2):31, Aug 2016. doi: 10.3847/0067-0049/225/2/31.

LSST Science Collaboration, P. A. Abell, J. Allison, S. F. Anderson, J. R. Andrew, J. R. P. Angel, L. Armus, D. Arnett, S. J. Asztalos, T. S. Axelrod, S. Bailey, D. R. Ballantyne, J. R. Bankert, W. A. Barkhouse, J. D. Barr, L. F. Barrientos, A. J. Barth, J. G. Bartlett, A. C. Becker, J. Becla, T. C. Beers, J. P. Bernstein, R. Biswas, M. R. Blanton, J. S. Bloom, J. J. Bochanski, P. Boeshaar, K. D. Borne, M. Bradac, W. N. Brandt, C. R. Bridge, M. E. Brown, R. J. Brunner, J. S. Bullock, A. J. Burgasser, J. H. Burge, D. L. Burke, P. A. Cargile, S. Chandrasekharan, G. Chartas, S. R. Chesley, Y.-H. Chu, D. Cinabro, M. W. Claire, C. F. Claver, D. Clowe, A. J. Connolly, K. H. Cook, J. Cooke, A. Cooray, K. R. Covey, C. S. Culliton, R. de Jong, W. H. de Vries, V. P. Debattista, F. Delgado, I. P. Dell'Antonio, S. Dhital, R. Di Stefano, M. Dickinson, B. Dilday, S. G. Djorgovski, G. Dobler, C. Donalek, G. Dubois-Felsmann, J. Durech, A. Eliasdottir, M. Eracleous, L. Eyer, E. E. Falco, X. Fan, C. D. Fassnacht, H. C. Ferguson, Y. R. Fernandez, B. D. Fields, D. Finkbeiner, E. E. Figueroa, D. B. Fox, H. Francke, J. S. Frank, J. Frieman, S. Fromenteau, M. Furqan, G. Galaz, A. Gal-Yam, P. Garnavich, E. Gawiser, J. Geary, P. Gee, R. R. Gibson, K. Gilmore, E. A. Grace, R. F. Green, W. J. Gressler, C. J. Grillmair, S. Habib, J. S. Haggerty, M. Hamuy, A. W. Harris, S. L. Hawley, A. F. Heavens, L. Hebb, T. J. Henry, E. Hileman, E. J. Hilton, K. Hoadley, J. B. Holberg, M. J. Holman, S. B. Howell, L. Infante, Z. Ivezic, S. H. Jacoby, B. Jain, R, Jedicke, M. J. Jee, J. Garrett Jernigan, S. W. Jha, K. V. Johnston, R. L. Jones, M. Juric, M. Kaasalainen, Styliani, Kafka, S. M. Kahn, N. A. Kaib, J. Kalirai, J. Kantor, M. M. Kasliwal, C. R. Keeton, R. Kessler, Z. Knezevic, A. Kowalski, V. L. Krabbendam, K. S. Krughoff, S. Kulkarni, S. Kuhlman, M. Lacy, S. Lepine, M. Liang, A. Lien, P. Lira, K. S. Long, S. Lorenz, J. M. Lotz, R. H. Lupton, J. Lutz, L. M. Macri, A. A. Mahabal, R. Mandelbaum, P. Marshall, M. May, P. M. McGehee, B. T. Meadows, A. Meert, A. Milani, C. J. Miller, M. Miller, D. Mills, D. Minniti, D. Monet, A. S. Mukadam, E. Nakar, D. R. Neill, J. A. Newman, S. Nikolaev, M. Nordby, P. O'Connor, M. Oguri, J. Oliver, S. S. Olivier, J. K. Olsen, K. Olsen, E. W. Olszewski, H. Oluseyi, N. D. Padilla, A. Parker, J. Pepper, J. R. Peterson, C. Petry, P. A. Pinto, J. L. Pizagno, B. Popescu, A. Prsa, V. Radcka, M. J. Raddick, A. Rasmussen, A. Rau, J. Rho, J. E. Rhoads, G. T. Richards, S. T. Ridgway, B. E. Robertson, R. Roskar, A. Saha, A. Sarajedini, E. Scannapieco, T. Schalk, R. Schindler, S. Schmidt, S. Schmidt, D. P. Schneider, G. Schumacher, R. Scranton, J. Sebag, L. G. Seppala, O. Shemmer, J. D. Simon, M. Sivertz, H. A. Smith, J. Allyn Smith, N. Smith, A. H. Spitz, A. Stanford, K. G. Stassun, J. Strader, M. A. Strauss, C. W. Stubbs, D. W. Sweeney, A. Szalay, P. Szkody, M. Takada, P. Thorman, D. E. Trilling, V. Trimble, A. Tyson, R. Van Berg, D. Vanden Berk, J. VanderPlas, L. Verde, B. Vrsnak, L. M. Walkowicz, B. D. Wandelt, S. Wang, Y. Wang, M. Warner, R. H. Wechsler, A. A. West, O. Wiecha, B. F. Williams, B. Willman, D. Wittman, S. C. Wolff, W. M. Wood-Vasey, P. Wozniak, P. Young, A. Zentner, and H. Zhan. LSST Science Book, Version 2.0. *arXiv*

e-prints, art. arXiv:0912.0201, Dec. 2009.

L. M. Macri, R. C. Kraan-Korteweg, T. Lambert, M. V. Alonso, P. Berlind, M. Calkins, P. Erdoğdu, E. E. Falco, T. H. Jarrett, and J. D. Mink. The 2MASS Redshift Survey in the Zone of Avoidance. *ApJS*, 245(1):6, Nov. 2019. doi: 10.3847/1538-4365/ab465a.

K. Maeda, S. Benetti, M. Stritzinger, F. K. Röpke, G. Folatelli, J. Sollerman, S. Taubenberger, K. Nomoto, G. Leloudas, M. Hamuy, M. Tanaka, P. A. Mazzali, and N. Elias-Rosa. An asymmetric explosion as the origin of spectral evolution diversity in type Ia supernovae. *Nature*, 466(7302):82–85, Jul 2010a. doi: 10.1038/nature09122.

K. Maeda, S. Taubenberger, J. Sollerman, P. A. Mazzali, G. Leloudas, K. Nomoto, and K. Motohara. Nebular Spectra and Explosion Asymmetry of Type Ia Supernovae. *The Astrophysical Journal*, 708(2):1703–1715, Jan 2010b. doi: 10.1088/0004-637X/708/2/1703.

K. Maguire, M. Sullivan, Y. C. Pan, A. Gal-Yam, I. M. Hook, D. A. Howell, P. E. Nugent, P. Mazzali, N. Chotard, K. I. Clubb, A. V. Filippenko, M. M. Kasliwal, M. T. Kandrashoff, D. Poznanski, C. M. Saunders, J. M. Silverman, E. Walker, and D. Xu. Exploring the spectral diversity of low-redshift Type Ia supernovae using the Palomar Transient Factory. *MNRAS*, 444(4):3258–3274, Nov 2014. doi: 10.1093/mnras/stu1607.

K. Maguire, S. A. Sim, L. Shingles, J. Spyromilio, A. Jerkstrand, M. Sullivan, T. W. Chen, R. Cartier, G. Dimitriadis, C. Frohmaier, L. Galbany, C. P. Gutiérrez, G. Hosseinzadeh, D. A. Howell, C. Inserra, R. Rudy, and J. Sollerman. Using late-time optical and near-infrared spectra to constrain Type Ia supernova explosion properties. *Monthly Notices of the Royal Astronomical Society*, 477(3):3567–3582, Jul 2018. doi: 10.1093/mnras/sty820.

A. B. Mantz, A. von der Linden, S. W. Allen, D. E. Applegate, P. L. Kelly, R. G. Morris, D. A. Rapetti, R. W. Schmidt, S. Adhikari, M. T. Allen, P. R. Burchat, D. L. Burke, M. Cataneo, D. Donovan, H. Ebeling, S. Shandera, and A. Wright. Weighing the giants - IV. Cosmology and neutrino mass. *MNRAS*, 446(3):2205–2225, Jan. 2015. doi: 10.1093/mnras/stu2096.

J. Martínez-Palomera, F. Förster, P. Protopapas, J. C. Maureira, P. Lira, G. Cabrera-Vives, P. Huijse, L. Galbany, T. de Jaeger, S. González-Gaitán, G. Medina, G. Pignata, J. San Martín, M. Hamuy, and R. R. Muñoz. The High Cadence Transit Survey (HiTS): Compilation and Characterization of Light-curve Catalogs. *AJ*, 156(5):186, Nov. 2018. doi: 10.3847/1538-3881/aadfd8.

F. J. Masci, D. I. Hoffman, C. J. Grillmair, and R. M. Cutri. Automated Classification of Periodic Variable Stars Detected by the Wide-field Infrared Survey Explorer. *AJ*, 148(1): 21, Jul 2014. doi: 10.1088/0004-6256/148/1/21.

D. Masters and C. Luschi. Revisiting small batch training for deep neural networks, 2018. URL `http://arxiv.org/abs/1804.07612`. cite arxiv:1804.07612.

G. J. Mathews, B. M. Rose, P. M. Garnavich, D. G. Yamazaki, and T. Kajino. Detectability of Cosmic Dark Flow in the Type Ia Supernova RedshiftDistance Relation. *ApJ*, 827(1): 60, Aug. 2016. doi: 10.3847/0004-637X/827/1/60.

P. A. Mazzali, E. Cappellaro, I. J. Danziger, M. Turatto, and S. Benetti. Nebular Velocities in Type IA Supernovae and Their Relationship to Light Curves. *The Astrophysical Journal*, 499(1):L49–L52, May 1998. doi: 10.1086/311345.

P. A. Mazzali, M. Sullivan, A. V. Filippenko, P. M. Garnavich, K. I. Clubb, K. Maguire, Y. C. Pan, B. Shappee, J. M. Silverman, S. Benetti, S. Hachinger, K. Nomoto, and E. Pian. Nebular spectra and abundance tomography of the Type Ia supernova SN 2011fe: a normal SN Ia with a stable Fe core. *Monthly Notices of the Royal Astronomical Society*, 450(3): 2631–2643, Jul 2015. doi: 10.1093/mnras/stv761.

A. J. Mead, S. Brieden, T. Tröster, and C. Heymans. HMCODE-2020: improved modelling of non-linear cosmological power spectra with baryonic feedback. *MNRAS*, 502(1):1401–1422, Mar. 2021. doi: 10.1093/mnras/stab082.

G. Miknaitis, G. Pignata, A. Rest, W. M. Wood-Vasey, S. Blondin, P. Challis, R. C. Smith, C. W. Stubbs, N. B. Suntzeff, R. J. Foley, T. Matheson, J. L. Tonry, C. Aguilera, J. W. Blackman, A. C. Becker, A. Clocchiatti, R. Covarrubias, T. M. Davis, A. V. Filippenko, A. Garg, P. M. Garnavich, M. Hicken, S. Jha, K. Krisciunas, R. P. Kirshner, B. Leibundgut, W. Li, A. Miceli, G. Narayan, J. L. Prieto, A. G. Riess, M. E. Salvo, B. P. Schmidt, J. Sollerman, J. Spyromilio, and A. Zenteno. The ESSENCE Supernova Survey: Survey Optimization, Observations, and Supernova Photometry. *ApJ*, 666(2):674–693, Sept. 2007. doi: 10.1086/519986.

A. A. Miller, M. K. Kulkarni, Y. Cao, R. R. Laher, F. J. Masci, and J. A. Surace. Preparing for Advanced LIGO: A Star-Galaxy Separation Catalog for the Palomar Transient Factory. *AJ*, 153(2):73, Feb 2017. doi: 10.3847/1538-3881/153/2/73.

D. L. Miller and D. Branch. Type 1a Supernovae and Cosmic Peculiar Velocities. *AJ*, 103: 379, Feb. 1992. doi: 10.1086/116065.

J. Miller and R. Stone. Lick Obs. Tech. Rep. 66. Lick Obs., Santa Cruz, 1993.

A. Möller, V. Ruhlmann-Kleider, C. Leloup, J. Neveu, N. Palanque-Delabrouille, J. Rich, R. Carlberg, C. Lidman, and C. Pritchet. Photometric classification of type Ia supernovae in the SuperNova Legacy Survey with supervised learning. *J. Cosmology Astropart. Phys.*, 2016(12):008, Dec 2016. doi: 10.1088/1475-7516/2016/12/008.

D. Muthukrishna, G. Narayan, K. S. Mandel, R. Biswas, and R. Hložek. RAPID: Early Classification of Explosive Transients Using Deep Learning. *PASP*, 131(1005):118002, Nov 2019a. doi: 10.1088/1538-3873/ab1609.

D. Muthukrishna, D. Parkinson, and B. Tucker. DASH: Deep Learning for the Automated Spectral Classification of Supernovae and their Hosts. *arXiv e-prints*, art. arXiv:1903.02557, Mar 2019b.

V. Nair and G. E. Hinton. Rectified linear units improve restricted boltzmann machines. In J. Frnkranz and T. Joachims, editors, *Proceedings of the 27th International Conference on Machine Learning (ICML-10)*, pages 807–814, 2010.

G. Narayan, A. Rest, B. E. Tucker, R. J. Foley, W. M. Wood-Vasey, P. Challis, C. Stubbs, R. P. Kirshner, C. Aguilera, A. C. Becker, S. Blondin, A. Clocchiatti, R. Covarrubias, G. Damke, T. M. Davis, A. V. Filippenko, M. Ganeshalingam, A. Garg, P. M. Garnavich, M. Hicken, S. W. Jha, K. Krisciunas, B. Leibundgut, W. Li, T. Matheson, G. Miknaitis, G. Pignata, J. L. Prieto, A. G. Riess, B. P. Schmidt, J. M. Silverman, R. C. Smith, J. Sollerman, J. Spyromilio, N. B. Suntzeff, J. L. Tonry, and A. Zenteno. Light Curves of 213 Type Ia Supernovae from the ESSENCE Survey. *ApJS*, 224(1):3, May 2016. doi: 10.3847/0067-0049/224/1/3.

G. Narayan, T. Zaidi, M. D. Soraisam, Z. Wang, M. Lochner, T. Matheson, A. Saha, S. Yang, Z. Zhao, J. Kececioglu, C. Scheidegger, R. T. Snodgrass, T. Axelrod, T. Jenness, R. S. Maier, S. T. Ridgway, R. L. Seaman, E. M. Evans, N. Singh, C. Taylor, J. Toeniskoetter, E. Welch, S. Zhu, and ANTARES Collaboration. Machine-learning-based Brokers for Real-time Classification of the LSST Alert Stream. *ApJS*, 236(1):9, May 2018. doi: 10.3847/1538-4365/aab781.

U. M. Noebauer, S. Taubenberger, S. Blinnikov, E. Sorokina, and W. Hillebrandt. Type Ia supernovae within dense carbon- and oxygen-rich envelopes: a model for 'Super-Chandrasekhar' explosions? *MNRAS*, 463(3):2972–2985, Dec. 2016. doi: 10.1093/mnras/stw2197.

K. Nomoto, F.-K. Thielemann, and K. Yokoi. Accreting white dwarf models of Type I supernovae. III - Carbon deflagration supernovae. *ApJ*, 286:644–658, Nov. 1984. doi: 10.1086/162639.

P. Nugent, M. Phillips, E. Baron, D. Branch, and P. Hauschildt. Evidence for a Spectroscopic Sequence among Type 1a Supernovae. *The Astrophysical Journal*, 455:L147, Dec 1995. doi: 10.1086/309846.

P. E. Nugent, M. Sullivan, S. B. Cenko, R. C. Thomas, D. Kasen, D. A. Howell, D. Bersier, J. S. Bloom, S. R. Kulkarni, M. T. Kand rashoff, A. V. Filippenko, J. M. Silverman, G. W. Marcy, A. W. Howard, H. T. Isaacson, K. Maguire, N. Suzuki, J. E. Tarlton, Y.-C. Pan, L. Bildsten, B. J. Fulton, J. T. Parrent, D. Sand, P. Podsiadlowski, F. B. Bianco, B. Dilday, M. L. Graham, J. Lyman, P. James, M. M. Kasliwal, N. M. Law, R. M. Quimby, I. M. Hook, E. S. Walker, P. Mazzali, E. Pian, E. O. Ofek, A. Gal-Yam, and D. Poznanski. Supernova SN 2011fe from an exploding carbon-oxygen white dwarf star. *Nature*, 480 (7377):344–347, Dec. 2011. doi: 10.1038/nature10644.

A. Nusser. Velocity-density correlations from the cosmicflows-3 distance catalogue and the 2MASS Redshift Survey. *MNRAS*, 470(1):445–454, Sept. 2017. doi: 10.1093/mnras/stx1225.

J. E. O'Donnell. R v-dependent Optical and Near-Ultraviolet Extinction. *ApJ*, 422:158, Feb 1994. doi: 10.1086/173713.

J. B. Oke and A. Sandage. Energy Distributions, K Corrections, and the Stebbins-Whitford Effect for Giant Elliptical Galaxies. *ApJ*, 154:21, Oct 1968. doi: 10.1086/149737.

J. B. Oke, J. G. Cohen, M. Carr, J. Cromer, A. Dingizian, F. H. Harris, S. Labrecque, R. Lucinio, W. Schaal, H. Epps, and J. Miller. The Keck Low-Resolution Imaging Spectrometer. *PASP*, 107:375, Apr. 1995. doi: 10.1086/133562.

Y. C. Pan, M. Sullivan, K. Maguire, I. M. Hook, P. E. Nugent, D. A. Howell, I. Arcavi, J. Botyanszki, S. B. Cenko, J. DeRose, H. K. Fakhouri, A. Gal-Yam, E. Hsiao, S. R. Kulkarni, R. R. Laher, C. Lidman, J. Nordin, E. S. Walker, and D. Xu. The host galaxies of Type Ia supernovae discovered by the Palomar Transient Factory. *MNRAS*, 438(2): 1391–1416, Feb 2014. doi: 10.1093/mnras/stt2287.

Y. C. Pan, R. J. Foley, M. Kromer, O. D. Fox, W. Zheng, P. Challis, K. I. Clubb, A. V. Filippenko, G. Folatelli, M. L. Graham, W. Hillebrandt, R. P. Kirshner, W. H. Lee, R. Pakmor, F. Patat, M. M. Phillips, G. Pignata, F. Röpke, I. Seitenzahl, J. M. Silverman, J. D. Simon, A. Sternberg, M. D. Stritzinger, S. Taubenberger, J. Vinko, and J. C. Wheeler. 500 days of SN 2013dy: spectra and photometry from the ultraviolet to the infrared. *Monthly Notices of the Royal Astronomical Society*, 452(4):4307–4325, Oct 2015a. doi: 10.1093/mnras/stv1605.

Y. C. Pan, M. Sullivan, K. Maguire, A. Gal-Yam, I. M. Hook, D. A. Howell, P. E. Nugent, and P. A. Mazzali. Type Ia supernova spectral features in the context of their host galaxy properties. *MNRAS*, 446(1):354–368, Jan 2015b. doi: 10.1093/mnras/stu2121.

D. Parks, J. X. Prochaska, S. Dong, and Z. Cai. Deep learning of quasar spectra to discover and characterize damped Lyα systems. *MNRAS*, 476(1):1151–1168, May 2018. doi: 10.1093/mnras/sty196.

A. Paszke, S. Gross, F. Massa, A. Lerer, J. Bradbury, G. Chanan, T. Killeen, Z. Lin, N. Gimelshein, L. Antiga, A. Desmaison, A. Kopf, E. Yang, Z. DeVito, M. Raison, A. Tejani, S. Chilamkurthy, B. Steiner, L. Fang, J. Bai, and S. Chintala. Pytorch: An imperative style, high-performance deep learning library. In H. Wallach, H. Larochelle, A. Beygelzimer, F. d'Alché Buc, E. Fox, and R. Garnett, editors, *Advances in Neural Information Processing Systems 32*, pages 8024–8035. Curran Associates, Inc., 2019.

P. J. E. Peebles. *Principles of Physical Cosmology*. Princeton University Press, 1993.

D. A. Perley. Fully Automated Reduction of Longslit Spectroscopy with the Low Resolution Imaging Spectrometer at the Keck Observatory. *PASP*, 131(1002):084503, Aug 2019. doi: 10.1088/1538-3873/ab215d.

S. Perlmutter, G. Aldering, G. Goldhaber, R. A. Knop, P. Nugent, P. G. Castro, S. Deustua, S. Fabbro, A. Goobar, D. E. Groom, I. M. Hook, A. G. Kim, M. Y. Kim, J. C. Lee, N. J. Nunes, R. Pain, C. R. Pennypacker, R. Quimby, C. Lidman, R. S. Ellis, M. Irwin, R. G. McMahon, P. Ruiz-Lapuente, N. Walton, B. Schaefer, B. J. Boyle, A. V. Filippenko, T. Matheson, A. S. Fruchter, N. Panagia, H. J. M. Newberg, W. J. Couch, and T. S. C. Project. Measurements of Ω and Λ from 42 High-Redshift Supernovae. *ApJ*, 517:565–586, June 1999. doi: 10.1086/307221.

M. M. Phillips. The absolute magnitudes of Type IA supernovae. *ApJ*, 413:L105–L108, Aug. 1993. doi: 10.1086/186970.

M. M. Phillips, L. A. Wells, N. B. Suntzeff, M. Hamuy, B. Leibundgut, R. P. Kirshner, and C. B. Foltz. SN 1991T: Further Evidence of the Heterogeneous Nature of Type IA Supernovae. *AJ*, 103:1632, May 1992. doi: 10.1086/116177.

M. M. Phillips, W. Li, J. A. Frieman, S. I. Blinnikov, D. DePoy, J. L. Prieto, P. Milne, C. Contreras, G. Folatelli, N. Morrell, M. Hamuy, N. B. Suntzeff, M. Roth, S. González, W. Krzeminski, A. V. Filippenko, W. L. Freedman, R. Chornock, S. Jha, B. F. Madore, S. E. Persson, C. R. Burns, P. Wyatt, D. Murphy, R. J. Foley, M. Ganeshalingam, F. J. D. Serduke, K. Krisciunas, B. Bassett, A. Becker, B. Dilday, J. Eastman, P. M. Garnavich, J. Holtzman, R. Kessler, H. Lampeitl, J. Marriner, S. Frank, J. L. Marshall, G. Miknaitis, M. Sako, D. P. Schneider, K. van der Heyden, and N. Yasuda. The Peculiar SN 2005hk: Do Some Type Ia Supernovae Explode as Deflagrations?1,. *PASP*, 119(854):360–387, Apr. 2007. doi: 10.1086/518372.

R. W. Pike and M. J. Hudson. Cosmological Parameters from the Comparison of the 2MASS Gravity Field with Peculiar Velocity Surveys. *ApJ*, 635(1):11–21, Dec. 2005. doi: 10.1086/497359.

Planck Collaboration, P. A. R. Ade, N. Aghanim, M. Arnaud, M. Ashdown, J. Aumont, C. Baccigalupi, A. J. Banday, R. B. Barreiro, J. G. Bartlett, N. Bartolo, E. Battaner, R. Battye, K. Benabed, A. Benoît, A. Benoit-Lévy, J. P. Bernard, M. Bersanelli, P. Bielewicz, J. J. Bock, A. Bonaldi, L. Bonavera, J. R. Bond, J. Borrill, F. R. Bouchet, M. Bucher, C. Burigana, R. C. Butler, E. Calabrese, J. F. Cardoso, A. Catalano, A. Challinor, A. Chamballu, R. R. Chary, H. C. Chiang, P. R. Christensen, S. Church, D. L. Clements, S. Colombi, L. P. L. Colombo, C. Combet, B. Comis, F. Couchot, A. Coulais, B. P. Crill, A. Curto, F. Cuttaia, L. Danese, R. D. Davies, R. J. Davis, P. de Bernardis, A. de Rosa, G. de Zotti, J. Delabrouille, F. X. Désert, J. M. Diego, K. Dolag, H. Dole, S. Donzelli, O. Doré, M. Douspis, A. Ducout, X. Dupac, G. Efstathiou, F. Elsner, T. A. Enßlin, H. K. Eriksen, E. Falgarone, J. Fergusson, F. Finelli, O. Forni, M. Frailis, A. A.

Fraisse, E. Franceschi, A. Frejsel, S. Galeotta, S. Galli, K. Ganga, M. Giard, Y. Giraud-Héraud, E. Gjerløw, J. González-Nuevo, K. M. Górski, S. Gratton, A. Gregorio, A. Gruppuso, J. E. Gudmundsson, F. K. Hansen, D. Hanson, D. L. Harrison, S. Henrot-Versillé, C. Hernández-Monteagudo, D. Herranz, S. R. Hildebrandt, E. Hivon, M. Hobson, W. A. Holmes, A. Hornstrup, W. Hovest, K. M. Huffenberger, G. Hurier, A. H. Jaffe, T. R. Jaffe, W. C. Jones, M. Juvela, E. Keihänen, R. Keskitalo, T. S. Kisner, R. Kneissl, J. Knoche, M. Kunz, H. Kurki-Suonio, G. Lagache, A. Lähteenmäki, J. M. Lamarre, A. Lasenby, M. Lattanzi, C. R. Lawrence, R. Leonardi, J. Lesgourgues, F. Levrier, M. Liguori, P. B. Lilje, M. Linden-Vørnle, M. López-Caniego, P. M. Lubin, J. F. Macías-Pérez, G. Maggio, D. Maino, N. Mandolesi, A. Mangilli, M. Maris, P. G. Martin, E. Martínez-González, S. Masi, S. Matarrese, P. McGehee, P. R. Meinhold, A. Melchiorri, J. B. Melin, L. Mendes, A. Mennella, M. Migliaccio, S. Mitra, M. A. Miville-Deschênes, A. Moneti, L. Montier, G. Morgante, D. Mortlock, A. Moss, D. Munshi, J. A. Murphy, P. Naselsky, F. Nati, P. Natoli, C. B. Netterfield, H. U. Nørgaard-Nielsen, F. Noviello, D. Novikov, I. Novikov, C. A. Oxborrow, F. Paci, L. Pagano, F. Pajot, D. Paoletti, B. Partridge, F. Pasian, G. Patanchon, T. J. Pearson, O. Perdereau, L. Perotto, F. Perrotta, V. Pettorino, F. Piacentini, M. Piat, E. Pierpaoli, D. Pietrobon, S. Plaszczynski, E. Pointecouteau, G. Polenta, L. Popa, G. W. Pratt, G. Prézeau, S. Prunet, J. L. Puget, J. P. Rachen, R. Rebolo, M. Reinecke, M. Remazeilles, C. Renault, A. Renzi, I. Ristorcelli, G. Rocha, M. Roman, C. Rosset, M. Rossetti, G. Roudier, J. A. Rubiño-Martín, B. Rusholme, M. Sandri, D. Santos, M. Savelainen, G. Savini, D. Scott, M. D. Seiffert, E. P. S. Shellard, L. D. Spencer, V. Stolyarov, R. Stompor, R. Sudiwala, R. Sunyaev, D. Sutton, A. S. Suur-Uski, J. F. Sygnet, J. A. Tauber, L. Terenzi, L. Toffolatti, M. Tomasi, M. Tristram, M. Tucci, J. Tuovinen, M. Türler, G. Umana, L. Valenziano, J. Valiviita, B. Van Tent, P. Vielva, F. Villa, L. A. Wade, B. D. Wandelt, I. K. Wehus, J. Weller, S. D. M. White, D. Yvon, A. Zacchei, and A. Zonca. Planck 2015 results. XXIV. Cosmology from Sunyaev-Zeldovich cluster counts. *A&A*, 594:A24, Sept. 2016. doi: 10.1051/0004-6361/201525833.

Planck Collaboration, N. Aghanim, Y. Akrami, M. Ashdown, J. Aumont, C. Baccigalupi, M. Ballardini, A. J. Banday, R. B. Barreiro, N. Bartolo, S. Basak, R. Battye, K. Benabed, J. P. Bernard, M. Bersanelli, P. Bielewicz, J. J. Bock, J. R. Bond, J. Borrill, F. R. Bouchet, F. Boulanger, M. Bucher, C. Burigana, R. C. Butler, E. Calabrese, J. F. Cardoso, J. Carron, A. Challinor, H. C. Chiang, J. Chluba, L. P. L. Colombo, C. Combet, D. Contreras, B. P. Crill, F. Cuttaia, P. de Bernardis, G. de Zotti, J. Delabrouille, J. M. Delouis, E. Di Valentino, J. M. Diego, O. Doré, M. Douspis, A. Ducout, X. Dupac, S. Dusini, G. Efstathiou, F. Elsner, T. A. Enßlin, H. K. Eriksen, Y. Fantaye, M. Farhang, J. Fergusson, R. Fernandez-Cobos, F. Finelli, F. Forastieri, M. Frailis, A. A. Fraisse, E. Franceschi, A. Frolov, S. Galeotta, S. Galli, K. Ganga, R. T. Génova-Santos, M. Gerbino, T. Ghosh, J. González-Nuevo, K. M. Górski, S. Gratton, A. Gruppuso, J. E. Gudmundsson, J. Hamann, W. Handley, F. K. Hansen, D. Herranz, S. R. Hildebrandt, E. Hivon, Z. Huang, A. H. Jaffe, W. C. Jones, A. Karakci, E. Keihänen, R. Keskitalo, K. Kiiveri, J. Kim, T. S. Kisner, L. Knox, N. Krachmalnicoff, M. Kunz, H. Kurki-Suonio,

G. Lagache, J. M. Lamarre, A. Lasenby, M. Lattanzi, C. R. Lawrence, M. Le Jeune, P. Lemos, J. Lesgourgues, F. Levrier, A. Lewis, M. Liguori, P. B. Lilje, M. Lilley, V. Lindholm, M. López-Caniego, P. M. Lubin, Y. Z. Ma, J. F. Macías-Pérez, G. Maggio, D. Maino, N. Mandolesi, A. Mangilli, A. Marcos-Caballero, M. Maris, P. G. Martin, M. Martinelli, E. Martínez-González, S. Matarrese, N. Mauri, J. D. McEwen, P. R. Meinhold, A. Melchiorri, A. Mennella, M. Migliaccio, M. Millea, S. Mitra, M. A. Miville-Deschênes, D. Molinari, L. Montier, G. Morgante, A. Moss, P. Natoli, H. U. Nørgaard-Nielsen, L. Pagano, D. Paoletti, B. Partridge, G. Patanchon, H. V. Peiris, F. Perrotta, V. Pettorino, F. Piacentini, L. Polastri, G. Polenta, J. L. Puget, J. P. Rachen, M. Reinecke, M. Remazeilles, A. Renzi, G. Rocha, C. Rosset, G. Roudier, J. A. Rubiño-Martín, B. Ruiz-Granados, L. Salvati, M. Sandri, M. Savelainen, D. Scott, E. P. S. Shellard, C. Sirignano, G. Sirri, L. D. Spencer, R. Sunyaev, A. S. Suur-Uski, J. A. Tauber, D. Tavagnacco, M. Tenti, L. Toffolatti, M. Tomasi, T. Trombetti, L. Valenziano, J. Valiviita, B. Van Tent, L. Vibert, P. Vielva, F. Villa, N. Vittorio, B. D. Wandelt, I. K. Wehus, M. White, S. D. M. White, A. Zacchei, and A. Zonca. Planck 2018 results. VI. Cosmological parameters. *A&A*, 641: A6, Sept. 2020. doi: 10.1051/0004-6361/201833910.

J. L. Prieto, A. Rest, and N. B. Suntzeff. A New Method to Calibrate the Magnitudes of Type Ia Supernovae at Maximum Light. *ApJ*, 647(1):501–512, Aug. 2006. doi: 10.1086/504307.

J. W. Richards, D. Homrighausen, P. E. Freeman, C. M. Schafer, and D. Poznanski. Semi-supervised learning for photometric supernova classification. *MNRAS*, 419(2):1121–1135, Jan. 2012. doi: 10.1111/j.1365-2966.2011.19768.x.

M. W. Richmond and H. A. Smith. BVRI Photometry of SN 2011fe in M101. *Journal of the American Association of Variable Star Observers (JAAVSO)*, 40(2):872, Apr. 2012.

A. G. Riess. The expansion of the Universe is faster than expected. *Nature Reviews Physics*, 2(1):10–12, Dec. 2019. doi: 10.1038/s42254-019-0137-0.

A. G. Riess, W. H. Press, and R. P. Kirshner. Determining the Motion of the Local Group Using Type IA Supernova Light Curve Shapes. *ApJ*, 445:L91, June 1995. doi: 10.1086/187897.

A. G. Riess, W. H. Press, and R. P. Kirshner. A Precise Distance Indicator: Type IA Supernova Multicolor Light-Curve Shapes. *ApJ*, 473:88, Dec. 1996. doi: 10.1086/178129.

A. G. Riess, M. Davis, J. Baker, and R. P. Kirshner. The Velocity Field from Type IA Supernovae Matches the Gravity Field from Galaxy Surveys. *ApJ*, 488(1):L1–L5, Oct. 1997a. doi: 10.1086/310917.

A. G. Riess, A. V. Filippenko, D. C. Leonard, B. P. Schmidt, N. Suntzeff, M. M. Phillips, R. Schommer, A. Clocchiatti, R. P. Kirshner, and P. Garnavich. Time Dilation from Spectral Feature Age Measurements of Type IA Supernovae. *AJ*, 114:722–729, Aug 1997b. doi: 10.1086/118506.

A. G. Riess, A. V. Filippenko, D. C. Leonard, B. P. Schmidt, N. Suntzeff, M. M. Phillips, R. Schommer, A. Clocchiatti, R. P. Kirshner, P. Garnavich, P. Challis, B. Leibundgut, J. Spyromilio, and R. C. Smith. Time Dilation from Spectral Feature Age Measurements of Type IA Supernovae. *AJ*, 114:722–729, Aug. 1997c. doi: 10.1086/118506.

A. G. Riess, A. V. Filippenko, P. Challis, A. Clocchiatti, A. Diercks, P. M. Garnavich, R. L. Gilliland, C. J. Hogan, S. Jha, R. P. Kirshner, B. Leibundgut, M. M. Phillips, D. Reiss, B. P. Schmidt, R. A. Schommer, R. C. Smith, J. Spyromilio, C. Stubbs, N. B. Suntzeff, and J. Tonry. Observational Evidence from Supernovae for an Accelerating Universe and a Cosmological Constant. *AJ*, 116:1009–1038, Sept. 1998. doi: 10.1086/300499.

A. G. Riess, P. Nugent, A. V. Filippenko, R. P. Kirshner, and S. Perlmutter. Snapshot distances to type ia supernovae: All in "one" night's work. *The Astrophysical Journal*, 504(2):935, 1998. URL `http://stacks.iop.org/0004-637X/504/i=2/a=935`.

A. G. Riess, R. P. Kirshner, B. P. Schmidt, S. Jha, P. Challis, P. M. Garnavich, A. A. Esin, C. Carpenter, R. Grashius, R. E. Schild, P. L. Berlind, J. P. Huchra, C. F. Prosser, E. E. Falco, P. J. Benson, C. Briceño, W. R. Brown, N. Caldwell, I. P. dell'Antonio, A. V. Filippenko, A. A. Goodman, N. A. Grogin, T. Groner, J. P. Hughes, P. J. Green, R. A. Jansen, J. T. Kleyna, J. X. Luu, L. M. Macri, B. A. McLeod, K. K. McLeod, B. R. McNamara, B. McLean, A. A. E. Milone, J. J. Mohr, D. Moraru, C. Peng, J. Peters, A. H. Prestwich, K. Z. Stanek, A. Szentgyorgyi, and P. Zhao. BVRI Light Curves for 22 Type IA Supernovae. *AJ*, 117(2):707–724, Feb 1999. doi: 10.1086/300738.

A. G. Riess, L.-G. Strolger, S. Casertano, H. C. Ferguson, B. Mobasher, B. Gold, P. J. Challis, A. V. Filippenko, S. Jha, W. Li, J. Tonry, R. Foley, R. P. Kirshner, M. Dickinson, E. MacDonald, D. Eisenstein, M. Livio, J. Younger, C. Xu, T. Dahlén, and D. Stern. New Hubble Space Telescope Discoveries of Type Ia Supernovae at z >= 1: Narrowing Constraints on the Early Behavior of Dark Energy. *ApJ*, 659:98–121, Apr. 2007. doi: 10.1086/510378.

A. G. Riess, L. M. Macri, S. L. Hoffmann, D. Scolnic, S. Casertano, A. V. Filippenko, B. E. Tucker, M. J. Reid, D. O. Jones, J. M. Silverman, R. Chornock, P. Challis, W. Yuan, P. J. Brown, and R. J. Foley. A 2.4% Determination of the Local Value of the Hubble Constant. *The Astrophysical Journal*, 826(1):56, Jul 2016. doi: 10.3847/0004-637X/826/1/56.

A. G. Riess, S. Casertano, W. Yuan, L. M. Macri, and D. Scolnic. Large Magellanic Cloud Cepheid Standards Provide a 1% Foundation for the Determination of the Hubble Constant and Stronger Evidence for Physics beyond ΛCDM. *The Astrophysical Journal*, 876(1):85, May 2019. doi: 10.3847/1538-4357/ab1422.

C. Rockosi, R. Stover, R. Kibrick, C. Lockwood, M. Peck, D. Cowley, M. Bolte, S. Adkins, B. Alcott, S. L. Allen, B. Brown, G. Cabak, W. Deich, D. Hilyard, M. Kassis, K. Lanclos, J. Lewis, T. Pfister, A. Phillips, L. Robinson, M. Saylor, M. Thompson, J. Ward, M. Wei,

and C. Wright. The low-resolution imaging spectrograph red channel CCD upgrade: fully depleted, high-resistivity CCDs for Keck. In *Proc. SPIE*, volume 7735 of *Society of Photo-Optical Instrumentation Engineers (SPIE) Conference Series*, page 77350R, Jul 2010. doi: 10.1117/12.856818.

K. Said, M. Colless, C. Magoulas, J. R. Lucey, and M. J. Hudson. Joint analysis of 6dFGS and SDSS peculiar velocities for the growth rate of cosmic structure and tests of gravity. *MNRAS*, 497(1):1275–1293, Sept. 2020. doi: 10.1093/mnras/staa2032.

M. Sasdelli, E. E. O. Ishida, R. Vilalta, M. Aguena, V. C. Busti, H. Camacho, A. M. M. Trindade, F. Gieseke, R. S. de Souza, Y. T. Fantaye, and P. A. Mazzali. Exploring the spectroscopic diversity of Type Ia supernovae with DRACULA: a machine learning approach. *MNRAS*, 461(2):2044–2059, Sep 2016. doi: 10.1093/mnras/stw1228.

A. Savitzky and M. J. E. Golay. Smoothing and differentiation of data by simplified least squares procedures. *Analytical Chemistry*, 36(8):1627–1639, 1964. doi: 10.1021/ac60214a047. URL `https://doi.org/10.1021/ac60214a047`.

R. A. Scalzo, G. Aldering, P. Antilogus, C. Aragon, S. Bailey, C. Baltay, S. Bongard, C. Buton, M. Childress, N. Chotard, Y. Copin, H. K. Fakhouri, A. Gal-Yam, E. Gangler, S. Hoyer, M. Kasliwal, S. Loken, P. Nugent, R. Pain, E. Pécontal, R. Pereira, S. Perlmutter, D. Rabinowitz, A. Rau, G. Rigaudier, K. Runge, G. Smadja, C. Tao, R. C. Thomas, B. Weaver, and C. Wu. Nearby Supernova Factory Observations of SN 2007if: First Total Mass Measurement of a Super-Chandrasekhar-Mass Progenitor. *ApJ*, 713(2):1073–1094, Apr. 2010. doi: 10.1088/0004-637X/713/2/1073.

E. F. Schlafly and D. P. Finkbeiner. Measuring Reddening with Sloan Digital Sky Survey Stellar Spectra and Recalibrating SFD. *ApJ*, 737:103, Aug. 2011. doi: 10.1088/0004-637X/737/2/103.

D. J. Schlegel, D. P. Finkbeiner, and M. Davis. Maps of Dust Infrared Emission for Use in Estimation of Reddening and Cosmic Microwave Background Radiation Foregrounds. *ApJ*, 500:525–553, June 1998. doi: 10.1086/305772.

D. Scolnic, S. Casertano, A. Riess, A. Rest, E. Schlafly, R. J. Foley, D. Finkbeiner, C. Tang, W. S. Burgett, K. C. Chambers, P. W. Draper, H. Flewelling, K. W. Hodapp, M. E. Huber, N. Kaiser, R. P. Kudritzki, E. A. Magnier, N. Metcalfe, and C. W. Stubbs. Supercal: Cross-calibration of Multiple Photometric Systems to Improve Cosmological Measurements with Type Ia Supernovae. *ApJ*, 815(2):117, Dec. 2015. doi: 10.1088/0004-637X/815/2/117.

D. Scolnic, S. Perlmutter, G. Aldering, D. Brout, T. Davis, A. Filippenko, R. Foley, R. Hložek, R. Hounsell, D. Jones, P. Kelly, D. Rubin, A. Riess, S. Rodney, J. Roberts-Pierel, Y. Wang, J. Asorey, A. Avelino, C. Bavdhankar, P. J. Brown, A. Challinor, C. Balland, A. Cooray, S. Dhawan, G. Dimitriadis, C. Dvorkin, J. Guy, W. Handley, R. E. Keeley,

J.-P. Kneib, B. L'Huillier, M. Lattanzi, K. Mandel, J. Mertens, M. Rigault, P. Motloch, S. Mukherjee, G. Narayan, A. Nomerotski, L. Page, L. Pogosian, G. Puglisi, M. Raveri, N. Regnault, A. Rest, C. Rojas-Bravo, M. Sako, F. Shi, S. Sridhar, A. Suzuki, Y.-D. Tsai, W. M. Wood-Vasey, Y. Copin, G.-B. Zhao, and N. Zhu. The Next Generation of Cosmological Measurements with Type Ia Supernovae. *Astro2020: Decadal Survey on Astronomy and Astrophysics*, 2020:270, May 2019.

D. M. Scolnic, D. O. Jones, A. Rest, Y. C. Pan, R. Chornock, R. J. Foley, M. E. Huber, R. Kessler, G. Narayan, A. G. Riess, S. Rodney, E. Berger, D. J. Brout, P. J. Challis, M. Drout, D. Finkbeiner, R. Lunnan, R. P. Kirshner, N. E. Sand ers, E. Schlafly, S. Smartt, C. W. Stubbs, J. Tonry, W. M. Wood-Vasey, M. Foley, J. Hand, E. Johnson, W. S. Burgett, K. C. Chambers, P. W. Draper, K. W. Hodapp, N. Kaiser, R. P. Kudritzki, E. A. Magnier, N. Metcalfe, F. Bresolin, E. Gall, R. Kotak, M. McCrum, and K. W. Smith. The Complete Light-curve Sample of Spectroscopically Confirmed SNe Ia from Pan-STARRS1 and Cosmological Constraints from the Combined Pantheon Sample. *ApJ*, 859(2):101, Jun 2018. doi: 10.3847/1538-4357/aab9bb.

B. J. Shappee, A. L. Piro, T. W. S. Holoien, J. L. Prieto, C. Contreras, K. Itagaki, C. R. Burns, C. S. Kochanek, K. Z. Stanek, E. Alper, U. Basu, J. F. Beacom, D. Bersier, J. Brimacombe, E. Conseil, A. B. Danilet, S. Dong, E. Falco, D. Grupe, E. Y. Hsiao, S. Kiyota, N. Morrell, J. Nicolas, M. M. Phillips, G. Pojmanski, G. Simonian, M. Stritzinger, D. M. Szczygieł, F. Taddia, T. A. Thompson, J. Thorstensen, M. R. Wagner, and P. R. Woźniak. The Young and Bright Type Ia Supernova ASASSN-14lp: Discovery, Early-time Observations, First-light Time, Distance to NGC 4666, and Progenitor Constraints. *ApJ*, 826(2):144, Aug 2016. doi: 10.3847/0004-637X/826/2/144.

I. Shivvers, W. K. Zheng, J. Mauerhan, I. K. W. Kleiser, S. D. Van Dyk, J. M. Silverman, M. L. Graham, P. L. Kelly, A. V. Filippenko, and S. Kumar. SN 2015U: a rapidly evolving and luminous Type Ibn supernova. *MNRAS*, 461(3):3057–3074, Sep 2016. doi: 10.1093/mnras/stw1528.

I. Shivvers, M. Modjaz, W. Zheng, Y. Liu, A. V. Filippenko, J. M. Silverman, T. Matheson, A. Pastorello, O. Graur, R. J. Foley, R. Chornock, N. Smith, J. Leaman, and S. Benetti. Revisiting the Lick Observatory Supernova Search Volume-limited Sample: Updated Classifications and Revised Stripped-envelope Supernova Fractions. *PASP*, 129(975):054201, May 2017. doi: 10.1088/1538-3873/aa54a6.

M. R. Siebert, R. J. Foley, D. O. Jones, R. Angulo, K. Davis, A. Duarte, E. Strasburger, M. Conlon, N. Kazmi, R. Nishimoto, M. Schubert, L. Sun, and R. Tippens. Investigating the diversity of Type Ia supernova spectra with the open-source relational data base KAEPORA. *MNRAS*, 486(4):5785–5808, Jul 2019. doi: 10.1093/mnras/stz1209.

J. M. Silverman, M. Ganeshalingam, W. Li, A. V. Filippenko, A. A. Miller, and D. Poznanski. Fourteen months of observations of the possible super-Chandrasekhar mass Type Ia

Supernova 2009dc. *Monthly Notices of the Royal Astronomical Society*, 410(1):585–611, Jan 2011. doi: 10.1111/j.1365-2966.2010.17474.x.

J. M. Silverman, R. J. Foley, A. V. Filippenko, M. Ganeshalingam, A. J. Barth, R. Chornock, C. V. Griffith, J. J. Kong, N. Lee, D. C. Leonard, T. Matheson, E. G. Miller, T. N. Steele, B. J. Barris, J. S. Bloom, B. E. Cobb, A. L. Coil, L.-B. Desroches, E. L. Gates, L. C. Ho, S. W. Jha, M. T. Kandrashoff, W. Li, K. S. Mandel, M. Modjaz, M. R. Moore, R. E. Mostardi, M. S. Papenkova, S. Park, D. A. Perley, D. Poznanski, C. A. Reuter, J. Scala, F. J. D. Serduke, J. C. Shields, B. J. Swift, J. L. Tonry, S. D. Van Dyk, X. Wang, and D. S. Wong. Berkeley Supernova Ia Program - I. Observations, data reduction and spectroscopic sample of 582 low-redshift Type Ia supernovae. *MNRAS*, 425:1789–1818, Sept. 2012a. doi: 10.1111/j.1365-2966.2012.21270.x.

J. M. Silverman, M. Ganeshalingam, S. B. Cenko, A. V. Filippenko, W. Li, A. J. Barth, D. J. Carson, M. Childress, K. I. Clubb, A. Cucchiara, M. L. Graham, G. H. Marion, M. L. Nguyen, L. Pei, B. E. Tucker, J. Vinko, J. C. Wheeler, and G. Worseck. The Very Young Type Ia Supernova 2012cg: Discovery and Early-time Follow-up Observations. *The Astrophysical Journal*, 756(1):L7, Sep 2012b. doi: 10.1088/2041-8205/756/1/L7.

J. M. Silverman, M. Ganeshalingam, W. Li, and A. V. Filippenko. Berkeley Supernova Ia Program - III. Spectra near maximum brightness improve the accuracy of derived distances to Type Ia supernovae. *Monthly Notices of the Royal Astronomical Society*, 425(3):1889–1916, Sep 2012c. doi: 10.1111/j.1365-2966.2012.21526.x.

J. M. Silverman, J. J. Kong, and A. V. Filippenko. Berkeley Supernova Ia Program - II. Initial analysis of spectra obtained near maximum brightness. *MNRAS*, 425(3):1819–1888, Sep 2012d. doi: 10.1111/j.1365-2966.2012.21269.x.

J. M. Silverman, M. Ganeshalingam, and A. V. Filippenko. Berkeley Supernova Ia Program - V. Late-time spectra of Type Ia Supernovae. *Monthly Notices of the Royal Astronomical Society*, 430(2):1030–1041, Apr 2013. doi: 10.1093/mnras/sts674.

J. M. Silverman, J. Vinkó, G. H. Marion, J. C. Wheeler, B. Barna, T. Szalai, B. W. Mulligan, and A. V. Filippenko. High-velocity features of calcium and silicon in the spectra of Type Ia supernovae. *MNRAS*, 451(2):1973–2014, Aug 2015. doi: 10.1093/mnras/stv1011.

S. J. Smartt. Observational Constraints on the Progenitors of Core-Collapse Supernovae: The Case for Missing High-Mass Stars. *Publ. Astron. Soc. Australia*, 32:e016, Apr. 2015. doi: 10.1017/pasa.2015.17.

C. M. Springob, C. Magoulas, M. Colless, J. Mould, P. Erdoğdu, D. H. Jones, J. R. Lucey, L. Campbell, and C. J. Fluke. The 6dF Galaxy Survey: peculiar velocity field and cosmography. *MNRAS*, 445(3):2677–2697, Dec. 2014. doi: 10.1093/mnras/stu1743.

S. Srivastav, G. C. Anupama, D. K. Sahu, and C. D. Ravikumar. SN 2015bp: adding to the growing population of transitional Type Ia supernovae. *MNRAS*, 466(2):2436–2449, Apr 2017. doi: 10.1093/mnras/stw3263.

N. Srivastava, G. E. Hinton, A. Krizhevsky, I. Sutskever, and R. Salakhutdinov. Dropout: a simple way to prevent neural networks from overfitting. *J. Mach. Learn. Res.*, 15(1): 1929–1958, 2014. URL `http://dl.acm.org/citation.cfm?id=2670313`.

B. E. Stahl, W. Zheng, T. de Jaeger, A. V. Filippenko, A. Bigley, K. Blanchard, P. K. Blanchard, T. G. Brink, S. K. Cargill, C. Casper, S. Channa, B. Y. Choi, N. Choksi, J. Chu, K. I. Clubb, D. P. Cohen, M. Ellison, E. Falcon, P. Fazeli, K. Fuller, M. Ganeshalingam, E. L. Gates, C. Gould, G. Halevi, K. T. Hayakawa, J. Hestenes, B. T. Jeffers, N. Joubert, M. T. Kand rashoff, M. Kim, H. Kim, M. E. Kislak, I. Kleiser, J. J. Kong, M. de Kouchkovsky, D. Krishnan, S. Kumar, J. Leja, E. J. Leonard, G. Z. Li, W. Li, P. Lu, M. N. Mason, J. Molloy, K. Pina, J. Rex, T. W. Ross, S. Stegman, K. Tang, P. Thrasher, X. Wang, A. Wilkins, H. Yuk, S. Yunus, and K. Zhang. Lick Observatory Supernova Search follow-up program: photometry data release of 93 Type Ia supernovae. *MNRAS*, 490(3):3882–3907, Dec 2019. doi: 10.1093/mnras/stz2742.

B. E. Stahl, J. Martínez-Palomera, W. Zheng, T. de Jaeger, A. V. Filippenko, and J. S. Bloom. deepSIP: linking Type Ia supernova spectra to photometric quantities with deep learning. *MNRAS*, 496(3):3553–3571, June 2020a. doi: 10.1093/mnras/staa1706.

B. E. Stahl, W. Zheng, T. de Jaeger, T. G. Brink, A. V. Filippenko, J. M. Silverman, S. B. Cenko, K. I. Clubb, M. L. Graham, G. Halevi, P. L. Kelly, I. Kleiser, I. Shivvers, H. Yuk, B. E. Cobb, O. D. Fox, M. T. Kandrashoff, J. J. Kong, J. C. Mauerhan, X. Wang, and X. Wang. Berkeley supernova Ia program: data release of 637 spectra from 247 Type Ia supernovae. *MNRAS*, 492(3):4325–4343, Mar 2020b. doi: 10.1093/mnras/staa102.

B. E. Stahl, T. de Jaeger, S. S. Boruah, W. Zheng, A. V. Filippenko, and M. J. Hudson. Peculiar-velocity cosmology with Types Ia and II supernovae. *arXiv e-prints*, art. arXiv:2105.05185, May 2021a.

B. E. Stahl, T. de Jaeger, W. Zheng, and A. V. Filippenko. The snapshot distance method: estimating the distance to a Type Ia supernova from minimal observations. *arXiv e-prints*, art. arXiv:2105.04446, May 2021b.

M. A. Strauss and J. A. Willick. The density and peculiar velocity fields of nearby galaxies. *Phys. Rep.*, 261:271–431, Jan. 1995. doi: 10.1016/0370-1573(95)00013-7.

M. Stritzinger and T. Moriya. Workshop 8: Supernovae. *arXiv e-prints*, art. arXiv:1801.06643, Jan. 2018.

M. Stritzinger, M. Hamuy, N. B. Suntzeff, R. C. Smith, M. M. Phillips, J. Maza, L. G. Strolger, R. Antezana, L. González, M. Wischnjewsky, P. Candia, J. Espinoza, D. González,

C. Stubbs, A. C. Becker, E. P. Rubenstein, and G. Galaz. Optical Photometry of the Type Ia Supernova 1999ee and the Type Ib/c Supernova 1999ex in IC 5179. *AJ*, 124(4): 2100–2117, Oct. 2002. doi: 10.1086/342544.

M. D. Stritzinger, M. M. Phillips, L. N. Boldt, C. Burns, A. Campillay, C. Contreras, S. Gonzalez, G. Folatelli, N. Morrell, W. Krzeminski, M. Roth, F. Salgado, D. L. DePoy, M. Hamuy, W. L. Freedman, B. F. Madore, J. L. Marshall, S. E. Persson, J.-P. Rheault, N. B. Suntzeff, S. Villanueva, W. Li, and A. V. Filippenko. The Carnegie Supernova Project: Second Photometry Data Release of Low-redshift Type Ia Supernovae. *AJ*, 142 (5):156, Nov. 2011. doi: 10.1088/0004-6256/142/5/156.

M. Sullivan, J. Guy, A. Conley, N. Regnault, P. Astier, C. Balland, S. Basa, R. G. Carlberg, D. Fouchez, D. Hardin, I. M. Hook, D. A. Howell, R. Pain, N. Palanque-Delabrouille, K. M. Perrett, C. J. Pritchet, J. Rich, V. Ruhlmann-Kleider, D. Balam, S. Baumont, R. S. Ellis, S. Fabbro, H. K. Fakhouri, N. Fourmanoit, S. González-Gaitán, M. L. Graham, M. J. Hudson, E. Hsiao, T. Kronborg, C. Lidman, A. M. Mourao, J. D. Neill, S. Perlmutter, P. Ripoche, N. Suzuki, and E. S. Walker. SNLS3: Constraints on Dark Energy Combining the Supernova Legacy Survey Three-year Data with Other Probes. *ApJ*, 737(2):102, Aug. 2011. doi: 10.1088/0004-637X/737/2/102.

N. Suzuki, D. Rubin, C. Lidman, G. Aldering, R. Amanullah, K. Barbary, L. F. Barrientos, J. Botyanszki, M. Brodwin, N. Connolly, K. S. Dawson, A. Dey, M. Doi, M. Donahue, S. Deustua, P. Eisenhardt, E. Ellingson, L. Faccioli, V. Fadeyev, H. K. Fakhouri, A. S. Fruchter, D. G. Gilbank, M. D. Gladders, G. Goldhaber, A. H. Gonzalez, A. Goobar, A. Gude, T. Hattori, H. Hoekstra, E. Hsiao, X. Huang, Y. Ihara, M. J. Jee, D. Johnston, N. Kashikawa, B. Koester, K. Konishi, M. Kowalski, E. V. Linder, L. Lubin, J. Melbourne, J. Meyers, T. Morokuma, F. Munshi, C. Mullis, T. Oda, N. Panagia, S. Perlmutter, M. Postman, T. Pritchard, J. Rhodes, P. Ripoche, P. Rosati, D. J. Schlegel, A. Spadafora, S. A. Stanford, V. Stanishev, D. Stern, M. Strovink, N. Takanashi, K. Tokita, M. Wagner, L. Wang, N. Yasuda, H. K. C. Yee, and T. S. C. Project. The hubble space telescope cluster supernova survey. v. improving the dark-energy constraints above z ¿ 1 and building an early-type-hosted supernova sample. *ApJ*, 746(1):85, 2012. URL `http://stacks.iop.org/0004-637X/746/i=1/a=85`.

C. Szegedy, W. Liu, Y. Jia, P. Sermanet, S. Reed, D. Anguelov, D. Erhan, V. Vanhoucke, and A. Rabinovich. Going Deeper with Convolutions. *arXiv e-prints*, art. arXiv:1409.4842, Sep 2014.

J. Tonry and M. Davis. A survey of galaxy redshifts. I - Data reduction techniques. *AJ*, 84: 1511–1525, Oct. 1979. doi: 10.1086/112569.

J. L. Tonry, C. W. Stubbs, K. R. Lykke, P. Doherty, I. S. Shivvers, W. S. Burgett, K. C. Chambers, K. W. Hodapp, N. Kaiser, R. P. Kudritzki, E. A. Magnier, J. S. Morgan, P. A.

Price, and R. J. Wainscoat. The Pan-STARRS1 Photometric System. *ApJ*, 750(2):99, May 2012. doi: 10.1088/0004-637X/750/2/99.

J. L. Tonry, L. Denneau, A. N. Heinze, B. Stalder, K. W. Smith, S. J. Smartt, C. W. Stubbs, H. J. Weiland, and A. Rest. ATLAS: A High-cadence All-sky Survey System. *PASP*, 130 (988):064505, June 2018. doi: 10.1088/1538-3873/aabadf.

R. Tripp. A two-parameter luminosity correction for Type IA supernovae. *A&A*, 331:815–820, Mar. 1998.

R. B. Tully, H. M. Courtois, and J. G. Sorce. Cosmicflows-3. *AJ*, 152(2):50, Aug. 2016. doi: 10.3847/0004-6256/152/2/50.

S. J. Turnbull, M. J. Hudson, H. A. Feldman, M. Hicken, R. P. Kirshner, and R. Watkins. Cosmic flows in the nearby universe from Type Ia supernovae. *MNRAS*, 420(1):447–454, Feb. 2012. doi: 10.1111/j.1365-2966.2011.20050.x.

J. Vinkó, K. Sárneczky, K. Takáts, G. H. Marion, T. Hegedüs, I. B. Bíró, T. Borkovits, E. Szegedi-Elek, A. Farkas, P. Klagyivik, L. L. Kiss, T. Kovács, A. Pál, R. Szakáts, N. Szalai, T. Szalai, K. Szatmáry, A. Szing, K. Vida, and J. C. Wheeler. Testing supernovae Ia distance measurement methods with SN 2011fe. *A&A*, 546:A12, Oct. 2012. doi: 10.1051/0004-6361/201220043.

X. Wang, A. V. Filippenko, M. Ganeshalingam, W. Li, J. M. Silverman, L. Wang, R. Chornock, R. J. Foley, E. L. Gates, B. Macomber, F. J. D. Serduke, T. N. Steele, and D. S. Wong. Improved Distances to Type Ia Supernovae with Two Spectroscopic Subclasses. *The Astrophysical Journal*, 699(2):L139–L143, Jul 2009. doi: 10.1088/0004-637X/699/2/L139.

X. Wang, L. Wang, A. V. Filippenko, T. Zhang, and X. Zhao. Evidence for Two Distinct Populations of Type Ia Supernovae. *Science*, 340(6129):170–173, Apr 2013. doi: 10.1126/science.1231502.

R. F. Webbink. Double white dwarfs as progenitors of R Coronae Borealis stars and type I supernovae. *The Astrophysical Journal*, 277:355–360, Feb 1984. doi: 10.1086/161701.

A. Weyant, M. Wood-Vasey, L. Wasserman, and P. Freeman. An Unbiased Method of Modeling the Local Peculiar Velocity Field with Type Ia Supernovae. *ApJ*, 732(2):65, May 2011. doi: 10.1088/0004-637X/732/2/65.

J. Whelan and J. Iben, Icko. Binaries and Supernovae of Type I. *The Astrophysical Journal*, 186:1007–1014, Dec 1973. doi: 10.1086/152565.

W. M. Wood-Vasey, G. Miknaitis, C. W. Stubbs, S. Jha, A. G. Riess, P. M. Garnavich, R. P. Kirshner, C. Aguilera, A. C. Becker, J. W. Blackman, S. Blondin, P. Challis, A. Clocchiatti, A. Conley, R. Covarrubias, T. M. Davis, A. V. Filippenko, R. J. Foley, A. Garg, M. Hicken,

K. Krisciunas, B. Leibundgut, W. Li, T. Matheson, A. Miceli, G. Narayan, G. Pignata, J. L. Prieto, A. Rest, M. E. Salvo, B. P. Schmidt, R. C. Smith, J. Sollerman, J. Spyromilio, J. L. Tonry, N. B. Suntzeff, and A. Zenteno. Observational Constraints on the Nature of Dark Energy: First Cosmological Results from the ESSENCE Supernova Survey. *ApJ*, 666(2):694–715, Sept. 2007. doi: 10.1086/518642.

S. Woosley and T. Janka. The physics of core-collapse supernovae. *Nature Physics*, 1(3): 147–154, Dec. 2005. doi: 10.1038/nphys172.

D. E. Wright, S. J. Smartt, K. W. Smith, P. Miller, R. Kotak, A. Rest, W. S. Burgett, K. C. Chambers, H. Flewelling, K. W. Hodapp, M. Huber, R. Jedicke, N. Kaiser, N. Metcalfe, P. A. Price, J. L. Tonry, R. J. Wainscoat, and C. Waters. Machine learning for transient discovery in Pan-STARRS1 difference imaging. *MNRAS*, 449(1):451–466, May 2015. doi: 10.1093/mnras/stv292.

M. Yamanaka, K. Maeda, M. Kawabata, M. Tanaka, K. Takaki, I. Ueno, K. Masumoto, K. S. Kawabata, R. Itoh, Y. Moritani, H. Akitaya, A. Arai, S. Honda, K. Nishiyama, F. Kabashima, K. Matsumoto, D. Nogami, and M. Yoshida. Early-phase Photometry and Spectroscopy of Transitional Type Ia SN 2012ht: Direct Constraint on the Rise Time. *ApJ*, 782(2):L35, Feb 2014. doi: 10.1088/2041-8205/782/2/L35.

O. Yaron and A. Gal-Yam. WISeREP—An Interactive Supernova Data Repository. *PASP*, 124(917):668, Jul 2012. doi: 10.1086/666656.

J.-J. Zhang, X.-F. Wang, J.-M. Bai, T.-M. Zhang, B. Wang, Z.-W. Liu, X.-L. Zhao, and J.-C. Chen. Optical and Ultraviolet Observations of the Narrow-lined Type Ia SN 2012fr in NGC 1365. *AJ*, 148(1):1, Jul 2014. doi: 10.1088/0004-6256/148/1/1.

K. Zhang and J. S. Bloom. deepCR: Cosmic Ray Rejection with Deep Learning. *ApJ*, 889 (1):24, Jan 2020. doi: 10.3847/1538-4357/ab3fa6.

K. Zhang, X. Wang, J. Zhang, T. Zhang, M. Ganeshalingam, W. Li, A. V. Filippenko, X. Zhao, W. Zheng, J. Bai, J. Chen, J. Chen, F. Huang, J. Mo, L. Rui, H. Song, H. Sai, W. Li, L. Wang, and C. Wu. Optical Observations of the Type Ia Supernova SN 2011fe in M101 for Nearly 500 Days. *ApJ*, 820(1):67, Mar. 2016. doi: 10.3847/0004-637X/820/1/67.

X. Zhao, X. Wang, K. Maeda, H. Sai, T. Zhang, J. Zhang, F. Huang, L. Rui, Q. Zhou, and J. Mo. The Silicon and Calcium High-velocity Features in Type Ia Supernovae from Early to Maximum Phases. *ApJS*, 220(1):20, Sep 2015. doi: 10.1088/0067-0049/220/1/20.

X. Zhao, K. Maeda, X. Wang, L. Wang, H. Sai, J. Zhang, T. Zhang, F. Huang, and L. Rui. The Oxygen Features in Type Ia Supernovae and Implications for the Nature of Thermonuclear Explosions. *ApJ*, 826(2):211, Aug 2016. doi: 10.3847/0004-637X/826/2/211.

W. Zheng, J. M. Silverman, A. V. Filippenko, D. Kasen, P. E. Nugent, M. Graham, X. Wang, S. Valenti, F. Ciabattari, P. L. Kelly, O. D. Fox, I. Shivvers, K. I. Clubb, S. B. Cenko, D. Balam, D. A. Howell, E. Hsiao, W. Li, G. H. Marion, D. Sand, J. Vinko, J. C. Wheeler, and J. Zhang. The Very Young Type Ia Supernova 2013dy: Discovery, and Strong Carbon Absorption in Early-time Spectra. *The Astrophysical Journal*, 778(1):L15, Nov 2013. doi: 10.1088/2041-8205/778/1/L15.

W. Zheng, I. Shivvers, A. V. Filippenko, K. Itagaki, K. I. Clubb, O. D. Fox, M. L. Graham, P. L. Kelly, and J. C. Mauerhan. Estimating the First-light Time of the Type Ia Supernova 2014J in M82. *ApJ*, 783(1):L24, Mar. 2014. doi: 10.1088/2041-8205/783/1/L24.

W. Zheng, A. V. Filippenko, J. Mauerhan, M. L. Graham, H. Yuk, G. Hosseinzadeh, J. M. Silverman, L. Rui, R. Arbour, R. J. Foley, B. Abolfathi, L. E. Abramson, I. Arcavi, A. J. Barth, V. N. Bennert, A. P. Brand el, M. C. Cooper, M. Cosens, S. P. Fillingham, B. J. Fulton, G. Halevi, D. A. Howell, T. Hsyu, P. L. Kelly, S. Kumar, L. Li, W. Li, M. A. Malkan, C. Manzano-King, C. McCully, P. E. Nugent, Y.-C. Pan, L. Pei, B. Scott, R. O. Sexton, I. Shivvers, B. Stahl, T. Treu, S. Valenti, H. A. Vogler, J. L. Walsh, and X. Wang. Discovery and Follow-up Observations of the Young Type Ia Supernova 2016coj. *The Astrophysical Journal*, 841(1):64, May 2017. doi: 10.3847/1538-4357/aa6dfa.

W. Zheng, P. L. Kelly, and A. V. Filippenko. An Empirical Fitting Method to Type Ia Supernova Light Curves. III. A Three-parameter Relationship: Peak Magnitude, Rise Time, and Photospheric Velocity. *ApJ*, 858(2):104, May 2018a. doi: 10.3847/1538-4357/aabaeb.

W. Zheng, P. L. Kelly, and A. V. Filippenko. An Empirical Fitting Method to Type Ia Supernova Light Curves. III. A Three-parameter Relationship: Peak Magnitude, Rise Time, and Photospheric Velocity. *ApJ*, 858(2):104, May 2018b. doi: 10.3847/1538-4357/aabaeb.